

HYDROGEN PRODUCTION FROM BIOMASS FOR USE IN SOLID OXIDE FUEL CELLS

by

Anwar Sattar

A thesis submitted to the University of Birmingham for the
degree of DOCTOR OF PHILOSOPHY

School of Chemical Engineering
College of Engineering and Physical Sciences
University of Birmingham

June 2015

UNIVERSITY OF
BIRMINGHAM

University of Birmingham Research Archive

e-theses repository

This unpublished thesis/dissertation is copyright of the author and/or third parties. The intellectual property rights of the author or third parties in respect of this work are as defined by The Copyright Designs and Patents Act 1988 or as modified by any successor legislation.

Any use made of information contained in this thesis/dissertation must be in accordance with that legislation and must be properly acknowledged. Further distribution or reproduction in any format is prohibited without the permission of the copyright holder.

Abstract

This thesis presents an investigation into the use of four biochars (wood, rapeseed, miscanthus and sewage sludge) to generate a hydrogen-rich syngas that can be utilised in solid oxide fuel cells. Experimental investigations are split into three sections; (i) biochar characterisation, (ii) biochar gasification and (iii) the use of syngas in a single, microtubular solid oxide fuel cell. Characterisation revealed that wood biochar had the highest carbon content at 71.58%, sewage sludge had the lowest at 30% and rapeseed had the highest mineral content. The effects of temperature on gasification were investigated over a temperature range of 650 – 850°C at a steam flow of 172 g min⁻¹ kg⁻¹ biochar and effects of steam flow at 850°C over a steam flow range of 54 – 277 g min⁻¹ kg⁻¹ biochar. Results revealed the transient behaviour of the process as well as the effects of temperature and steam flow. Dry gas yield increases with both temperature and steam flow, with wood biochar giving maximum values of 2.58 m³ kg⁻¹ at 850°C and 277 g min⁻¹ kg⁻¹ biochar. Hydrogen content decreases at high temperatures and peak hydrogen content, 58.7%, was achieved at 750°C from the rapeseed biochar.

Syngas from wood and rapeseed biochars was collected and used in a microtubular solid oxide fuel cell. Gas from rapeseed had a negative effect on the fuel cell performance, leading to a 28% decrease in the performance over the 30 minutes of potentiostatic operation of 0.7 V. Gas from wood biochar was more suitable and was used in the solid oxide fuel cell for approximately 500 minutes, giving an initial electrical efficiency of 16.8% at 0.7 V.

بِسْمِ اللَّهِ الرَّحْمَنِ الرَّحِيمِ

1. Blessed is He in Whose Hand is the dominion, and He is Able to do all things.
2. Who has created death and life, that He may test you which of you is best in deed. And He is the All-Mighty, the Oft-Forgiving;
3. Who has created the seven heavens one above another, you can see no fault in the creations of the Most Beneficent. Then look again: "Can you see any rifts?"
4. Then look again and yet again, your sight will return to you in a state of humiliation and worn out.

In loving memory of Bashir Osman

1988-2015

This thesis is dedicated to

My Family

My Friends

My Teachers

Acknowledgements

First and foremost I want to acknowledge Allah Almighty for endowing me with the ability, patience and inspiration to carry out this research. It was not always easy but 'Verily in the remembrance of Allah do hearts find peace'.

I want to express my deep and sincere gratitude towards my supervisor Professor Joseph Wood for guiding me through the process. His kind and helpful demeanour enabled me to achieve what I would not have otherwise. Special thanks also go towards my co-supervisors Dr Gary A. Leeke and Professor Andreas Hornung, both of whom were instrumental in my research.

I would like to thank my family for their support and patience throughout the years, in particular, my father, Mohammed Sattar, who has always inspired me to achieve.

I would like to thank my friends, in particular, Dr Naser Al-Mufachi who has become like a brother to me. The PhD would not have been the same without their presence.

Finally, I would like to thank the School of Chemical Engineering at the University of Birmingham for giving me the opportunity to carry out this PhD.

Publications

The following publications were published during the course of the PhD

Journal Articles

A. Sattar, G. A. Leeke, A. Hornung, J. Wood. Steam Gasification of Rapeseed, Wood, Sewage Sludge and Miscanthus Biochars for the Production of a Hydrogen-Rich Syngas. *Biomass and Bioenergy* 69, P276-286

Oral Presentations

A. Sattar. Hydrogen Production from Biochar for Use in Solid Oxide Fuel Cells. Biorefinery I: Chemicals and Materials from Thermo-Chemical Biomass Conversion and Related Processes. 29/09/2015. Crete, Greece.

Posters

A. Sattar, G. A. Leeke, A. Hornung, J. Wood. Hydrogen and Synthesis Gas Production from Biomass for Use in Solid Oxide Fuel Cells. SuperGen Bioenergy Hub. 5th November 2014, Aston University, Birmingham.

A. Sattar, G. A. Leeke, A. Hornung, J. Wood. Hydrogen and Synthesis Gas Production from Intermediate Pyrolysis Biochars for use in Solid Oxide Fuel Cells. 22nd European Biomass Conference and Biomass. 23-26th June 2014, Hamburg, Germany

A. Sattar, G. A. Leeke, A. Hornung, J. Wood. Hydrogen and Synthesis Gas Production from Biomass for Use in Solid Oxide Fuel Cells. 9th International Hydrogen and Fuel Cell Conference. 20-21st March 2013, Millennium Point, Birmingham

A. Sattar, W. Bujalski, K. Kendall, A. Hornung. Hydrogen and Synthesis Gas Production from Biomass and the Related Clean Up. 7th International Hydrogen and Fuel Cell Conference. 2011, NEC

Table of Contents

1	Introduction	1
1.1	Motivation.....	3
1.2	Scope of Research and Thesis Structure.....	4
2	Literature Review	6
2.1	Pyrolysis.....	6
2.1.1	Slow Pyrolysis.....	8
2.1.2	Fast pyrolysis.....	8
2.1.3	Intermediate Pyrolysis	9
2.1.4	Intermediate Pyrolysis Conclusions.....	11
2.2	Biochar	13
2.2.1	Biochar Structure and Engineering.....	13
2.2.2	Biochar Properties	15
2.2.3	Biochar Conclusions.....	17
2.3	Gasification	17
2.3.1	Air and Oxygen Gasification	19
2.3.2	Gasification Reactions.....	19
2.3.3	Boudouard Reaction.....	21
2.3.4	Water Gas Reaction	21
2.3.5	Water Gas Shift Reaction	22
2.3.6	Char combustion Reaction	22
2.4	Reactors for Biomass Gasification	22
2.4.1	Operating principles of Biomass Gasifiers.....	23
2.5	Steam Gasification of Biomass	25
2.5.1	Non Catalytic Steam Gasification	26
2.5.2	Dolomite Catalytic Steam Gasification.....	27
2.5.3	Thermal Decomposition of Dolomite.....	30
2.6	Biochar Gasification	32
2.6.1	Effects of Steam Gasification on Biochar Structure	35
2.6.2	Effects of Mineral Content on Biochar Reactivity.....	36
2.7	Conclusions.....	37
2.8	Fuel Cells	37

2.9	Fuel Cell Fundamentals	38
2.10	Solid Oxide fuel cells.....	40
2.11	Syngas Powered Solid Oxide Fuel Cells: A Literature Review.....	41
2.12	Effects of Syngas on the Performance of Solid Oxide Fuel Cells.....	42
2.13	Effects of Syngas Constituents on the performance of Solid Oxide Fuel Cells	44
2.13.1	Effects of Carbon Monoxide Content on Solid Oxide Fuel Cell Performance.....	44
2.13.2	Effects of Carbon Dioxide on Solid Oxide Fuel Cell Performance	47
2.13.3	Effects of Methane on Solid Oxide Fuel Cell Performance.....	48
2.13.4	Conclusions.....	50
2.14	Effects of Contaminants on the Performance of Solid Oxide Fuel Cells ...	51
2.14.1	Effects of Phosphorus Contaminants on Solid Oxide Fuel Cell Performance.....	51
2.14.2	Effects of Hydrogen Sulphide on Solid Oxide Fuel Cell Performance	52
2.14.3	Effects of Ammonia on the Performance of Solid Oxide Fuel Cells....	54
2.14.4	Effects of Hydrochloric Acid on the Performance of Solid Oxide Fuel Cells	56
2.14.5	Effects of Syngas Trace Species on the Performance of Solid Oxide Fuel Cells	57
2.14.6	Conclusions.....	60
3	Materials and Methods.....	61
3.1	Chapter Overview.....	61
3.2	Introduction	61
3.3	Biochars	63
3.4	Dolomite	64
3.5	Solid Oxide Fuel Cells	64
3.6	Characterisation of Biochars	66
3.6.1	Elemental Analysis and Ash Content.....	66
3.6.2	BET Surface Area Analysis	67
3.6.3	Mineral Content	67
3.6.4	Volatile Content	68
3.6.5	Microstructure Analysis.....	68

3.6.6	Particle Size Distribution.....	69
3.6.7	Higher Heating Value.....	69
3.6.8	Bulk Density Analysis	70
3.7	Calcination of Dolomite	70
3.7.1	Characterisation of Dolomite	71
3.7.2	Thermo Gravimetric Analysis.....	71
3.8	Characterisation of Solid Oxide Fuel Cell.....	72
3.9	Experimental Rig Design.....	72
3.9.1	Valves and Tubing	73
3.9.2	Furnace	73
3.9.3	Reactor Design	74
3.10	Steam Generator	78
3.10.1	Steam Flow Calibration	79
3.11	Condensers.....	80
3.12	Gasification Experiments	82
3.12.1	Gas collection and Transfer.....	83
3.12.2	Injection into the Refinery Gas Analyser.....	84
3.12.3	Gas Analysis	85
3.12.4	Correction Factor for Carbon Dioxide	86
3.13	Data Processing.....	88
3.14	Solid Oxide Fuel Cell Testing.....	89
3.14.1	Method of Preparation	89
3.14.2	Fuel Delivery System.....	91
3.14.3	Buffer Tank design	92
3.14.4	Providing Constant Flow.....	93
3.14.5	Solid Oxide Fuel Cell Test Rig.....	94
3.14.6	Test Programme and Cylinder Change	94
3.15	Other Experimental Methods	95
3.15.1	Removing Alkali and Alkaline Earth Metallic Species.....	95
3.15.2	Hydrogen Sulphide Detection.....	96
4	Characterisation of Materials.....	97
4.1	Chapter Overview.....	97

4.2	Introduction	97
4.3	Elemental Analysis	97
4.3.1	Mineral Content Analysis	100
4.3.2	Higher Heating Value.....	101
4.3.3	Brunauer-Emmet-Teller (BET) Surface Area	102
4.3.4	Volatile Content Analysis	102
4.3.5	Removal of AAEM Species through Acid Washing.....	103
4.3.6	Scanning Electron Microscopy Analysis	104
4.3.7	Particle Size Distribution and Bulk Density	106
4.4	Characterisation of Dolomite	108
4.4.1	X-Ray Fluorescence Spectroscopy.....	108
4.4.2	BET Surface Area and Bulk Density Analysis.....	110
4.4.3	Particle Size Distribution.....	111
4.4.4	Thermo Gravimetric Analysis.....	112
4.5	Characterisation of Solid Oxide Fuel Cells	114
4.6	Conclusions.....	115
5	Steam Gasification of Biochar: Effects of Temperature and Steam Flow	117
5.1	Chapter Overview.....	117
5.2	Introduction	118
5.3	Effects of Temperature on Product Flow Rate	119
5.4	Effects of Temperature on Transient Gas Composition.....	121
5.4.1	Transient Gas Composition: 650°C	122
5.4.2	Transient Gas Composition: 750°C	123
5.4.3	Transient Gas Composition: 850°C	124
5.5	Effects of Temperature on Gas Composition	128
5.5.1	Effects on Hydrogen	128
5.5.2	Effects on Carbon Monoxide	131
5.5.3	Effects of Temperature on Carbon Dioxide.....	134
5.5.4	Effects of Temperature on Methane	135
5.6	Effects of Temperature on Hydrocarbon Content, Conversion and Associated Results.....	137
5.7	Effects of Temperature on Biochar Conversion, Carbon Conversion and Carbon Conversion Efficiency.....	140

5.7.1	Biochar Conversion	140
5.7.2	Carbon Conversion and Carbon Conversion Efficiency.....	141
5.7.3	Effect of Temperature on Elemental Analysis.....	144
5.8	Effects of Steam Flow on Steam Gasification of Biochar	146
5.8.1	Effects of Steam Flow on Product Flow	146
5.8.2	Effect of Steam Flow on Transient Gas Composition	148
5.8.1	Effects of Steam Flow on Gas Composition	150
5.8.2	Pyrolysis Composition	151
5.8.3	Effects of Steam Flow on Hydrogen Composition.....	152
5.8.4	Effects of Steam Flow on Carbon Monoxide Composition.....	155
5.8.5	Effects of Steam Flow on Carbon Dioxide Composition	156
5.8.6	Effects of Steam Flow on Methane Composition	158
5.8.7	Effects of Steam Flow on Hydrocarbon content, Conversion and Associated Results.....	159
5.9	Effects of Steam Flow on Biochar Conversion, Carbon Conversion and Carbon Conversion Efficiency.....	161
5.9.1	Biochar Conversion	161
5.9.2	Carbon Conversion and Carbon Conversion Efficiency.....	162
5.10	Effect of Steam Flow on Elemental Analysis.....	164
5.11	Conclusions	166
6	Effects of Alkali and Alkaline Earth Metallic Species, Dolomite, and Particle Size on Steam Gasification of Biochar	169
6.1	Chapter Overview.....	169
6.2	Biochar Reactivity.....	170
6.3	Effects of Alkali and Alkaline Earth Metallic Species	172
6.3.1	Effects of Alkali and Alkaline Earth Metallic Species on Product Flow.	173
6.3.2	Effect of AAEM Species on Product Composition and Associated Results 175	
6.4	Effects of Particle Size on the Steam Gasification of Biochar	179
6.4.1	Effects of Particle Size on Product Flowrate.....	180
6.4.2	Effects of Particle Size on Product Composition, Carbon Conversion Efficiency and Associated Results	181
6.5	Effects of Dolomite	184

6.6	Effects of Dolomite on Product Composition	184
6.7	Conclusions.....	188
7	Performance of Solid Oxide Fuel Cells using Syngas from Steam Gasification of Biochar	191
7.1	Chapter Overview.....	191
7.2	Introduction	191
7.3	Steam Gasification Experiments	192
7.3.1	Determination of Actual Compositions.....	193
7.4	Performance of a Solid Oxide Fuel Cell with Syngas from Rapeseed Biochar	194
7.5	Performance of a Solid Oxide Fuel Cell with Syngas from Wood Pellet Biochar.....	201
7.5.1	Performance of a Solid Oxide Fuel Cell on WPB Syngas for an Extended Period	204
7.6	Conclusions.....	208
7.7	Summary of Mass and Energy Balances	210
7.7.1	Overview.....	210
7.7.2	Mass Balance	210
7.7.3	Mass Balance Discussions	212
7.8	Energy Balance Summary.....	212
7.8.1	Energy Balance Discussions	213
8	Conclusions and Recommendations.....	216
8.1	Chapter Overview.....	216
8.2	Further Work and Recommendations.....	219
9	References.....	222
10	Appendices	232
10.1	Appendix I: Calibration Curves for the Refinery Gas Analyser.....	233
10.2	Appendix II: Calculating the Mass Loss with Conversion.....	235
10.3	Appendix III: Mass and Energy Balances.....	242

List of Figures

Figure 2.1: Schematic of the Pyroformer reactor [25].....	10
Figure 2.2: Micrographs from a Scanning Electron Microscope showing the structure of switchgrass and its biochars; (a) feedstock, (b) slow pyrolysis (c) fast pyrolysis and (d) gasification [35]	15
Figure 2.3: Ternary diagram showing the likely products of each gasifying medium as well as fast and slow pyrolysis [37].....	18
Figure 2.4: Comparison of syngas composition from Limestone, Olivine and Dolomite catalysts [45]	29
Figure 2.5: Comparison of the reactivity of peat and biomass char. Adapted from [37]	33
Figure 2.6: Schematic of a Solid Oxide Fuel Cell [64]	38
Figure 2.7: showing the two types of SOFC geometries (left) tubular and (right) planar [68]	41
Figure 2.8: Effects of various concentrations of CO and H ₂ on the performance of a Ni-YSZ SOFC at 1000°C [11]	46
Figure 2.9: Ternary diagram showing regions where carbon deposition is likely to occur thermodynamically [86].....	50
Figure 2.10: Effects of NH ₃ on the performance of a SOFC at various temperatures and concentrations [103]	55
Figure 2.11: Effects of AsH ₃ on the performance of solid oxide fuel cells over an extended period of time. Adapted from [91]	59
Figure 3.1: Biochar storage and cover in a desiccators.....	63
Figure 3.2: Biochar appearance where; (a) WPB, (b) RSB, (c) SSB and (d) MCB....	63
Figure 3.3: Microtubular solid oxide fuel cell, where; the black area is the cathode, the white strips are the separation boundaries and the grey represent non-catalytically active areas.....	65
Figure 3.4: Cross section of the microtubular solid oxide fuel cell.....	65
Figure 3.5: Pelletised Biochar for XRF Analysis	67
Figure 3.6: Furnace used in the experiments	74
Figure. 3.7: Furnace ramp rate.....	74

Figure 3.8: Schematic of reactor complex, where (a) B60 connecting cone, (b) reactor and (c) sample holder. All measurements are in mm	76
Figure 3.9: Glass to metal joint used as a connector to connect the quartz reactor complex to metal tubes	77
Figure 3.10: Steam flow profile as a function of pump setting	79
Figure 3.11: Downstream process items; (left to right), primary condenser, secondary condenser and bubble flowmeter.	80
Figure 3.12: Top picture of the gasification rig. Bottom, schematic of the gasification rig, where; 1; deionised water reservoir, 2; pump, 3; zero grade nitrogen supply, 4; pre-heater, 5; temperature read out, 6; Furnace, 7; quartz sample holder, 8; quartz reactor, 9; condenser and ice bath, 10; secondary condenser, 11; water trap, 12; bubble flow meter, 13; gas bag.	81
Figure 3.13: 50 ml SGE syringe with a Luer lock to Swagelok fitting.....	84
Figure 3.14: Gas collection method using serum a bottle.....	84
Figure 3.15: Schematic of the RGA valves and columns [114].....	86
Figure 3.16: Peak areas given by the RGA for the two methods of gas collection to derive a correlation for the dissolution of CO ₂	87
Figure 3.17: Schematic and photo of the SOFC ceramic manifold.....	91
Figure 3.18: Buffer tank design and syngas transfer mechanism.....	92
Figure 3.19: Induced flowrate of syngas by pumping water into the buffer tank.....	93
Figure 3.20: SOFC test rig, where; (1) deionised water reservoir, (2) peristaltic pump, (3) bottled gas supply, (4) buffer tank, (5) mixer, (6) dryer, (7) ceramic manifold, (8) microtubular SOFC and (9) furnace	94
Figure 4.1: SEM micrographs of WPB and RSB at magnifications of (a) WPB 120X, (b) RSB 86X, (c) WPB 800X and (d) RSB 800X.....	105
Figure 4.2: SEM micrographs of biochars, where (a) MCB 100X, (b) MCB 800X, (c) SSB 100X and (d) SSB 1000X	106
Figure 4.3: TGA and DTG analysis of the natural (uncalcined) dolomite.....	113
Figure 4.4: TGA and DTG analysis of the calcined dolomite	114
Figure 4.5: EDS micrograph of the SOFC anode	115
Figure 5.1: Effects of temperature on product flow (2 minute average) of (a) WPB, (b) RSB (c) SSB and (d) MCB at 172 g min ⁻¹ kg ⁻¹ biochar.....	120

Figure 5.2: Transient gas composition at 650°C for (a) WPB, (b) RSB, (c) SSB and (d) MCB at a steam flow of 172 g min ⁻¹ kg ⁻¹ biochar.....	123
Figure 5.3: Transient gas composition at 750°C for (a) WPB, (b) RSB, (c) SSB and (d) MCB at a steam flow of 172 g min ⁻¹ kg ⁻¹ biochar.....	124
Figure 5.4: Transient gas composition at 850°C for (a) WPB, (b) RSB, (c) SSB and (d) MCB at a steam flow of 172 g min ⁻¹ kg ⁻¹ biochar.....	125
Figure 5.5: Effects of temperature on H ₂ volume fraction at a steam flow of 172 g min ⁻¹ kg ⁻¹ biochar.....	130
Figure 5.6: Effects of temperature on the CO volume fraction at 650 - 850°C and a constant steam flow of 172 g min ⁻¹ kg ⁻¹ biochar	133
Figure 5.7: Effects on temperature on CO ₂ volume fraction at 650 - 850°C using a constant steam flow of 172 g min ⁻¹ kg ⁻¹ biochar	135
Figure 5.8: Effects of temperature on CH ₄ volume fraction at 650 - 850°C using a constant steam flow of 172 g min ⁻¹ kg ⁻¹ biochar	136
Figure 5.9: Effects of temperature on biochar conversion at 650 - 850°C at a constant steam flow of 172 g min ⁻¹ kg ⁻¹ biochar.....	141
Figure 5.10: Effects of temperature on carbon conversion and carbon efficiency at 650, 750 and 850°C for (a) WPB, (b) RSB, (c) SSB and (d) MCB. The steam flow was kept constant at 172 g min ⁻¹ kg ⁻¹ biochar	143
Figure 5.11: Comparison of tar fouling the sample holder; (left to right) clean sample holder - sample holder after RSB gasification and sample holder after WPB gasification. Experiments were carried out 850°C using a steam flow rate of 172 g min ⁻¹ kg ⁻¹ biochar.....	143
Figure 5.12: Effects of steam flow on the product flow (2 minute average) of (a) WPB, (b) RSB, (c) SSB and (d) MCB at a temperature of 850°C, where S ₀ , S ₂ and S ₅ are 0, 54 and 277 g min ⁻¹ kg ⁻¹ biochar steam flowrates.....	148
Figure 5.13: Effects of steam flow on the transient gas composition at 850°C, where (a) and (b) are WPB at 54 and 277 g min ⁻¹ kg ⁻¹ biochar respectively and (c) and (d) are RSB at the same steam flowrates.....	150
Figure 5.14: Effects of steam flow on the H ₂ composition of the syngas from the four biochars at 850°C over a steam flow range of 54 - 277 g min ⁻¹ kg ⁻¹ biochar	154

Figure 5.15: Effects of steam flow on the volume fraction of CO at 850°C over a temperature range of 54 - 277 g min ⁻¹ kg ⁻¹ biochar	156
Figure 5.16: Effects of steam flow on the volume fraction of CO ₂ at 850°C over a steam flow range of 54 - 277 g min ⁻¹ kg ⁻¹ biochar	157
Figure 5.17: Effects of steam flow on the volume fraction of CH ₄ at 850°C over a steam flow range of 54 - 277 g min ⁻¹ kg ⁻¹ biochar	158
Figure 5.18: Effects of steam flow on the biochar conversion at 850°C over a steam flow range of 54 - 277 g min ⁻¹ kg ⁻¹ biochar	162
Figure 5.19: Effects of steam flow at 850°C on the carbon conversion, and carbon conversion efficiency of (a) WPB, (b) RSB, (c) SSB and (d) MCB at 54, 172 and 277 g min ⁻¹ kg ⁻¹ biochar steam flow.....	164
Figure 6.1: Changes in Reactivity with conversion (2 minute average) at 850°C and 172 g min ⁻¹ kg ⁻¹ biochar, where R is the reactivity	172
Figure 6.2: Effects of AAEM species on the two minute average product flowrate produced by the rapeseed biochar, where RSB is the original biochar, RSB _c is by carbon basis and RSB _m is by mass basis. Mass basis and carbon basis steam flows = 172 and 285 g min ⁻¹ kg ⁻¹ biochar.....	174
Figure 6.3: Effects of removal of AAEM species from Rapeseed biochar at 850°C and a steam flow of 0.516 g min ⁻¹ , corresponding to 172 g min ⁻¹ kg ⁻¹ biochar on a mass basis and 285 g min ⁻¹ kg ⁻¹ carbon on a carbon basis. RSB _m and RSB _c refer to mass and carbon basis respectively	177
Figure 6.4: Effect of particle size on product flowrate (2 minute average) at 850°C and 172 g min ⁻¹ kg ⁻¹ biochar, where (a) RSB, (b) SSB and (c) MCB.....	181
Figure 6.5: Effects of particle size on syngas composition at 850°C and a steam flowrate of 172 g min ⁻¹ kg ⁻¹ biochar	182
Figure 6.6: Effects of the addition of natural and calcined dolomite to wood pellet biochar at 850°C at two different steam flows, where (a) natural dolomite at 172 g min ⁻¹ kg ⁻¹ biochar steam flow, (b) calcined dolomite at the same steam flow, (c) natural dolomite at 277 g min ⁻¹ kg ⁻¹ biochar steam flow and (d) calcined dolomite at the same steam flowrate	186

Figure 6.7: Effects of Dolomite on the dry gas yield from WPB at 850°C and steam flows of (a) 172 and (b) 277 g min ⁻¹ kg ⁻¹ biochar respectively, where ND is natural dolomite and CD is calcined dolomite	187
Figure 7.1: Performance of microtubular SOFC on pure H ₂ 60 ml min ⁻¹ and RSB syngas at 70 ml min ⁻¹ and 800°C.....	197
Figure 7.2: Results of the lead acetate test confirming the presence of H ₂ S, (left) N ₂ , (right) RSB syngas	198
Figure 7.3: SOFC current and fuel utilisation using the RSB syngas at 0.7 V, at 800°C	199
Figure 7.4: Electrical and overall efficiencies of the microtubular SOFC operating on RSB syngas at 0.7 V and 800°C	201
Figure 7.5: Performance of a microtubular SOFC using syngas from WPB at 800°C	203
Figure 7.6: SOFC performance showing potentiostatic mode and fuel utilisation at 0.7 V for WPB syngas at 800°C	204
Figure 7.7: Initial and final performance of the SOFC using pure H ₂ at 800°C	206
Figure 7.8: Initial and final performance of the SOFC using WPB syngas at 800°C.....	207
Figure 7.9: Operation of the SOFC in potentiostatic mode for an extended period of time at 800°C.....	208
Figure 10.1: RGA calibration curve for hydrogen	233
Figure 10.2. RGA calibration curve for carbon monoxide.....	233
Figure 10.3: RGA calibration curve for carbon dioxide	234
Figure 10.4: RGA calibration curve for methane	234
Figure 10.5: Energy balance over the process	249
Figure 10.6: Specific heat capacity of biochar as a function of temperature [170]...	252

List of Tables

Table 2-1: Comparison of the three different pyrolysis modes [16] [17]	7
Table 2-2: Product Distribution from Intermediate pyrolysis of sewage sludge and other biomass mixtures	12
Table 2-3: Heating values of the product gases given by each gasifying medium	18
Table 2-4: Summary of the main gasification reactions and their enthalpies of reaction at standard temperature and pressure of 298.15 K and 101.3 kPa [14] [35]	20
Table 2-5: Summary of advantages and disadvantages of various biomass gasifiers [39] [40]	24
Table 2-6: The various types of fuel cells and their operating principles as well as their half reactions at the electrodes [64].....	39
Table 3-1: Information regarding the acquisition of precursor biomass substrates of the biochars.....	62
Table 3-2: Dimensions and properties of the reactor.....	78
Table 3-3: Operational Parameters of the steam generator	78
Table 3-4. Areas given by the RGA for the two collection methods.....	87
Table 4-1: Elemental analysis of the biochars	99
Table 4-2: Mineral content of the biochars	100
Table 4-3: Higher Heating Values and other characteristics of the biochars	101
Table 4-4: Characteristics of the rapeseed biochar after acid washing	104
Table 4-5: Mineral content of the rapeseed biochar after acid washing	104
Table 4-6: Particle size distribution of the biochars showing powdered and pellet form	107
Table 4-7: Bulk density of the biochars	108
Table 4-8: Mineral content of the dolomite samples used in this study as found using X-ray Fluorescence Spectroscopy.....	110
Table 4-9: Comparison of Derbyshire dolomite to other uncalcined dolomites from around the world, where Ch D is Chinese, Sw D is Swedish, In D is Indian, Ma D is Malaysian, and Fn D is Finnish Dolomite [137].	110
Table 4-10: BET surface area and bulk density of the dolomite samples.....	111
Table 4-11: Effect of calcination on particle size distribution	112
Table 4-12: EDS analysis of a microtubular SOFC anode.	115

Table 5-1: Effects of temperature on the Arrhenius rate constants for the three ‘char consuming’ gasification reactions assuming first order reactions [144].	120
Table 5-2: Standard thermodynamic properties of chemicals at 298K and 1.01kPa [147]	132
Table 5-3: Effects of temperature on hydrocarbon content, dry gas yield, higher heating value and H ₂ /CO ratio at a steam flow of 172 g min ⁻¹ kg ⁻¹ biochar. The results are the mean of three experiments and the error represents the maximum deviation for that particular result.	139
Table 5-4: Effects of temperature on the elemental composition of the wood pellet biochar at 172 g min ⁻¹ kg ⁻¹ biochar	144
Table 5-5: Effects of temperature on the elemental composition of the rapeseed biochar at 172 g min ⁻¹ kg ⁻¹ biochar	145
Table 5-6: Effects of temperature on the elemental composition of the sewage sludge biochar at 172 g min ⁻¹ kg ⁻¹ biochar	145
Table 5-7: Effects of temperature on the elemental composition of the miscanthus biochar at 172 g min ⁻¹ kg ⁻¹ biochar	145
Table 5-8: Pyrolysis gas composition from the biochars at 850°C where the error represents the maximum deviation from the mean of an average of three experiments	152
Table 5-9: Effects of steam flow on hydrocarbon content, dry gas yield, higher heating value and H ₂ /CO ratio at 850°C, where S2 and S5 are; 54 and 277 g min ⁻¹ kg ⁻¹ biochar respectively	159
Table 5-10: Effects of temperature on the elemental composition on the wood pellet biochar at 850°C, where S2, S3 and S5 correspond to 54, 172 and 277 g min ⁻¹ kg ⁻¹ biochar respectively	165
Table 5-11: Effects of temperature on the elemental composition on the rapeseed biochar at 850°C, where S2, S3 and S5 correspond to 54, 172 and 277 g min ⁻¹ kg ⁻¹ biochar respectively	165
Table 5-12: Effects of temperature on the elemental composition on the sewage sludge biochar at 850°C, where S2, S3 and S5 correspond to 54, 172 and 277 g min ⁻¹ kg ⁻¹ biochar respectively	166

Table 5-13: Effects of temperature on the elemental composition on the miscanthus biochar at 850°C, where S2, S3 and S5 correspond to 54, 172 and 277 g min ⁻¹ kg ⁻¹ biochar respectively.....	166
Table 6-1: Effects of AAEM removal on carbon conversion, carbon conversion efficiency, H ₂ /CO ratio and higher heating values at 850°C.	178
Table 6-2: Effects of particle size on hydrocarbon content, dry gas yield, carbon conversion efficiency, H ₂ /CO ratio and higher heating values for rapeseed, sewage sludge and miscanthus biochars at 850°C and 172 g min ⁻¹ kg ⁻¹ biochar steam flow	183
Table 7-1: Syngas compositions on a N ₂ -free basis.....	193
Table 7-2: Actual syngas compositions for RSB and WPB	194
Table 7-3: Summary of mass balance for the gasifier	211
Table 7-4: Summary of mass balance for the solid oxide fuel cell.....	211
Table 7-5: Energy balance for the steam gasification of WPB at 850°C.....	215
Table 10-1: Changes in constituent composition with time.....	235
Table 10-2: Individual constituent flowrates	236
Table 10-3: Moles of each constituent produced per minute.....	238
Table 10-4: Reactivity calculation.....	240
Table 10-5: Biochar Composition	242
Table 10-6: Syngas composition and moles.....	243
Table 10-7: Spent biochar composition	243
Table 10-8: Composition of gas from devolatilisation	246
Table 10-9: Final gas minus the devolatilisation contribution	246
Table 10-10: Component balance	247
Table 10-11: Syngas composition leaving the SOFC assuming only H ₂ fraction is used up	248
Table 10-12: Thermodynamic properties of constituents [165] [169].....	250

List of Abbreviations

AAEM	Alkali and alkaline earth metallic species
BET surface area	Brunauer, Emmett and Teller surface area ($\text{m}^2 \text{g}^{-1}$)
CC	Carbon conversion (%)
CCE	Carbon conversion efficiency (%)
CD	Calcined dolomite
DGY	Dry gas yield
HC	Hydrocarbons (excluding CH_4)
HHV	Higher heating value (MJ m^{-3})
MCB	Miscanthus biochar
ND	Natural dolomite (uncalcined)
η_e	Electrical efficiency
η_o	Overall efficiency
OCV	Open circuit voltage (V)
RSB	Rapeseed biochar
RSB_{AW}	Acid washed rapeseed biochar
S/B ratio	Steam-to-biomass ratio ($\text{g steam min}^{-1} \text{kg}^{-1} \text{biomass}$)
S/C ratio	Steam-to-carbon ratio ($\text{g steam min}^{-1} \text{kg}^{-1} \text{biomass}$)
SSB	Sewage sludge biochar
S0	Steam flow of $0 \text{ g min}^{-1} \text{kg}^{-1} \text{biochar}$
S2	Steam flow of $54 \text{ g min}^{-1} \text{kg}^{-1} \text{biochar}$
S3	Steam flow of $172 \text{ g min}^{-1} \text{kg}^{-1} \text{biochar}$
S5	Steam flow of $277 \text{ g min}^{-1} \text{kg}^{-1} \text{biochar}$
U_f	Utilisation of fuel
WGSR	Water gas shift reaction
WPB	Wood pellet biochar
YSZ	Ytria stabilised Zirconia

1 Introduction

The global supply of energy has been dominated by fossil fuels. In 2013, approximately 87% of the world's primary energy demand was supplied by fossil fuels; with coal, oil and natural gas providing around 30, 33 and 24% of that energy, respectively [1]. Fossil fuel combustion leads to the release of greenhouse gases (GHG), in particular CO₂, which has a warming effect on the Earth's climate [2]. Fossil fuels, by their very nature are unsustainable as they take millions of years to develop. Their finite nature and the release of harmful gases during combustion have led to two pressing issues facing the world; (i) to provide a safe and reliable supply of energy and (ii) to mitigate climate change [3].

Both fossil fuel depletion and climate change can be mitigated in two ways; (i) use of renewable resources and (ii) increased energy efficiency. Renewable resources such as wind, solar, hydro and biomass are abundant and their share of the total supply of world energy is increasing. According to the BP statistical review of world energy statistics 2014, renewable electricity from modern renewable sources such as wind, solar and biomass accounted for 5.3% of the world's electricity supply, an increase of 16.7% from 2012 [1]. Generally, renewable technologies suffer from intermittence but biomass is one of the few sources that is both abundant, and can be available on demand [4].

Biomass is defined as the only source of carbon if fossil fuels are excluded [5]. The term biomass is used to describe living or recently living matter. It encompasses plants and wastes from living organisms, and unlike fossil fuels, does not take millions of years to develop. Biomass energy is able to offer many advantages; the

energy in the biomass originates from the sun and is captured by plants to metabolise carbon dioxide in the atmosphere. Plants are able to reproduce, making biomass a renewable source of energy. Energy generation from biomass reduces the amount of CO₂ released, given that the release of carbon is offset by its consumption during photosynthesis [6]. A disadvantage of biomass energy can be the use of crops grown on agricultural land which can lead to competition with food, leading to an increase food prices [7]. Biomass is also a flexible fuel as it can be used for heating purposes, converted to transportation fuels or used to generate electricity. Biomass is mostly used in traditional applications such as cooking and heating and could account for up to 14% of the world's total energy use [8].

Biomass conversion methods can be split into three types; thermochemical, biochemical and mechanical conversion methods [9]. Thermochemical conversions encompass pyrolysis, gasification, combustion and liquefaction. Biochemical conversions include fermentation for ethanol and digestion for biogas production. Mechanical extraction includes oil extraction which may be followed by chemical treatment to produce bio-diesel [9]. The choice of conversion method depends on the final application. Gasification of biomass produces a gas which contains mainly H₂, CO, CH₄ CO₂, alongside smaller quantities of hydrocarbons and tars. This gas mixture is known as syngas and can be utilised in many applications such as fuel cells to generate electricity.

Fuel cells are electrochemical devices that convert the chemical energy in a fuel directly into electrical energy [10]. Most of electricity is generated using combustion processes that require many steps before the chemical energy in the fuel is converted into electrical energy, this makes the process inefficient. By converting the

chemical energy directly into electrical energy, fuel cells achieve much higher efficiencies. Solid oxide fuel cells (SOFCs) are particularly attractive since they are able to utilise syngas to generate electricity thus enabling the coupling of a renewable technology with an efficient device to be achieved. This combination is ideal for long term sustainability and provides a safe and reliable supply of energy.

The preferred fuel for SOFCs is hydrogen [11] therefore, increasing the content of H₂ in the syngas is vital. Air gasification generally gives a low H₂ content but this can be increased by using steam as the gasifying medium. It can be further increased by utilising biochar as the biomass material. Biochar is a by-product of pyrolysis and consists mainly of carbon, it has very little volatile matter and is reactive enough to be gasified by steam [12]. Previous work has shown that greater than 50% H₂ by volume, can be realised by gasifying biochar with steam [13] [14]. This is possible since the main reaction is the steam-char, or water-gas reaction (reaction 2-3, page 20) which produces CO and H₂. Excess steam enables the shift of CO into H₂ and CO₂ via the water gas shift reaction (reaction 2-10, page 20).

1.1 Motivation

Biomass gasification coupled with SOFCs has the ability to generate electricity in a very efficient manner. The motivations for this work were as follows;

- To investigate if intermediate pyrolysis biochars can be gasified to produce a syngas rich in hydrogen.

- To optimise the gasification process to achieve a high volume fraction of H₂. This will be done by varying operating parameters such as temperature and steam flow and with the addition of sorbent materials such as dolomite to adsorb carbon dioxide.
- To increase the understanding of the gasification process with respect to transient behaviour and the role of ash content.
- To investigate the performance of solid oxide fuel cells using syngas.

1.2 Scope of Research and Thesis Structure

The main aim of the investigation was to generate a syngas that was rich in hydrogen and to utilise this gas in an SOFC. The experiments were conducted on a bench scale using a quartz gasifier and a single microtubular SOFC. The thesis is organised as follows;

Chapter 2 presents a literature survey into the various topics that are linked to this investigation. It gives a brief introduction to the pyrolysis types and surveys the literature for previous work carried out on intermediate pyrolysis. Next, it introduces biochar and its chemical and physical make up. It then reviews gasification and the various processes and reactions involved in gasification. It then presents a brief literature survey of steam gasification of conventional biomass and how catalysts such as dolomite have been used to improve H₂ yield. The chapter then moves onto a literature survey of biochar gasification. The next section of the chapter focuses on fuel cells, in particular SOFCs, and looks at some of the work carried out on biomass

powered SOFCs. The final part of the thesis focuses on what effects the various contaminants found in syngas have on the performance of SOFCs.

Chapter 3 describes the methods and materials used in the investigation. It describes the design process that was used to construct the biomass gasification rig, the various characterisation techniques that were used to characterise the biochars and experimental techniques that were used in the gasification and fuel cell experiments.

Chapter 4 presents the results obtained from the characterisation of the various materials used in the experiments; namely biochars, dolomite and SOFCs.

Chapter 5 is the main gasification chapter in the thesis. It presents an investigation into the following aspects of biochar gasification; (i) effects of temperature on product flow, transient composition, syngas composition (ii) effects of steam flow on product flow, transient gas composition and syngas composition.

Chapter 6 follows on from chapter 5. It reports in more detail some of the aspects introduced in chapter 5, such as effects of ash content on product flow, reactivity and syngas composition. It also presents an investigation into the effects of dolomite addition on the syngas composition, dry gas yield (DGY) and carbon conversion efficiency of the process.

Chapter 7 presents an investigation into the use of syngas in single cell, microtubular SOFCs and the summary of the mass and energy balances for the process.

Chapter 8 presents all the conclusions that were derived from chapters 2-7 and makes suggestions for further research.

2 Literature Review

This chapter presents a literature survey of previous work that has been carried out on the topics concerning the investigation into hydrogen production from biomass for use in solid oxide fuel cells (SOFC). The topics covered are; pyrolysis, biochar, steam gasification of biochar and finally, syngas powered SOFCs and the effects of various contaminants on SOFC performance. It begins with a review of the intermediate pyrolysis work carried out on various biomass substrates and the products and product distributions obtained. It then moves onto literature review on biochar and its chemical make-up before presenting a literature review on biochar gasification. The final section reviews the work carried out on SOFCs powered by biomass syngas, and finally a review of the effects of syngas constituents and impurities on the SOFC anodes is presented.

2.1 Pyrolysis

Pyrolysis is described as the thermal decomposition of organic matter under medium to high temperatures in the absence of an oxidising agent to limit gasification reactions [15]. Pyrolysis produces three distinct products; permanent gases such as H₂, CO, CH₄ and CO₂, bio-oil, and a solid-charcoal. The operating parameters are set depending on the type of feed used and the final product distribution desired. Generally, temperatures in the range of 300 – 650°C are employed alongside pressures ranging from hypobaric to elevated pressures [16].

During the process, the feed is subjected to rapid heating rates and high temperatures, at which it is held for a specified time. These conditions ensure that

the following steps occur; (i) heat is transferred from a heat source to the fuel particle, increasing its temperature; (ii) the initiation of primary pyrolysis reactions at this higher temperature releases volatiles and forms char. (iii) The flow of hot volatiles towards the cooler solids results in heat transfer between hot volatiles and cooler unpyrolysed biomass; (iv) condensation of some of the volatiles in the cooler parts of the biomass, followed by secondary reactions resulting in tar formation. (v) Autocatalytic secondary pyrolysis reactions proceed while primary pyrolytic reactions simultaneously occur in competition. (vi) Further thermal decomposition, reforming, water gas shift reactions, radicals recombination and dehydration can also occur, which are a function of the process's residence time/temperature/pressure profile [15]. There are three modes of pyrolysis that have been developed, these are; slow pyrolysis, fast pyrolysis and intermediate pyrolysis. The three modes are distinguished by their heating rates, solid residence times and the reaction temperatures involved. Table 2-1 summarises the main differences between the three;

Table 2-1: Comparison of the three different pyrolysis modes [16] [17]

Mode	Conditions	Liquid (wt%)	Solid char (wt%)	Gas (wt%)
Fast	Reactor temperature: ~ 500°C Heating Rates: > 1000°C sec ⁻¹ Hot vapour residence time: ~ 1 s Solid residence time: ~1 s	75	12	13
Intermediate	Reactor temperature ~ 400-500°C Heating rate range: 1-1000°C sec ⁻¹ Hot vapour residence time ~ 10-30 s Solid residence time: 60 – 1800 s	50	25	25
Slow	Reactor temperature ~ 300 - 500°C Heating rate: up to 1°C sec ⁻¹ Solid residence times: ~hours – days.	30	35	35

2.1.1 Slow Pyrolysis

Slow pyrolysis, also known as carbonisation, is optimised to produce char or if biomass is used as a feedstock, biomass-derived-char or biochar. Traditionally, the process is carried out in batch, using kilns, where the slow heating of lignocellulosic biomass to temperatures in excess of 400°C induces thermal decomposition leading to approximately equal masses of char, gas and liquid. The gas and condensable liquids are traditionally vented out, making the process polluting and inefficient whilst the biochar is sold for domestic cooking and heating purposes or to the metallurgical industry. Modern slow pyrolyzers either recycle the vapours and burn them as a source for heat or for electricity generation or capture them for synthesising chemicals. Slow pyrolyzers offer many advantages; they are small, inexpensive and can accept a variety of feedstock which does not need to be finely ground. However, they are difficult to scale up due to the slow heat transfer through coarse particles meaning that relatively long residence times required [18].

2.1.2 Fast pyrolysis

The primary aim of fast pyrolysis is to maximise the yield of liquid or bio-oil fraction. The biomass is heated so rapidly that it reaches peak pyrolysis temperature before it decomposes. Heating rates of up to 10000°C s⁻¹ [16] can be used but the peak temperature is kept below 650°C so as to avoid cracking of the bio-oil. There are four important features that increase the liquid yield; (i) very high heating rates, (ii) reaction temperatures of 425 – 600°C, (iii) short vapour residence times and (iv) rapid quenching of the product gas [15]. The short vapour residence times may increase

the liquid yield but they are insufficient for cracking high molecular weight compounds. Successful applications have been developed with woody biomass but non-woody biomass can lead to bituminous products which solidify at room temperature [19]. The feed needs to be dried and reduced to < 2 mm to obtain optimum heat transfer. The grinding needed to achieve this requires significant amounts of energy, it is estimated that up to 50 kWh of electrical energy is required per 1 tonne of biomass [20]. Drying the biomass is essential since fast pyrolysis requires a moisture content of less than 7% [21] and in practice, at least 50% more energy is required to evaporate one kg of moisture than the standard 2442 kJ kg^{-1} often stated [22].

2.1.3 Intermediate Pyrolysis

Intermediate pyrolysis bridges the gap between slow and fast pyrolysis and offers the advantages of both. As shown in Table 2-1, solid and vapour residence times are longer than those of fast pyrolysis enabling a range of lower molecular weight pyrolysis oil to be formed [23]. Intermediate pyrolysis has specifically been designed to handle non woody biomass with high amounts of inert content. Two designs in particular; Haloclean and Pyroformer reactors have overcome the shortcomings of fast pyrolysis. Haloclean was the original design and although successful trials were carried out on straw pyrolysis, its biggest disadvantage was its operating pressure which was limited by its use of a kiln. The low operating pressure causes difficulties in coupling the Haloclean reactor to a process downstream. The second design is the pyroformer (Figure 2.1), like the Haloclean, it uses a two coaxial rotating screws to

control the residence time the feed spends within the reactor but its gas tight reaction chamber enables it to operate up to 1 MPa [24]. The advances in reactor design enables intermediate pyrolysis to handle much larger particles than fast pyrolysis with up to 40 wt% moisture content [24].

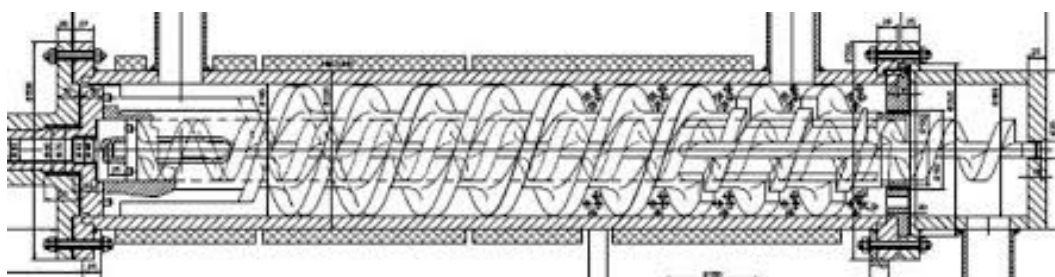


Figure 2.1: Schematic of the Pyroformer reactor [25]

Many feeds have now been tested using intermediate pyrolysis. In an early study, rapeseed, an oil-bearing crop, was pyrolysed at 450 and 500°C in the Haloclean reactor. It was found that the gas yield increased from 13 to 22 wt% and the biochar yield decreased from 30 to 19 wt% at 450 and 500°C respectively [26]. Yang *et al* [27] pyrolysed wood pellets and barley straw in a pyroformer at 450°C. They obtained oil yields of 34.1 and 12 wt% respectively with a biochar yield of around 30 wt% in both cases. The wood biochar contained 75.6% carbon and had a higher heating value (HHV) of 30.1 MJ kg⁻¹. The barley straw biochar had 74.83% carbon with a heating value of 32.9 MJ kg⁻¹. Ouadi *et al* [28] used the pyroformer to pyrolyse de-inking sludge obtained from the paper industry, at 450°C. They obtained a typical oil yield of 9 wt% with 15 wt% gases and 75 wt% biochar. The biochar had a very low heating value of between 3.3 and 4.9 kJ kg⁻¹, arising from its very high, inert, ash content. Mahmood *et al* [19] pyrolysed brewers spent grain in the pyroformer at

450 °C and obtained 29 wt% biochar, 51 wt% bio oil and 19 wt% gases. The biochar had a heating value of 26 – 28 MJ kg⁻¹.

Tinwala *et al* [29] investigated the intermediate pyrolysis of various agricultural biomass substrates that are abundantly available in India, at 500°C. Substrates tested were; Neem Seed, Pigeon Pea Husk, Yellow Pea Husk, Ground Nut Shell, Channa Straw, Soybean Straw, Wheat Straw and Sawdust. The authors obtained the highest liquid yield from the Neem Seed, the highest biochar yield from the straws with the highest gas yield from the soybean straw. The highest HHV obtained by the authors was 29.43 MJ kg⁻¹, from the sawdust biochar, whilst the lowest, 20.09 MJ kg⁻¹, was from the channa straw. Samanya *et al* [30] used intermediate pyrolysis to co-pyrolyse sewage sludge with 40% wood, rapeseed and straw. They found that sewage sludge + 40% wood gave the highest biochar yield of 37.2% whilst 40% straw gave the lowest at 27.8%. The results are all summarised in Table 2-2 below:

2.1.4 Intermediate Pyrolysis Conclusions

From the above studies it is clear that intermediate pyrolysis is able to handle a variety of feeds and produce three distinct products; liquids, gases and biochars. The product distribution varies greatly with the type of feed and pyrolysis temperature used. The biochar fraction varies substantially with the feed used but 30 wt% at 450 and 500°C is a common number.

Table 2-2: Product Distribution from Intermediate pyrolysis of sewage sludge and other biomass mixtures

Reference	Feedstock	Temperature (°C)	Pyrolysis Fractions (%) ^a			Biochar C content (%)	Biochar HHV (MJ kg ⁻¹)
			C	O	G		
[26]	Rapeseed	450	30	59	22	-	-
	Rapeseed	500	30	57	13	-	-
[27]	Wood	450	28.5	54.3	17.7	75.6	30.1
	Barley	450	30.1	49	20.9	74.8	32.9
[31]	Deinking Sludge	450	75	9	15	17 – 20	3.3 – 4.9
[19]	Brewers Spent Grain	450	29	51	19	61.8	26 – 28
[29]	Neem Seed	500	47.5	32	29.5	-	25.8
	Pigeon Pea Husk	500	30	32.5	32.5	-	28.0
	Yellow Pea Husk	500	40	30	30	-	26.0
	Ground Nut Shell	500	30	37	30	-	24.2
	Channa Straw	500	24.5	40	34.5	-	20.1
	Wheat Straw	500	34.5	40	24.5	-	20.0
	Soybeab Straw	500	20.5	40	40.5	-	23.3
	Saw Dust	500	42.5	27.5	24.5	-	29.4
[30]	SS ^b + 40% wood	450	37.2	46.8	20.5	-	-
	SS + 40% Rapeseed	450	31.2	53.3	13.5	-	-
	SS + 40% Straw	450	27.8	28.7	23.5	-	-

^a C is char, O is oil and G is gas

^b SS is sewage sludge

2.2 Biochar

Biochar is the carbonaceous material formed during biomass pyrolysis. Along with C, H and O, it also contains many minerals such as Na, Ca, Mg, etc [32]. Historically, biochar has been used in agricultural processes to enhance soil fertility. The most famous example of this is the terra preta (black soil) of the Amazon rain forest where pre-Columbus natives produced biochar and deposited it into the soil, building up layers over time. Eventually, this led to a nutrient rich soil with contents of some nutrients up to 500x higher than the natural surrounding soil [20]. Modern biochar has many uses, according to HP Schmidt, [33], there are at least 55 uses for biochars, including but not limited to; air decontamination, humidity control, insulation, pesticide adsorbent, activated carbon, filters, biogas production, combustion, etc.

2.2.1 Biochar Structure and Engineering

The structure of the biochars varies greatly depending on the initial feed and the conditions it is formed under. Their defining property is the organic portion of high carbon content aromatic rings comprising of 6-C rings linked together without hydrogen or oxygen. Unlike graphite, which is layered, biochar structure is very irregular and consists of large sized pores which feed smaller pores within the lower dimensions of the structure- i.e. meso and micropores. The overall structure is amorphous in nature with some conductive crystalline areas of highly conjugated aromatic compounds. The rest of the biochar matrix is made from non-conductive aromatic-aliphatic compounds of complex structure and mineral compounds within the inorganic ash [32].

The biomass, upon entering the reactor undergoes many changes that lead to the final biochar product. These changes and the intensity at which they occur determine the physical properties of the biochar. Initially, the biomass particles experience drying as the heat from the reactor vaporises the inherent moisture content, this starts at around 100 °C. The next step is devolatilisation; biomass contains a large amount of volatile matter; 65 – 85% on a dry basis, which is driven off [34]. The building blocks of biomass; hemicelluloses, cellulose and lignin decompose at different temperatures with hemicelluloses degrading at 200 - 260 °C, cellulose at 240 – 350 °C and lignin at 280 – 500 °C. In general, operating conditions play a huge role in the final biochar structure. Parameters such as heating rate, pressure, residence time and pre-treatment all play a role but it is generally accepted that the most important factor is the temperature at which the pyrolysis reactions occur. Heating rates and pressure are perhaps the second most important factors that determine the biochar structure as they affect the physical mass transfer of the volatiles evolving at the given temperature [32].

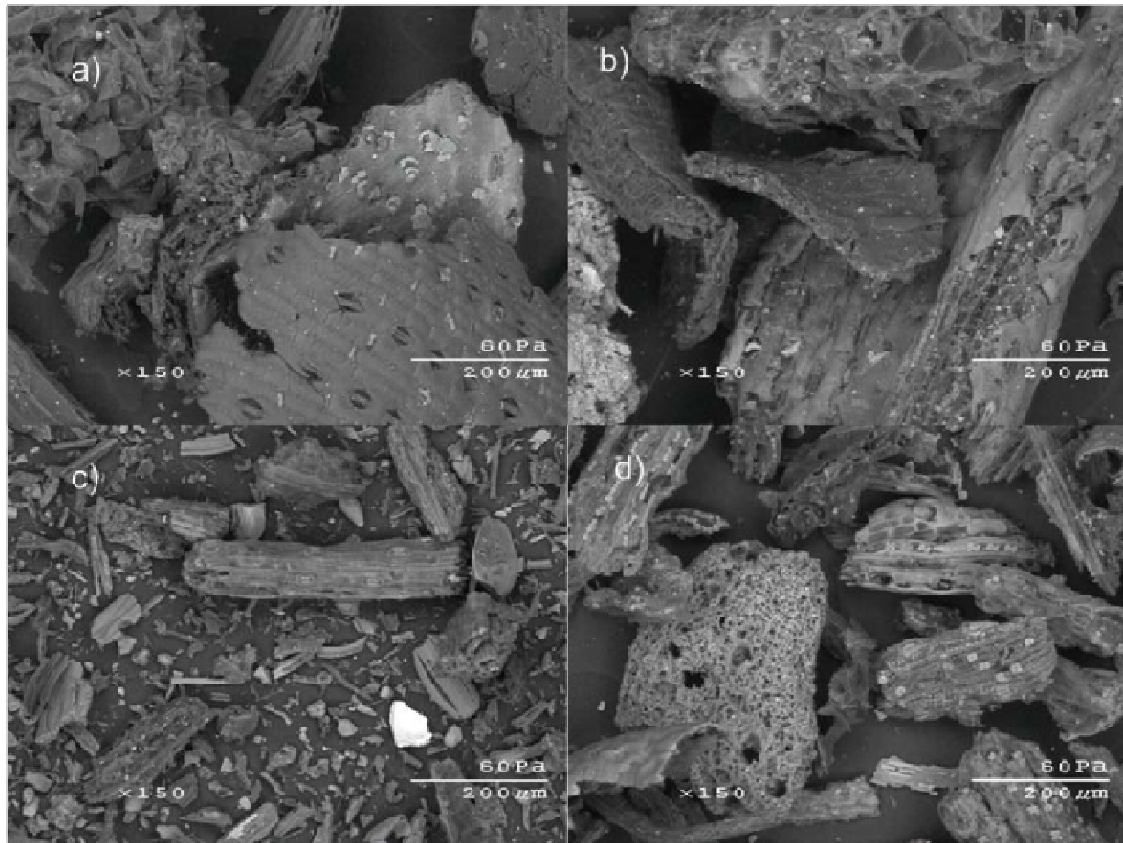


Figure 2.2: Micrographs from a Scanning Electron Microscope showing the structure of switchgrass and its biochars; (a) feedstock, (b) slow pyrolysis (c) fast pyrolysis and (d) gasification [35]

2.2.2 Biochar Properties

Biochars have various properties that determine their suitability for a particular application. Physical properties of biochars include density, porosity, surface area and particle size. Density can be measured in two ways; particle density or bulk density. Particle density is also known as skeletal or true density; it is the measure of the mass occupied by a unit volume of the solid material only. Bulk density measurements take account of the volumes occupied by structure, pore and voids. Particle density is measured by a pycnometer and bulk density is measured manually by adding a known quantity of biochar sample into a container of a known volume.

Compaction can have a large impact on the final value but each standard has a protocol for sample packing [35].

The porosity of the biochar is affected by the rate at which it experiences devolatilisation [35]. Porosity can be split into the following classifications based on the internal diameters of the pores; micropores (<2 nm), mesopores (2 – 50 nm) and macropores (>200 nm). The size of the pores determines the application that best suits the biochar. For example, microporous biochars are used in the activated carbon industry whilst macroporous biochars are best suited as soil enhancers [5]. Surface area is another important property of biochars as it determines its chemical reactivity. The higher the surface area a biochar has, the more chemical interactions it is able to participate in, per gram [35]. Surface area is affected by the reactor temperature which affects the devolatilisation and residence time it spends in the reactor. Prolonged residence time leads to increased conversion leading to the opening up of new pores [36].

Chemical properties of biochars include heating value, aromaticity and surface functionality. The former is essential to this study but the latter two are not in the scope of this investigation, so will not be discussed further. Heating value of a biochar is its most important property when considered as a fuel. The high carbon content of biochars makes it a high value fuel. During pyrolysis, the biomass loses most of its volatile matter such as H, O and N but retains a lot of its structural carbon which gives it its high heating value [36].

2.2.3 Biochar Conclusions

Biochar is a carbon rich material which is at least partly amorphous in structure. It has historically been used as a fuel and a soil conditioner to enhance its fertility. Modern methods of forming biochar allow for the engineering of certain traits by varying process parameters. Temperature is the most important parameter, followed by heating rate and pressure.

2.3 Gasification

This part of the literature survey will present some of the core tenets of gasification. Gasification differs from pyrolysis in that it is carried out at higher temperatures and utilises a gasifying medium which reacts with the biomass to form what is known as syngas. Syngas from biomass is a mixture of CO, H₂, CH₄, CO₂ (collectively known as permanent gases) and some lower hydrocarbons. Technically, gasification is the conversion of a solid or liquid fuel into a gaseous fuel that can either be used to release energy or converted into a range of other useful chemicals [37]. Typically, oxygen, air or steam is used as a gasifying medium [37] or they could be used in conjunction, for example; air and steam mixture. Oxygen and air gasification are not in the scope of this work, hence a brief outline is provided below. The main focus of the chapter is steam gasification.

The products given by each medium are summarised in a ternary diagram shown in Figure 2.3. As can be seen, each gasifying medium leads to different types of products. Pure oxygen is more likely to give CO and CO₂ depending on the amount

used, hydrogen is likely to give CH₄ and steam is likely to give a combination of CO and H₂. The heating value of the product gas is heavily dependent upon the gasifying medium; the use of air results in a gas that is diluted with nitrogen. Pure oxygen produces a gas rich in CO but is expensive to make. Steam produces a gas that has an intermediate heating value and a high H₂/CO ratio. The range of heating values for each medium are displayed in Table 2-3.

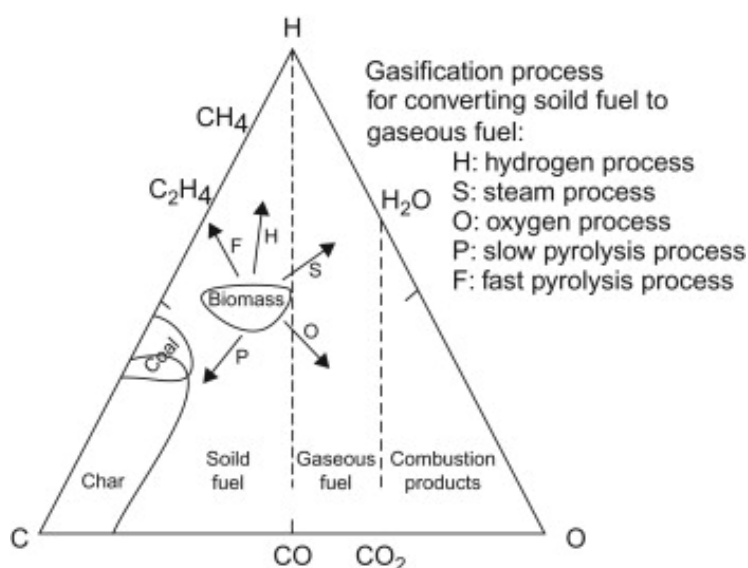


Figure 2.3: Ternary diagram showing the likely products of each gasifying medium as well as fast and slow pyrolysis [37]

Table 2-3: Heating values of the product gases given by each gasifying medium

Gasifying Medium	Heating Value (MJ m ⁻³)
Air	4-7
Steam	10-18
Oxygen	12-28

2.3.1 Air and Oxygen Gasification

As the biomass enters the gasification reactor, it undergoes the following processes; (i) drying, (ii) devolatilisation and (iii) char gasification. Biomass is normally pre-dried to reduce the moisture content to below 20%, this minimises the energy losses in the reactor. Once the dried biomass particles enter the reactor, they experience high temperatures leading to the vaporisation of the loosely bound water molecules on the surface. As temperature increases above 100°C, low molecular weight compounds are released and the process continues until 200°C, when pyrolysis processes begin to take over, producing gases, vapours and char. The char further reacts with the gases and vapours to produce a final gas with composition being dependent upon the contact time between the gases and the char, as well as the residence time in the reactor [37].

2.3.2 Gasification Reactions

During gasification, numerous reactions can occur at any one time, some of the main reactions are summarised in Table 2-4. The extent to which a specific reaction occurs is heavily dependent on the process conditions and gasifying medium being used. The process conditions affect the thermodynamics of the system which in turn affects the final product distribution. Finally, kinetics also plays a vital role in determination of the final product as it determines which reaction occurs fastest, therefore, using up the oxidant. Taking all these things into consideration, the most important gasification reactions will be discussed in detail.

Table 2-4: Summary of the main gasification reactions and their enthalpies of reaction at standard temperature and pressure of 298.15 K and 101.3 kPa [14] [35]

Reaction Type	Reaction	ΔH° (kJ mol ⁻¹)	Reaction
Pyrolysis Reaction			
Devolatilisation	$C_x H_y O_z \rightarrow aCO_2 + bH_2O + cCH_4 + dCO + eH_2 + fC_2$		2-1
Carbon Reactions			
Boudouard	$C + CO_2 \rightleftharpoons 2CO$	+ 172	2-2
Water-gas	$C + H_2O \rightleftharpoons CO + H_2$	+ 131	2-3
Hydrogasification	$C + 2H_2 \rightleftharpoons CH_4$	- 74.8	2-4
Oxygen-char	$C + 0.5O_2 \rightarrow CO$	- 111	2-5
Oxidation Reactions			
Oxidation of carbon	$C + O_2 \rightarrow CO_2$	- 394	2-6
Oxidation of CO	$CO + 0.5O_2 \rightleftharpoons CO_2$	- 284	2-7
Oxidation of CH ₄	$CH_4 + 2O_2 \rightleftharpoons CO_2 + 2H_2O$	- 803	2-8
Oxidation of H ₂	$H_2 + 0.5O_2 \rightarrow H_2O$	- 242	2-9
Shift Reaction			
Water gas shift reaction	$CO + H_2O \rightleftharpoons CO_2 + H_2$	- 41.2	2-10
Methanation Reactions			
	$2CO + 2H_2 \rightarrow CH_4 + CO_2$	- 274	2-12
	$CO + 3H_2 \rightleftharpoons CH_4 + H_2O$	- 206	2-13
	$CO_2 + 4H_2 \rightarrow CH_4 + 2H_2O$	- 165	2-14
Steam-Reforming Reactions			
Steam reforming of CH ₄	$CH_4 + H_2O \rightleftharpoons CO + 3H_2$	+ 206	2-15
Partial combustion of CH ₄	$CH_4 + 0.5O_2 \rightarrow CO + 2H_2$	- 36	2-16

2.3.3 Boudouard Reaction

The Boudouard reaction (Reaction 2-2) is the reaction between C and CO₂ to produce CO. The forward reaction is highly endothermic and therefore, is preferred at very high temperatures. The rate of this reaction is 6 – 7 orders of magnitude slower than the oxygen-char reaction (Reaction 2-5) and is about 2 – 5 times slower than the steam char reaction (Reaction 2-3) [37]. The reaction has been extensively studied and is thought to occur in the following manner [38]:

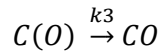


Where k_1 , k_2 , and k_3 are Arrhenius rate constants, C_f is an active carbon site and $C(O)$ is a carbon-oxygen complex.

2.3.4 Water Gas Reaction

The water gas reaction is also known as the steam-char reaction. It is perhaps the most important reaction in gasification [37] with the forward reaction being endothermic. The products it gives are CO and H₂, making it very important in the production of H₂. The reaction mechanism is thought to occur in the following manner [38]:





2-22

2.3.5 Water Gas Shift Reaction

The water gas shift reaction (WGSR) (Reaction 2-10, page 20) is a fundamental reaction when it comes to the determination of the final syngas composition. Unlike the other reactions, it is a homogeneous reaction involving a product (CO) of the Boudouard and water gas reactions. The forward reaction is slightly exothermic, therefore prefers lower temperature and equilibrium is reached at 1000°C if no catalyst is used [37].

2.3.6 Char combustion Reaction

The partial oxidation of char is the fastest of the gasification reactions. It is an exothermic reaction and generally uses up all the O present in the char. The extent to which Reaction 2-5 occurs depends on the temperature with higher temperatures favouring Reaction 2-5 as opposed to Reaction 2-6 [37].

2.4 Reactors for Biomass Gasification

Depending upon the application, many reactor types are available for gasification. Some are more suited for smaller scale applications whilst others are only suited for industrial scale applications. A summary of the types of gasifiers is presented in Table 2-5, page 24.

2.4.1 Operating principles of Biomass Gasifiers

Updraft gasifiers are called updraft since the biomass is fed at the top and the oxidant enters at the bottom and rises up. The syngas is rich in CH_4 and tar. The resultant char falls onto the grate and is combusted to provide heat for the process. Downdraft gasifiers differ slightly in that the outlet for the product gas is located at the bottom of the gasifier, this forces the biomass and oxidant to travel in the same direction and the product gas must pass through the char bed to exit. This enables many of the gasification reactions to occur, reducing the tar content in the product gas to give a high quality gas.

Entrained flow gasifiers require powdered biomass particles that are entrained in the oxidant stream. Upon entering the reactor, some of the biomass is combusted to provide heat for the process with temperatures reaching $1200 - 1500^\circ\text{C}$. At these temperatures, the ash in the biomass melts and trickles down the reactor walls and is collected at the bottom. Fluidised bed gasifiers make use of a bed of fine material, which the oxidant is blown upwards through, creating agitation. Biomass is fed in from the sides and combusts. Operation must be below 900°C to avoid ash melting which can cause agglomeration of the bed material. Plasma gasifiers make use of a plasma torch to generate a plasma flame which can reach temperatures of up to 5000°C . They are able to handle a variety of feeds including medical wastes and can convert any type of organic matter into a very high quality syngas [39].

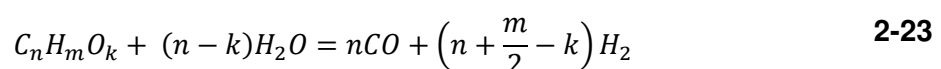
Table 2-5: Summary of advantages and disadvantages of various biomass gasifiers [39] [40]

Gasifier Type	Advantages	Disadvantages
Updraft	<ul style="list-style-type: none"> High thermal efficiency Less sensitive to fuel size High moisture content (up to 50%) possible No scale up problem 	<ul style="list-style-type: none"> High tar content in syngas 20% of the energy in the tar Lower H₂ and CO generation Downstream catalytic tar cracking required Longer star-up times
Downdraft	<ul style="list-style-type: none"> High carbon conversion Low tar production Low ash carry Over High solids residence time Simple construction Short start up time 	<ul style="list-style-type: none"> Limited scale-up potential Needs uniform sized feed Slag formation on fixed grate Requires dry fuels Poor turndown capability
Bubbling Fluidized Bed (BFB)	<ul style="list-style-type: none"> Good gas-solid contact and mixing High specific heat capacity Good temperature control Can accommodate variations in fuel quality Good turndown Easy start up and shut down 	<ul style="list-style-type: none"> Carbon loss with ash Feed pre-processing required Limitation of scale

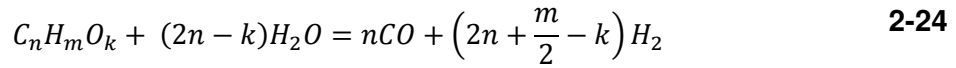
Gasifier Type	Advantages	Disadvantages
Circulating fluidised bed (CFB)	As for BFB Can be designed for very large scale	As for BFB except for the scale issue. [largest CFB biomass combustor is 205MW in Poland [31]]
Entrained Flow	Produces tar free gas syngas has low CH ₄ content High conversion	Slagging of ash Carbon loss with ash Feed material requires size reduction and slurring Poor gas-solid contact Exotic materials required Operation at pressure
Plasma	Good control of syngas composition Higher calorific value of gas produced Low tar, CO ₂ , hydrocarbons, etc Wide variety of feeds Smaller reactor size	High operating costs

2.5 Steam Gasification of Biomass

Steam gasification is an alternative to the conventional biomass gasification route. It offers higher heating values for product gases (refer to Table 2-3) as well as a significantly higher H₂ content. The generic steam gasification reaction can be represented by the following equation [41]:



The presence of steam and CO enables the water gas shift reaction to refine the product distribution. The overall equation can be written as thus [41]:



Unlike air or oxygen gasification, steam gasification is an allothermal process, requiring an external supply of energy to enable the (mainly endothermic) reactions to occur. The steam also helps to break up the tar more efficiently thus enabling a cleaner gas to be produced.

2.5.1 Non Catalytic Steam Gasification

Nipattummakul *et al* [42] carried out steam gasification of sewage sludge at temperatures ranging from 700 – 1000°C. They reported that sewage sludge showed lower rates of reaction than food and paper waste and that sewage sludge gasification should be carried out at temperatures >800°C. Regarding hydrogen, they reported that the yield increases with increasing temperature and using steam as the gasifying agent led to a H₂ content that was three times higher than for air gasification at 1000°C. Gao *et al* [43] studied the effects of steam to biomass ratio (S/B ratio), which was defined as the ratio of the flowrate of steam to the flowrate of biomass on a mass basis. They studied its effects on the various characteristics of the syngas, focusing on; composition, density, yield and lower heating value at a temperature of 850°C. The authors gasified pine saw dust in a stainless steel cylindrical tube, upstream of which was a porous ceramic reformer. They reported

that both gas density and gas yields decreased from 0.59 kg m^{-3} and $1.83 \text{ m}^3 \text{ kg}^{-1}$ to 0.47 kg m^{-3} and $1.77 \text{ m}^3 \text{ kg}^{-1}$ at an S/B ratio (by mass) of 1.05 and 3.47 respectively. The H_2 content increased from ~44% to over 55% at the aforementioned S/B ratios. Moon *et al* [44] gasified Korean pine wood chips to determine the transient behaviour of the devolatilisation and char reactions during steam gasification. They split the biomass gasification process into two stages; devolatilisation and char reactions. The devolatilisation stage was mainly controlled by heat transfer rate, the convection and diffusion of gases and the chemical bond strength of the biomass. The char reactions were a mixture of homogeneous and heterogeneous reactions between the major product gases, steam and the char. With increasing temperature, the devolatilisation process occurred faster and the tars were cracked thermally but there still remained significant amounts of benzene, indene and naphthalene. With regards to char gasification, the authors reported that the addition of steam at 900°C had a major effect on the transient behaviour of the char reactions. An increase in H_2 was observed during the devolatilisation stage suggesting that devolatilisation and char gasification occur simultaneously whilst reactions such as char gasification and steam CH_4 reforming were considered to be the main contributors.

2.5.2 Dolomite Catalytic Steam Gasification

Dolomite is a naturally occurring rock that has a general formula of $\text{MgCO}_3 \cdot \text{CaCO}_3$. It has received much attention as a bed material for biomass gasification as it is inexpensive and abundant and has the ability to reduce tar content from a biomass gasifier. Historically, dolomite has been used in the Pidgeon process to produce

magnesium by thermal reduction. The chemical composition of dolomite varies from place to place but using its formula, it can be calculated as containing around 30.4 wt% CaO, 21.8 wt% MgO and slightly more than 47.8 wt% CO₂.

Wei *et al* [45] gasified legume straw and pine saw dust with steam in a down flow concurrent free fall reactor. Their results are displayed in Figure 2.4. They found that the tar and char yields decreased when steam flow was increased and that the water gas shift reaction played a major role in determining the final gas composition. The H₂ content increased with increasing temperature whilst that of CO and CH₄ decreases. The optimal ratio of steam to biomass for syngas yield and H₂ content was found to be 0.6 g g⁻¹ biomass. The authors also investigated using naturally occurring catalysts namely; limestone, olivine and dolomite to determine their ability to crack tars and increase gas yield. They found that dolomite performed better than olivine and limestone but the reaction would have benefitted from longer vapour residence times.

Luo *et al* [46] carried out steam gasification of pine saw dust particles in a fixed bed reactor over a temperature range of 600 – 900°C using Chinese dolomite as the catalyst and a steam to biomass (S/B) ratio (by mass) of 0 - 2.80. The authors reported that steam gasification occurs in two steps; first, there is the thermal decomposition of biomass which produces tar char and volatiles, this is followed by the cracking and reforming of the volatiles and the gasification of the char. The use of steam and dolomite enhanced the reforming reactions to such an extent that no tar was present at 900°C at a S/B ratio of 0.73 or above. With respect to temperature, the authors reported that increases in temperature led to an increase in hydrogen content, dry gas yield and carbon conversion. The optimal S/B ratio was

found to be 1.43 in terms of carbon conversion (92.6%) and dry gas yield (2.53 m³ kg⁻¹) but higher hydrogen content was achieved at an S/B ratio of 2.10.

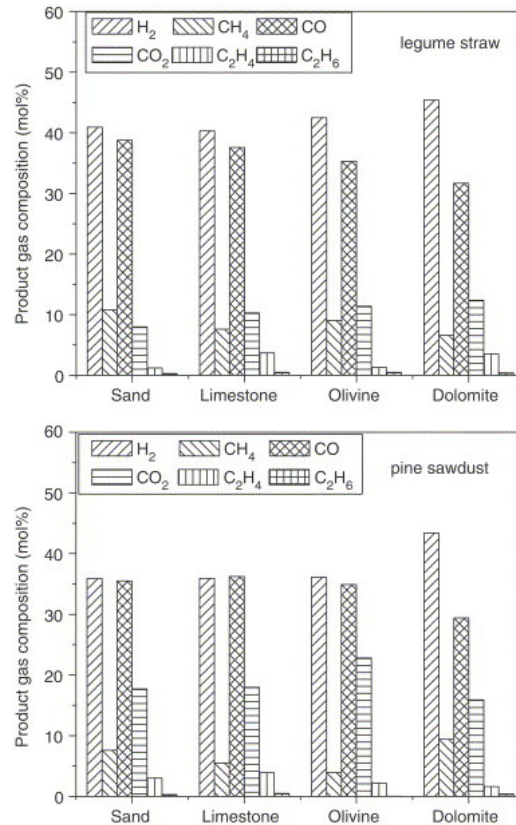


Figure 2.4: Comparison of syngas composition from Limestone, Olivine and Dolomite catalysts [45]

Hu *et al* [47] studied the effects of reaction temperature, particle size and calcination of naturally occurring catalysts using steam gasification of apricot stones. They reported that calcination of dolomite improves its catalytic activity for tars but has no effect on the reforming of CH₄. Using X-ray Diffraction (XRD), they found that the raw dolomite consisted primarily of CaMg(CO₃)₂ whereas calcined dolomite is a mixture

of MgO and CaO which the authors attributed to as being the active components in tar cracking reactions.

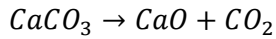
2.5.3 Thermal Decomposition of Dolomite

The thermal decomposition of dolomite using thermogravimetric methods has been studied extensively by many researchers. A review of the literature yields a great deal of variability in the decomposition temperature [48]. Usually, researchers report a two step process, the first one is assumed to be the decomposition of $MgCO_3$ via reaction 2-25 (page 30) and the second being the decomposition of $CaCO_3$ as depicted by reaction 2-26 (page 30). The first step is thought to occur at a lower temperature and the second step at higher temperatures. In inert atmospheres (so as to avoid reverse reaction 2-26), the first step has been reported to start below $600^\circ C$ [48] and peaking at $760-770^\circ C$ [49]. The second step starts at around $780^\circ C$, peaking at $800-900^\circ C$ [50].

The presence of CO_2 in and around the dolomite sample leads to a decrease in the temperature at which the decomposition occurs. McIntosh et al [50] studied dolomite decomposition in N_2 and CO_2 atmospheres using thermal gravimetric analysis. They reported that the presence of CO_2 has the opposite effects on both peaks. For example, the temperature at which the first step occurs is reduced, whilst that of the second step is increased.



2-25



2-26

If there is sufficient CO_2 in the atmosphere and the temperature is below 760°C , the CaO can react with the CO_2 to produce CaCO_3 via the reverse reaction 2-26. At higher temperatures however, CaCO_3 fully calcines into CaO , regardless of the CO_2 pressure [49] [50].

The basis of the tar cracking ability of dolomite is still up for discussion in the literature. Various authors have put forward suggestions as to the cause of the catalytic activity. Contrary to the suggestions of Hu *et al* [47], other researchers have suggested that the catalytically active components in dolomite might be the presence of various impurities, such as Fe_2O_3 , that exist within the dolomite complex. For example dolomites with a higher Fe_2O_3 content were shown to have a higher activity than those with a lower Fe_2O_3 content even though they had lower surface areas [51]. Wang *et al* [52] enhanced the Fe_2O_3 content of dolomite and compared it with various other catalysts including natural dolomite. They reported a trivial increase in the tar cracking ability of the modified dolomite as compared to natural dolomite. Yu *et al* [53] used steam gasification of birch in a fluidised bed gasifier equipped with a downstream catalyst bed made up of calcined dolomite. The study compared four Chinese dolomites and used a Swedish dolomite for reference. Though the authors did not focus on the gas composition, they reported that the most important factor that determines the tar cracking ability of dolomite is their pore sizes.

2.6 Biochar Gasification

Until now, the review has mainly focused on the steam gasification of conventional biomass. Conventional biomass contains high levels of volatile matter which leads to the formation of unwanted products such as tars and hydrocarbons. To obtain high contents of H_2 , it is better to react the biochar with steam since biochars contain negligible amounts of moisture, are low in volatiles and contain higher amounts of carbon. By utilising biochar and steam, the entire dynamics of the gasification process are changed. For example; it is generally accepted that the gasification process occurs in three steps; (i) drying, (ii) pyrolysis and (iii) gasification. With steam gasification of biochar, the first step is completely eliminated as biochar is almost completely dry, the second step is vastly reduced and the third and most important step is enhanced.

Biomass char is more reactive than coke char, its pores are much larger (20 – 30 μm) than coke chars (0.5 nm) and its reaction behaviour is different than that of coke or peat chars. The reactivity of peat chars decreases with conversion whereas it has been reported that for biomass chars, it increases due to the activity of the alkali and alkaline earth metallic species (AAEM) [37]. This phenomenon can be seen in Figure 2.5.

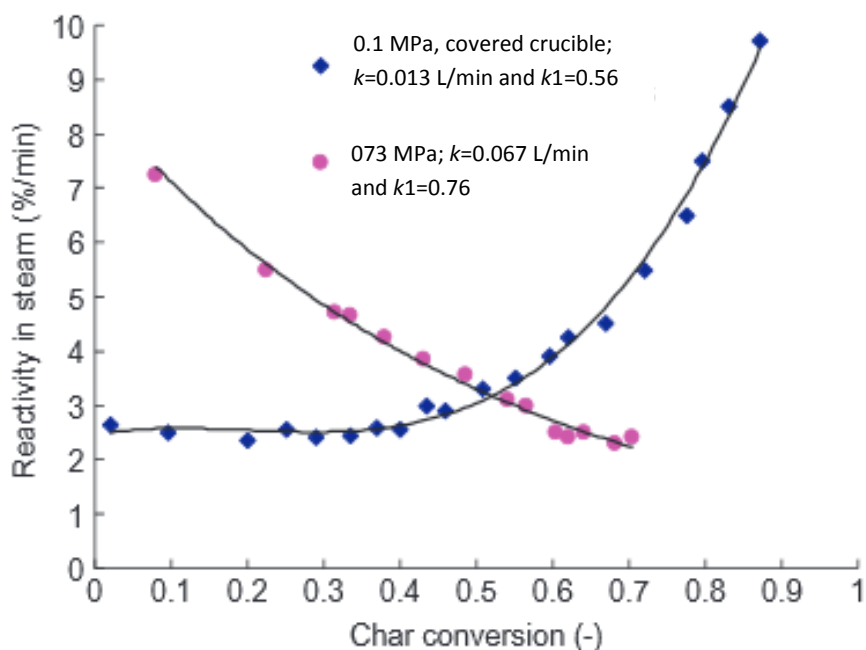


Figure 2.5: Comparison of the reactivity of peat and biomass char. Adapted from [37]

Interest in the area of steam gasification of biochars has grown considerably. Yan, *et al* [14] investigated the effects of reaction temperatures and steam flow rates upon biochar gasification. They reported that the dry gas yield and carbon conversion efficiency increased from 0.19 to 2.44 m³ kg⁻¹ and 13.16 to 95.78%, respectively, when the temperature was raised from 600 to 850°C. The findings were attributed to three factors; (1) more unconverted volatiles were released at higher temperatures, (2) endothermic reactions favour higher temperatures and (3) higher temperatures also helps with the tar cracking. The H₂ content of the syngas also increased from 29.54 to 52.41% with the H₂ yield changing from 2.55 to 57.07 mol kg⁻¹ as temperature increased from 600 to 850°C. The CO content peaked at 600°C at 22.69%, and then decreased at 700 °C to 10.94% before increasing to 14.03% at 850°C. In another study, Yan *et al* [54] investigated the effects of particle size and

temperature on biochar derived from the fast pyrolysis of cyanobacterial blooms. They reported that varying the particle size had little effect on the gaseous composition or the yield of gas produced.

Chaudhari et al [12] investigated the steam gasification of biomass derived char from fast pyrolysis. They varied the flow rates of steam from 42 to 250 g min⁻¹ kg⁻¹ biochar whilst maintaining a 700°C temperature. They found that increasing the steam flow rate from 0 to 166 g min⁻¹ kg⁻¹ biochar, increased the biochar conversion from 20 – 72%, as the steam-char reaction consumed the carbon in the biochar. Increasing the flow rate further had little effect on the conversion. In another study, Chaudhari et al [13] gasified bagasse and commercial biochars in a fixed bed microreactor. They reported a very high H₂ content (76.2%) at 700°C and low steam flow rates (20.8 g min⁻¹ kg⁻¹ char), which decreased to 70% at 800°C at the same steam flow rate. At higher steam flow rates (167 g min⁻¹ kg⁻¹ char), no overall trend was reported in the H₂ content as it behaved differently with respect to the chars tested.

Zhang et al [55] scaled up biochar gasification using a fluidised bed reactor and reported that although the content of H₂ increases slightly with increasing temperature from 750 – 900°C, there was no clear trend. Chen et al [56] studied the effects of pyrolysis temperature and residence time on the reactivity of wood biochar in a pressurised fluidised bed reactor. The authors carried out both the gasification and pyrolysis using the same conditions; temperature; (650-710°C) and pressure (3.4-10 bar) and found that during pyrolysis, the retention time and temperature have little effect on the yield of the biochars produced. The authors further reported that biochars which were gasified straight after formation showed a higher reactivity than those that were allowed to cool and then subsequently gasified. The difference was

attributed to the residence time the char spends in the reactor. During cooling, the biochars are exposed to high temperatures for a longer period of time thus giving the biochar structure time to anneal and become less reactive. Zeng *et al* [57] gasified biochar from fast pyrolysis using steam. The authors used long residence times of 3 hours and reported that high temperatures favour H₂ production which peaked at 74 vol%. Sun *et al* [58] carried out steam gasification of biochar from catalytic fast pyrolysis in a fixed bed reactor. They also used long residence times and reported that gas yield and conversion efficiency increases with temperature whilst a H₂ content exceeding 85% was achieved at 800°C.

2.6.1 Effects of Steam Gasification on Biochar Structure

Fu *et al* [40] studied the evolution of the biochar structure of rice husks during steam gasification at 900°C. They reported that the biochar structure experiences drastic changes even when conversion is minimal. The elemental compositions of C, H and O all experienced reductions of 85, 67 and 91% respectively. Similar findings were also reported by Keown *et al* (2008), who investigated the changes in the biochar structure with steam gasification. They found that biochar is highly reactive towards steam and that just 20 seconds of exposure to steam drastically reduces the reactivity of biochars with air at 400°C. The reduction in reactivity was attributed to changes in the ring structure of the biochar as smaller rings (3-5 fused rings) transformed into larger rings (>6 rings). They speculated that the intermediates of the char-steam reactions, especially H, penetrated deep into the biochar matrix and induced the condensation reactions.

2.6.2 Effects of Mineral Content on Biochar Reactivity

Biochar reactivity influences the residence time over which the biochar spends in the reactor by controlling the rate of gasification. Much research has been carried out to investigate the reactivity of biochars and the factors that influence biochar reactivities. Ollero *et al* [59] reported that biochar reactivity is affected by the following factors; particle size, size distribution, char porosity, mineral content of the char, temperature and the partial pressure of the gasifying agent. Particular attention has been paid to the effects of the inherent content of AAEM species which can catalyse the oxygen-char reactions [60]. Many authors have reported that biochars which lack AAEM species display a lower reactivity. Keown *et al* [61] reported that the structure of the carbonaceous matter within the biochar, the concentration of the AAEM species acting as catalysts and the physico-chemical forms and the dispersion of AAEM species within the biochar were the dominating factors in char gasification.

Kajita *et al* [62] investigated the effects of AAEM species on biochar gasification with steam. They tested two types of biochars; with and without AAEM species. The AAEM species were removed using acid washing and then rinsed thoroughly with deionised water until no trace of acid was left over. They managed to successfully remove species such as K and Na but little Mg and Ca. The acid washed biochars displayed a lower reactivity throughout the gasification process. The authors concluded that K was the most active catalyst of the AAEM species and that the Mg and Ca also play an appreciative catalytic role. Yip *et al* [36] gasified various biochars from parts of a malee tree using steam and ranked the catalytic activity of the minerals in the following order: $K > Na > Ca$. They further went on to suggest that the AAEM species remain in the biochar throughout the reaction. They also reported that

those biochars which had the AAEM species removed, showed a lower reactivity than the original ones.

2.7 Conclusions

From the above literature survey, it is clear that biochar can be gasified using steam to produce a syngas that is rich in H₂. The volume fraction of H₂ varied with each experiment but all the authors attained at least 50% H₂ by volume at temperatures greater than 800°C. All the previous studies on steam gasification were carried out on biochars that were formed via fast pyrolysis. Intermediate pyrolysis also produces high quality biochars that can be gasified using steam and that is the aim of this study. None of the previous authors have utilised the syngas and the second aim of this investigation is to test the suitability of the syngas for use in solid oxide fuel cells.

2.8 Fuel Cells

This part of the literature survey will review the fundamentals of fuel cell technology. It is split into three parts; the first part is an overview of the various types of fuel cells and their basic principles. The second part is a literature survey of syngas powered SOFCs and the final part is a review of the effects of the various syngas constituents and contaminants on SOFC performance.

2.9 Fuel Cell Fundamentals

Fuel cells are electrochemical devices that convert the chemical energy in a fuel directly into electrical energy, thereby promising higher efficiencies than a combustion engine which requires many steps to do the same [10]. The basic building blocks of a fuel cell consist of an electrolyte which is in contact with porous anode and cathode electrodes on either side. A combustion reaction is split into two electrochemical half reactions (reactions 2-27 and 2-28), provided that the reactants are available at their designated electrode. By employing a selectively conductive electrolyte and spatially separating the two half reactions, electrons transferred from the fuel can be forced to do work by making them flow through an external circuit [63]. This configuration can be seen in Figure 2.6.

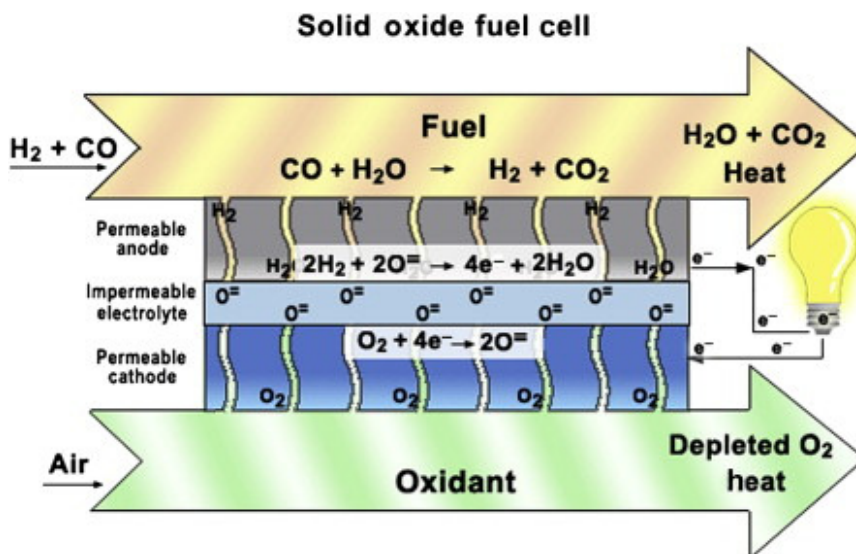


Figure 2.6: Schematic of a Solid Oxide Fuel Cell [64]

It can be seen from Figure 2.6 above, that the SOFC operation is as follows; fuel (syngas) is fed into the SOFC at the anode. In the case of H₂, the anode splits it into protons and electrons. The membrane is impermeable to electrons and forces them to go around in an external circuit and into the cathode where they are picked up by oxygen to become O²⁻. The O²⁻ diffuses through the cathode and reacts with the fuel to produce H₂O or CO₂.

There are many forms of fuel cells that have been developed, the major categories are shown in Table 2-6, which shows the types of fuel cells, the charge carrier through the electrolyte and the anode and cathode half reactions.

Table 2-6: The various types of fuel cells and their operating principles as well as their half reactions at the electrodes [64]

Fuel Cell	Charge carrier through electrolyte	Anode Reaction	Cathode Reaction
Direct Carbon	O ²⁻	C + O ²⁻ → CO ₂ + 2e ⁻	½O ₂ + 2e ⁻ → O ²⁻
Polymer Electrolyte	H ⁺	H ₂ → 2H ⁺ + 2e ⁻	½O ₂ + 2H ⁺ + 2e ⁻ → H ₂ O
Phosphoric Acid	H ⁺	H ₂ → 2H ⁺ + 2e ⁻	½O ₂ + 2H ⁺ + 2e ⁻ → H ₂ O
Alkaline	OH ⁻	H ₂ + 2OH ⁻ → 2H ₂ O + 2e ⁻	½ O ₂ + H ₂ O + 2e ⁻ → 2OH ⁻
Molten Carbonate	CO ₃ ²⁻	H ₂ + CO ₃ ²⁻ → H ₂ O + CO ₂ + 2e ⁻ CO + CO ₃ ²⁻ → 2CO ₂ + 2e ⁻	½O ₂ + CO ₂ + 2e ⁻ → CO ₃ ²⁻
Solid Oxide	O ²⁻	H ₂ + O ²⁻ → H ₂ O + 2e ⁻ CO + O ²⁻ → CO ₂ + 2e ⁻ CH ₄ + 4O ²⁻ → 2H ₂ O + CO ₂ + 8e ⁻	½O ₂ + 2e ⁻ → O ²⁻

The two most common forms of fuel cells are polymer electrolyte membrane (PEM) and solid oxide fuel cells (SOFC). Typically, in a continuous operation of a PEM fuel

cell, air is fed to the cathode and hydrogen is fed to the anode. With the help of a catalyst such as Platinum, hydrogen is split into protons and electrons. The protons diffuse through the membrane whilst the electrons generate a current that can be utilised before combining with the oxygen and reacting with the protons to make water [64]. PEM fuel cells require ultra-pure hydrogen and have virtually no tolerance to impurities such as CO [65] and S [66].

2.10 Solid Oxide fuel cells

Unlike PEMFC, SOFCs have a solid, metallic oxide and ceramic (cermet) membrane, hence the alternative name of ceramic fuel cells. [67]. They operate at 600 – 1000°C, typically using a Yttria stabilised zirconia (YSZ); Co-ZrO₂ or Ni-ZrO₂ cermet anode with a Sr LaMnO₃ cathode [67] [68]. SOFCs are very fuel flexible and do not require a precious metal catalyst. Their high temperature of operation makes them ideal for use in combined heat and power (CHP) systems where theoretical efficiencies greater than 80% can be achieved [67].

There are two common cell designs associated with SOFCs; planar and tubular. Planar cells are thin flat plates with ribbed interconnects that form gas flow channels and acts as a bipolar gas separator contacting the cathode and anode of adjoining cells [69]. Variations with cell manufacturing techniques have led to two types of planar cells; electrode supported and electrolyte supported cells. Electrolyte supported cells typically employ a YSZ electrolyte of 50 – 150 µm thickness, leading to high ohmic resistance. Their operating temperature is high, at around 1000°C. Electrode supported cells use an electrolyte of 5 – 20 µm thickness, leading to lower

ohmic resistance reducing their operating temperature to $\sim 800^{\circ}\text{C}$. This in turn leads to many benefits such as; lower rates of degradation for cell and stack, cheaper interconnects, reduces the warm up and cool down time and is less demanding on seals [69].

Tubular cells are formed by depositing thin layers of cell components onto an electrolyte which itself is formed via extrusion and sintering. The various layers that make up the cell components are deposited either by electrochemical vapour deposition or plasma spraying [69]. Tubular cells have the advantage of not requiring a seal since the oxidant and fuel are separated naturally by its geometry, enabling very stable operation for an extended period of time.

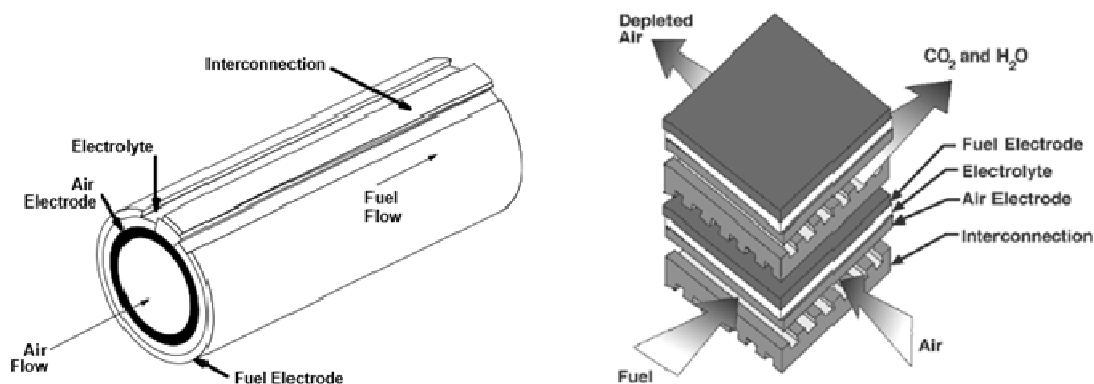


Figure 2.7: showing the two types of SOFC geometries (left) tubular and (right) planar [68]

2.11 Syngas Powered Solid Oxide Fuel Cells: A Literature Review

This part of the literature survey will review some of the previous work carried out on using syngas in solid oxide fuel cells. The first part of the survey reviews previous

work where real syngas from biomass gasification was utilised in SOFCs. The second part focuses on the effects individual components within syngas, have on SOFC performance. The second part of the literature survey is specific to Ni-YSZ and avoids work on other types of anode materials.

2.12 Effects of Syngas on the Performance of Solid Oxide Fuel Cells

Most of the previous work studying the effects of syngas on SOFC performance has used simulated syngas whereby mass flow controllers were used to synthesise a gas representing syngas. There are few studies that have used real syngas (derived from biomass). One such study was carried out by Hofmann *et al* [70] who investigated the performance of a high temperature electrolyte supported Ni-GDC/YSZ/LSM SOFC using syngas from a fixed bed two-stage downdraft gasifier. The gas was first treated to remove particulates and contaminants such as HCl and H₂S and was then fed into a SOFC operating at 850°C using a steam to carbon ratio (S/C ratio) of 0.5. These conditions ensured that the SOFC was operating thermodynamically 'carbon free'. The authors reported that the SOFC ran for 150 hours without any performance losses and the cell was operated using a fuel utilisation factor of 30% and a current density of 260 mA cm⁻².

In another study, Hoffman *et al* [71] studied the effects of using syngas from two different gasifiers; fixed bed down-draft gasifier and a bubbling fluidised bed gasifier. They used wood chips as fuel in both gasifiers and studied the effects of tars, composition fluctuations and particulates on the Ni-GDC (Ni-Gadolinia doped ceria) anode. A low fuel utilisation was deliberately used so as to avoid contamination of the

anode and the product gas was first treated to remove sulphur and chlorine contaminants. Removal of tars and particulates were varied to study their effects. The authors reported that differing tar loads did not have a major impact on the performance of the SOFC at 850°C, since the measured cell voltage was constant for all the tar loadings tested and the IV (current density-voltage) curves 'before' and 'after' showed that the cells maintained their initial performance. With respect to particulates, the authors reported a drastic decrease in the performance of the SOFC when particulates and char were allowed to enter the SOFC anode. The decrease in performance was attributed to the clogging up of the anode porous structure, thereby hindering gas diffusion, or blocking of catalytically active sites or causing anode layer delamination due to mechanically induced tensions.

In a follow up study, Hofmann *et al* [72] investigated the operation of a SOFC that was operated on syngas derived from biomass gasification of wood pellets, with tar levels above 10 g m⁻³. The syngas was produced in a circulating fluidised bed gasifier and it was treated to remove H₂S, HCl and particulates. The SOFC was operated at 850°C with a 20% fuel utilisation factor and a current density of 130 mA cm⁻². They reported that there was no performance loss as a result of the heavily tar laden gas. Oudhuis *et al* [73] operated a 1 kW SOFC stack using two fuels; willow and rofire, which is a mixture of plastics (60%) and paper residue (40%). The fuels were first pyrolysed and the vapours and gases were then sent to an air blown gasifier. The resulting syngas was fed into a SOFC and was operated up to 48 hours. The authors reported that during fuel heating inside the SOFC, soot formation was observed which negatively affected the performance of the SOFC. In a similar study, Nagel *et al* [74] operated a 1 kW SOFC stack using syngas from an updraft gasifier. The tar

loading was around 8 g m^{-3} and a performance loss of 6% was observed after 30 hours of operation.

2.13 Effects of Syngas Constituents on the performance of Solid Oxide Fuel Cells

The syngas composition varies with biomass type, operating conditions etc; this will affect the SOFC in different ways. This part of the literature survey will review previous work that has investigated what effects the various constituents in the syngas have, on SOFC performance. It will focus particularly on CO, CO₂, CH₄, H₂S and HCl as well as other contaminants such as NH₃, PH₃ etc. The review will focus specifically on Ni-YSZ anode SOFCs since the anode material makes a big difference to the overall performance on certain fuels.

2.13.1 Effects of Carbon Monoxide Content on Solid Oxide Fuel Cell Performance

Carbon monoxide is one of the main constituents of syngas and is able to be utilised in SOFCs [11]. The CO can be utilised in two ways; either through direct oxidation (reaction 2-7, page 20) or the CO can be shifted to H₂ via the WGSR (reaction 2-10, page 20) so that the H₂ can be utilised. Costa-Nunez *et al* [75] investigated the effects of CO content on two different SOFC anodes; Ni-YSZ and Cu-CeO₂-YSZ. They reported that the Ni-YSZ anode was more sensitive to the presence of CO and its performance was substantially lower than that of the Cu-CeO₂-YSZ wrt CO

content. Many researchers have reported a decrease in performance when using CO instead of H₂ as a fuel in Ni-YSZ based SOFCs. Matsuzaki *et al* [76] studied the electrochemical oxidation of H₂ and CO in a H₂-H₂O-CO-CO₂ system and found that the electrochemical oxidation rate of H₂ was 1.9-2.3 and 2.3-3.1 times faster than that of CO at 750 and 1000°C, respectively. Sukeshini *et al* [77] investigated the electrochemical oxidation of H₂, CO and CO/H₂ mixtures on patterned Ni anodes on YSZ electrolytes. They reported that higher polarisation resistances were observed when CO was used as opposed to H₂ and when the CO was shifted to H₂ using H₂O, there was a detrimental effect on the power densities as open circuit voltage dropped and no changes in polarisation resistances were observed. Eguchi *et al* [11] compared the performance of H₂-H₂O mixtures with CO-CO₂ mixtures over a Ni-YSZ anode at 1000°C. Their results are displayed in Figure 2.8. It can be seen that although the OCV was similar in both cases, the current density was drastically lower for CO, meaning that the H₂ was more preferentially consumed by the electrode reaction. The authors attributed the differences in performances to the activation and/or concentration polarisations.

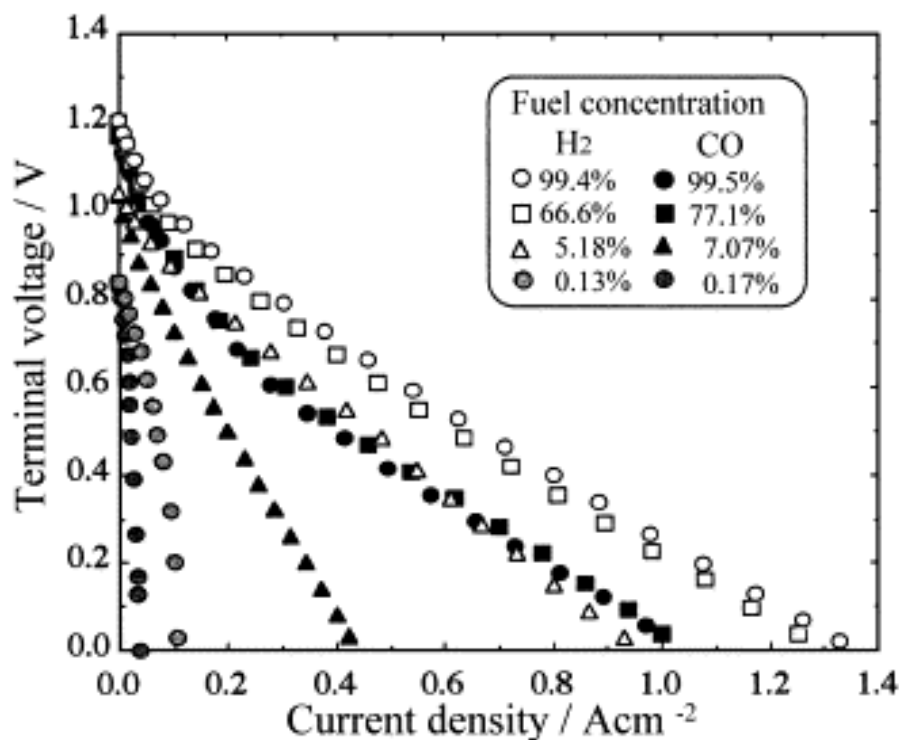


Figure 2.8: Effects of various concentrations of CO and H₂ on the performance of a Ni-YSZ SOFC at 1000°C [11]

Kromp *et al* [78] carried out a detailed study into the fuel – Ni-YSZ interactions, they used mixtures of H₂/H₂O and CO/CO₂ and reported that only H₂ was electrochemically oxidised at the anode. The CO is oxidised only after partaking in the WGSR to form H₂ and CO₂. The two biggest problems that CO causes in SOFCs are; its propensity for carbon deposition and its higher anodic over-potential, meaning that more energy is used up at the anode than is thermodynamically required [79]. However, there have been successful studies on the use of CO in Ni-YSZ SOFCs. Homel *et al* [79] investigated the use of CO as a primary fuel source for SOFCs with a Ni-YSZ anode for both tubular and planar geometries. They reported that a power density of 0.67 W cm⁻² was achieved from the tubular cell, which was only slightly below the 0.74 W cm⁻² obtained using H₂ in the same cell at 850°C. The tubular cell

was operated for a period of 375 hours and there was no reported loss in performance. To investigate the planar cells, the authors constructed a 50 cell, 1 kW stack and operated it 800°C using 95% CO and 5% CO₂ and concluded that CO is a viable alternative to H₂.

2.13.2 Effects of Carbon Dioxide on Solid Oxide Fuel Cell Performance

Carbon dioxide is an inert gas that acts as a diluent, however, inside an SOFC, it can partake in various reactions that affects the SOFC performance. Suwanwarankgul *et al* [80] investigated the effects of SOFC performance using various constituents found within syngas. They used a mixture of H₂ and CO₂ and reported that the effects of CO₂ concentration were more pronounced than the effects of N₂. The authors attributed their findings to the ability of the CO₂ to take part in the WGSR and Boudouard reaction. The WGSR used some of the H₂ and CO₂ to form H₂O and CO, which led a decrease in the OCV by 20 and 26% at 800 and 900°C, respectively. Borello *et al* [81] studied the effects of varying the composition of syngas components on the performance and degradation of Ni/GDC-Ni-YSZ single cell planar SOFC. They varied the composition of CO₂ over a range of 0 – 21% and reported that the variation had no effect on the cell performance apart from a dilution effect which led to lower OCVs as compared to pure H₂. Miao *et al* [82] investigated among other things the effects of adding CO₂ and H₂O alongside pure H₂ to a planar SOFC cell operating at 750°C. They reported that the OCV of the cell drops with the

addition of 10% CO₂ from 1074 mV to 990 mV which led to a drop in the power density obtained from the cell.

2.13.3 Effects of Methane on Solid Oxide Fuel Cell Performance

Methane is known to act as a fuel for solid oxide fuel cells [83] [84]. The CH₄ can be used directly as a fuel since it can be reformed into CO and H₂ inside the fuel cell via reaction 2-15, (page 20). The reformation can be 'dry' or 'wet'. Dry reformation takes place in the presence of CO₂ as shown by reaction 2-29, whilst wet reformation takes places in the presence of steam.



One of the major problems with using CH₄ as a fuel is that it can deposit carbon on the anode surface as shown by reaction 2-30 below. The deposited carbon can foul pores and voids and form various products such as graphite or high molecular weight hydrocarbons which can lead to a loss in electrochemical performance. The formation of these products can proceed either by CH₄ dissociation or the Boudouard Reaction [85].



The carbon deposition reaction as well as the methane reforming reaction is catalysed by the Ni catalyst and factors such as temperature, Ni-YSZ formulation, use of additives and S/C ratio govern the amount of carbon deposited [86]. According to Koh *et al* [86], wet carbon deposition is reversible and its oxidation has no effect on the cell performance but dry carbon deposition is irreversible and it has a negative effect on the cell performance.

In general, once the carbon is adsorbed onto the surface of the Ni-YSZ cermet, it migrates into the structure and begins to form fibres. The rate at which the Ni adsorbs the carbon is much faster than the rate at which electrochemical oxidation occurs either by oxygen or steam, hence it is kinetically driven [87]. The carbon deposition can be controlled by operating the fuel cell in conditions that would make it thermodynamically unfavourable for carbon formation reactions to occur. These conditions can be seen in Figure 2.9 below. For dry reforming, carbon deposition occurs at a current density less than 300 mA cm^{-2} whereas for wet reforming of CH_4 , carbon deposition occurs at a current less than 100 mA cm^{-2} . Marinsek [88] investigated the use of CH_4 in a SOFC at temperatures of $600 - 800^\circ\text{C}$ using various S/C ratios. The author reported that dry reforming always led to carbon deposition but in wet reforming, S/C ratio of 0.82 avoids carbon deposition and shows was no sign of diminished catalytic activity of the Ni-YSZ cermet for all the temperatures studied.

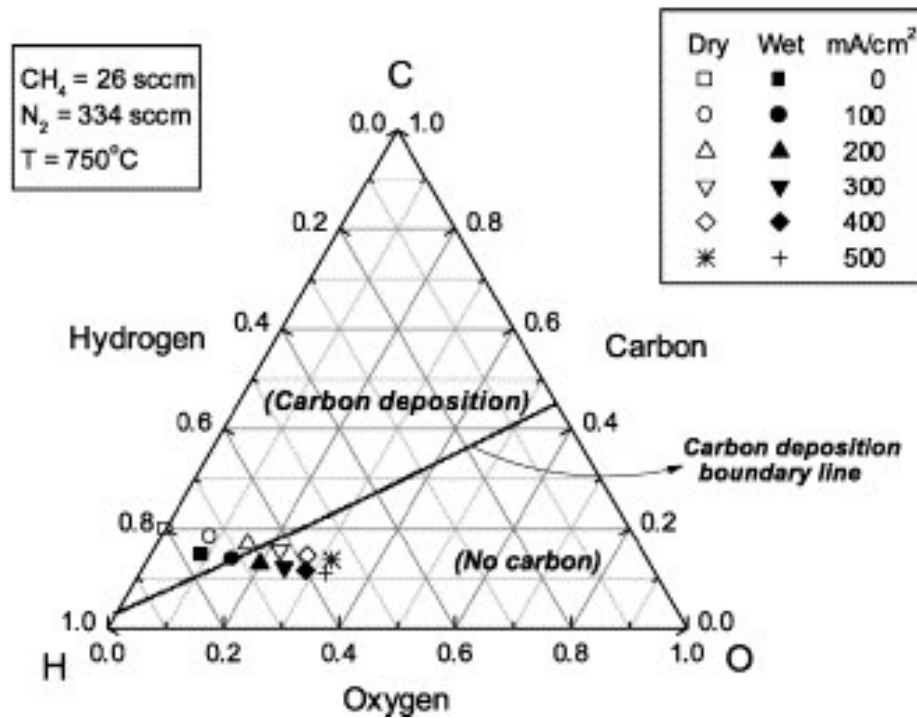


Figure 2.9: Ternary diagram showing regions where carbon deposition is likely to occur thermodynamically [86]

2.13.4 Conclusions

From the above studies, it can be concluded that the majority of the syngas constituents pose no real threat to the SOFC so long as correct operating conditions are used. CO and CH₄ are perhaps the biggest threats to the SOFC performance due to their ability to deposit carbon on the anode surface but this can be mitigated by introducing steam in the fuel mixture.

2.14 Effects of Contaminants on the Performance of Solid Oxide Fuel

Cells

This part of the literature survey will focus on the various syngas contaminants and their effects on the performance of a Ni-YSZ anode SOFC.

2.14.1 Effects of Phosphorus Contaminants on Solid Oxide Fuel Cell Performance

Some biomass substrates such as rapeseed [89] and sewage sludge [90] have a high P content. The behaviour of P containing compounds is not fully understood but studies have shown that it may exist as diphosphorus trioxide (P_2O_3)₂ or more likely, phosphine, (PH_3), and under normal SOFC operating conditions, the PH_3 is hydrolysed to form HPO_2 vapour [91]. Much research has focused on the effects of PH_3 on the Ni-YSZ anode, Xu *et al* [92] studied the effects of exposing a Ni-YSZ anode surface to a syngas containing 10 ppm PH_3 at 800°C The authors reported a dramatic and irreversible degradation of the cell performance resulting from the deterioration of the functional layer near the electrolyte. The loss in electrochemical performance was attributed to the formation of Ni_5P_2 . In another study, Xu *et al* [93] investigated the effects of PH_3 on a Ni-YSZ anode under various operating conditions. They reported that the cell degradation was more pronounced at higher temperatures but the PH_3 is more reactive to the Ni at lower temperatures forming an intermediary species Ni_xP_y . The authors also reported that the presence of steam does not suppress the degradation process. Similar results were also obtained by Channa *et al* [94] who investigated the effects of PH_3 (10-20 ppm) in syngas with 8, 16

and 27.1% steam content. They reported that the steam content had no effect on the rate of degradation of the SOFC and that the rate of cell degradation at 900°C was greater than that at 800°C. The authors attributed the finding to two causes; (i) formation of liquid phosphates which hindered mass transport and (ii) greater volume expansion affecting the structural integrity of the catalyst layers.

Other authors have also reported similar findings; Haga *et al* [95] studied the effects of PH₃ on the Ni-YSZ anode and reported that Ni₅P₂ is readily formed even if PH₃ is present in parts per billion (ppb) concentration. The changes in the Ni-YSZ chemistry lead to anodic overpotentials which obstructs internal fuel reforming. Marina *et al* [96] investigated the effects of PH₃ on both anode and electrolyte supported cells at 700 and 800°C. They reported that two primary modes of degradation exist that lead to a loss in performance. The first one is what has been reported by previous authors, namely that the Ni is converted into a P containing species such as Ni₅P₂, Ni₃P, etc. The second mode is the diffusion of the phosphorus to the active anode/electrolyte interface to form an adsorption layer.

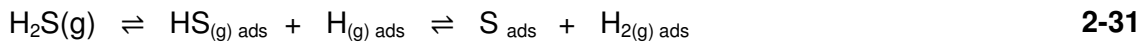
2.14.2 Effects of Hydrogen Sulphide on Solid Oxide Fuel Cell Performance

The most common sulphur containing gas that is likely to be formed during biomass gasification and hence likely to found in syngas is H₂S [97]. The H₂S content is a function of the sulphur content in the initial biomass substrate and the operating conditions of the gasification process. The effects of H₂S on performance of SOFCs have been thoroughly investigated. Matsuzaki and Yasuda [98] studied the effects of

various H₂S concentrations in a gas mixture containing H₂ and H₂O on a Ni-YSZ anode cermet at 750 – 1000°C. They reported that the anode overpotential increased with 0.05, 0.5 and 2 pmm H₂S at 750, 900 and 1000°C respectively. The authors noted that the adsorbance of the sulphur onto the Ni surface was temperature dependent and the time taken to saturate the surface was independent of concentration. The authors also found that the performance loss was reversible when the H₂S was removed from the fuel and pure H₂ was used as a fuel. Sasaki *et al* [99] investigated the effects of H₂S impurity by measuring the cell voltage at a constant current density. They reported that H₂S poisoning at 1000°C was reversible but at lower temperatures, the poisoning was irreversible. The authors also found that the cell degradation occurs in two stages; initially there is a drop in cell voltage which occurs in a short period of time and the cell then stabilises at this voltage. This is then followed by a more gradual and larger cell voltage drop. Zha *et al* [100] also reported similar findings when they introduced a gas stream containing H₂S into a Ni-YSZ SOFC anode. They reported an initial sharp drop in the performance which was followed by a gradual but persistent degradation that lasted for days. Also, the extent of degradation increased with increasing H₂S concentration, increasing cell voltage and decreasing cell operating temperature. Finally, they reported that the process can be reversible at high temperatures but depends upon the extent of exposure to the H₂S.

Rasmussen *et al* [101] investigated the effects H₂S on the performance of Ni-YSZ at 850°C. They found that the poisoning effects of the H₂S were due to it chemisorbing onto the catalyst surface and not due to any changes in the microstructure of the surface, or the formation of an insulating layer. Gong *et al* [102] reported that there

are two primary mechanisms of H₂S degradation of Ni-YSZ anodes. The first one is a physical adsorption of the sulphur onto the Ni surface which blocks the active sites and reduced the electrochemical activity. The second mechanism is the reaction of the S with the Ni to form NiS. The two mechanisms are shown below [102] [101]:



2.14.3 Effects of Ammonia on the Performance of Solid Oxide Fuel Cells

Ammonia is the most common N contaminant found in syngas [97]. It forms when the N in the biomass is released during the devolatilisation stage and reacts with H₂. The NH₃ generally decomposes into molecular N₂ under gasification conditions but the product gas can still contain up to a few thousand ppm of NH₃ [97]. The effects of NH₃ on SOFC performance have received some attention and NH₃ has even been suggested as a possible fuel for SOFCs since the Ni containing anode can break down NH₃ into N₂ and H₂ which can then be utilised by the SOFC [103]. Up to 5000 ppm NH₃ have been used in SOFCs for 2500 hours with no adverse effects [104]. Dekker *et al* [103] utilised NH₃ as a fuel in a SOFC by varying the concentration from 0 – 100 vol%. Their results are shown in Figure 2.10. It can be seen that the performance of the fuel cell is not affected by the increase in NH₃ concentration as it works equally as well on NH₃ as it does on H₂. The authors also pointed out that the use of NH₃ is a lot simpler than the use of hydrocarbons since

the reforming does not cause any carbon deposition, therefore negating the need for steam and a pre-reformer.

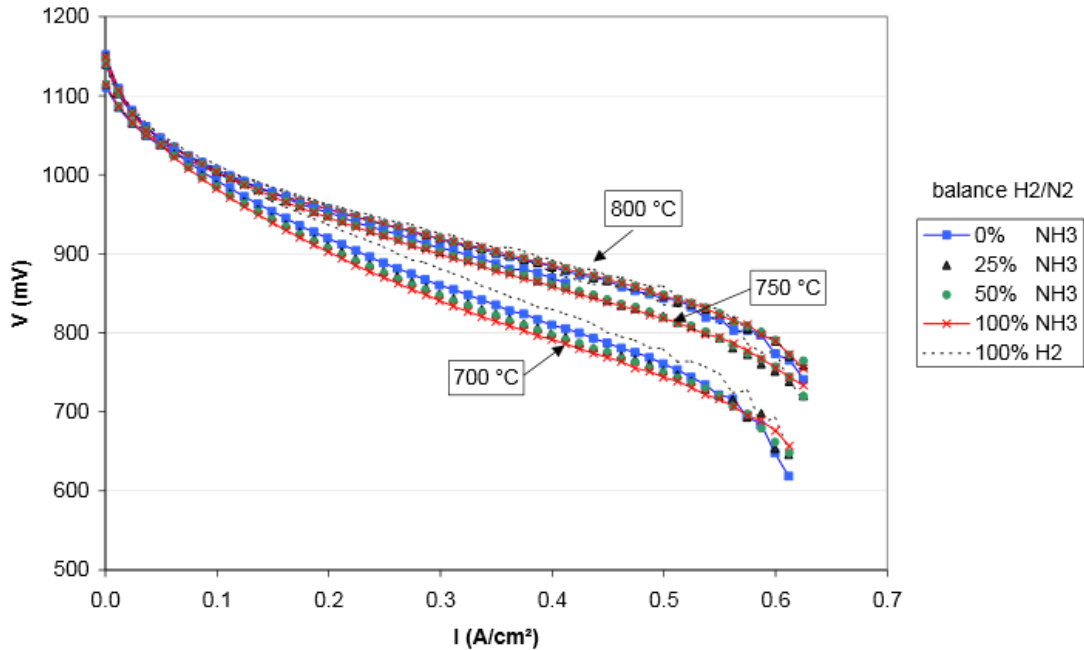
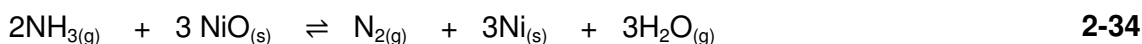


Figure 2.10: Effects of NH₃ on the performance of a SOFC at various temperatures and concentrations [103]

The decomposition of NH₃ into N₂ and H₂ is perhaps the most important step in the utilisation of NH₃ in SOFCs. A possible mechanism for its decomposition is as follows (1) NH₃ is adsorbed onto the catalyst surface, (2) the cleavage of N-H bonds and (3) the recombinative desorption of the N atoms [105]. The thermal decomposition of NH₃ is inhibited by the presence of H₂ at low temperatures (below 673 K) and low NH₃ concentrations; however, this is expected to be negligible at operating temperatures [105]. Zhang *et al* [106] investigated the use of NH₃ in a tubular SOFC at 800°C. They reported that there was no deterioration in performance after operation for 100 hours. Ma *et al* [107] also investigated direct use of NH₃ on the

performance of SOFCs. They reported that the maximum power densities of 299 and 526 mWcm⁻² were given at 750 and 850°C respectively, which were slightly lower than those of H₂ at the same temperatures. The authors also reported that temperatures below 600°C were insufficient for direct utilisation of NH₃ in SOFCs since the reduction of NiO in the anode was too slow and pre-reforming was required. However, at temperatures of 750°C or above, direct utilisation was possible. The utilisation of NH₃ by SOFCs occurs according to the following mechanisms [107];

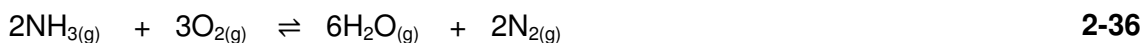
Initial Reduction of the NiO anode



Ammonia Decomposition



Overall Reaction



2.14.4 Effects of Hydrochloric Acid on the Performance of Solid Oxide Fuel Cells

Chlorine occurs in biomass as an alkaline salt which vaporises in the high temperature of gasification and reacts with the water vapour to form HCl [97]. The effects of HCl on the performance of SOFCs have been widely studied and reported.

Trembley *et al* [108] investigated the effects of HCl on a SOFCs operating at 800 and 900°C. They used a syngas mixture with an HCl concentration of up to 160 ppm. Their results showed that that the HCl degrades the SOFC performance but the performance was recoverable once the HCl was removed from the fuel. The degradation was more substantial at 900°C due to the increase in the ohmic resistance caused by the delamination of the current collecting mesh away from the anode. Stable operation of the cell was achieved after 100 hours of operation. Xu *et al* [109] operated a SOFC at 800 and 850°C with a syngas containing 100 ppm HCl for 300 and 100 hours respectively. Over the 400 hours operating period, the authors reported a 3% loss in performance. By comparing their results to previous studies, they concluded that the anode supported cell have a higher resistance to HCl poisoning than electrolyte supported cells. By studying the microstructure using advanced imaging techniques, the authors found that the HCl leads to a loss of Ni at the surface. Bao *et al* [110] investigated the effects of various syngas impurities on the performance of SOFCs. They used 40 ppm HCl in the gas mixture and ran the experiments for 100 hours. They reported that there was no degradation of the SOFC performance at 800 and 850°C in the time it was used.

2.14.5 Effects of Syngas Trace Species on the Performance of Solid Oxide Fuel Cells

So far, this review has focused on the major contaminants found in syngas and their effects on the performance of SOFCs. Syngas from biomass can also contain other species, albeit in minute quantities. These trace species, such as Arsenic (As),

Antimony (Sb) and Lead (Pb) have been studied for their effects on SOFC performance. This section will review the effects of these species.

Bao *et al* [110] reported that As has a very detrimental effect on SOFC performance. The introduction of a low concentration of 10 ppm As at 750°C led to a continuous decline in power density for 10 hours before stabilising for a period of 60 hours. Once the temperature was increased to 800°C, the cell performance became erratic and after 120 hours of operation, no further current could be drawn from the cell. Cayan *et al* [91] reviewed several papers relating to the effects of syngas impurities on the anodes of SOFCs. Using previous work, they derived the results shown in Figure 2.11. It can be seen that the effects of As are more severe at higher temperatures and there is generally a constant decrease in power density over time. Upon exposure to As, the Ni is converted into NiAs, which is a less electrically conductive phase. The authors concluded that the As should not pose as great a risk as HCl or H₂S which attack critical regions near the electrolyte [91].

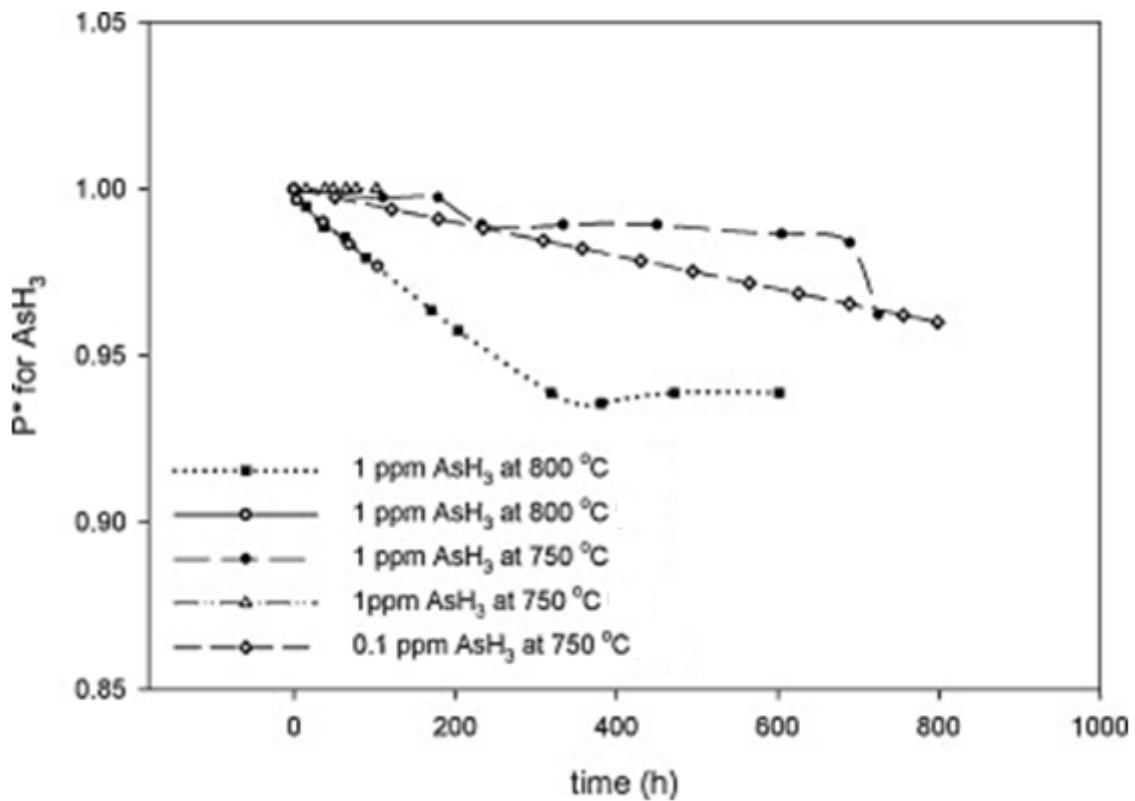


Figure 2.11: Effects of AsH₃ on the performance of solid oxide fuel cells over an extended period of time. Adapted from [91]

Much work has been carried out on other trace species such as Zinc (Zn), Sb, Cadmium (Cd) and Mercury (Hg) but these species are more likely to be found in coal derived producer gas and their concentrations are very low [91]. In general however, Zn is not expected to be deposited on the anode surface and Sb does not lead to any major degradation of the SOFC performance. Hg was thought to condense and deposit on the anode surface [91] but studies have revealed that this is not the case as no significant degradation occurred even at concentrations of 1 ppm [111] and 7 ppm [110]. Cadmium affects the SOFC at high temperatures of

850°C where it forms a compound with the Ni [91]. Similar results were also reported in [110] where no degradation was reported at 800°C after 150 hours exposure but at 850°C, significant degradation occurred after 50 hours exposure.

2.14.6 Conclusions

From the above survey it was found that the most harmful contaminant to SOFC performance is PH_3 . The PH_3 is potent in ppb level and leads to the formation of Ni_2P_5 which has a much lower electrochemical activity leading to anodic over-potential. H_2S causes degradation of the SOFC performance but it is not as severe as PH_3 and at higher temperatures, it is reversible but at lower temperatures, it is irreversible. Ammonia can be utilised directly in a SOFC and at temperatures above 750°C and its presence does not affect the performance of the SOFC. HCl also leads to the degradation of the SOFC performance but the performance is recoverable once HCl is removed from the fuel and pure H_2 is used. Of the trace components, As is perhaps the most potent contaminant. It leads to the performance loss even at levels of 1 ppm.

3 Materials and Methods

3.1 Chapter Overview

This chapter covers the materials and the methods used over the course of the experiments. It describes the visual appearance, physical characteristics and medium of storage of the biochars and dolomite. It also describes the methods used to characterise the biochars and dolomite; physical characteristics such density and surface area, chemical characteristics such as the elemental analyses that were carried out to find the carbon, hydrogen, nitrogen sulphur and ash contents of the biochars.

The next part of the chapter describes the design of the steam gasification experimental rig - focusing on the design of the reactor, feed delivery, steam generator and condensers. It also describes the product flow measurement system, product collection system as well as the product analysis kit and the method used to transfer the product to the gas chromatograph. The final part of the chapter describes the design of the syngas delivery system into a solid oxide fuel cell test rig. It focuses on gas transfer and the method used to obtain a consistent flow.

3.2 Introduction

The biochars used in the study were formed using intermediate pyrolysis and obtained from the European Bioenergy Research Institute (EBRI) at Aston University, Birmingham. Four different biochars were used; wood pellet (WPB), rapeseed (RSB), sewage sludge (SSB) and Miscanthus biochar (MCB). The biochars were all formed

in the pyroformer reactor at 500°C, except for the WPB, which was formed at 450°C to avoid transfer of tars into the bio-oil. Information regarding the precursor biomass substrates is shown in Table 3-1.

Table 3-1: Information regarding the acquisition of precursor biomass substrates of the biochars

Biomass Substrate	Form	Company	Location of growth
WPB	Pellets (debarked mixture of pine and spruce)	Midlands Bioenergy Ltd	Forest Stewardship Council (FSC), Scotland
RSB	Seeds		Allgau, Germany
SSB	Pellets	Severn Trent Water Ltd	Midlands, UK
MCB	Pellets (leaves)	Agri Pellets Ltd	Shropshire, Uk

The biochars were kept in desiccators and a moisture free environment was created by placing moisture absorbing silica gel beads (Sigma Aldrich) inside the desiccators. Although biochars are not known to be affected by light, an opaque cover was used to limit the amount of light that reached the biochars as a precautionary measure to ensure repeatability of results over the course of the experiments. The cover came with the gas bags (VWR Ltd) which were used to collect the syngas.



Figure 3.1: Biochar storage and cover in a desiccators

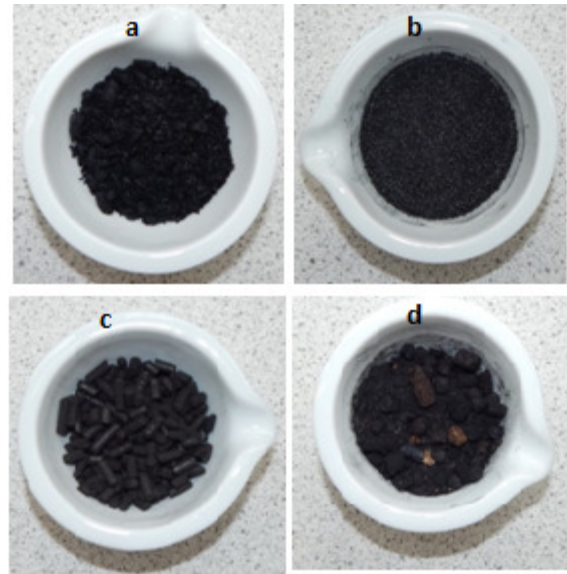


Figure 3.2: Biochar appearance where; (a) WPB, (b) RSB, (c) SSB and (d) MCB

3.3 Biochars

Each of the biochars exhibit unique characteristics, for example, WPB had a very 'oily' texture as it still retained some of the pyrolysis oils. This made the char particles coalesce and unable to be sieved. WPB came in pellets and broken pellets with no powder form. MCB was a mixture of pellets and powder and was very brittle and sharp. Some of the larger MCB pellets did not seem to have pyrolysed fully, this can be observed in Figure 3.2d. The unpyrolysed material could increase the volatile content of the biochar, thus affecting the gasification results. RSB resembled miniature rapeseed seeds; it was brittle and easily broken into smaller pieces. SSB came as pellets that had a uniform diameter, it was the densest biochar of the four, and most resistant to breakage.

3.4 Dolomite

The dolomite used in the experiments was mined in Derbyshire, UK. The dolomite sample was obtained from the School of Chemical Engineering with permission, where it was used as an example specimen and was purchased from Longcliffe Calcium Carbonate. It was received in a fine powdered form; therefore, it was likely that the dolomite sample had been processed beforehand.

3.5 Solid Oxide Fuel Cells

The solid oxide fuel cells (SOFC) used in this study were of a microtubular SOFC variety, the dimensions of which are shown in Figure 3.3. The cell consists of an anode, a cathode, an electrolyte and boundary layers. The anode is on the inside of the tube where fuel gas flows through. The cathode is on the outside – represented by the large black area in Figure 3.3. The electrolyte inhibits the electrons and protons from passing onto the surface whilst allowing O^{2-} to pass through. The white separation layers are there to maintain cell integrity as the cathode and anode are made from materials that are chemically incompatible with each other. The anode is a Nickel based Ytria stabilised Zirconia (Ni/YSZ), the electrolyte is YSZ and the cathode is Lanthanum Strontium Cobalt Ferrite (LSCF). A Scandia doped Ceria barrier is placed between the cathode and anode to prevent the reaction between LSCF and YSZ.

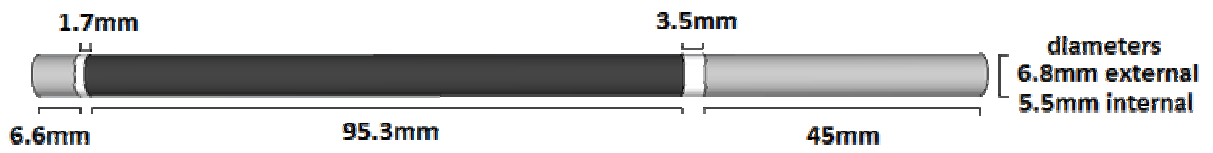


Figure 3.3: Microtubular solid oxide fuel cell, where; the black area is the cathode, the white strips are the separation boundaries and the grey represent non-catalytically active areas

The catalytically active surface area of the SOFC is 20.358 cm^2

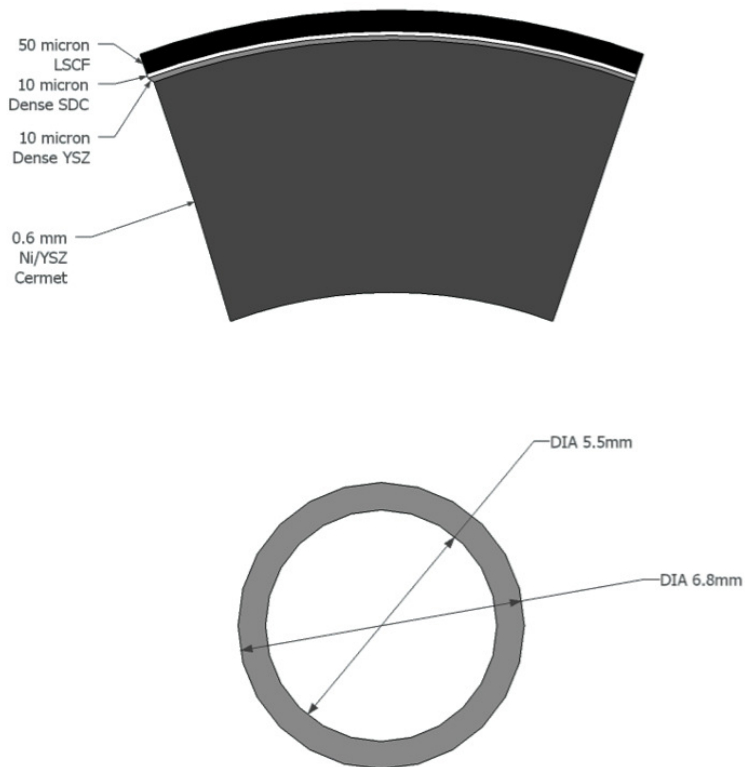


Figure 3.4: Cross section of the microtubular solid oxide fuel cell

3.6 Characterisation of Biochars

The biochars were characterised using the following characterisation methods; Elemental analysis, ash content, BET surface area analysis, mineral content, Higher Heating Value (HHV), moisture content, volatile content, Scanning Electron Microscopy (SEM), particle size distribution and bulk density analysis.

3.6.1 Elemental Analysis and Ash Content

Elemental analysis and ash content determination were carried out by MEDAC Ltd, Surrey UK, using the Thermo FlashEA 1112. The company uses a technique based on the 'dynamic flash combustion' method to determine the CHN and S composition. A 100 mg sample is held in an autosampler, inside a tin capsule, which is continuously purged using helium gas. The tin capsule and biochar sample are dropped into a quartz tube at 900°C and simultaneously, pure oxygen is introduced into the chamber. The sample and tin both melt with the tin catalysing a violent combustion reaction which combusts all the organic matter to produce CO₂, H₂O, NO_x and SO₂. The gas mixture is then passed over a copper catalyst which removes excess oxygen and reduces the NO_x into elemental N₂. The mixture is then sent to a gas chromatograph for analysis. Duplicate analyses were carried for each sample.

The ash content is determined by heating the sample in an oven. A muffle furnace is heated to 600°C. 1 g of sample is weighed into a ceramic crucible and placed in the furnace for four hours until all the organic matter has reacted and only the ash remains. The crucible is then allowed to cool and weighed.

3.6.2 BET Surface Area Analysis

The BET surface area analysis was carried out by a lab technician using Micromeritics A.S.A.P 2010 Gas Porosimetry Surface Area. 3 g sample was degassed for two hours at 300°C under vacuum. Liquid nitrogen was used as the adsorbate and the analysis was carried out over a relative pressure range of 0.06 – 0.199.

3.6.3 Mineral Content

The mineral content of the biochars was determined by X-Ray Fluorescence spectroscopy (XRF) using the pellet press method. 500 mg biochar was crushed using an agate pestle and mortar. It was mixed with 100 mg of inert, wax (cellulose) and pressed into a pellet (Figure 3.5) using a pellet press. The pellet was inserted into a sample cup and placed into a Bruker S8 Tiger with a lithium fluoride (200) crystal for the analyser. A full elemental analysis was carried out, which took eight minutes.



Figure 3.5: Pelletised Biochar for XRF Analysis

3.6.4 Volatile Content

The volatile content was determined according to ASTM D1762-84 using a Carbolite 1300 muffle furnace and a Toledo Sartorius LA120S scale. Biochar was crushed and sieved through a mesh with 250 μm openings (except the WPB which could not be sieved). 1 g \pm 0.1 mg was weighed out and placed into a preheated ceramic crucible with a lid. A muffle furnace was heated to 950°C, the door of the oven was opened and using 51 cm tongs, the crucible was placed on the ledge of the furnace. After two minutes, the crucible was moved to the edge of the furnace for three minutes. Finally, the crucible was moved to the rear of the furnace, the door was closed and the crucible was kept there for six minutes. Finally, the crucible was taken out of the oven, allowed to cool and weighed.

3.6.5 Microstructure Analysis

Microstructure and surface topography were analysed using scanning electron microscopy (SEM). A small but representative sample was separated from the bulk biochar (in its original shape) and stuck onto an SEM stub using conductive tape. SEM requires a conductive sample, hence, a nano-particle gold coating was applied to the sample. The sample was mounted into a Phillips XL30ESEM and the chamber and vacuum pumps were activated to create a vacuum. Once sufficient vacuum was created, the sample was analysed using various magnifications.

3.6.6 Particle Size Distribution

Particle size distributions for RSB, MCB and SSB were determined using a sieve column and or a digital calliper. The sieve column contained the following mesh openings; 850, 300, 106, 63 μm . A 3 g representative sample was placed at the top of the sieve column. The first sieve was dislodged from the column in a way so that it could be shaken but so the biochar fell into the next sieve. It was shaken manually for two minutes and the biochar remaining on top was removed and weighed. The next sieve in the column was then dislodged from the column and shaken for three minutes (longer time was necessary for the smaller particles) and the biochar remaining on top was removed and weighed. The procedure was repeated until the biochar was sieved through the final, 63 μm sieve. Using this method, an average of 96% $\pm 2\%$ of the biochar could be accounted for; the rest was lost in the process. The results were normalised. The procedure was repeated three times for each sample.

To measure the diameter and lengths of the pellets, a digital caliper was used. 3 g representative samples were weighed out at random and the pellets were separated from the powder and measured for their diameters and their lengths. The procedure was repeated five times for each sample.

3.6.7 Higher Heating Value

The HHV of the biochars was determined using a Parr Instruments 1600 bomb calorimeter and 1108 oxygen combustion bomb. Biochar was crushed using pestle and mortar and sieved through a mesh with 250 μm openings (except the WPB). 1 g

(±0.001 g) of the sieved biochar was weighed out and placed into a crucible. The crucible was inserted in the bomb and connected using two 10 cm fuses. The bomb was then filled with high purity oxygen and pressurised to 206.8 bar. A water bucket was filled with 2 kg of water and placed inside the calorimeter. The bomb was transferred into the bucket and the cover of the calorimeter was closed and the bomb fired.

The results were verified using equation 3-1, developed by Channiwala and Parikh [112]

$$\text{HHV (MJ kg}^{-1}\text{)} = 0.3491 (\text{C}) + 1.1783 (\text{H}) + 0.1005 (\text{S}) - 0.1034 (\text{O}) - 0.0151 (\text{N}) - 0.0211 (\text{Ash}) \quad \mathbf{3-1}$$

3.6.8 Bulk Density Analysis

Bulk density was determined for three biochars; RSB, MCB and SSB. The biochars were crushed and sieved through a mesh with 160 µm openings. An empty 25 ml graduated measuring cylinder was dried in a drying oven and weighed out. It was then filled up to a volume of 10 ml with the biochars. With the filling of every 2 ml, the cylinder was dropped three times from a height of 10 cm onto a padded surface to achieve compaction. Each experiment was repeated two times.

3.7 Calcination of Dolomite

Upon receiving the sample, the dolomite was split into two samples of equal mass. One of the samples was calcined at high temperatures using the gasification reactor

(described in Chapter 3.9.3) under a nitrogen-steam atmosphere. The calcination procedure was as follows; a nitrogen flow of 600 ml min^{-1} was used for 20 minutes to purge the air. The reactor was then heated to 900°C using the same nitrogen flowrate. Upon reaching 900°C , the nitrogen flowrate was reduced to 250 ml min^{-1} . Steam was introduced into the reactor at a flowrate of 0.162 g min^{-1} . The dolomite sample was spread out along the sample holder and inserted into the reactor. The dolomite was kept under these conditions for four hours, after which, the steam was shut off and the reactor was shut down but the nitrogen flow remained constant at 250 ml min^{-1} . When the temperature of the reactor had cooled to ambient, the sample was taken out and placed into an air-tight glass container.

3.7.1 Characterisation of Dolomite

Dolomite (calcined and natural) was characterised using the following characterisation methods; bulk density analysis, BET surface area analysis, Thermo Gravimetric Analysis (TGA), X-ray Fluorescence (XRF) and particle size distribution. Most of these methods have been previously described in Chapter 3.6.

3.7.2 Thermo Gravimetric Analysis

The dolomite samples were characterised using TGA to determine the following characteristics; degradation characteristics, mass of CO_2 , extent of calcination and presence of impurities in the sample. The experimental procedure was as follows; 5 – 10 mg sample was weighed in an alumina crucible and placed into a Netzsch TG209

F1 Thermo Gravimetric Analyser. The test programme was set as follows; using a N₂ flowrate of 25 ml min⁻¹, the sample was heated from ambient to 900°C at a rate of 15°C min⁻¹ and held isothermally at 900°C for 20 minutes before the programme terminated and the device cooled.

3.8 Characterisation of Solid Oxide Fuel Cell

The SOFC was characterised using Energy Dispersive spectroscopy (EDS). A new SOFC microtube was broken using a hammer and a 2 cm piece was taken from the centre of the anode. It was stuck onto an SEM stub using conductive tape and a gold coat was applied to it to make it conductive. The analysis was carried out using a Jeol 6060 machine. The Jeol 6060 is equipped with an INCA EDS software which was used to determine the elemental composition of the SOFC anode. Analysis was carried out at 20 keV.

3.9 Experimental Rig Design

A bench scale biochar gasification process requires the following process items in addition to the valves and tubing; steam generation kit, preheater, reactor, furnace, sample delivery, condensers, product flow measurement and product collection.

3.9.1 Valves and Tubing

All the tubes used in the experimental rig were 6.35 mm (1/4") stainless steel tubes (FTI Ltd, East Sussex, UK). The valves were Ham-Let 1/4" quarter turn, on/off valves (FTI Ltd, East Sussex, UK).

3.9.2 Furnace

The endothermic nature of the reactions required a furnace to provide the necessary heat. An Elite Thermal Systems Ltd model number: THH 12/90/305 – 2408cm & 2116 O/T was used to heat the reactor. The furnace is shown in Figure 3.6; it had a 360 mm length heating cavity with a 100 mm diameter.

Some previous researchers carrying out steam gasification of biochar have placed the biochar into the reactor at ambient temperature, then heated it up and finally introduced steam when desired temperature is achieved [12]. There are two main drawbacks with this method; firstly, it does not represent commercial gasification processes as they employ feed systems that introduce the biomass into the reactor at high temperatures. Secondly, if the feed contains any volatile matter, it will devolatilise before the temperature is reached since it took around 36 minutes to heat up to 850°C as shown in Figure. 3.7.



Figure 3.6: Furnace used in the experiments

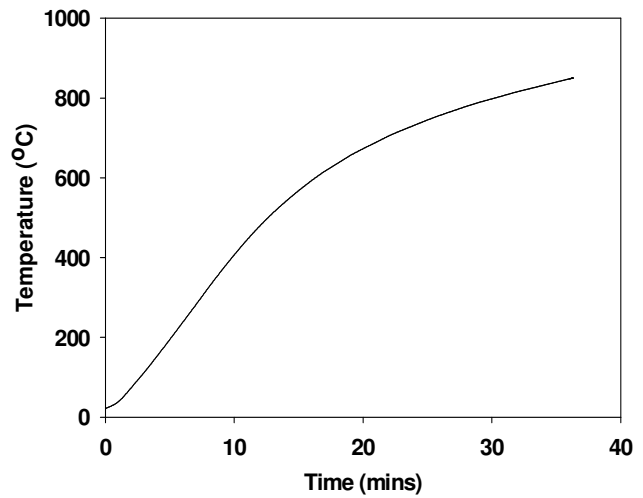


Figure. 3.7: Furnace ramp rate

3.9.3 Reactor Design

To overcome the problems described above, the reactor design needed to meet the following specifications;

- To be able to withstand high temperatures of at least 900°C
- Able to be cleaned
- Able to accept biochar whilst at high temperature
- Able to be opened up without becoming contaminated with air

The most important criteria was the ability of the reactor to withstand high temperature. Steel, which is a common reactor material, is able to withstand moderate to high temperatures but begins to creep during prolonged exposure to, or

at very high temperatures such as those used in gasification. Inconel, a nickel-chromium alloy has been utilised previously in such experiments [12] but it is very expensive and the presence of nickel makes it susceptible to sulphur poisoning and could cause catalysis of certain gasification reactions such as tar cracking or the water gas shift reactions. Quartz has been used by some researchers to carry out the gasification experiments [14]. It is relatively cheap, easy to fabricate designs with, and has a melting point of 1610°C [113] and was therefore chosen as the reactor material.

In order to satisfy the rest of criteria, the set up shown in Figure 3.8 was designed. It consists of three parts labelled a, b, and c. All the quartz parts were ordered from Multilab Ltd, Newcastle upon Tyne, UK. Part 'a' was a B60 connector cone which slotted into the B60 socket and allowed the reactor to connect to the process upstream. Part 'b' was the main reactor, it had two outlets, one, a B19 socket and the other, a ¼" tube which connected it to the rest of process downstream. The B19 socket had two roles; (i) it acted as a secondary outlet and (ii) it accepted the B19 cone. The final part was the sample holder, which extruded from a B19 extended cone. 320 mm of the sample holder were hollowed out to allow the biochar sample to be placed upon it.

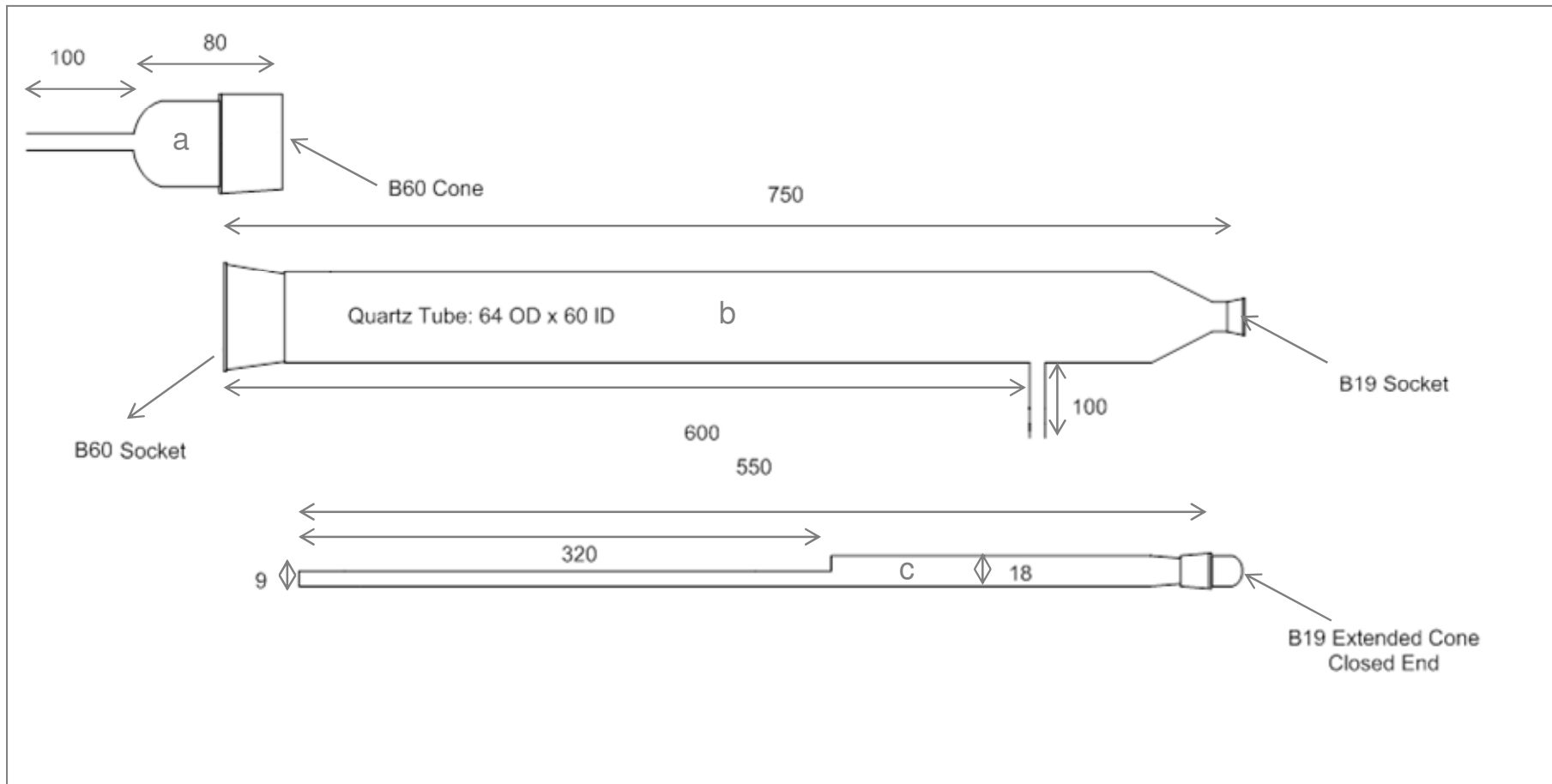


Figure 3.8: Schematic of reactor complex, where (a) B60 connecting cone, (b) reactor and (c) sample holder. All measurements are in mm

The design enabled the reactor to be heated to desired temperature and purged of air as well as accepting the sample holder without allowing contamination from air. This was possible as the nitrogen outflow from the outlet stopped air from getting in. When the sample holder was inserted into the reactor, the nitrogen flow was switched off and the reaction could proceed. The reactor was connected to the metal tubes comprising the rest of the rig via glass-to-metal joints (Moores Glassworks, Walton-on-Thames, Surrey, UK) shown in Figure 3.9. A quartz-Pyrex adapter (Moores Glassworks) was used to connect the Pyrex-metal joint to the quartz reactor complex.



Figure 3.9: Glass to metal joint used as a connector to connect the quartz reactor complex to metal tubes

The dimensions of the reactor (shown in Table 3-2) were determined by the dimensions of the heating cavity in the furnace. The diameter of the reactor was chosen to fit comfortably into the heating space and avoid unnecessary movements. Heat resistant material was shaped around the reactor and moulded using a temperature resistant ceramic material. This ensured that the reactor was placed in the middle of the furnace and the ends were adequately insulated.

Table 3-2: Dimensions and properties of the reactor

Property	Value
Overall Length (mm)	775
Diameter (mm)	64 OD, 60 ID
Thickness (mm)	4
Outlet tube length (mm)	100
Outlet tube diameter (mm)	10 OD, 8 ID
Heated Length (mm)	360
Total Volume (m ³)	0.002026

3.10 Steam Generator

The operational parameters of the steam generator are given below in Table 3-3.

Table 3-3: Operational Parameters of the steam generator

Parameter	Value
Heated Length (m)	1.5
Maximum Temperature (°C)	200
Operational Temperature (°C)	180
Maximum Flow of Steam (g min ⁻¹)	1

Heating tape (RS components Ltd, UK) was bound around the ¼” diameter, 1.5 m long pipe. Insulating material was used to cover the trace tape/pipe to provide insulation and provide support to hold it in place. A final layer of aluminium foil was used to cover up the whole system. A temperature fuse was used as a safety device, it allowed safe operation of up 200°C, and melted if this was exceeded, cutting off the power to the trace heating.

3.10.1 Steam Flow Calibration

The steam flow was determined by diverting the steam into a metal coil which was immersed in an ice bath, in order to condense the steam and collect the condensate. The outlet of the coil drained into a measuring cylinder. The results of the experiments are displayed in Figure 3.10.

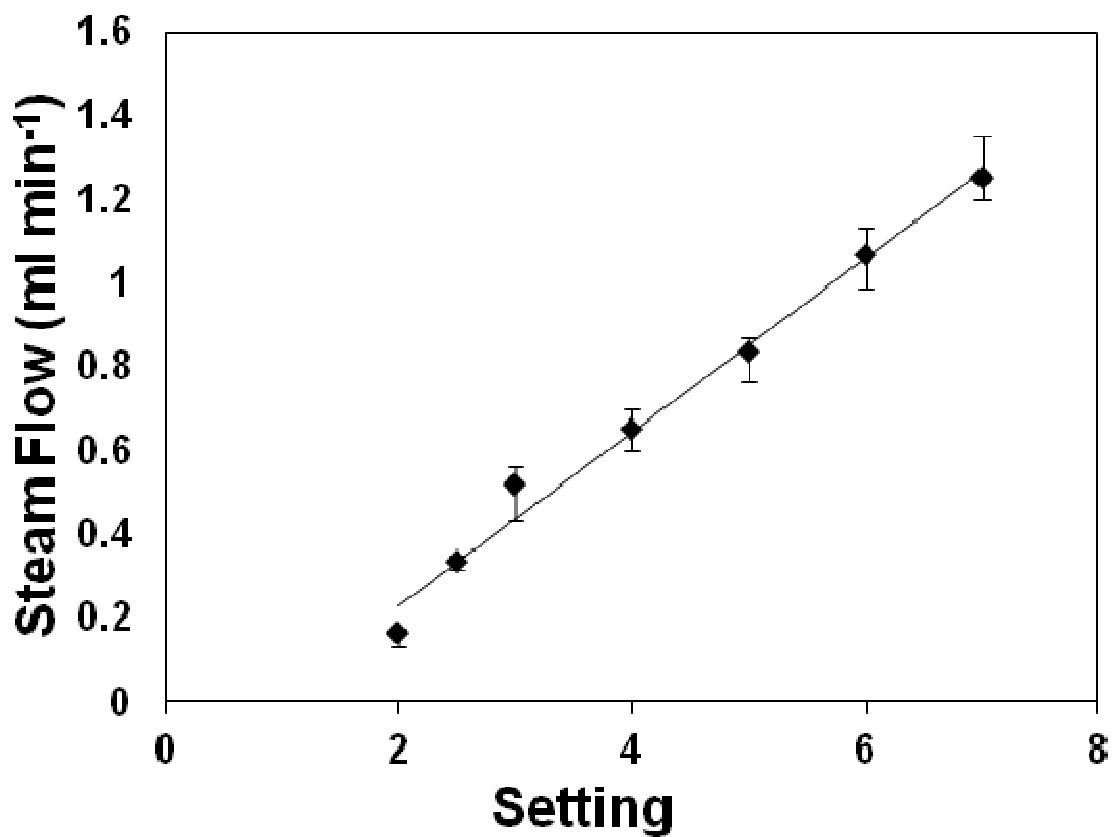


Figure 3.10: Steam flow profile as a function of pump setting

3.11 Condensers

Initially, the set up was designed to accommodate one metal condenser but due to the position of the condenser and the fragility of glass-to-metal joint needed to attach it to the reactor, the initial design was not feasible. Instead, the design was changed to incorporate two condensers; one, a glass coil connected to a modified two neck round bottom flask, called the tar collector. The tar collector was essentially a 75 ml round bottom flask with two glass to metal joints attached to it on either side, this enabled the condensate to flow into it and the syngas to flow out. The second condenser was a 3 m, 0.635 mm stainless steel pipe bent into a coil, which was placed into a shell and operated in a counter current mode with a chiller providing the cooling water.

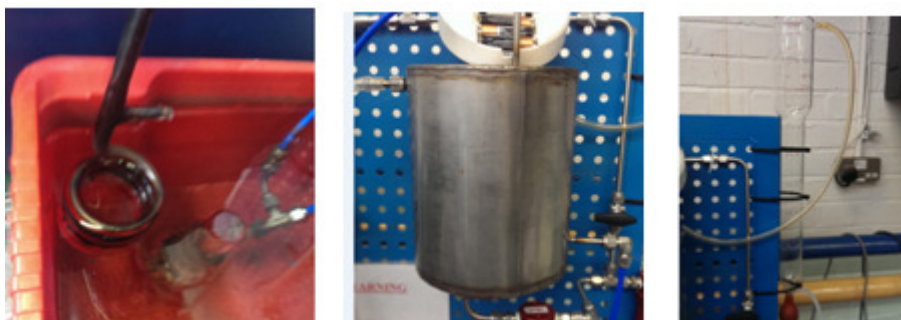


Figure 3.11: Downstream process items; (left to right), primary condenser, secondary condenser and bubble flowmeter.

The last major process item on the experimental rig was the 500 ml Supelco 2-0427 bubble flow meter, purchased from Sigma Aldrich. Calibration was carried out using a nitrogen rotameter placed upstream of the reactor. The flow meter was marked so that a new bubble could be induced which reached zero at the same time as the previous bubble reached the 500 ml mark. According to the manufacturer's instructions, the bubble flow meter will give an inaccurate reading if

water vapour is present in the gas stream. Two water traps (HeadlineFilters) were fitted before the bubble flow meter to ensure no water vapour reached the bubble flow meter. They were equipped with Type C filter elements (HeadlineFilters) which are specifically designed to retain vapours and aerosols. The overall process is shown in Figure 3.12.

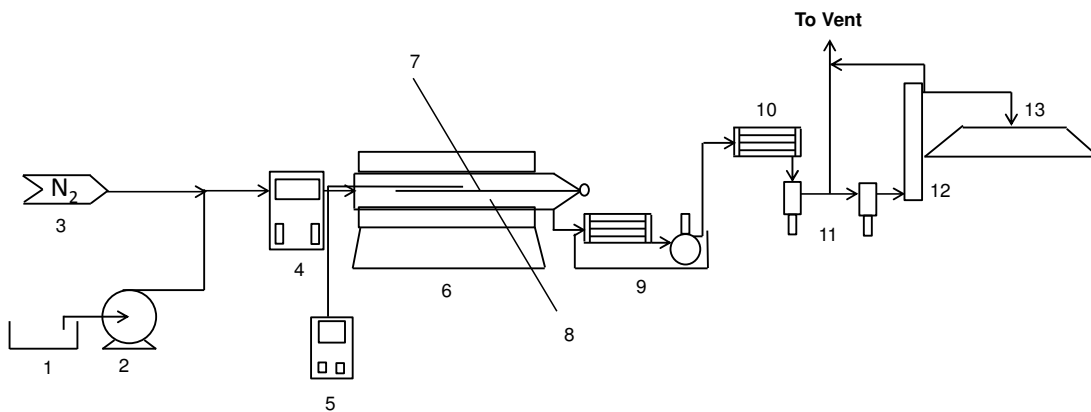


Figure 3.12: Top picture of the gasification rig. Bottom, schematic of the gasification rig, where; 1; deionised water reservoir, 2; pump, 3; zero grade nitrogen supply, 4; pre-heater, 5; temperature read out, 6; Furnace, 7; quartz sample holder, 8; quartz reactor, 9; condenser and ice bath, 10; secondary condenser, 11; water trap, 12; bubble flow meter, 13; gas bag.

3.12 Gasification Experiments

The gasification experiments were carried out as follows; 3 g (± 1.0 mg) of biochar was weighed out using a Sartorius LA120S scale (± 0.1 mg) and spread out evenly onto the sample holder. The preheater, furnace and condenser were switched on. After achieving desired temperature, the steam generation kit was switched on. When steam began to flow out of the reactor, the system was purged with N₂ at a flow rate of 600 ml min⁻¹. After 15 minutes, the sample holder was inserted into the reactor and N₂ was switched off. Gas collection was performed using two methods; by a gas bag or 30 ml serum bottles which were used as reservoirs to obtain a representative sample at gasification times of 1, 3, 5, 7.5, 10, 15, 20, 25 and 30 minutes. A correction factor was calculated to account for the dissolution of CO₂ in the water using standard gas mixtures (procedure is described in Chapter 3.12.4). After 30 minutes, the reaction was stopped and the furnace, preheater, heated line and pump were switched off. The reactor was purged with N₂ for a further 10 minutes. The spent biochars (those produced at 650, 750, 850°C and a steam flow of 54 and 277 g min⁻¹ kg⁻¹ biochar) were sent to MEDAC Labs Ltd for further elemental analyses.

The biochars were gasified in their original form unless stated; experiments were performed in order to study (i) the effects of differing particle sizes, (ii) the selection of the biochar most suitable for gasification and (iii) their effects on efficiency. Each experiment was carried out three times and the mean was taken as the final result.

3.12.1 Gas collection and Transfer

Two methods were developed for gas collection, one was used to capture all the gas produced during the experiment and the other was used to obtain a transient gas composition over the course of the experiment. The first method of gas collection was carried out using a Chemware, Tedlar, gas/liquid sampling bag with dimensions; 381 x 381 ml and 8100 ml capacity (VWR International). The gas bags have a nickel plated on/off valve which was used to connect each of them to the outlet of the bubble flow meter via a short plastic hose of the same diameter. After the experiment had finished, a 50 ml SGE gas tight syringe (Sigma Aldrich), shown in Figure 3.13, was connected to the gas bag using a 2 cm silicon tube and used to collect a representative 50 ml sample from the gas bag.

The second method of collection involved collecting a representative sample at specified times. A 50 ml sample was collected using the aforementioned syringe and transferred into 30 ml serum bottles (Sigma Aldrich). The serum bottles were first filled with water and sealed off using grey butyl rubber stoppers and held in place using aluminium seals (both Sigma Aldrich). The syringe was connected to the gasification rig using a custom made Luer lock-to-Swagelok fitting (The Westgroup Ltd) (Figure 3.13). Once 50 ml of gas was collected, the outlet valve was closed and a needle was attached to the syringe. Another needle was inserted into the serum bottle to allow for the displacement of water by the gas. Gas was injected into the bottle for collection. The configuration is shown in Figure 3.14. Gas was taken out of the bottle using the reverse method. The outlet of the second needle was dipped into a water reservoir. Gas was sucked out of the bottle using the syringe to induce a vacuum which allowed water to refill the bottle.

The gas in the syringe was then injected into the refinery gas analyser (RGA) using the method described in section 3.12.2.

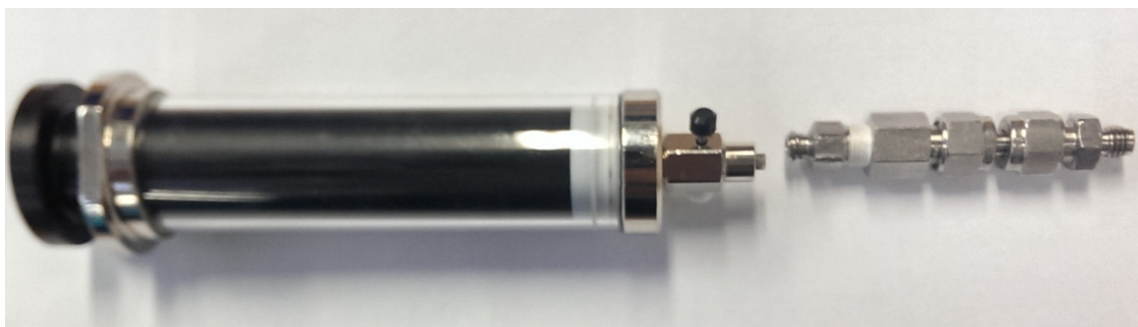


Figure 3.13: 50 ml SGE syringe with a Luer lock to Swagelok fitting



Figure 3.14: Gas collection method using serum a bottle

3.12.2 Injection into the Refinery Gas Analyser

Two methods of injections could be used to inject the gas into the Refinery Gas Analyser (RGA); (i) manual injection and (ii) automatic or 'live' injection. Manual injection is carried out using a gas tight GC syringe; a known quantity is collected from the sample and injected directly into the RGA via the injection port. Although this method is simple, there are drawbacks – human error in particular being the most obvious. To eliminate human error, the second method was used. This

method allowed the RGA to automatically inject a set volume of gas into the columns - overcoming human error and allowing for more precise results. The 50 ml syringe was connected to a carrier pipe upstream of the RGA via Swagelok fittings, using the set up shown in Figure 3.13. The gas was pumped into the line for 5 seconds, after which, the 'start' button was pressed. The RGA automatically injects a set volume of gas into its columns and the analysis can proceed. This way, repeatable results could be obtained.

3.12.3 Gas Analysis

Gas analysis was carried out using an Agilent 7890A refinery gas analyser (RGA). The 7890A uses seven columns, five valves and three detectors - of which two are thermal conductivity detectors (TCD) and one is a flame ionising detector (FID). The valves split the gases into their respective columns. For example; valves 4 and 5 divert hydrocarbons into columns 6 and 7 which in turn take them into the FID detector. The green TCD in Figure 3.15 is used specifically to detect hydrogen whilst the yellow is used to detect permanent gases such as CO₂, CH₄, CO and N₂. Zero grade nitrogen is used as the carrier gas in the green TCD whilst helium is used in the other. For calibration curves, refer to Appendix I.

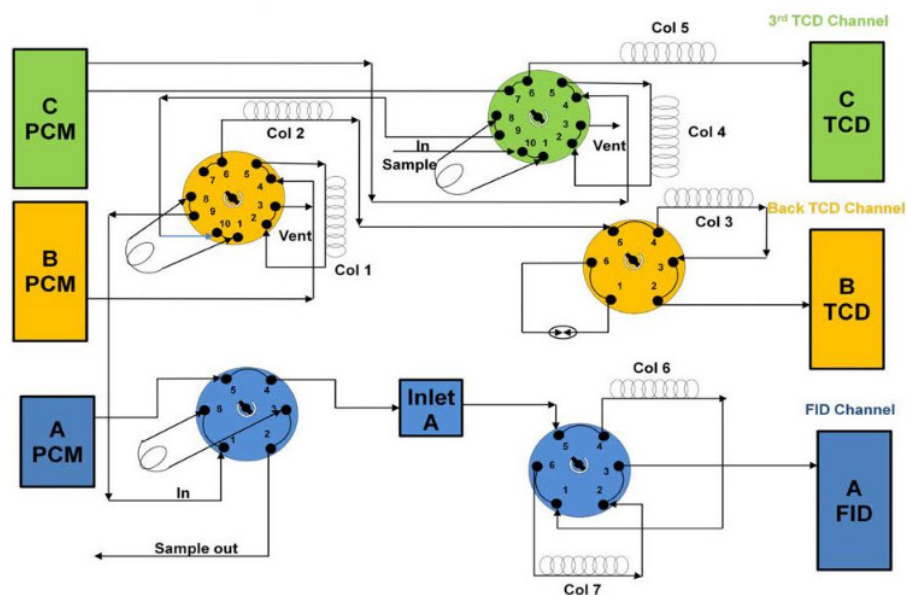


Figure 3.15: Schematic of the RGA valves and columns [114].

3.12.4 Correction Factor for Carbon Dioxide

Collecting the syngas using serum bottles meant that the CO₂ came into contact with water. CO₂ is known to dissolve in water and this was noticed during the analysis of the results, when the areas for the peaks given by the RGA were lower for the CO₂ than was expected. To obtain a correction factor, pure gas mixtures (Scientific and technical Gas Ltd) containing H₂, CO, CO₂, CH₄, C₂H₆, C₃H₈ and N₂ were collected using the serum bottle method and analysed using the RGA. The results were plotted against those using a straight injection and a correction factor was obtained. It was found that the area of the peaks for all the other gases were within the error range of the machine (± 1000) but the CO₂ was substantially lower.

The gas mixtures contained the following CO₂ volume fractions; 1%, 10%, 20% and the final one was a syngas from the gasification of rapeseed biochar at 850°C

and 172 g min⁻¹ kg⁻¹ biochar. The syngas was collected in a gas bag and a sample was injected directly into the RGA using the procedure described in Chapter 3.12.2. The serum method was then used to collect the gas to obtain the CO₂ dissolution. The original areas given by the RGA as well as those obtained after the serum collection are displayed in Table 3-4.

Table 3-4. Areas given by the RGA for the two collection methods

Concentration	Original Area	New Area
1%	1245 ± 9	1108 ± 105
10%	14362 ± 756	9374 ± 1460
20%	23092 ± 1367	18276 ± 1069
syngas sample	28023 ± 1496	25020 ± 1134

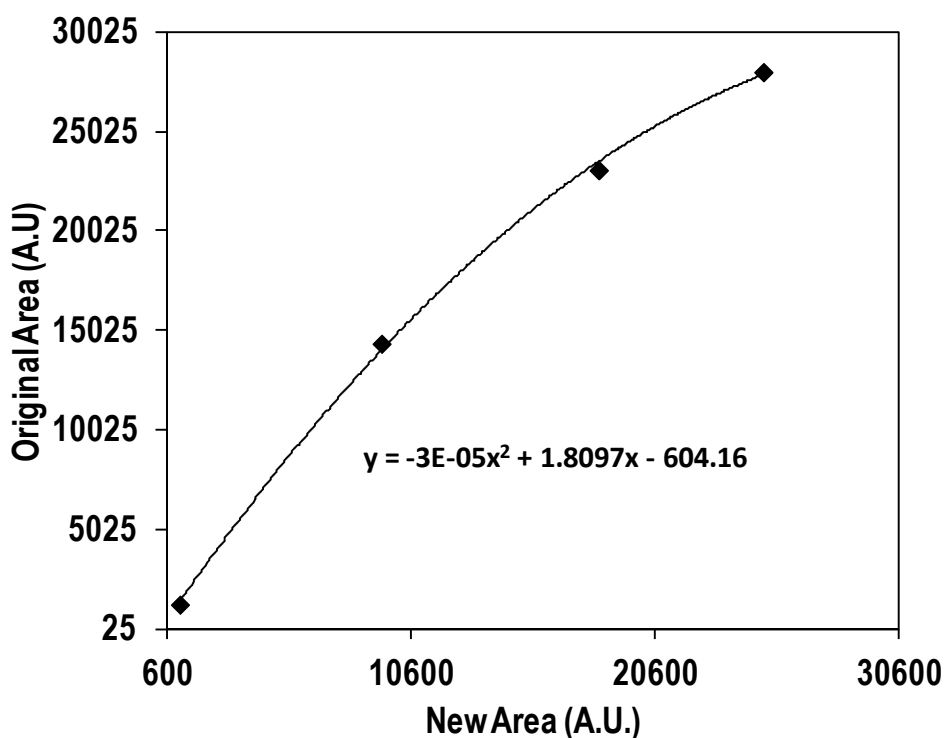


Figure 3.16: Peak areas given by the RGA for the two methods of gas collection to derive a correlation for the dissolution of CO₂

3.13 Data Processing

The following definitions and equations were used in evaluating the efficiency of char conversion and heating value of the syngas;

- Biochar Conversion (BC); mass of biochar lost from the initial biochar sample during the reaction

$$BC (\%) = \left[1 - \left(\frac{m_o}{m_i} \right) \right] \times 100$$

Where m_o and m_i are mass of biochar 'out' and 'in' respectively

- Carbon Conversion (CC); moles of carbon lost from the biochar during the reaction,

$$CC (\%) = \left[1 - \left(\frac{C_o}{C_i} \right) \right] \times 100 \quad \mathbf{3-2}$$

where; C_o is the moles of carbon in the spent biochar and C_i is the moles of carbon in the initial biochar.

- Carbon Conversion Efficiency (CCE); moles of carbon transferred to the syngas during the reaction.

$$CCE (\%) = \left[\frac{C_g}{C_i} \right] \times 100 \quad \mathbf{3-3}$$

where C_i is the moles of carbon in the initial biochar and C_g is defined in equation

3-4:

$$C_g (\text{mols}) = P \frac{(1 - X_{H_2}) V}{RT} \quad \mathbf{3-4}$$

where P is atmospheric pressure 101325 Pa, X_{H_2} is the volume fraction of H_2 in the syngas. R is the universal gas constant, $8.314 \text{ J mol}^{-1} \text{ K}^{-1}$ and T is the Temperature, K, and V is the total volume of gas produced, m^3 .

- Higher Heating Value (HHV) of the syngas was calculated from;

$$HHV (\text{MJ kg}^{-1}) = \sum X_i H_i \quad \mathbf{3-5}$$

where X_i is the volume fraction of component i in the gas mixture and H_i is its corresponding higher heating value.

- Dry Gas Yield (DGY) is the volume of gas produced from the reaction at room temperature and pressure.

$$DGY (\text{m}^3 \text{kg}^{-1}) = \frac{V}{3000} \quad \mathbf{3-6}$$

where V is the total volume of gas produced during the reaction.

- Reactivity (R) is the rate at which the biochar reaction takes place.

$$R (\% \text{ min}^{-1}) = \frac{1}{m} \frac{dm}{dt} \quad \mathbf{3-7}$$

where m is the mass of the biochar at time t during the reaction.

3.14 Solid Oxide Fuel Cell Testing

3.14.1 Method of Preparation

The SOFC required an anode and a cathode connection. Since the anode was on the inside of the tube, some of the tube had to be filed down to expose it. This was

done using a 3 mm diameter, 140 mm length needle file to expose 10 mm (width) of the electrolyte in the middle of the larger grey area of the SOFC to expose the anode. Non-porous (to hydrogen) silver paste (Shanghai Research Institute of Synthetic Resins, China) was applied to cover the exposed anode before the SOFC was placed in an oven at 120°C for 45 minutes. A drill was used to fabricate a 300 mm long, eight strand thick silver wire. This was achieved by starting with 2400 mm, 0.375 mm thick, silver wire. The silver wire was folded four times to make a 600 mm long wire, which were spun using the drill. The four stranded wire was then folded into two and spun again using the drill to make it into an eight stranded, 300 mm long wire. The wire was then wrapped around the anode two times, and a further coat of silver paste was applied on top to keep it in place. It was placed in the oven for 45 minutes to dry.

For the cathode connection, another eight stranded wire was fabricated and wrapped around the cathode as shown in Figure 3.17. The SOFC was connected to the SOFC test rig using ceramic manifolds. The cylindrical manifolds were 30 mm in length and 20 mm in diameter. They were machined as follows; 7 mm diameter hole was machined into its centre to a length of 15 mm. On the other side of the manifold, a 0.3175 mm hole was machined into its centre that extended all the way through to the bigger 7 mm hole. A 0.3175 mm stainless steel tube was inserted into the smaller hole and pushed all the way through so that it protruded out of the other side. It was connected to the manifold using temperature resistant Al₂O₃ based ceramic adhesive or 'ceramabond' (Ceramabond 552, PI-Kem Ltd). The SOFC tube was then inserted into the 7 mm hole and the ends were sealed off by applying a thin layer of ceramabond around the edges. The set-up, shown in Figure 3.17, allows the fuel gas to be fed directly into the SOFC and enables the

coupling of a ceramic SOFC to a metal tube which could be connected to the test rig via Swagelok fittings. The outlet side of the SOFC was connected using the same set up.

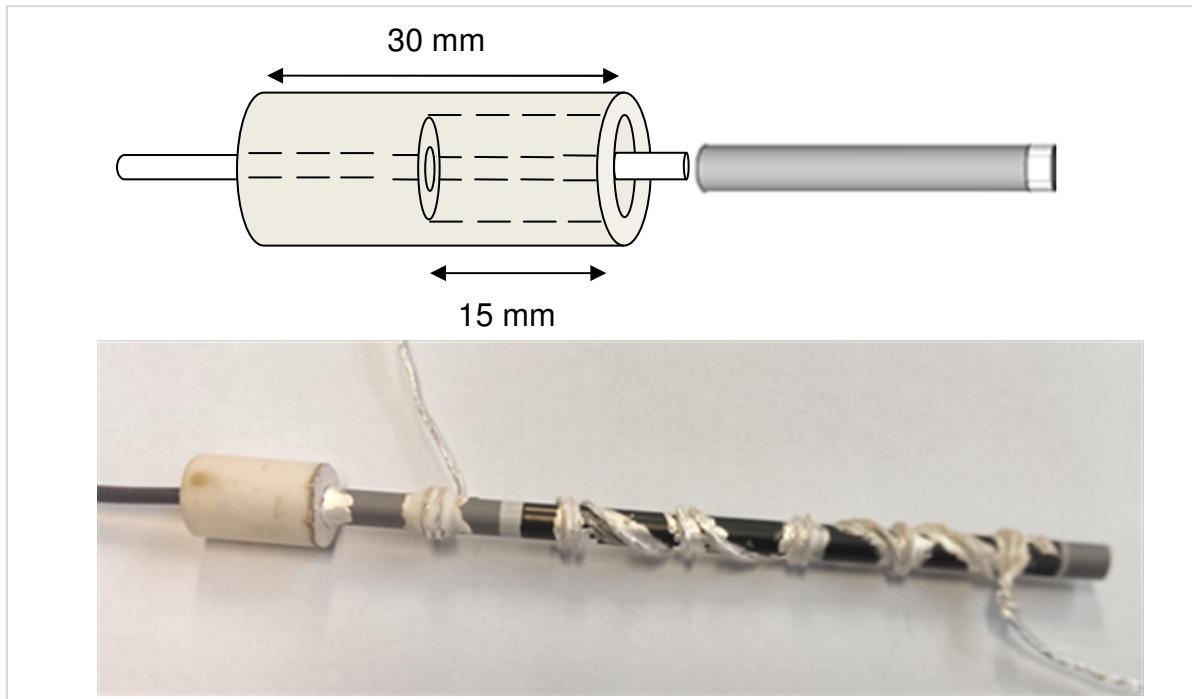


Figure 3.17: Schematic and photo of the SOFC ceramic manifold

3.14.2 Fuel Delivery System

Solid oxide fuel cells require a constant supply of fuel. Syngas from biomass – in particular a batch-type, bench scale process, cannot supply a constant flow rate since the feed diminishes as the reaction progresses. To overcome this, a buffer tank and a delivery system were designed so that syngas could be stored and a constant flow into the SOFC could be achieved. The buffer tank was connected to the SOFC test rig using silicone tubes.

3.14.3 Buffer Tank design

The buffer tank had to be able to store at least 8 L of syngas (determined by the volume of syngas produced during reactions). It had to have a mechanism whereby the gas could enter and leave without contamination from air. To achieve this, the design shown in Figure 3.18 was implemented. As can be seen, the buffer tank has three valves, two at the top and one at the bottom. To fill the tank with water, the valve at the bottom was closed off and the two at the top were opened. Water was directed into the tank through one of the valves using a flexible hose and the air was displaced through the other valve. Once the tank was filled up, the water was stopped and both the valves were closed off.

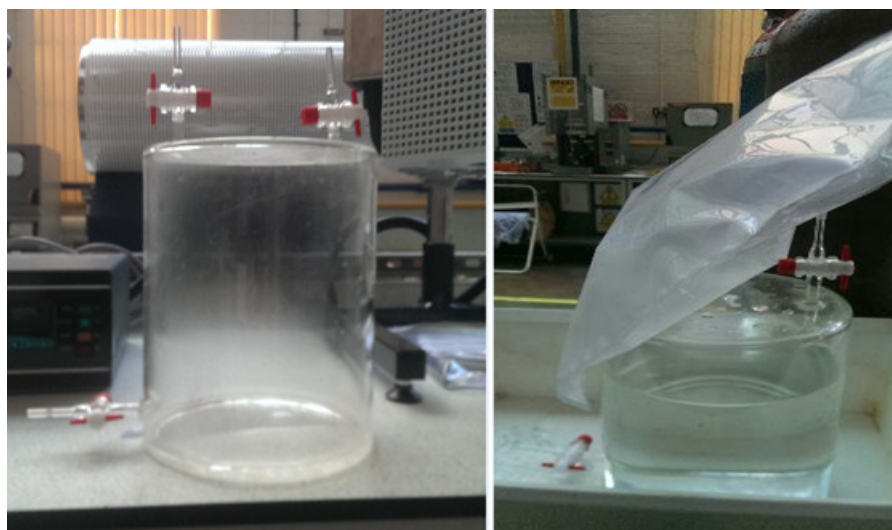


Figure 3.18: Buffer tank design and syngas transfer mechanism

To transfer syngas into the tank, the gas bag containing the gas was connected to one of the valves at the top using a short silicon tube. The bottom valve was opened as well as the outlet valve for the gas bag. Upon opening the valve connecting the gas bag, the outflow of the water created suction and forced the

syngas into the buffer tank. Once no more water came out of the buffer tank, all the valves were closed off and the gas bag was removed.

3.14.4 Providing Constant Flow

To achieve a constant flow, a pump was used to transfer water into the buffer tank, thus displacing the gas. The calibration was carried out by connecting the outlet from the storage tank to the bubble flow meter on the gasification rig. The results are shown in Figure 3.19.

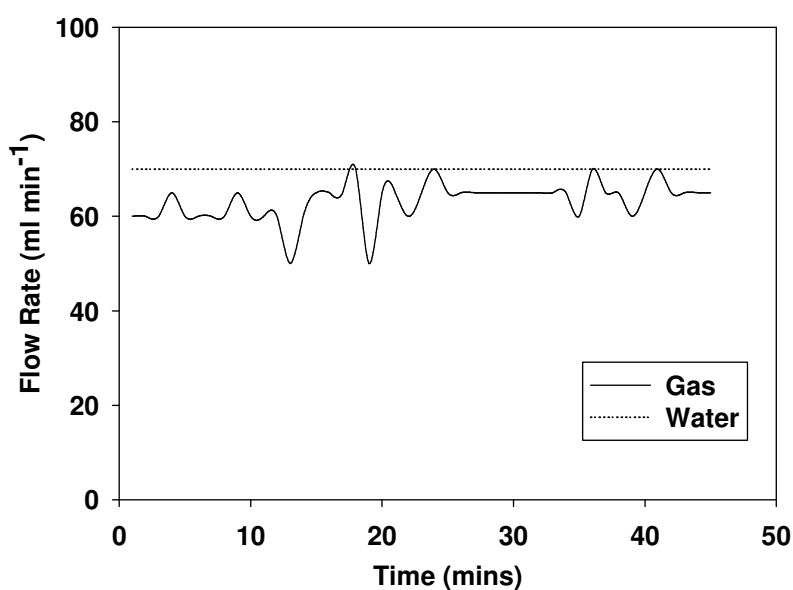


Figure 3.19: Induced flowrate of syngas by pumping water into the buffer tank

It can be seen in Figure 3.19 that although the flow is not entirely constant, it varies by ± 10 ml min⁻¹, this is as a result of the compressibility of the gas. Initially, the flow starts up slightly low but as the pressure in the tank builds up, it remains relatively constant, fluctuating by ± 5 ml min⁻¹.

3.14.5 Solid Oxide Fuel Cell Test Rig

The SOFC test rig is shown in Figure 3.20. Pure N₂ and H₂ are supplied via bottled gases (BOC Ltd), a peristaltic pump is used to pump water into the glass buffer tank to provide syngas flow into the SOFC. A furnace is used to heat the SOFC to 800°C and ceramic mainfolds are used to hold the SOFC in the furnace and connect it to the metal tubes. A Solartron 1470E potentiostat was used to carry out the measurements.

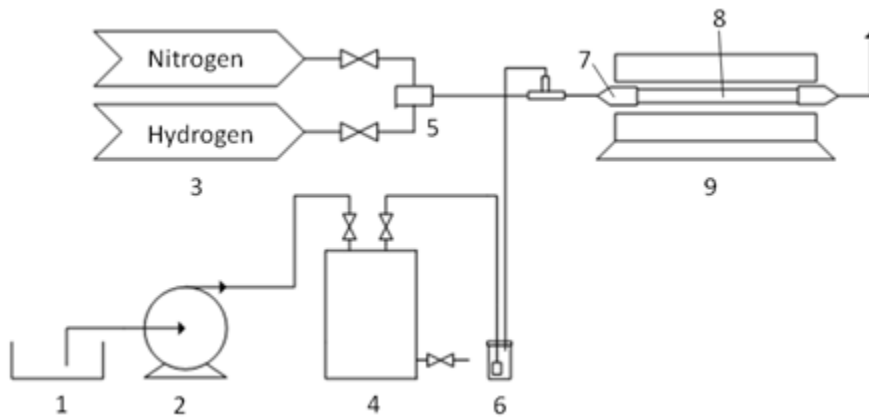


Figure 3.20: SOFC test rig, where; (1) deionised water reservoir, (2) peristaltic pump, (3) bottled gas supply, (4) buffer tank, (5) mixer, (6) dryer, (7) ceramic manifold, (8) microtubular SOFC and (9) furnace

3.14.6 Test Programme and Cylinder Change

The SOFC was tested using the following programme; (i) 10 minute open circuit voltage (OCV), (ii) Potentio-stairstep mode where the voltage is reduced from OCV to 0.6 V in increments of 15 mV. (iii) Potentiostatic mode where the voltage is kept constant at 0.7 V for 30 minutes, (IV) Potentio-stairstep mode where the voltage is reduced from OCV to 0.6 V and finally (V) 10 minute OCV. Step one is designed to give the SOFC time to adjust to the new gas composition. Step two

tests the SOFC performance before it is put under strain in the Potentiostatic mode. Step three puts the cell under strain and tests its ability to produce current at 0.7 V. Step four tests the performance of the cell after the Potentiostatic mode to gauge the difference and finally step five enables the switching of the spent syngas cylinder to a full one.

To change the cylinder, the syngas was switched to pure H₂ and the spent cylinder was disconnected and replaced with a full one which was reconnected to the rig. The flowrate of the pure H₂ was incrementally reduced whilst simultaneously, syngas flowrate was increased. Eventually, the pure H₂ was switched off and the SOFC was operated only on syngas. The whole change over process took less than five minutes.

3.15 Other Experimental Methods

3.15.1 Removing Alkali and Alkaline Earth Metallic Species

To remove AAEM species, a procedure similar to that used by Wu et al [115] was employed. 300 ml of 5.0 M HCl solution was made according to the Sigma Aldrich Normality and Molarity calculator [38]. A slight difference in the procedure was the use of concentrated NaOH to neutralise the acid. Wu et al [115] used deionised water to dilute the acid, but this was not feasible for the following reasons; (i) a huge quantity of deionised water is required to dilute 300 ml of 5 M HCl (ii) such a concentrated solution could not be discharged down the sink and (iii) washing the biochars would have meant the loss of the smaller particles of the biochars thereby affecting the results. Once the acid had been neutralised, the Na⁺ and Cl⁻ ions were removed from the biochars according to the procedure described below.

The neutralised solution was sieved through a 106 μm aperture, which retained the majority of the biochar sample. The biochars (on the sieve) were soaked in deionised water and stirred. The water was then replaced with another batch and the procedure was repeated for a total of 10 times. The biochars were then left to dry overnight and analysed using XRF to determine the extent of the AAEM removal.

3.15.2 Hydrogen Sulphide Detection

Hydrogen sulphide was detected using a Whatman H_2S lead acetate indicator paper (Sigma Aldrich). These papers are designed to detect H_2S at a concentration of 5 ppm. The test is qualitative and not quantitative; hence the actual concentration of H_2S cannot be determined. Verification that the indicator paper works, was carried out in a fume hood by passing a 5 ppm H_2S standard gas mixture (Scientific and Technical Gas Ltd) over the papers. The indicator paper was wetted using deionised water and excess water was allowed to drip away. Gas from the bottle was released and allowed to flow over the indicator paper. After 30 s, the bottle was closed off and H_2S confirmation was made.

The syngas was collected in a gas bag and taken to a fume hood. A 5 cm strip was wetted with deionised water. Once excess water had dripped away, it was placed over the top of the outlet of the bag and the valve was opened. The bag was pressed down gently enabling the gas to make contact with the indicator paper. After 30 s, the valve was closed and the indicator paper was removed. The excess gas was vented out in the fume hood.

4 Characterisation of Materials

4.1 Chapter Overview

This chapter presents the results that were obtained from the characterisation studies that were carried out on the biochars, dolomite and the SOFC. The first part focuses on the characterisation of the four biochars to find the elemental analysis, mineral content, Higher Heating Value (HHV), Brunauer Emmet-Teller (BET) surface area, volatile content, surface topography using Scanning Electron Microscopy (SEM), particle size distribution and bulk density. The second part focuses on the characterisation of dolomite and the final part on the Solid Oxide Fuel Cell (SOFC)

4.2 Introduction

Various biochar from fast pyrolysis have been extensively characterised and much information can be found in the literature, some of which is reviewed in Chapter 2.2. There is scant information regarding the characterisation of biochar from intermediate pyrolysis and this chapter addresses that issue. It also characterises and compares Derbyshire dolomite to others from around the world.

4.3 Elemental Analysis

The elemental analysis of the biochars was carried out by MEDAC Ltd, Surrey, UK. The results are displayed in Table 4-1 (page 99). It can be seen that WPB had the highest carbon content at 71.6 wt%, this was the result of the lower

temperature, 450°C used during pyrolysis. Its nitrogen and ash contents were low at 2.64 and 0.54 wt% respectively. Temperature is the most important variable in the determination of the biochar composition and yield as higher pyrolysis temperatures lead to further release of volatile components [116]. The initial make-up of the original biomass substrate also influences the final biochar composition, for example, previous studies have shown that feedstock with high lignin contents produce higher biochar yields when pyrolysed at 500°C [117].

The results differ slightly from those of Yang *et al* [27], who pyrolysed pine sawdust and off-cuts using intermediate pyrolysis at 450°C and reported CHN contents of 75.6, 3.38 and 0.22 wt% respectively. The biggest difference was found in the ash contents with Yang *et al* [27] reporting 10.2 wt% as opposed to 2.64% in this study, and may be attributed to the type of biomass substrate used initially. Sewage sludge biochar (SSB) had the lowest carbon and highest ash contents at 30 and 35.5 wt% respectively. The low carbon content results from it being processed in an anaerobic digester prior to pyrolysis, removing up to 60% of the organic matter [118]. Biochar is the largest product fraction of sewage sludge pyrolysis – independent of pyrolysis mode, up to 50 wt% has been reported for intermediate pyrolysis and 35 – 87% for other pyrolysis types [119]. Ash is the largest constituent of sewage sludge biochar, resulting from the various inorganic impurities that are associated with sewage sludge – such as metals, glass, ceramics, sand and stones [24]. The biochar composition differs from that reported by Samanya *et al* [119] who obtained CHN contents of 25.5, 1.8 and 3.1 wt% respectively and an ash content of 54.8 wt% at 450°C using intermediate pyrolysis. Sewage sludge is notorious for its inconsistent composition and can vary from day to day [120] so the difference is not surprising.

RSB had 60 wt% carbon and the highest nitrogen content at 4.19 wt%. High nitrogen concentration is a consistent feature of rapeseed biochars, ranging from 4.4 – 7.5 wt% in the literature [121] [122] and results from the high nitrogen demand of the rapeseed plant. Miscanthus (MCB) biochar had a similar carbon content to the rapeseed biochar but a much higher ash content at 10.31 wt% and a lower nitrogen content at 0.8 wt%.

In general, biochars used in this study had a lower carbon content than those in previous studies which had; 76.38 [12]; 67.3, 76.38 [13], 70.68 [14] and 54.68 [54] wt% C respectively. Previous studies utilised biochars from fast pyrolysis where the residence time of the solid is lower than that of the pyroformer, hence the higher carbon contents for most of the biochars. Carbon content is critical in biochar-steam gasification given that the water gas reaction is generally accepted to be the most important reaction in biomass gasification [37], especially in steam gasification where it is the initiating reaction and allows for the production of CO and H₂ which can partake in further reactions.

Table 4-1: Elemental analysis of the biochars

Biochar	Ultimate Analysis (wt %)					
	C %	H %	N %	S %	Ash %	O % *
Wood Pellet	71.58	4.62	0.54	0.22	2.64	20.4
Rapeseed	60.25	4.03	4.19	0.1	4.2	27.61
Sewage Sludge	30.03	4.19	1.83	0.88	35.46	27.23
Miscanthus	62.2	4.37	0.8	0.28	10.31	22.04

* By difference

4.3.1 Mineral Content Analysis

Table 4-2 displays the mineral composition of the biochars. WPB had the lowest mineral content with Fe being the most abundant mineral, its K and Ca concentrations were very low compared to the other biochars – this could result from the wood growing on natural soil where no fertiliser is applied. RSB had high Ca, K as well as P contents. In addition to N, the high K and P contents could enable the rapeseed biochar to be used as a soil enhancer. Miscanthus biochar had a high Ca content with moderate contents of K, Fe, Si and low P. Sewage sludge biochar had high P, Si, Fe and Ca contents. Research has shown that biomass with high silica contents have a greater tendency to cause slagging at high temperatures [123]. High ash content is not necessarily a negative characteristic; ash contains mineral matter which has been shown to increase the rate of gasification reactions [62]. The effects of AAEM species such as K, Na and Ca on syngas composition has yet to be fully studied; though one study has suggested they have no effect on the water gas shift reaction – which the authors considered the dominant reaction in biomass gasification [36]. This work will study whether the removal of AAEM species leads to a change in syngas composition.

Table 4-2: Mineral content of the biochars

Biochar	Concentration (wt %)					
	Ca	K	Fe	Si	P	Al
WPB	1.07	0.77	3.08			
RSB	8.19	9.28	0.87		5.36	
SSB	12.46	1.13	7.56	8.07	5.02	4.4
MCB	6.24	4.24	3.34	3.18	0.41	

4.3.2 Higher Heating Value

The HHV obtained from the bomb calorimeter were verified using the 'Unified Correlation for Fuels' formula (equation 3-1, page 70) developed by Channiwala and parikh [112] and are displayed in Table 4-3. As can be seen, the highest HHV of 28.28 MJ kg⁻¹ was given by WPB and the lowest by the SSB at 11.97 MJ kg⁻¹. HHV is an essential feature of biomass as it determines the amount of energy entering the reactor per unit mass, and hence, the amount of energy leaving the reactor. The higher the carbon content, the more gas that can be theoretically produced since it is able to partake in more reactions.

Table 4-3: Higher Heating Values and other characteristics of the biochars

Biochar	HHV (MJ/kg)		BET Surface Area (m ² g ⁻¹)	Moisture Content (wt %)	Volatile Content (wt %)
	Bomb Calorimeter	Formula			
Wood Pellet	28.78 ± 0.3	28.28	0.073 ± 0.0086	N/A	61.2 ± 2.1
Rapeseed	24.04 ± 0.22	22.82	0.4058 ± 0.0325	N/A	21.5 ± 1.5
Sewage Sludge	11.02 ± 0.6	11.97	15.4667 ± 0.009	N/A	21.6 ± 0.4
Miscanthus	24.71 ± 0.54	24.38	0.9646 ± 0.0348	N/A	30.9 ± 1.7

4.3.3 Brunauer-Emmet-Teller (BET) Surface Area

The BET surface areas are shown in Table 4-3. In general, all the biochars had very low BET surface areas compared to commercial activated carbons which can have areas over $1000 \text{ m}^2 \text{ g}^{-1}$ [124]. The low BET areas result from (a) lower temperatures of formation and (b) lack of activating agent being used. Higher temperatures lead to increased BET surface areas [125] and activating agents such as steam or (KOH) are used to increase surface areas [126]. The formation of surface areas during pyrolysis is thought to be associated with devolatilisation processes – which lead to the loss of organic compounds, creating voids in the biochar matrix, and at lower temperatures, volatiles can condense, clogging up pores and reducing surface area [127].

4.3.4 Volatile Content Analysis

The volatile contents of the biochars varied greatly with SSB and RSB both having similar contents at just over 21% whilst the WPB had over 60%. The high volatile content is the result of (i) lower formation temperature and (ii) chemical make-up. The lower pyrolysis temperature ensured that more volatiles remained in the WPB, which were released when it experienced a temperature greater than 450°C . (ii) Wood biochar in general is made up of the lignin fraction which continues to decompose up to 900°C [128]. Upon release of the volatile constituents, they react with each other to form mainly CO , CO_2 , H_2 , CH_4 and other hydrocarbons as well as tars and longer chain hydrocarbons which are known as bio-oil.

4.3.5 Removal of AAEM Species through Acid Washing

Table 4-4 and Table 4-5 show the physico-chemical properties of the RSB after it has been washed with 5 molar HCl. The properties can be compared to the original RSB displayed in Table 4-2 and Table 4-3. It can be seen that there is a reduction in the oxygen and hydrogen contents. Carbon was the main beneficiary of acid washing; its content increased from 60.25 to 72.36 wt%. A side-effect of this was that direct comparison with normal biochar has to be made in terms of carbon equivalence. For example; for normal, inter-biochar experiments, assessments were made using the S/B ratio. To study the effects of AAEM removal, the rapeseed biochars were assessed using S/B ratio as well as S/C ratio, which can be defined as $\text{g min}^{-1} \text{ steam kg}^{-1} \text{ carbon in biochar}$.

A big change was observed in the BET surface area, increasing from 0.4058 to 5.1671 $\text{m}^2 \text{ g}^{-1}$ upon acid washing. Biochar mineral content was also modified, with significant reductions to the Ca, K and P content. Na is reported to be the second most active mineral, after K [36] and previous studies have shown that acid washing is a very efficient method of removing Na [36] [62], hence, it could be assumed that the majority of the Na inherent in the biochar, had been removed. It was concluded that the removal of the mineral content left behind vacant pores which might previously have been clogged up thus explaining the increase in surface area. Increased surface area has been reported to increase gasification reaction rates [115].

The presence of Cl indicates that washing the biochars with deionised water did not remove all of the NaCl. However, the concentration of Na was low since Na is

less than a third of the mass of Cl, its presence should not have had a major impact on the gasification reactions.

Table 4-4: Characteristics of the rapeseed biochar after acid washing

Biochar	Ultimate Analysis (wt%)						HHV (MJ kg ⁻¹)	BET Surface Area (m ² g ⁻¹)
	C	H	N	S	Ash	O*		
Rapeseed	72.36	3.08	4.61	0.73	2.39	16.83	27.10	5.1671 ±0.026

*by difference

Table 4-5: Mineral content of the rapeseed biochar after acid washing

Biochar	Concentration (wt %)					
	Ca	K	Fe	Si	P	Cl
Rapeseed	2.47	0.33	1.46		1.00	2.61

4.3.6 Scanning Electron Microscopy Analysis

Figure 4.1 and Figure 4.2 shows the surface topography and particle structures of the biochars as observed by the SEM. It is shown that WPB had a relatively flat, non-porous surface that looked similar at both low and high magnifications. The structure is unlike that reported by other researchers who have shown that pine biochar has a porous structure with fibrous elements that disappear when higher heating rates are used [129]. There appear to be very few cracks and holes; giving credence to the idea that low temperature pyrolysis leads to condensation of volatiles that subsequently block pores.

MCB was a collection of sharp elongated fibres with cracks in between them. Its structure was very disordered resulting from a combination of pelletisation and pyrolysis. The rate of devolatilisation the biomass experiences during pyrolysis determines the porosity of its biochar [130] and this in turn is affected by the AAEM content of the biomass (which increases its reactivity) and the pyrolysis temperature [62]. This helps explain why rapeseed and miscanthus biochars had such fragmented structures.

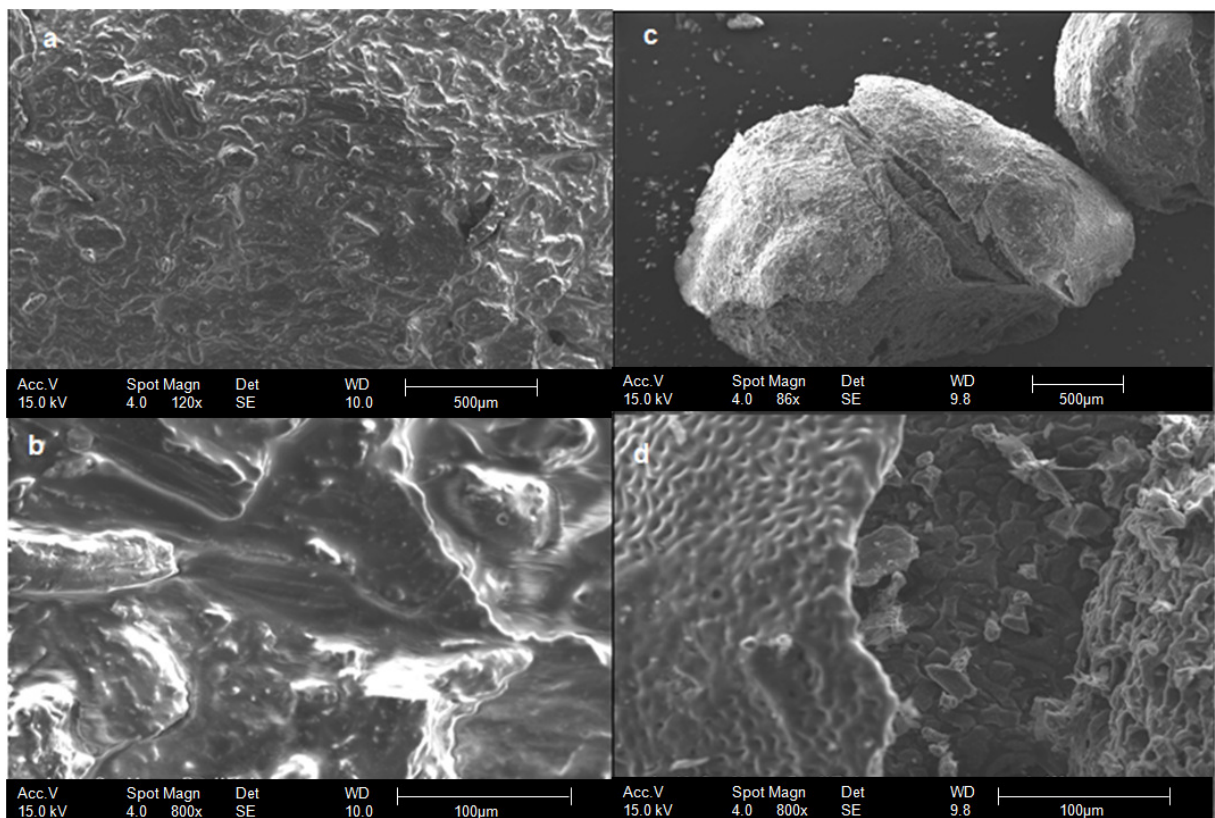


Figure 4.1: SEM micrographs of WPB and RSB at magnifications of (a) WPB 120X, (b) RSB 86X, (c) WPB 800X and (d) RSB 800X

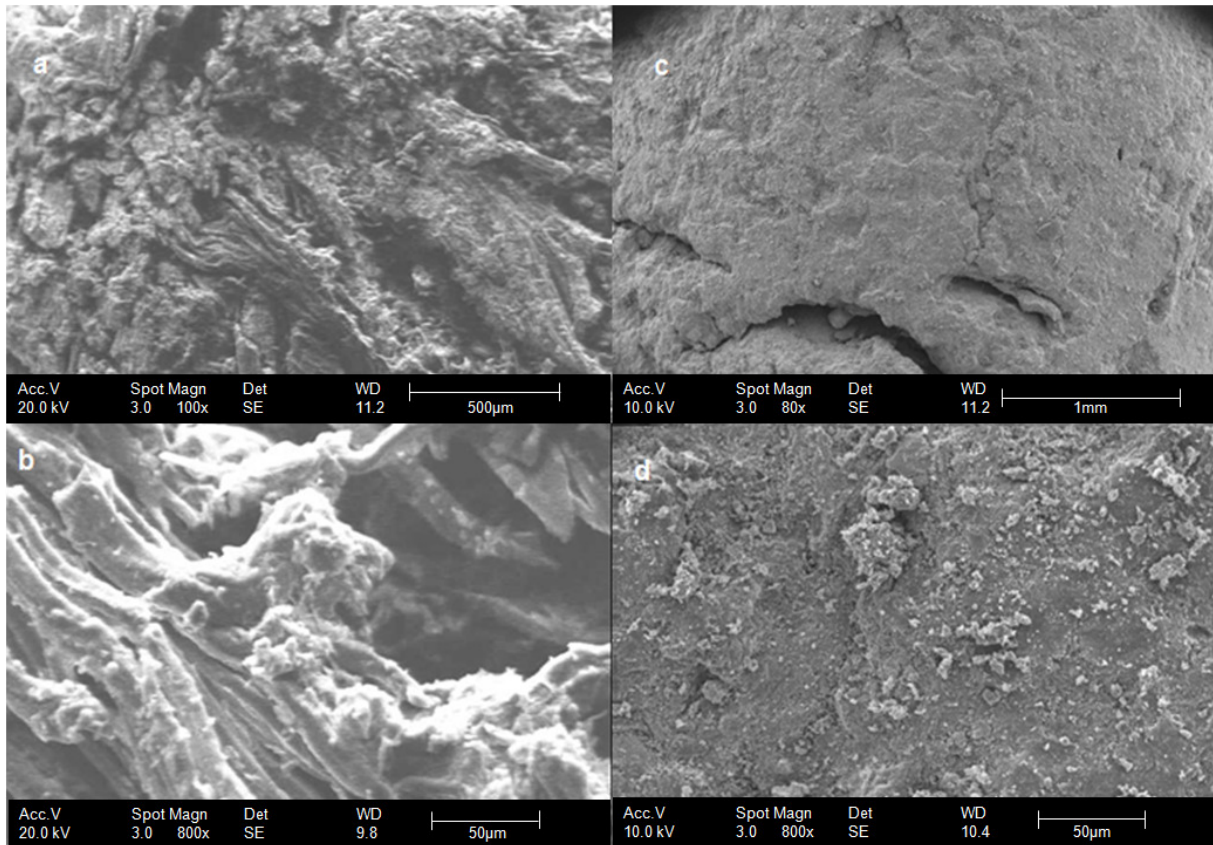


Figure 4.2: SEM micrographs of biochars, where (a) MCB 100X, (b) MCB 800X, (c) SSB 100X and (d) SSB 1000X

4.3.7 Particle Size Distribution and Bulk Density

Particle size distribution was calculated using the procedure described in Chapter 3.6.6. The procedure was carried out using a digital caliper and a sieve column. The results are displayed in Table 4-6. It is shown that for all the biochars, the majority of the mass was concentrated in larger particles and pellets. Previous work has shown that smaller particle sizes exhibit faster reaction rates [131] during gasification. MCB biochar showed the most variation and it had the highest percentage of very small particles ($< 63 \mu\text{m}$). SSB had the most consistent particle sizes and least amount of broken pellets.

Table 4-6: Particle size distribution of the biochars showing powdered and pellet form

Biochar	Powder	Pellet
WPB	-	47.6 wt% pellets 52.4 wt% broken pellets/shavings Pellet length range = 4.7 – 9.5 mm Mean L = 8.9 Mean D = 4.8 mm
RSB	42 wt% > 850 μm 40 wt% > 300 μm 13.6 wt% > 106 μm 3.6 wt% > 63 μm 0.8 wt% < 63 μm	-
SSB	-	Pellet length range = 0.4 – 1.7 mm Mean L = 9.4 mm Mean D = 4.8 mm
MCB	20 wt% powder 8.61 wt% > 300 μm 6.9 wt% > 106 μm 2.39 wt% > 63 μm 1.71 wt% < 63 μm .	80 wt% pellets Pellet length range = 2.3 – 11.1 mm Mean L = 8.6 Mean D = 7.8 mm

Bulk density is a measure of the mass of the biochar per unit volume. It accounts for structural as well as pore volumes and is heavily affected by the ash content as the heavier mineral contribution replaces the carbon contribution [35]. Bulk density was measured by crushing the biochar and sieving it through a 160 μm aperture, then transferring it into a graduated cylinder and recording the mass. The procedure is explained in detail in Chapter 3.6.8. The WPB could not be sieved therefore its bulk density was not determined. The results for the other biochars are shown in Table 4-7 and unsurprisingly, SSB had the highest bulk density –

contributed to by its high ash and mineral content. RSB, with its high mineral content, had a higher bulk density than MCB. The bulk density influences reactor packing; biochars which have a low bulk density will need a greater volume to satisfy the mass demand, therefore a greater surface area of that biochar will be exposed to the steam, which could lead to faster reaction rates.

Table 4-7: Bulk density of the biochars

Biochar	Bulk Density (g cm ⁻³)
Wood Pellet	-
Rapeseed	0.68 ± 0.008
Sewage Sludge	0.879 ± 0.018
Miscanthus	0.424 ± 0.027

4.4 Characterisation of Dolomite

4.4.1 X-Ray Fluorescence Spectroscopy

XRF was carried out using the pellet press method. 0.5 g of dolomite was mixed with 0.1 g of inert wax (cellulose) and pressed into a pellet which was then analysed. The procedure is described in Chapter 3.6.3. Table 4-8 shows the chemical makeup of natural dolomite (ND) and calcined dolomite (CD) used in this study. According to the Institute of Geological Sciences, UK, pure mineral dolomite (Ca.Mg(CO₃)₂) contains 21.9% MgO and 31.4% CaO [132]. Using this classification, it can be said that the dolomite used in the study was not pure dolomite, but, rather it was a dolomitic limestone, which is common around Derbyshire [133]. Another study by the Institute of Geological Sciences found that the mean composition of Derbyshire dolomites was 35.28% CaO and 15.34%

MgO [134]. The dolomite used in this study had a lower MgO content but an average CaO content. Dolomite is thought to form when magnesium rich brine solution infiltrates limestone layers and reacts with the deposits to form dolomite in a process that takes centuries or millennia to complete [135]. Calcined dolomite has a higher concentration of most of the minerals per unit mass. This is expected since over 46% of the natural dolomite mass is lost as CO₂ which is given off during the calcination process [47].

Dolomite can affect the gasification process in two ways; (i) it can lead to enhanced tar cracking which improves the syngas volume and composition [46] and (ii) it can adsorb CO₂ [49], thus improving the heating value of the gas. Some researchers have reported that MgO and in particular CaO are the active components in calcined dolomite [47] [136]. If this is the case, calcined Derbyshire dolomite compares favourably with others from around the world as shown by Wiedermann and Bayer [49], since it has 54.1% CaO, which is a lot higher than the next highest, which is 30.72% CaO of the Chinese dolomite. The MgO content of 30% of the calcined Derbyshire dolomite is also higher than the other dolomites by almost 10%. If these are the active components of dolomite, then the calcined Derbyshire dolomite should be a very good catalyst for tar cracking and improving the dry gas yield.

Table 4-8: Mineral content of the dolomite samples used in this study as found using X-ray Fluorescence Spectroscopy

Mineral/Constituent	Concentration (wt %)	
	ND	CD
Ca	26.51	45.77
Mg	5.18	15.63
Si	0.71	0.98
S	0.68	0.18
Fe	0.51	0.91
Al	0.29	0.53

Table 4-9: Comparison of Derbyshire dolomite to other uncalcined dolomites from around the world, where Ch D is Chinese, Sw D is Sewdish, In D is Indian, Ma D is Malaysian, and Fn D is Finnish Dolomite [137].

Dolomite/Mineral Oxide	ND	CD	Ch D	Sw D	In D	Ma D	Fn D
CaO	36	54.1	30.72	30.5	30.24	30.0	26.6
MgO	9.77	30	20.12	20.2	21.33	21.0	18.3
SiO ₂	1.6	2.2	1.35	2.21	0.18	0.07	2.5
SO ₃	1.2	0.42					
Fe ₂ O ₃	0.875	1	0.03	0.54	0.63	0.07	2.1
Al ₂ O ₃	0.6	1.1	0.14	0.11	0.25	0.04	0.6

4.4.2 BET Surface Area and Bulk Density Analysis

The surface area and bulk density of dolomite before and after calcination are reported in Table 4-10, showing that calcination had a noticeable effect on

dolomite surface area and bulk density compared with the non-calcined sample. Increases in surface area upon calcination is well known and results from the opening of pores at higher temperatures [138]. Previous studies have reported a surface area range of 5.1 – 12 m² g⁻¹ [138] [139] [140] [116], at 900°C calcination temperature.

Bulk density decreases as a result of the CO₂ being given off. This is seen in Table 4-10 where the density of calcined dolomite is 56% of that of natural dolomite. The results are consistent with those in the literature which report the same phenomena [141].

Table 4-10: BET surface area and bulk density of the dolomite samples

Dolomite	BET Surface Area (m² g⁻¹)	Micropore Area (m² g⁻¹)	Bulk Density (g cm⁻³)
Natural	1.7507 ± 0.0103	0.311	1.552 ± 0.45
Calcined	8.372 ± 0.0028	1.301	0.8669 ± 0.36

4.4.3 Particle Size Distribution

The dolomite particle size distribution was measured using a sieve column. 3 g of dolomite sample was sprinkled onto a sieve column and the first sieve in the column was lifted slightly and shaken manually for two minutes. The particles remaining on top was removed and weighed. The procedure is described in more detail in section 3.6.6. The results, presented in Table 4-11, show that calcination

leads to a reduction in dolomite particle size. Previous authors have reported that calcination under an inert atmosphere leads to greater sintering, resulting in more compact particles [138]. The smaller sized particles are much softer than naturally occurring dolomite and erode readily under gasification conditions, leading to dust in the product gas [139].

Table 4-11: Effect of calcination on particle size distribution

Dolomite	Particle Size Distribution
Natural Dolomite	14.5% > 106 μm 45.5% > 63 μm 39% < 63 μm
Calcined Dolomite	1.7% > 106 μm 16.7% > 63 μm 81.6% < 63 μm

4.4.4 Thermo Gravimetric Analysis

The test programme for TGA was as follows; 5 – 10 mg dolomite sample was weighed out in an alumina crucible and heated at a rate of $15^{\circ}\text{C min}^{-1}$ to 850°C where it was held isothermally for 20 minutes. The procedure is described in further detail in section 3.7.2. The results are displayed in Figure 4.3. Mass loss occurs between $620 - 820^{\circ}\text{C}$ and reaches a maximum of $7.8\% \text{ min}^{-1}$ at $\sim 780^{\circ}\text{C}$. Upon completion, around 45% of the initial mass is lost in the process. The mechanism by which dolomite decomposes in a low partial pressure CO_2 atmosphere has been described in equations 2-25 and 2-26. The CO_2 may react with the CaO to form CaCO_3 at low temperatures, but it does not seem to be the case in Figure 4.3 since the mass loss is continuous.

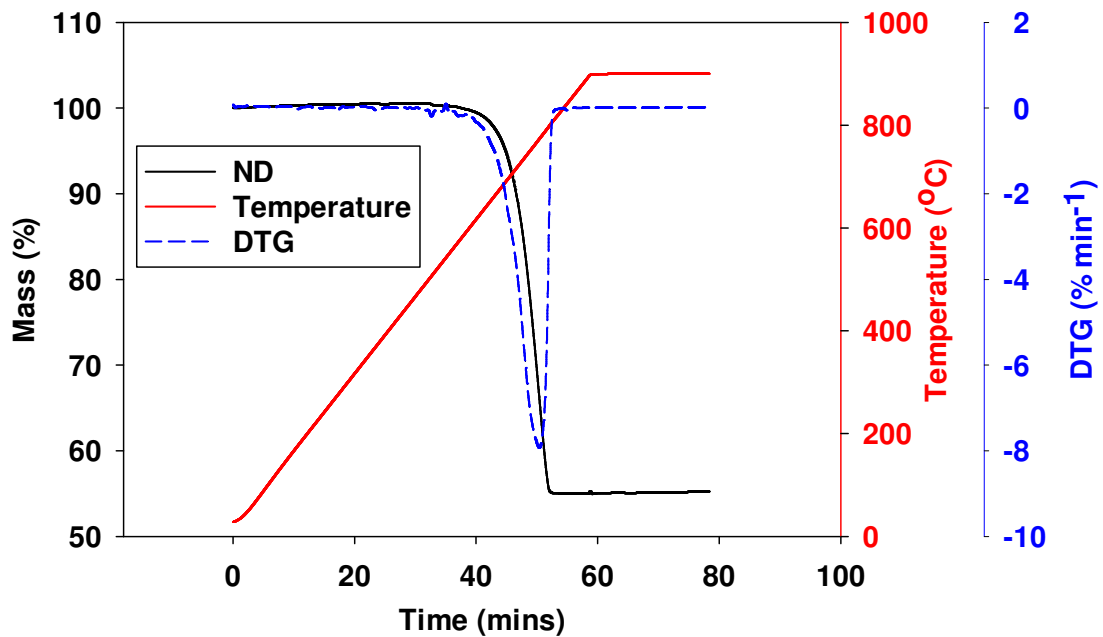


Figure 4.3: TGA and DTG analysis of the natural (uncalcined) dolomite

To determine the extent of the dolomite calcination, the calcined dolomite was analysed using the same programme; the results are shown in Figure 4.4. It can be seen that around 6.5% mass loss occurs from the calcined dolomite, this was much lower than the mass lost from the uncalcined dolomite, meaning that the degree of calcination was high. Unlike natural dolomite, calcined dolomite loses mass between 300 and 420°C with maximum mass loss occurring at ~400°C. This suggests that something other than $\text{CaMg}(\text{CO}_3)_2$ is decomposing. It is likely that after the calcination procedure, during the cooldown, some of the CaO and MgO reacted with moisture in the atmosphere to form $\text{Ca}(\text{OH})_2$ and $\text{Mg}(\text{OH})_2$. The onset of decomposition for $\text{Mg}(\text{OH})_2$ and $\text{Ca}(\text{OH})_2$ occur at approximately 300 and 420°C respectively [142].

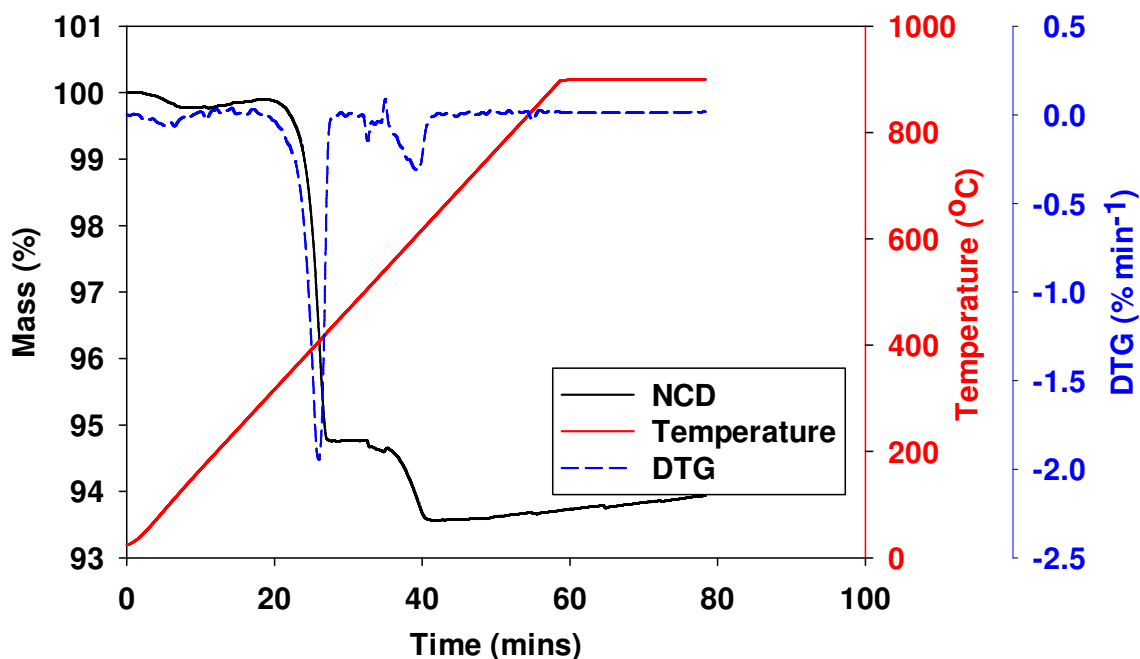


Figure 4.4: TGA and DTG analysis of the calcined dolomite

4.5 Characterisation of Solid Oxide Fuel Cells

The SOFC was characterised using EDS analysis. An unused SOFC tube was broken using a hammer and a 2 cm piece was taken from the centre of the anode and analysed using a Jeol 6060 machine. The results are displayed in Figure 4.5 and Table 4-12. Elements such as Ni and Zr can clearly be seen, although there is no sign of Y. Impurities such as oxygen and carbon were present in very low concentrations but these disappear once the anode is exposed to reducing conditions such as those when pure H₂ is used as a fuel. The Ni is an excellent catalyst for the oxidation of H₂ as well as the reforming of CH₄, which will be present in the syngas but it is a poor catalyst for the oxidation of CO. This could lead to problems when syngas with a high CO content is used.

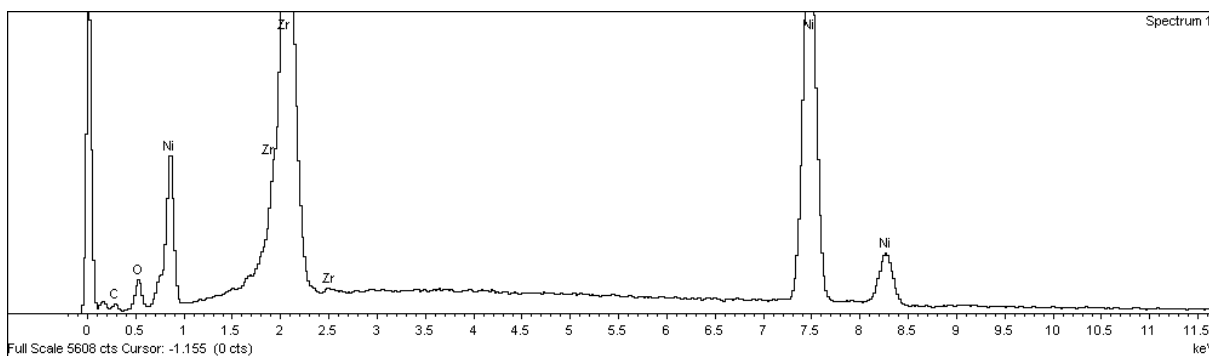


Figure 4.5: EDS micrograph of the SOFC anode

Table 4-12: EDS analysis of a microtubular SOFC anode.

Element	Weight%	Atomic%
C K	1.81	8.49
O K	3.77	13.26
Ni K	58.38	56.00
Zr L	36.04	22.25
Total	100.00	

4.6 Conclusions

Chapter four presented the results of the various characterisation methods that had been used to characterise the biochars, dolomite and the SOFC. The following characterisation techniques were carried out on the biochars and dolomite; elemental analysis, bomb calorimetry, BET surface area, volatile content, particle size distribution, bulk density analysis and XRF. The highest carbon content was found in the wood pellet biochar at 71.58% and the lowest was in sewage sludge biochar at 30%. The highest mineral content was in the rapeseed biochar which contained 8% Ca, 9% K and 5% P. The higher heating

values of the biochars were as follows; 28.8, 24, 11, 24.7 MJ kg⁻¹ for WPB, RSB, SSB and MCB respectively.

The surface areas of the biochars were very low with SSB having the highest at 15 m² g⁻¹. The other biochars were all below 1 m² g⁻¹. The volatile contents of the biochars ranged from 21 (RSB) – 61 wt% (WPB) and the particle size distribution showed that the greatest variety in particle sizes was found in the MCB. Upon removal of the AAEM species, the carbon content of the rapeseed biochar increased from 60% to 72%, the BET surface area also increased from 0.4 to 5.2 m² g⁻¹ as did the HHV from 24 to 27 MJ kg⁻¹.

Dolomite was characterised using the following techniques; XRF, BET surface area, particle size distribution, TGA, and bulk density. It was found that the dolomite was not a pure dolomite but rather a dolomitic limestone since it contained a lower than expected MgO content. The BET surface area improved upon calcination from 1.75 to 8.37 m² g⁻¹ but the density decreased from 1.55 to 0.87 g cm⁻³.

5 Steam Gasification of Biochar: Effects of Temperature and Steam Flow

5.1 Chapter Overview

This chapter presents an investigation of the effects of temperature and steam flow on various aspects of biochar gasification and relates these to the physico-chemical characteristics of the biochars. Aspects such as product flow, transient gas composition, final gas composition and conversion efficiencies were studied.

All the experiments were carried out in a quartz tubular reactor, the dimensions of which were; 750 mm length and 64 mm OD. Energy for the reactions was provided by an Elite Thermal Systems Ltd, THH 12/90/305 – 2408cm & 2116 O/T furnace. The heated length of the furnace was 360 mm, with a 100 mm diameter. Each experiment was carried out using 3 g of biochar. Anoxic conditions inside the reactor were achieved using nitrogen at a flowrate of 600 ml min⁻¹ for at least 15 minutes and was verified using gas analysis.

The first part of the chapter focuses on the effects of temperature on the product flowrate and transient gas composition with time as well as the changes in the individual components of the syngas. All the reactions were carried out using a steam flowrate of 172 g min⁻¹ kg⁻¹ biochar and the temperature was varied between 650 – 850°C in increments of 50°C.

The second part of the chapter focuses on the effects of steam flow on the abovementioned aspects. Temperature was kept constant at 850°C and steam flow was varied from 24 g min⁻¹ kg⁻¹ biochar to 277 g min⁻¹ kg⁻¹ biochar.

5.2 Introduction

The work in this chapter follows on from that of previous authors [12] [13] [14] [54] who showed that steam gasification of biochar is a very promising method for generating a hydrogen-rich syngas. The authors of the aforementioned studies all used biochar produced from fast pyrolysis and did not employ a catalyst. It has been shown that significant differences exist between pyrolysis types and these differences can have a major impact during the gasification process. For example, Chen et al [143] investigated the reactivity of biomass chars from rapid and slow pyrolysis using steam and CO₂. They reported that chars from rapid pyrolysis showed a reactivity that was three times higher than those formed by slow pyrolysis. Furthermore, previous authors of steam gasification of biochar have failed to provide any links between the physico-chemical characteristics of the biochars and their effect on its gasification behaviour.

This chapter addresses this paucity and also addresses the changes in the gasification behaviour during the reaction; both the transient gas composition and changes in product flow with time. These are very important characteristics that need attention since scaling up of the process requires continuous operation which must be designed to take such factors into consideration. Finally, as with previous studies, no catalyst was used in this study, this was done to (i) ascertain a baseline for which to compare the results to and (ii) determine whether the process can be operated without a catalyst therefore reducing costs.

5.3 Effects of Temperature on Product Flow Rate

The product flow from the reaction was measured using a 500 ml Supelco bubble flow meter as described in Chapter 3. For each experiment, the steam flow was kept constant at $172 \text{ g min}^{-1} \text{ kg}^{-1}$ biochar and the temperature was varied between $650 - 850^\circ\text{C}$. The product flow was measured at room temperature and pressure - once the gases had been cooled down and the tars condensed out. Each reaction lasted for 30 minutes and a cumulative volume was recorded for each minute which was then used to ascertain the product flow per minute. The results, showing a two minute average for the product flows are presented in Figure 5.1.

Two distinct trends are observed in Figure 5.1; (i) product flow increases with temperature and (ii) product flow decreases with time. Temperature had a significant effect on product flow. In all cases, an increase in temperature led to the following observations (i) increase in the initial gas mass being produced and (ii) a higher product flowrate for the remainder of the reaction as compared to a lower temperature. The overall product flow profile is a combination of two factors; devolatilisation and gasification. Devolatilisation is responsible for the initial gas mass, and biochars with highest volatile content produced the highest product flows in the initial stages. For example; WPB had the highest volatile content at 61.2 wt% and it produced an average of 725 ml min^{-1} in the first two minutes at 850°C . Once devolatilisation had finished, gasification reactions took over, but at lower temperatures, they were kinetically limited. However, at higher temperatures, rate constants for the gasification reactions increase as seen in Table 5-1 leading to enhanced reaction rates which lead to higher product flows. An example of this can be illustrated using Figure 5.1a, which shows the product flowrate from the WPB. At 850°C , the devolatilisation stage was over at around

3 minutes; the flowrate dropped off to around 200 ml min⁻¹ and slowly decreased as the reaction progressed. In contrast, at 650°C, the devolatilisation lasted for slightly longer, but at 5 minutes, the flowrate was around 30 ml min⁻¹, suggesting very sluggish reactions.

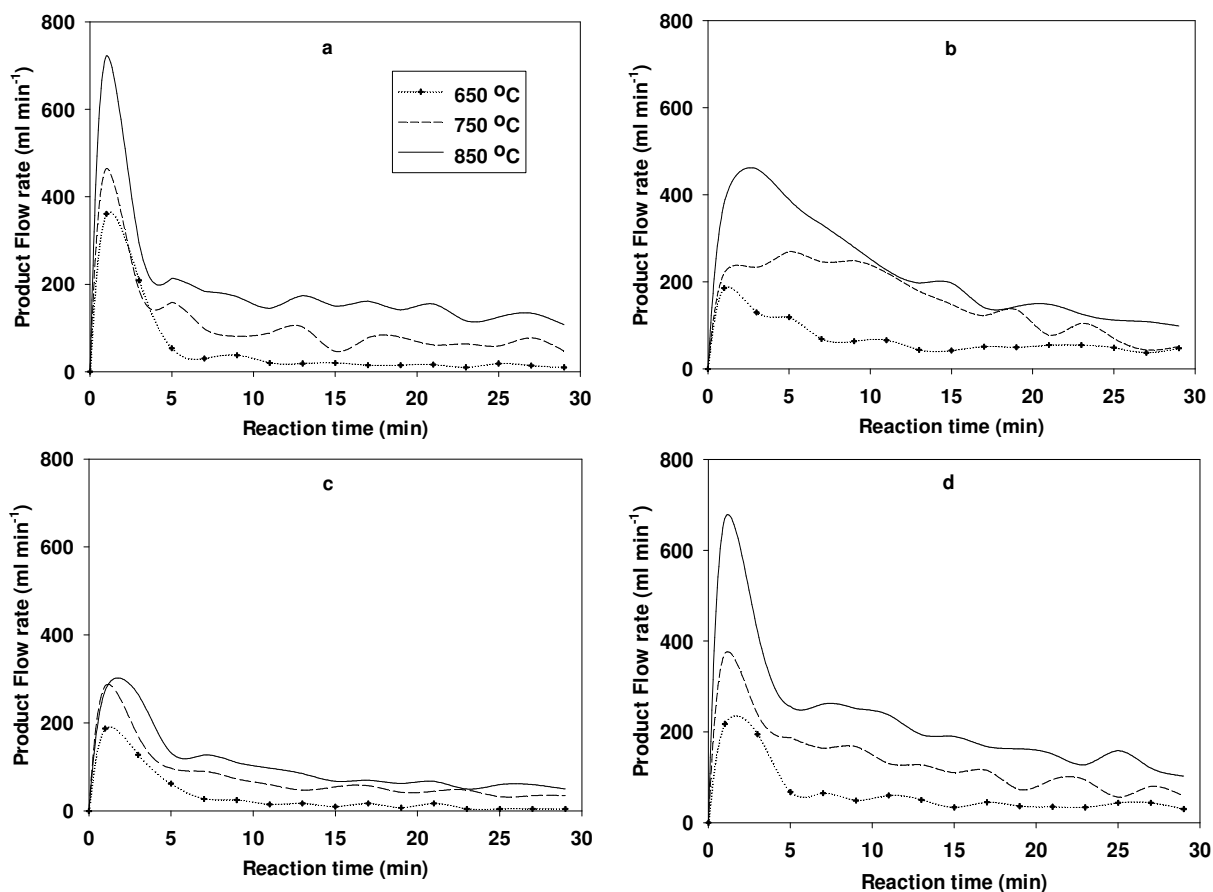


Figure 5.1: Effects of temperature on product flow (2 minute average) of (a) WPB, (b) RSB (c) SSB and (d) MCB at 172 g min⁻¹ kg⁻¹ biochar.

Table 5-1: Effects of temperature on the Arrhenius rate constants for the three ‘char consuming’ gasification reactions assuming first order reactions [144].

Reaction	Rate Constant, K at Temperature (s ⁻¹)			Data	
	650°C	750°C	850°C	E/R	A (s ⁻¹)
Boudouard	4x10 ⁻¹¹	9.3x10 ⁻¹⁰	1.25 x10 ⁻⁸	29884	4364
Char gasification	9.5 x10 ⁻⁹	6.8 x10 ⁻⁸	3.4 x10 ⁻⁷	18522	4.93
Methane formation	1.6 x10 ⁻¹⁰	8.15 x10 ⁻¹⁰	3.17x10 ⁻⁹	15600	0.00342

RSB displayed a different behaviour to the other biochars. It was the only biochar not to produce its highest flowrate in the first minute. This suggests that other reaction mechanisms are taking place since devolatilisation was the fastest process for the other biochars. It also maintained a higher flowrate for an extended period of time, particularly at 850°C where its product flowrate dropped below 200 ml min⁻¹ after 15 minutes. In comparison, the flowrate from WPB dropped below 200 ml min⁻¹ after 7 minutes. The difference in the product flows can be attributed to the reactivity of the biochars. RSB has the highest AAEM content, in particular, K, at 9.28 wt%, which is known to enhance gasification reactions [62]. The porous structure of the RSB enables steam to diffuse in and out of the biochar complex without much resistance. In contrast, WPB with its non-porous structure and low AAEM content displayed lower product flowrates, even though it had higher carbon content.

5.4 Effects of Temperature on Transient Gas Composition

All of the previous work on steam gasification of biochar has focused on the effects of various parameters on the final syngas composition. There is no work that studies the changes in the composition as the reaction progresses. Knowledge of the transient composition is crucial for three reasons; (i) it helps to explain the final composition and (ii) it is needed if the process is to be run continuously so as to be able to produce a consistent composition and (iii) it is needed if accurate models are to be developed.

To study the effects of the transient gas composition during the gasification reaction, a 50 ml syringe was used to collect the gas sample at times of 1, 3, 5,

7.5, 10, 15, 20, 25 and 30 minutes. The gas was transferred into a glass serum, displacing water. The gas was then taken out of the bottle using the same syringe and injected into an Agilent 7890A refinery gas analyser. The method is described in detail in Chapter 3. The transient composition was investigated at 650, 750 and 850°C at a steam flowrate of 172 g min⁻¹ kg⁻¹ biochar.

The results are split into three sections, corresponding to the temperature at which they were carried out; 650, 750 and 850°C.

5.4.1 Transient Gas Composition: 650°C

Figure 5.2 shows the transient gas composition at 650°C and 172 g min⁻¹ kg⁻¹ biochar. It is observed that major changes occurred during the reaction and the composition at the end was very different to the one at the beginning. All the biochars displayed a general behaviour with respect to H₂; it was low at the beginning and increased as the reaction proceeded. The time it took to reach a plateau varied with biochar, for example; RSB reached around 63% in 7 minutes but SSB and WPB both took over 20 minutes to get to a similar H₂ content. The CO₂ volume fraction was high at the beginning, then decreased before increasing again and CO and CH₄ displayed similar behaviours in that they both decreased as the reaction proceeded.

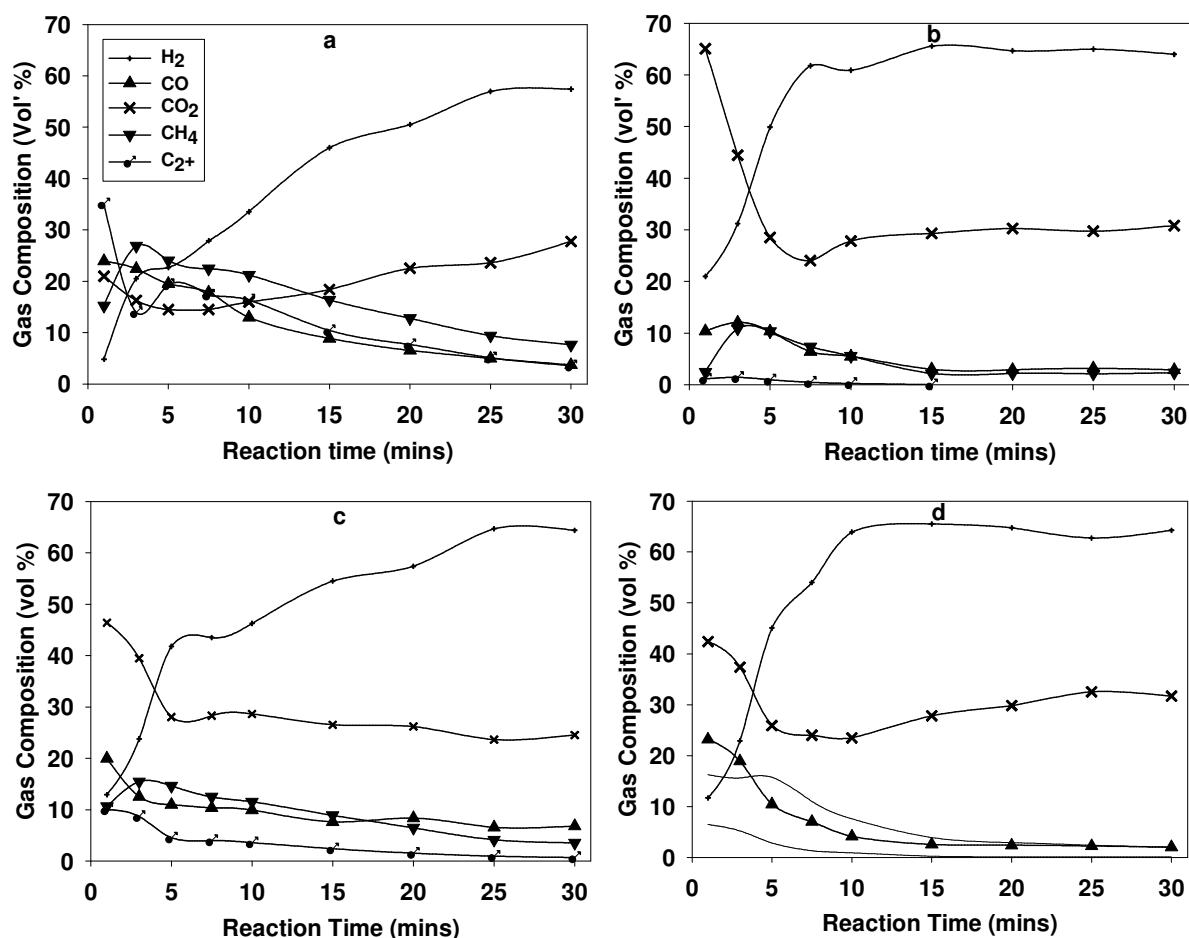


Figure 5.2: Transient gas composition at 650°C for (a) WPB, (b) RSB, (c) SSB and (d) MCB at a steam flow of 172 g min⁻¹ kg⁻¹ biochar

5.4.2 Transient Gas Composition: 750°C

It is observed from Figure 5.3 that there were some similarities in the general transient behaviour at 650°C and 750°C but significant differences existed in other areas. At both temperatures, H₂ content increased during the reaction after starting off low, however, the starting composition at 750°C was higher and the rate at which it reached a plateau was faster. For example; H₂ content for MCB started off at ~12% at 650°C and it reached a plateau in ~12 minutes. At 750°C, the starting content was ~29% and it reached a plateau in ~3 minutes. Furthermore, the initial hydrocarbon content was lower for all the biochars and the time it took before they disappeared was reduced. This was particularly evident in

WPB which had an initial hydrocarbon ($\geq C_2$) content of over 30% at 750°C but they were virtually finished after 10 minutes. The other major noticeable difference was the behaviour of the CO₂; at 650°C, it started off very high but at 750°C, it started off low and increased as the reaction proceeded.

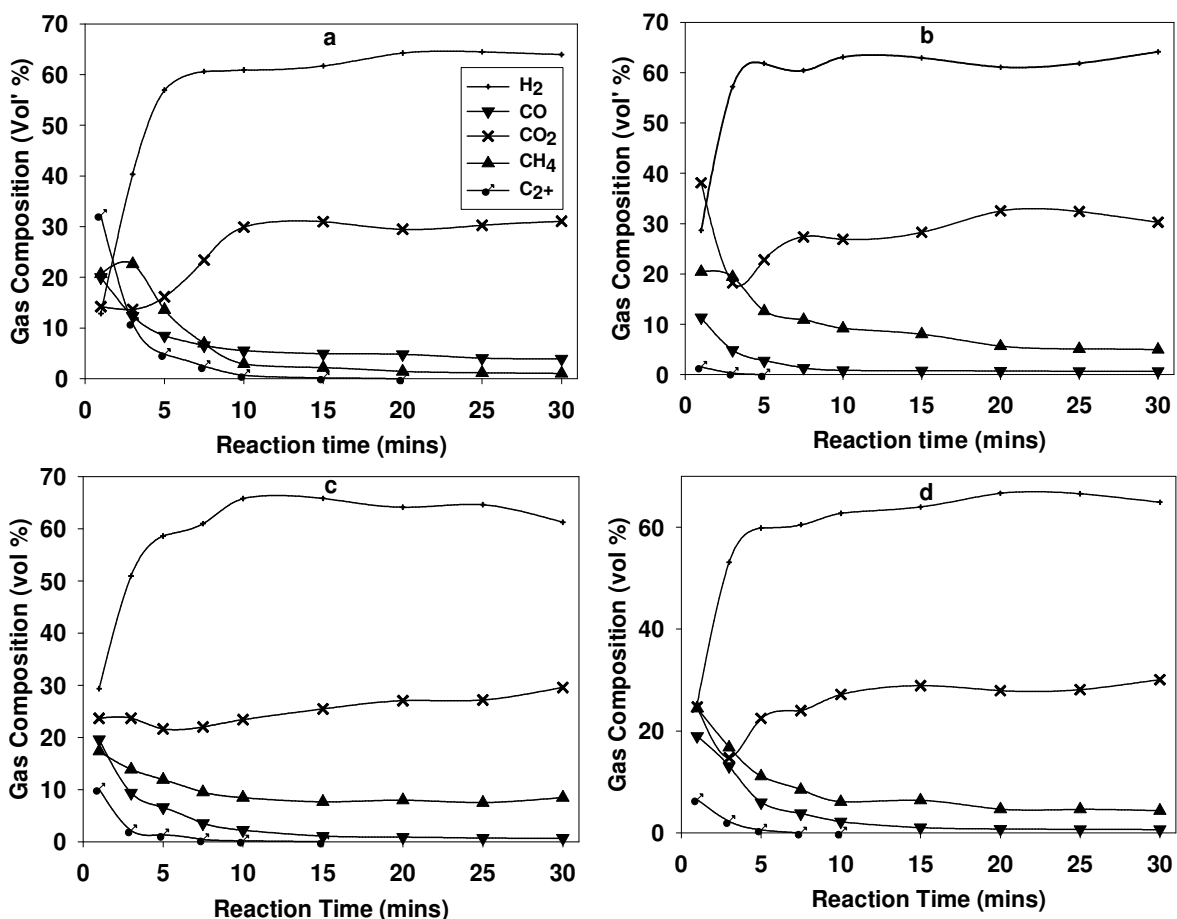


Figure 5.3: Transient gas composition at 750°C for (a) WPB, (b) RSB, (c) SSB and (d) MCB at a steam flow of 172 g min⁻¹ kg⁻¹ biochar

5.4.3 Transient Gas Composition: 850°C

Figure 5.4 shows that the transient behaviours of the constituents were more or less similar for all the biochars at 850°C. This behaviour is what would be expected in scaled up applications since the reaction would be carried out at high temperatures to maximise conversion and product yield. At low temperatures of

650°C and 750°C, reaction kinetics for gasification reactions are sluggish and devolatilisation has a disproportionately weighted impact on the gas composition.

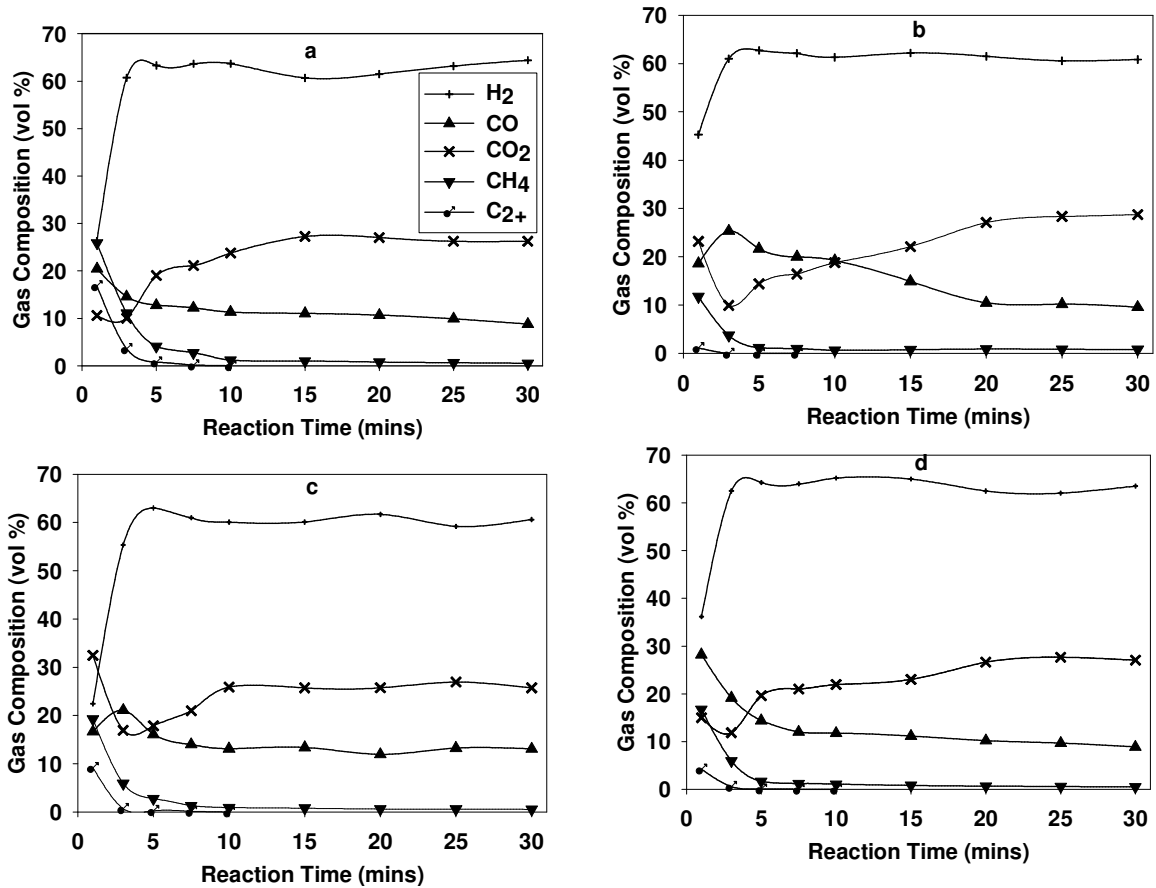


Figure 5.4: Transient gas composition at 850°C for (a) WPB, (b) RSB, (c) SSB and (d) MCB at a steam flow of 172 g min⁻¹ kg⁻¹ biochar

The results can be explained by referring to the types of reactions that occur and their thermodynamic behaviours at 850°C. As the biochar was placed into the reactor, it produced a gas that had a low H₂ content as the CO, CO₂ and hydrocarbons dominated – resulting from the (limited) combustion of char and devolatilisation of the volatile matter [15]. Once devolatilisation was over, the H₂ content began to increase as gasification reactions such as the water-gas reaction (reaction 2-3 page 20), followed by the water gas shift reaction (reaction 2-10, page 20) took over. Both of these reactions produce H₂ and CO or CO₂ as their

products but the H_2 reached a plateau faster than CO_2 and CO . This is attributed to the steam reforming of CH_4 and other hydrocarbons which produce more moles of hydrogen per one mole of CH_4 than moles of CO or CO_2 product. Beyond 5 minutes, there is not much of a change in the H_2 content as it remains at around 60% for the duration of the reaction.

The CO content is particularly high at the beginning of the reaction resulting from the partial oxidation of carbon(2-5, page 20) given that it is the fastest gasification reaction and quickly depletes all the oxygen in the biochar [37]. Once the oxygen is depleted, the overall reaction rate slows, leading to a reduction in product flow. Water gas reaction becomes the rate-controlling reaction, forming CO and H_2 . The CO reacts with H_2O to form H_2 and CO_2 via the WGSR, and while there is sufficient carbon in the biochar, the CO_2 can further react with it to form more CO via the Boudouard reaction (reaction 2-2, page 20). Methane content decreases as the reaction proceeds resulting from the slow reaction kinetics of the methanation reactions. It is known that the rates of methanation reactions are the slowest of all the char gasification reactions [37].

Most of the significant changes occurred within the first five minutes. The intersection between CO and CO_2 portrays the moment when the WGSR becomes more prominent than the partial oxidation reactions as a result of a lack of oxygen and more dominant than the Boudouard reaction as a result of reaction kinetics since WGSR is two to five times faster than Boudouard reaction [37]. This point occurred before 5 minutes for all the biochars except RSB which took around 10 minutes. Past 10 minutes, very few other changes occurred to the system except that the CO_2 content continued to rise. This was the result of two factors; (i), the steam to carbon (S/C) ratio increased due to the depletion of the carbon in

the char, yet the steam flow remained constant. (ii) The decrease in carbon ensured that the Boudouard reaction occurred less frequently even though it may have been thermodynamically favourable.

The results showed a few similarities and some significant differences with those of Moon *et al* [44]. The similarities are that both results show an initial low content of H₂ and CO₂ which increased as the reaction proceeded. The CH₄ content was initially high in both cases and decreased during the reaction. The most significant difference is that of the CO content. In all of their experiments, Moon *et al* [44] obtained very high CO contents at the beginning of their reactions. This was in contrast to the results of this investigation which showed that CO, although prominent in the early stages, is never the dominant gas. The results might be linked to the volatile content and in particular, the oxygen content which is responsible for the partial oxidation reaction. The oxygen contents in the biochars was much lower than the 44% used in [44], therefore it limits the oxidation.

Yan *et al* [54] reported that solid residence time within a fixed bed reactor has no effect on the final syngas composition at 850°C since the reaction mechanisms remain the same. This conclusion is in contrast to the results shown in Figure 5.2 - Figure 5.4, which show a clear change in the reaction mechanisms with time – particularly in the early stages. The differences might arise as a result of the different pyrolysis processes used, leading to different chemical compositions of the biochars and varying reactivities and volatile contents.

5.5 Effects of Temperature on Gas Composition

To study the effects of temperature on the individual gases within the syngas mixture, a temperature range of 650 – 850°C was used. The steam flow was kept constant in all cases at 172 g min⁻¹ kg⁻¹ biochar. Product gas was collected using 8.2 L gas bags and a 50 ml sample was taken and analysed using an Agilent 7890A Refinery Gas Analyser. A detailed description of the experimental procedure can be seen in Chapter 3.12. The results of the four most prominent gases (H₂, CO, CO₂ and CH₄) are presented in Figure 5.5 to Figure 5.8, whilst the rest are shown in Table 5-3. The results are presented as the average of three experiments and the error bars represent the range of the variation in data.

5.5.1 Effects on Hydrogen

Figure 5.5 shows the effects of temperature on hydrogen content from 650 – 850°C. It is observed that H₂ content increased with temperature and reached a peak at 700 – 750°C for all the biochars except WPB. This indicates the dominance of the WGSR which begins to reverse at temperatures above 700°C [145]. WPB had the lowest H₂ content for all the temperatures studied and showed an increase from 30% to 53% at 650 – 850°C respectively. At low temperatures, reaction rates of the gasification reactions are limited, therefore devolatilisation has a disproportionately weighted impact on the final composition. For example; at 650°C, 55% of the total volume was produced in the first 3 minutes and, at this point, Figure 5.2a shows that this gas was laden with HCs; hence the final composition will also have a high HC content. At higher temperatures, The HCs are cracked into H₂, CO and CO₂ while simultaneously, gasification reactions,

such as the water gas reaction, become more prominent, leading to an increase in hydrogen.

An important factor that determines the overall H₂ content is the rate at which H₂ reaches its maximum volume fraction. For example; it is observed from Figure 5.2 to Figure 5.4 that eventually the H₂ volume fraction levels off at over 60%, but, the time it takes to achieve this value varies considerably. At 650°C, it takes around 10 minutes for MCB, but by then, most of the gas has already been produced as observed in Figure 5.1d. This means that the overall H₂ volume fraction will be lower even though conditions might favour the forward WGSR. At 850°C, the H₂ volume fraction increases sharply within the first 3 minutes, coinciding with peak gas flow as seen in Figure 5.1 and Figure 5.4 and remains high for the duration of the reaction.

The results can be compared to previous studies in two ways; (i) using common trends and (ii) using steam flow and temperature. The first comparison only compares the trends that exist in the results and not the composition of the gas since this is also determined by the steam flow. This method allows for comparison with most of the previous literature. The latter comparison specifically looks at the volume fractions of individual gases and compares them. This can only be done by comparing the results to studies which used a similar steam flow to the one in this study; namely [13] and [14] which used a steam flow of 167 and 165 g min⁻¹ kg⁻¹ biochar respectively.

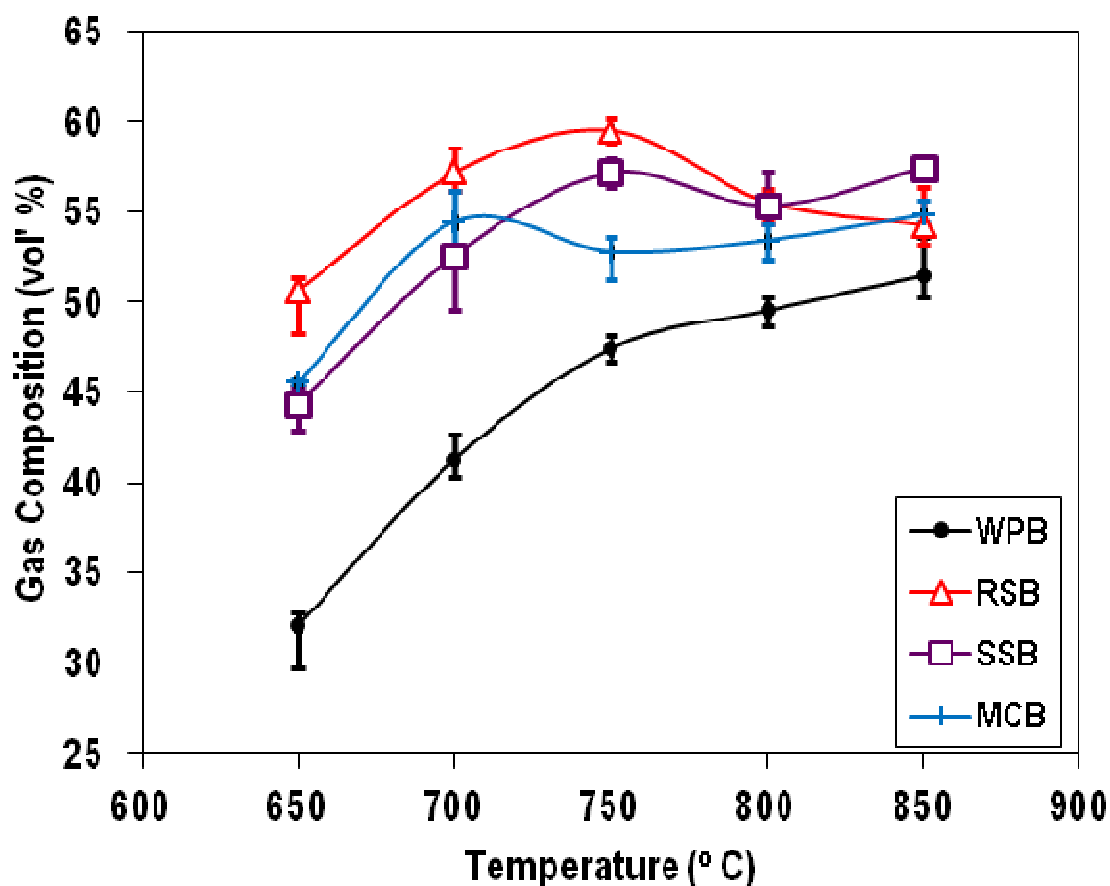


Figure 5.5: Effects of temperature on H₂ volume fraction at a steam flow of 172 g min⁻¹ kg⁻¹ biochar

The general trend of peak H₂ volume fraction at 700 or 750°C for most biochars was reported only in [13]. Other studies; [14], [12], [146] reported an increase with temperature. WPB gave very similar results to those in [14] where biochar produced via fast pyrolysis of pine sawdust was gasified and H₂ volume fractions of 40.6, 45.6, 49.6 and 52.4% were obtained at 700, 750, 800 and 850°C respectively. This could suggest that the pyrolysis type does not play such a major role when it comes to syngas composition from steam gasification of the biochars. Of the two studies which used a similar steam flowrate, the highest H₂ content from this study was higher than that obtained in [14] but significantly lower than

the 74.2% obtained in [13] at 700°C from commercial biochar. The difference might be attributed to two factors (i) the gasification procedure used in each experiment and (ii) the residence time the solid spends in the reactor. In [13], biochar was placed into the reactor prior to heating and steam was introduced once the reactor was at temperature. This would have led to release of volatile matter which was not included in the final gas composition, thereby showing a very high H₂ volume fraction as a result of a pure char gasification reaction. The second difference is the solid residence time the biochar spends in the reactor, it is known from Figure 5.2 to Figure 5.4 that the H₂ composition increases with time; hence the longer the residence time, the more hydrogen will be collected at the end. In [13], the biochar spent 45 minutes in the reactor, 15 minutes more than used in this study.

5.5.2 Effects on Carbon Monoxide

Figure 5.6 shows the effect of temperature on the CO volume fraction. It is observed that the CO content is higher at 650°C than it is at 750°C for all the biochars. This is unexpected since CO is known to increase with increasing temperature [37]. According to equation 5-1, and using the data in Table 5-2, the steam-biochar reaction is kinetically limited below ~700°C and the rate of the Boudouard reaction is insignificant below ~730°C [37]. This indicates that most of the CO produced at 650 and 700°C is as a result of the initial devolatilisation and partial oxidation. This also explains why the CO content of the WPB was so high at 650°C, since it produced most of its volume in the initial stages of the reaction when the CO content was high.

$$\Delta G = \Delta H - T\Delta S$$

5-1

where ΔG (J mol^{-1}) = Gibbs Free Energy, ΔH = Enthalpy change (J mol^{-1}) T = Temperature (K) and ΔS = Entropy change ($\text{J mol}^{-1} \text{K}^{-1}$).

Table 5-2: Standard thermodynamic properties of chemicals at 298K and 1.01kPa [147]

Substance	Enthalpy of Formation, $\Delta_f H^\circ$, kJ mol^{-1}	Entropy of Formation $\Delta_f H^\circ$ J mol^{-1}
C (graphite)	0	5.7
H ₂ O	-110.5	188.8
CO	-241.8	197.7
H ₂	0	130.7

Above 750°C, CO content increases for all the biochars. This is the result of the Boudouard reaction becoming less kinetically limited. RSB yielded the lowest CO volume fraction at 650 and 750°C but at 850°C; it had the highest at 21%. In contrast, WPB showed the highest CO content at 650°C (15%) which increased slightly to 15.9% at 850°C – a little higher than SSB, which had the lowest, 15% at 850°C. The AAEM content of the biochars (Table 4-2) explains why RSB and MCB have such high CO contents since it is known that AAEM species catalyse oxygen-char reactions [148]. The results also show that the catalytic activity of the AAEM species becomes prominent above temperatures of 700°C.

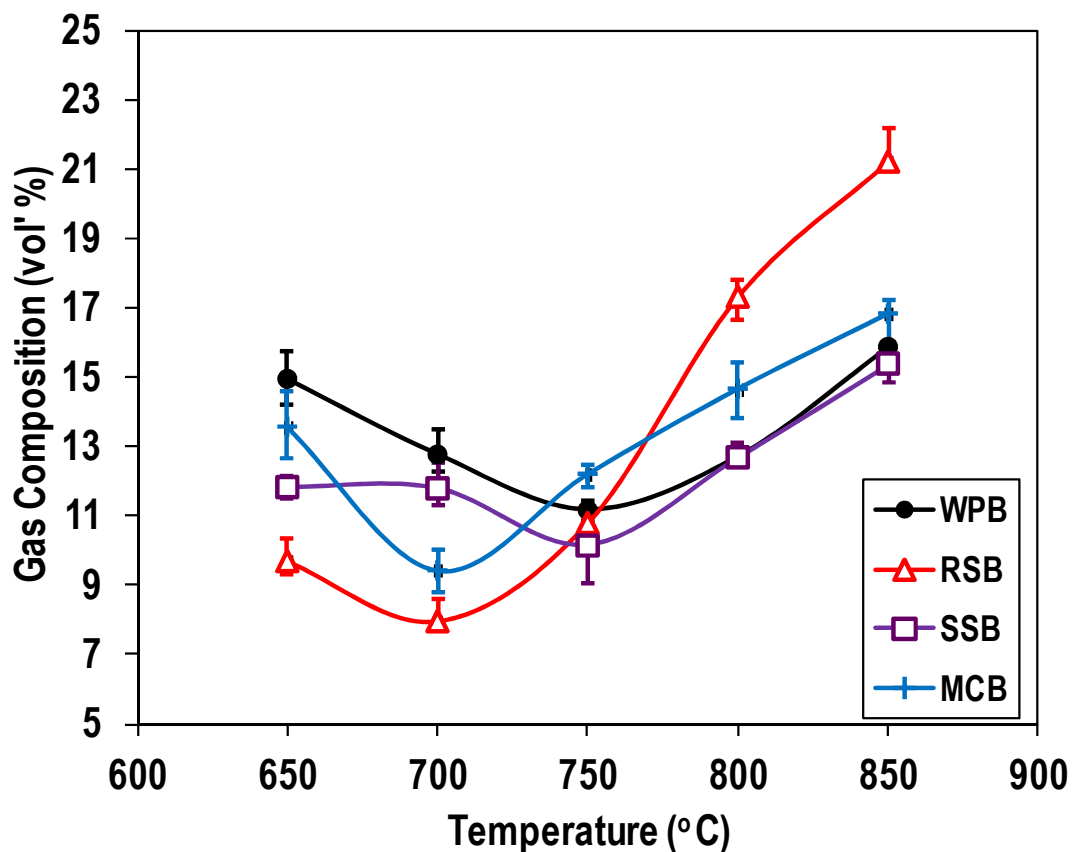
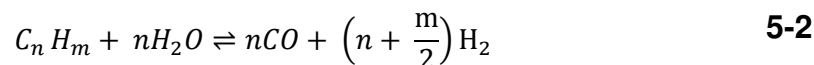


Figure 5.6: Effects of temperature on the CO volume fraction at 650 - 850°C and a constant steam flow of 172 g min⁻¹ kg⁻¹ biochar

The general trend of high CO at low temperatures, low CO at intermediate temperatures and high CO at higher temperatures was reported in [12] and [14] but [146] and [13] both reported an increase in CO with temperature. In terms of concentration, the 17.3 and 21.2% CO obtained from RSB at 800 and 850°C is higher than the 16.4% CO for bagasse biochar at 800°C reported in [13] and the 14% reported in [14] at 800°C for pine sawdust biochar.

5.5.3 Effects of Temperature on Carbon Dioxide

Figure 5.7 displays the effects of temperature on the CO₂ volume fraction of the biochars. It can be observed that all the biochars showed a general decrease with increasing temperature except the WPB, which showed an increase until 800°C before decreasing thereafter. It is likely that once the carbon reacts with the steam to form CO and H₂, the CO further reacts with steam to produce more H₂ and CO₂ via the WGSR. At higher temperatures the Boudouard reaction becomes more significant. WPB does not follow the general trend, its CO₂ content increases significantly from 17.9% to 24.1% at 650 – 800°C respectively before decreasing to 21.5% at 850°C. This can be explained by the presence of HCs in the WPB products. For example, at 650°C, HCs excluding CH₄ accounted for 18.94% volume fraction of the total gas. Steam reforming of hydrocarbons is enhanced at higher temperatures [149], therefore, the hydrocarbons are converted into H₂ and CO via equation 5-2 and CO₂ is formed as a result of the CO taking part in further reactions such as the WGSR.



Three biochars show a general decrease with temperature whilst WPB shows an increase until 800°C but decreases thereafter. The general trend of a decrease in CO₂ content with temperature was reported in [12], [13] and [14]. A low CO₂ content is desired since it dilutes the heating value of the gas, therefore, the lowest volume fractions of 24 and 21% given by WPB at 800 and 850°C, compares unfavourably with [13] where 15.5 and 8% were reported for bagasse and commercial biochars at 800°C. They do however compare favourably with the results in [14] where 27.6% was reported at 850°C.

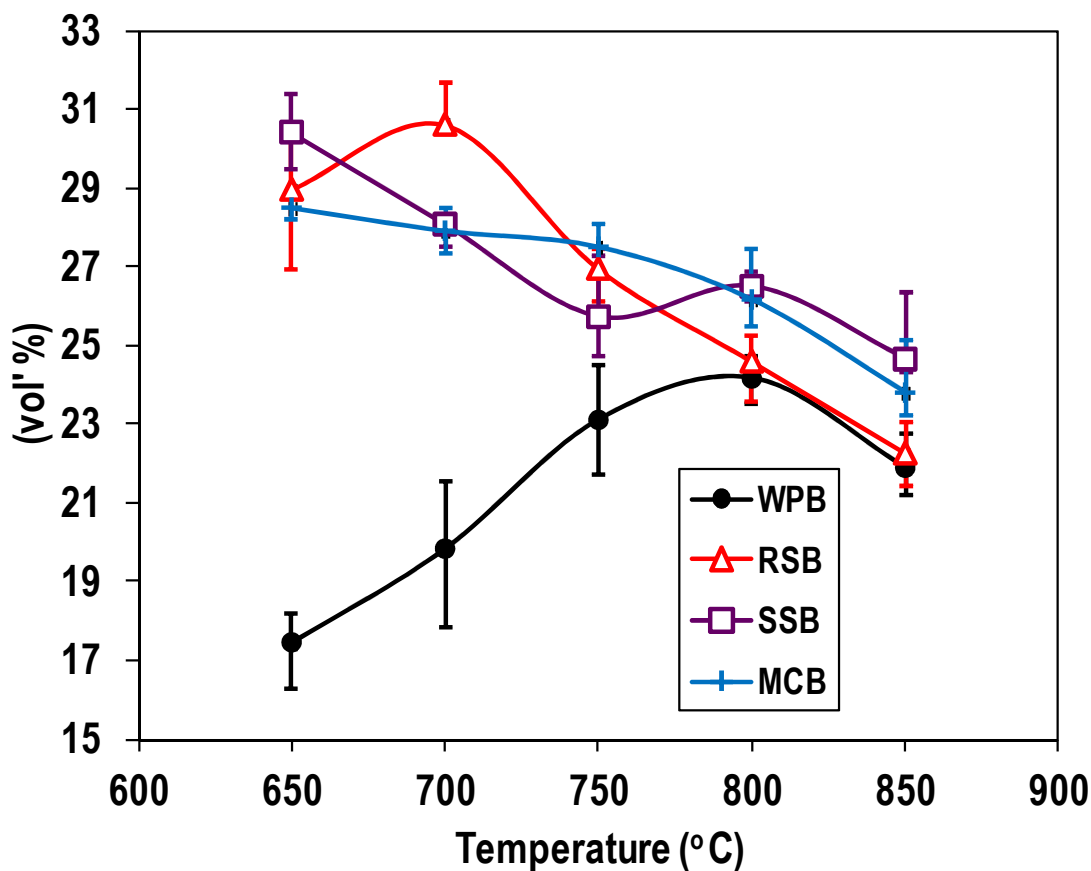


Figure 5.7: Effects on temperature on CO₂ volume fraction at 650 - 850°C using a constant steam flow of 172 g min⁻¹ kg⁻¹ biochar

5.5.4 Effects of Temperature on Methane

Figure 5.8 displays the effects of temperature on CH₄ volume fraction at a steam flow of 172 g min⁻¹ kg⁻¹ biochar. It can be seen that all the biochars followed the same trend; CH₄ content decreased with increasing temperature. At 850°C, the highest CH₄ content was given by the WPB at 6.5%, whilst the lowest was given by RSB at 1.98%. Most of the CH₄ is produced at the beginning of the reaction as a result of devolatilisation. As a result, it will have a greater weighting at lower temperatures when the fraction of initial volume of gas constitutes a large fraction

of the total final volume. The reformation of CH_4 is enhanced at higher temperatures, therefore, it will be reformed into CO and H_2 .

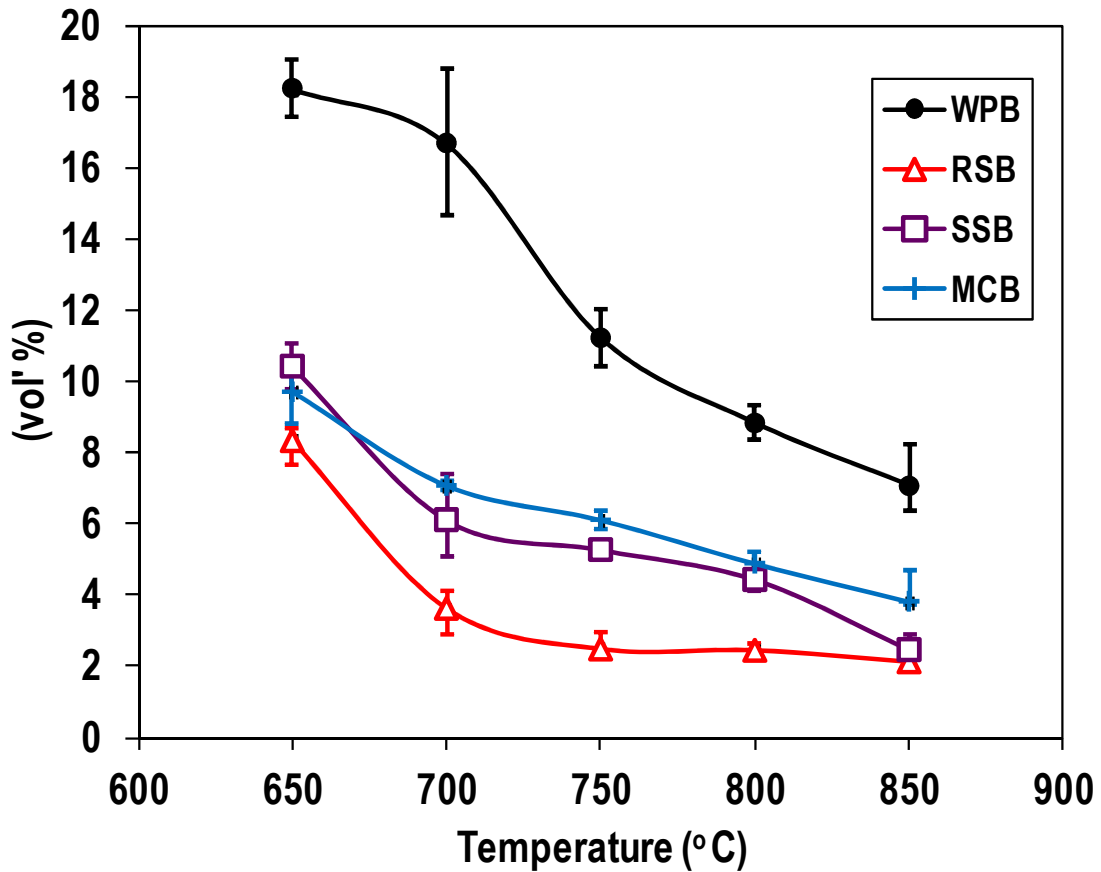


Figure 5.8: Effects of temperature on CH_4 volume fraction at 650 - 850°C using a constant steam flow of $172 \text{ g min}^{-1} \text{ kg}^{-1}$ biochar

The trend in CH_4 content is universal for all the biochars tested; it is one of a decrease with temperature. Only [14] reported a similar trend, the rest of the studies showed no overall trend. A high CH_4 content is advantageous since it increases the heating value of the gas and is used alongside hydrogen in SOFCs since its reforming is an endothermic reaction thereby cooling the fuel cell and reducing the cooling demand [150]. The highest methane content of 8.8 and 7% at

800 and 850°C was obtained from the WPB. This compares well with <1% in [13] at 800°C and the 1.74% in [14] at 850°C.

5.6 Effects of Temperature on Hydrocarbon Content, Conversion and Associated Results

Table 5-3 (page 139) shows the effects of temperature on the various results associated with biochar gasification. It is observed that C₂H₄ is the most prominent hydrocarbon and persists throughout the temperature range. Above 650°C, the volume fraction of C₂₊ is negligible, particularly those produced by gasification of RSB, in which case they disappear altogether. WPB had the highest HC content at all the temperatures, followed by SSB and then MCB.

The results in Figure 5.4 and Table 5-3 show a clear picture of how HCs are made during steam gasification of biochar. Almost all the HCs (>CH₄) are produced in the early stages of the reaction when the product flowrate was high, as a result, the residence time the HCs spend in the reaction zone is low, leading to inefficient thermal cracking. When the flowrate subsides, the residence time increases, leading to more efficient cracking. The cracking reactions are further enhanced by higher temperatures, resulting in less HCs.

Dry gas yield (DGY) increases significantly with temperature for all the biochars, with RSB producing the most at 650 and 750°C, but MCB producing the most at 850°C with 2.31 m³ kg⁻¹. It was expected that WPB would give the highest DGY, resulting from its higher carbon content but this was not the case as only SSB produced less volume throughout the temperature range. The increase in DGY is

mainly attributed to the increase in the rate of the char gasification reaction. At higher temperatures, the reaction becomes more prominent and converts char more rapidly, giving a greater volume of products.

The general trend in the HHVs of the produced gases is that of a decrease with reaction temperature. The highest HHV is given by gasification of WPB, with 27.6 and 13.8 MJ m⁻³ at 650 and 850°C. The lowest was given by RSB at 10.1 MJ m⁻³ at 750°C. The biggest differentiator between the heating values is the HC contents of the product gases, therefore it is unsurprising that WPB gave the highest whilst RSB, the lowest.

An important feature of a syngas is its H₂/CO ratio. The H₂/CO ratio determines the type of application that particular syngas is most suited for. For example; a syngas with a high H₂/CO ratio can be upgraded to produce pure hydrogen or it can be used directly in SOFCs whereas one with a low H₂/CO ratio is best used to make biodiesel via the Fischer-Tropsch process [12]. In all cases, the H₂/CO ratio was highest at 750°C, with RSB giving the highest at 5.57. The H₂/CO ratio decreases at 850°C, resulting from the increase in CO content. The H₂/CO results indicate that the forward WGS is most prominent at 750°C. At 850°C, the H₂/CO ratios for WPB, MCB and SSB indicate that the syngas has the potential for upgrading purposes whilst the RSB has potential to be used in the Fischer-Tropsch process.

Table 5-3: Effects of temperature on hydrocarbon content, dry gas yield, higher heating value and H₂/CO ratio at a steam flow of 172 g min⁻¹ kg⁻¹ biochar. The results are the mean of three experiments and the error represents the maximum deviation for that particular result

	Wood pellet Temperature			Rapeseed Temperature			Sewage sludge Temperature			Miscanthus Temperature		
	650°C	750°C	850°C	650°C	750°C	850°C	650°C	750°C	850°C	650°C	750°C	850°C
C ₂ H ₆	3.26±0.6	1.08±0.1	0.38±0.1	0.60±0.4	0.03		0.82±0.1	0.41±0.4	0.03	0.56±0.2	0.23±0.1	0.35±0.3
C ₂ H ₄	8.65±1.2	4.77±0.7	3.01±0.4	1.17±0.9	0.08	0.12	1.79±0.4	1.0±0.3	0.24	1.41±0.4	1.0±0.3	0.35±0.1
C ₂ +	5.35±0.7	1.19±0.2	0.30±0.1	0.60±0.5			0.42±0.3	0.28±0.2		0.62±0.3	0.12	0.03
DGY ^a	0.57	1.13±0.03	2±0.05	0.71±	1.6±0.05	2.23±0.01	0.36±0.02	0.78±0.02	1.05±0.03	0.67	1.38±0.01	2.31±0.02
HHV ^b	27.6	16.2	13.8	13.6	10.1	10.5	13.4	11.7	11.1	11.7	12.1	10.4
H ₂ /CO ratio	2.1±0.15	4.3±0.17	3.2±0.16	5.2±0.3	5.2±0.7	2.6±0.12	3.7±0.12	5.6±0.8	3.7±0.1	3.4±0.15	4.3±0.08	3.3±0.07

^a Dry Gas Yield (m³ kg⁻¹), see equation 3-6 (page 89)

^b Higher Heating Value see equation 3-5 (page 89)

All gas compositions are volume fractions (vol%)

5.7 Effects of Temperature on Biochar Conversion, Carbon Conversion and Carbon Conversion Efficiency

Biochar conversion is defined here as the fraction of mass loss that the biochar experiences during the steam gasification process (without considering the biochar that may be lost to elutriation and attrition in the gas stream). Carbon conversion (CC) is defined as the fraction of carbon that is lost from the biochar during the gasification process. Carbon conversion efficiency (CCE) is defined as the fraction of carbon that has been converted into the product gas. The difference between the CC and CCE is the carbon lost to tar, or the carbon that is carried over in the gas stream. Details on calculations can be found in section 3.13.

5.7.1 Biochar Conversion

Figure 5.9 displays the effects of temperature on biochar conversion. It is observed that there was a huge increase in biochar conversion with temperature. From 650 - 850°C, the biochars experienced 35, 47, 18 and 38% increase in conversion for WPB, RSB, SSB and MCB respectively. The largest increase was observed for the RSB with 47% but most of this increase occurred between two increments; 16% at 650 – 700 and 18% at 800 – 850°C. WPB displayed the highest conversion at all the temperatures, increasing from 57 – 89% from 650 – 850°C. This was expected since WPB had a carbon content of 71.58 wt%, which enabled it to participate in additional reactions. SSB displayed the lowest conversion at all the temperatures studied, giving a maximum conversion of 38% at 850°C. Its conversion was limited by its high ash and inert content inhibiting its ability to partake in reactions.

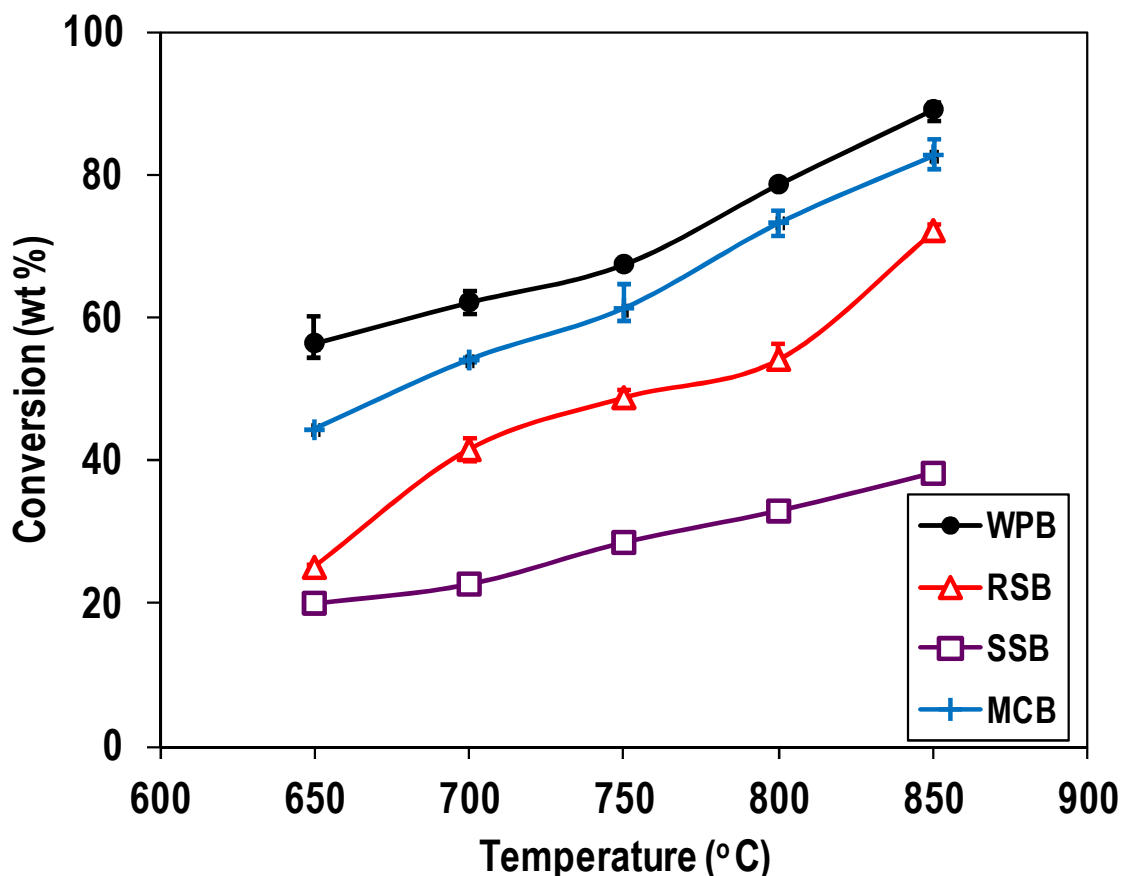


Figure 5.9: Effects of temperature on biochar conversion at 650 - 850°C at a constant steam flow of 172 g min⁻¹ kg⁻¹ biochar

5.7.2 Carbon Conversion and Carbon Conversion Efficiency

The reacted biochars were sent to an external lab (MEDAC Ltd) to evaluate their CHNS contents. Based on the results, the CC was calculated. Carbon conversion is the amount of carbon that had been lost from the biochar (not including carryover and elutriation). This is important since it can be compared to the CCE which tells how much of the carbon has reacted to form syngas.

Figure 5.10 (page 143) shows the carbon conversion and carbon conversion efficiency for the four biochars. It is observed that both carbon conversion and carbon conversion efficiency increase with temperature. From 650 – 850°C, the

carbon conversion increased from; 46 – 87, 30 – 90, 34.49 – 90 and 35 – 88% for WPB, RSB, SSB and MCB respectively. The extent of carbon conversion was high at 850°C, particularly for SSB and RSB, both of which achieved almost 90%.

A similar trend was observed in the carbon conversion efficiency. From 650 – 850°C, it increased from; 27 – 64, 29 – 81, 32 – 73 and 29 – 83% for WPB, RSB, SSB and MCB respectively. Clearly, there is a difference between the carbon conversion and the carbon conversion efficiency and this difference is attributed to the carbon lost as tar (as well as carbon lost to elutriation but that is not considered in this case as it cannot be ascertained). In all cases, WPB produced the most tar losing 19.5 and 23% of its carbon to tar at 650 and 850°C, respectively. In contrast, RSB produced virtually no tar at 650°C and MCB produced the least at 850°C with just 4.6% of the carbon lost to tar.

Tar is defined as hydrocarbons that are equal to or larger than C_6H_6 [151]. It forms when volatile content in the biomass vaporises at high temperatures inside the reactor and condenses at lower temperatures blocking and fouling process equipment [152]. During biochar gasification reactions, it was observed that the majority of the tar was formed in the first few minutes of the reaction. This was the result of two factors (i) volatile content being released and (ii) high initial product flowrate reducing gas and vapour residence times, leading to inefficient cracking. The tar manifested itself as a black layer deposited on the sample holder as seen in Figure 5.11 as well as a thin layer of bio-oil floating on top of the condensate.

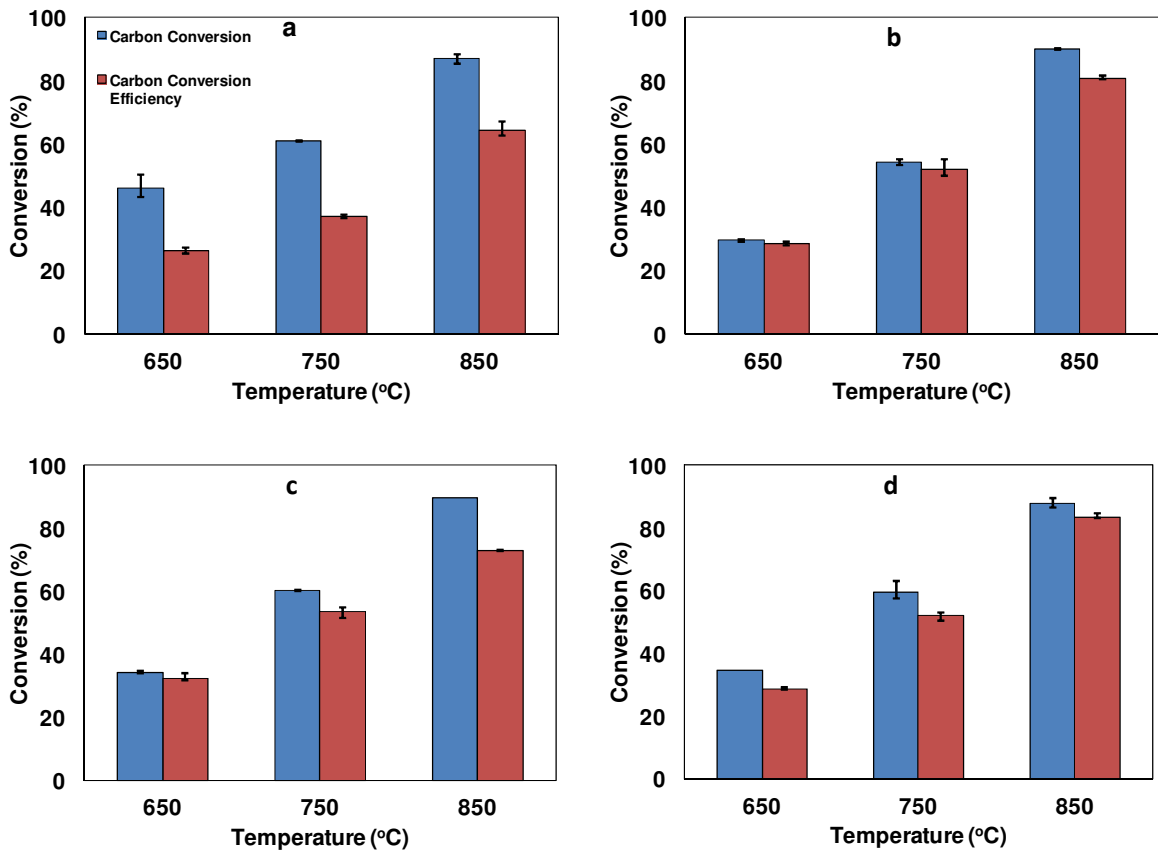


Figure 5.10: Effects of temperature on carbon conversion and carbon efficiency at 650, 750 and 850°C for (a) WPB, (b) RSB, (c) SSB and (d) MCB. The steam flow was kept constant at $172 \text{ g min}^{-1} \text{ kg}^{-1}$ biochar

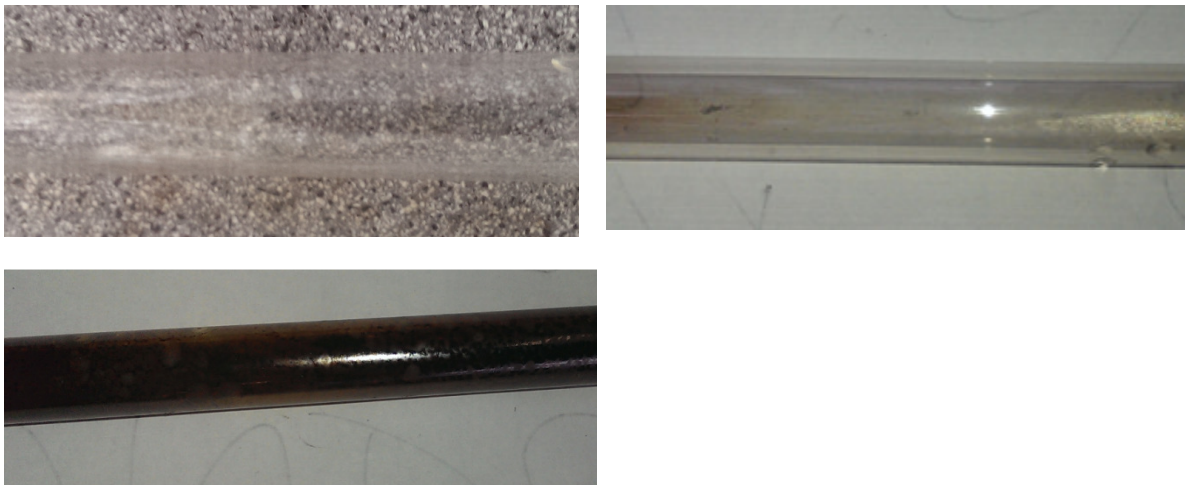


Figure 5.11: Comparison of tar fouling the sample holder; (left to right) clean sample holder - sample holder after RSB gasification and sample holder after WPB gasification. Experiments were carried out 850°C using a steam flow rate of $172 \text{ g min}^{-1} \text{ kg}^{-1}$ biochar

5.7.3 Effect of Temperature on Elemental Analysis

The post gasification biochars were sent to MEDAC Ltd for elemental analyses. Those gasified at 650, 750 and 850°C were sent for CHNS analysis and each biochar was analysed two times. The results are displayed in Table 5-4 to Table 5-7, the average is shown and the error represents the deviation from the mean.

It can be observed that the elemental content changed with increasing temperature but the change is not uniform across the biochars. For example; RSB and SSB showed a decrease in carbon content post gasification but the carbon content in WPB increased from the original biochar which had 71.58 wt% carbon to 88.5 wt% at 650°C and 84.6 wt% at 850°C. This can be attributed to two factors (i) low ash content of the WPB and (ii) the release of the volatile constituents such as O, and H to leave only the fixed carbon in the biochar. Miscanthus biochar displayed a similar behaviour to WPB at 650°C as its carbon content increased from 62.2 to 72.8 wt%. However, past 650°C, its carbon content decreased much more at higher temperature dropping to 43.7 wt% at 850°C.

Table 5-4: Effects of temperature on the elemental composition of the wood pellet biochar at 172 g min⁻¹ kg⁻¹ biochar

Constituent (wt%)	Wood Pellet Biochar			
	Original	650°C	750°C	850°C
C	71.58	88.5±0.12	85.5±0.26	84.6±0.29
H	4.62	1.85±0.04	1.32	1.13±0.09
N	0.54	0.31±0.03	<0.1	<0.1
S	0.22	<0.1	<0.1	<0.1

Table 5-5: Effects of temperature on the elemental composition of the rapeseed biochar at 172 g min⁻¹ kg⁻¹ biochar

Constituent (wt%)		Rapeseed Biochar			
	Original	650 °C	750 °C	850 °C	
C	60.25	56.5±0.05	53.8±0.2	21.7±0.04	
H	4.33	1.76±0.06	1.38±0.03	<0.1	
N	4.19	3.2±0.13	3.1±0.15	0.73±0.02	
S	0.1	0.27±0.01	0.3±0.02	0.26	

Table 5-6: Effects of temperature on the elemental composition of the sewage sludge biochar at 172 g min⁻¹ kg⁻¹ biochar

Constituent (wt%)		Sewage Sludge Biochar			
	Original	650°C	750°C	850°C	
C	30.03	24.9±0.04	16.8±0.03	5±0.13	
H	4.19	0.48±0.03	<0.1	<0.1	
N	1.83	2.1±0.04	0.99±0.01	0.24	
S	0.88	0.88	0.87±0.04	0.49	

Table 5-7: Effects of temperature on the elemental composition of the miscanthus biochar at 172 g min⁻¹ kg⁻¹ biochar

Constituent		Miscanthus Biochar			
	Original	650°C	750°C	850°C	
C	62.2	72.8±0.03	65.1±0.5	43.7±0.01	
H	4.37	1.59±0.03	1.31±0.01	<0.1	
N	0.8	0.53±0.01	0.34±0.09	<0.1	
S	0.28	<0.1	0.29±0.02	0.32±0.02	

5.8 Effects of Steam Flow on Steam Gasification of Biochar

In the previous section, the effects of temperature on the steam gasification of biochar were investigated. It was found that although 850°C did not produce peak H₂ content, it did give the highest product yields and conversions. To investigate the effects of steam flow on; product flow, transient gas composition, product composition and conversion, a steam flow range of 54 – 277 g min⁻¹ kg⁻¹ biochar was employed. Temperature was kept constant at 850°C and the same procedure to the one described in Chapter 3.12 was employed.

5.8.1 Effects of Steam Flow on Product Flow

Steam, being one of the two primary reactants is paramount to the steam gasification reaction. Its behaviour on the product flow has not been investigated by previous authors. The product flow was measured using a 500 ml bubble flow meter using the same method described in Chapter 2.4.7. Three measurements are shown on Figure 5.12 taken at steam flows of S0, S2 and S5. These correspond to 0, 54 and 277 g min⁻¹ kg⁻¹ biochar, respectively. It is observed that the addition of steam and subsequent increases in steam flow changed the dynamics of the reaction and led to a drastic increase in product flow. At steam flow S0, the reaction was effectively over within 5 minutes for all the biochars; as the volatile content devolatilised, there was no steam for any other reactions to occur. At S2, the product flow was very erratic and the initial product flows at 1 minute was similar to those of S0 for all the biochars. At S5, the product flows were higher for all the biochars but WPB was the only biochar that maintained it above S2 for the duration of the reaction. The other biochars had their product

flow profile shifted to the left as the reaction occurred much faster. They also showed a significant decrease in product flow as the reaction proceeded and their product flows dropped to that of S2, 10-15 minutes into the reaction, indicating that most of the carbon in the biochar had been used up.

The erratic behaviour of the product flow at S2 was thought to be the result of slow diffusion processes. The product flow depends upon three processes that involve diffusion; (i) diffusion of steam from the surrounding to the biochar surface, (ii) diffusion of products from biochar surface and into the reactor and (iii) diffusion of products from the reactor to the bubble flow meter. At S2, concentration of steam inside the reactor was low; therefore it took longer to diffuse to the biochar. The scarcity of steam led to a limited reaction with the biochar to produce products. Once the products were produced, they diffused out into the reactor, but had to wait until enough products were produced to induce diffusion out of the reactor. Once they diffused out, the process started again and the time lag between the diffusion and the next build-up of pressure was likely to be responsible for the erratic behaviour. At S5, the concentration of steam was much greater, enabling faster diffusion to the biochar surface and increasing the rate of reaction. Subsequently, the build-up of products within the reactor was enhanced and diffusion of products out of the reactor was more constant.

Previous authors have suggested that the biochar gasification process occurs in two steps; (i) devolatilisation followed by (ii) steam gasification of biochar [14]. Figure 5.12 shows that this is only limited to very low steam flows since the product flow from the devolatilisation stage is similar for both S0 and S2. Furthermore, at 3 minutes, once devolatilisation is finished, there is a clear drop in product flow which then recovers by 5 minutes - corresponding to the transition

between devolatilisation and gasification. At S5, devolatilisation and gasification reactions are occurring simultaneously and this is seen as the increase in the initial product flow.

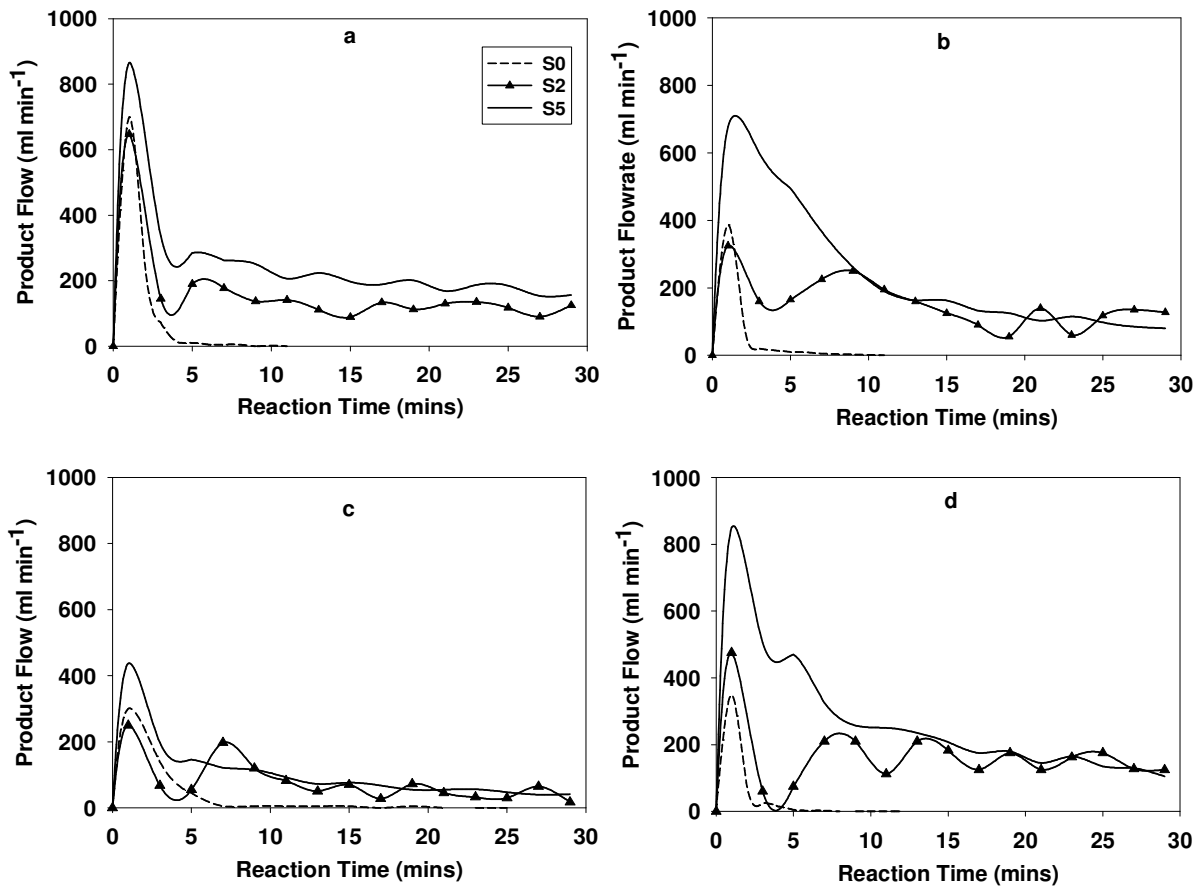


Figure 5.12: Effects of steam flow on the product flow (2 minute average) of (a) WPB, (b) RSB, (c) SSB and (d) MCB at a temperature of 850°C, where S0, S2 and S5 are 0, 54 and 277 g min⁻¹ kg⁻¹ biochar steam flowrates

5.8.2 Effect of Steam Flow on Transient Gas Composition

To study the effects of steam on the transient gas composition, samples of the product gas were collected at reaction time of 1, 3, 5, 7.5, 10, 15, 20, 25 and 30 minutes. The results for RSB and WPB are displayed in Figure 5.13 at steam flows of 54 and 277 g min⁻¹ kg⁻¹ biochar. It is observed that the overall gasification

process followed a general behaviour that was described in Chapter 5.5.4; H₂ and CO₂ volume fractions increased with time, CO, CH₄ and HC volume fractions decreased as the reaction proceeded. The increase in steam flow changed the transient behaviour of the reaction by enabling a stable condition to be reached much faster than would happen at lower steam flows. For example; it is observed that for WPB at S2, H₂ volume fraction was 30% at 1 minute and increased slowly to reach 60% by 15 minutes. At S3 (172 g min⁻¹ kg⁻¹ biochar) from Figure 5.4a, and S5, the initial H₂ volume fraction is 26% and 41% respectively and by 3 minutes, it had reached around 60% for both steam flows.

As the biochar is placed into the reactor, devolatilisation occurs at both S2 and S5 leading to the same products shown in Table 5-8. Once devolatilisation is finished, steam gasification of biochar takes over to produce CO and H₂ which can take part in further reactions to make the final syngas composition. The biggest difference between S2 and S5 is the extent to which those further reactions can take place. It can be seen in Figure 5.13 that the H₂ volume fraction at 1 minute for S2 was 30%; this was higher than the 14.8% in Table 5-8, which indicates that limited gasification reactions are occurring. At S5, the initial H₂ volume fraction is already above 40% indicating that gasification reactions are already well established by this point.

The main reactions which are directly affected by the increase in steam are; water gas, Boudouard, methane reforming and WGSR. An increase in steam leads to an increase in the rate of the char gasification reaction as well the steam reforming of CH₄. It also enables the forward WGSR to occur more frequently, and this affects the Boudouard reaction since the WGSR and Boudouard reaction compete with each other. The forward WGSR is an order of magnitude faster than the

Boudouard reaction, hence it is more likely to occur if the constituents are present [37]. The intersection between the profiles for CO and CO₂ is the point when the forward WGSR becomes more prominent than the Boudouard and/or the incomplete combustion of char. This point occurs earlier; 3 minutes at S5 as opposed to 7.5 minutes at S2 for WPB and 3 minutes and 10 minutes for RSB at S5 and S2 respectively.

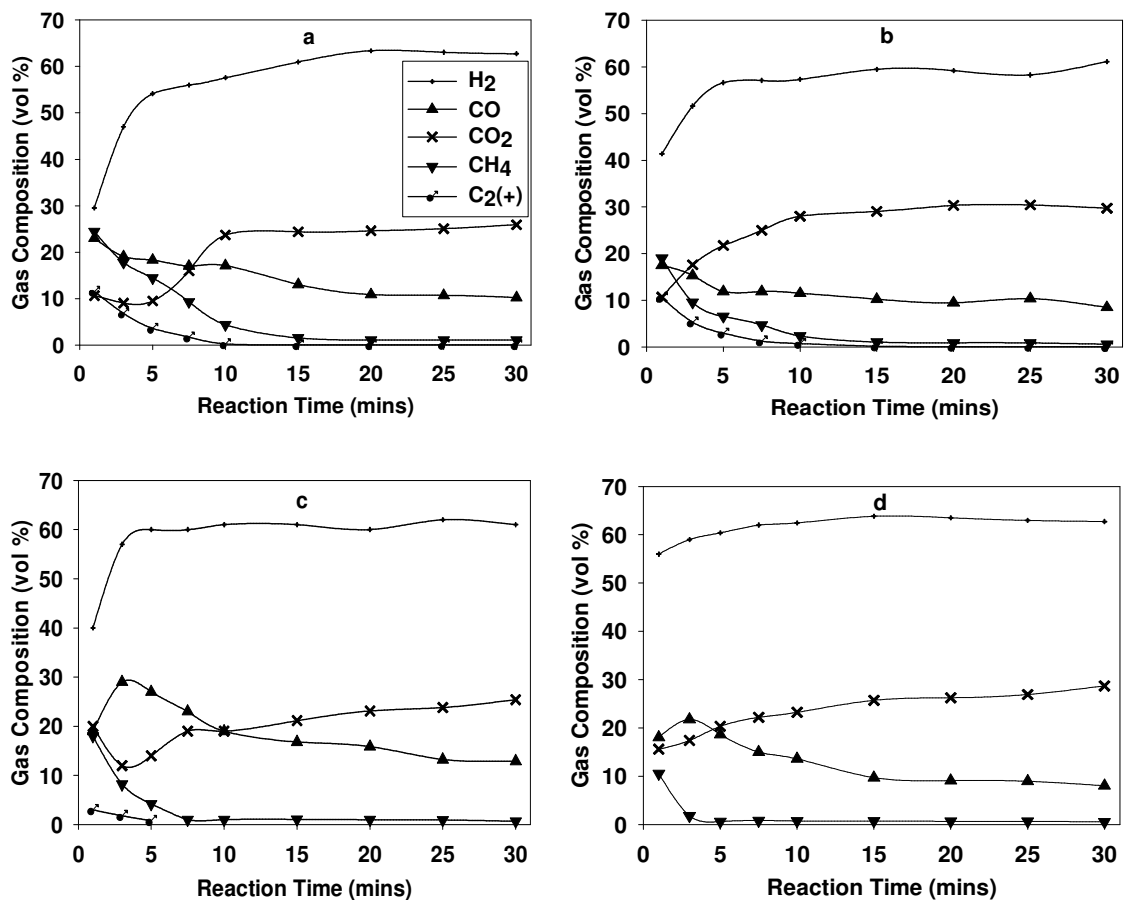


Figure 5.13: Effects of steam flow on the transient gas composition at 850°C, where (a) and (b) are WPB at 54 and 277 g min⁻¹ kg⁻¹ biochar respectively and (c) and (d) are RSB at the same steam flowrates

5.8.1 Effects of Steam Flow on Gas Composition

To study the effects of steam flow on the gas composition, the temperature was kept constant at 850°C and the steam flow was changed from 54 –

277 g min⁻¹ kg⁻¹ biochar. Each experiment was carried out three times and the average is presented in Figure 5.14 to Figure 5.17, which display the effects of steam flow on H₂, CO, CO₂ and CH₄. The error bars represent the range displaying the variation between experiments.

5.8.2 Pyrolysis Composition

In order to study the effects of steam flow on the steam gasification of biochar, it is necessary to know the composition and gas yield when no steam is used. This gives a baseline and allows for a comparison with experiments when steam is used. Table 5-8 shows the gas composition at 850°C, when no steam is used. It is observed that in all cases, H₂ volume fractions are low and the CH₄ contents are very high, with WPB producing the highest CH₄ of 28.2%. The highest H₂ volume fraction of 28.6% was produced by the RSB and the lowest, 14.78%, by the WPB. The HC composition (excluding CH₄) was relatively low except for C₂H₄, in which case it ranged from 2.9% for RSB to 18.5% for WPB. The DGY for the pyrolysis experiments of WPB, RSB, SSB and MCB were as follows; 0.54 ± 0.02, 0.26 ± 0.013, 0.26 ± 0.07 and 0.39 ± 0.09 m³ kg⁻¹ respectively. The yields are extremely low, even lower than the product yields obtained at 650°C. The lack of steam severely restricts further reactions from occurring once devolatilisation is complete.

Yan *et al* [14] carried out a similar experiment to this by pyrolysing pine sawdust biochar at 850°C. They reported the following results; H₂ content of 22%, a CO content of 25.3%, a CO₂ content of 22%, a CH₄ content of 10% and C₂H₄ content of 15.35%. The differences in the results can be attributed to two factors; (i)

different biochars used in each experiment and (ii) different mode of pyrolysis used in the formation of the biochars. Firstly, WPB is a mixture of pine and spruce whereas the biochars used in [14] were from pine sawdust. Secondly, the biochars used by Yan *et al* were formed using fast pyrolysis at 500°C; therefore, their biochars had less volatile matter, 23.95 wt%, compared to 61.2 wt% for WPB. This led to decreased hydrocarbon content and increased H₂ content.

Table 5-8: Pyrolysis gas composition from the biochars at 850°C where the error represents the maximum deviation from the mean of an average of three experiments

	H ₂	CO	CO ₂	CH ₄	C ₂ H ₆	C ₂ H ₄	C ₃ H ₆
WPB	14.78 ±	20.32 ±	13.59 ±	28.22 ±	2.25 ±	18.49 ±	2.31 ±
(Vol%)	0.52	0.03	0.79	1.55	0.03	0.98	0.31
RSB	28.55 ±	23.07 ±	28.42 ±	16.38 ±	0.42 ±	2.90 ±	0.22 ±
(Vol%)	3.09	0.29	1.55	1.65	0.16	1.40	0.14
SSB	22.95 ±	22.97 ±	24.27 ±	21.83 ±	0.62 ±	6.72 ±	0.63 ±
(Vol%)	3.08	2.65	1.85	4.36	0.19	2.8	0.23
MCB	25.1 ±	26.5 ±	28.1 ±	20.17 ±	0.61 ±	4.25 ±	0.32 ±
(Vol%)	2.02	2.92	0.02	0.62	0.03	0.22	0.01

5.8.3 Effects of Steam Flow on Hydrogen Composition

Figure 5.14 displays the effects of steam flow on hydrogen composition at 850°C for the four biochars. It is observed that all biochars exhibited an increase in H₂ volume fraction with increases in steam flow from 54 to 277 g min⁻¹ kg⁻¹ biochar. The largest increase was observed in the WPB, where H₂ content increased by 5.1% from 49.78 to 54.92% from 54 to 277 g min⁻¹ kg⁻¹ biochar respectively. The other biochars also showed an increase with RSB, SSB and MCB increasing by

2.2, 1.1, and 3.5% respectively. At $277 \text{ g min}^{-1} \text{ kg}^{-1}$ biochar, the highest H_2 content was given by the RSB at 58.1% and the lowest at the same steam flow was given by WPB at 54.9%. SSB was the only biochar to attain peak H_2 content at a low steam flow of $113 \text{ g min}^{-1} \text{ kg}^{-1}$ biochar with 57.7%. Further increases in steam flow led to a decrease of around 1%. The results indicate that the low carbon content of the SSB acted as the limiting factor in the reaction as the steam was already in excess even at low steam flows.

Steam flow mainly affects the following factors (i) rate of reaction and (ii) the extent of hydrocracking. As steam is one of the main reactants in the reaction, its presence or lack thereof affects the rate of reaction of the char-gasification reaction, therefore, at higher steam flows, a more complete reaction will occur in the given time. The presence of steam will also affect the water gas shift reaction, since the excess steam will react with the CO and it will affect the content of hydrocarbons by enabling more hydrocracking to occur. The results in Figure 5.14 can be explained by referring to the above explanations. H_2 content increases with steam flow due to all three factors but in particular, factors (ii) and (iii). At low steam flows, the steam inside the reactor is used up during the char gasification reaction and there is insufficient steam for other reactions such as the forward WGSR to occur. A similar effect occurs to the hydrocarbon content which is reformed further with increases in steam flow.

The results are most similar to those of Ma *et al* [146] who carried out experiments at 900°C and reported that increases in steam led to an increase in H_2 but only until a certain point, after which there were no further increases. The results differ from those of other authors who have reported no unanimous trend with respect to the effects of steam flow on H_2 volume fraction. Yan *et al* [14] carried out

experiments at 850°C and reported that H₂ content increased with steam flow from 0 - 165 g min⁻¹ kg⁻¹ but further increases in steam lead to a decrease in H₂. Chaudhari *et al* [13] carried out experiments at 800°C and reported an optimum H₂ content of 70% at 20.8 g min⁻¹ kg⁻¹ biochar. This decreased to 67% when steam flow was increased to 42 g min⁻¹ kg⁻¹ biochar and remained at that level with further increases in steam flow.

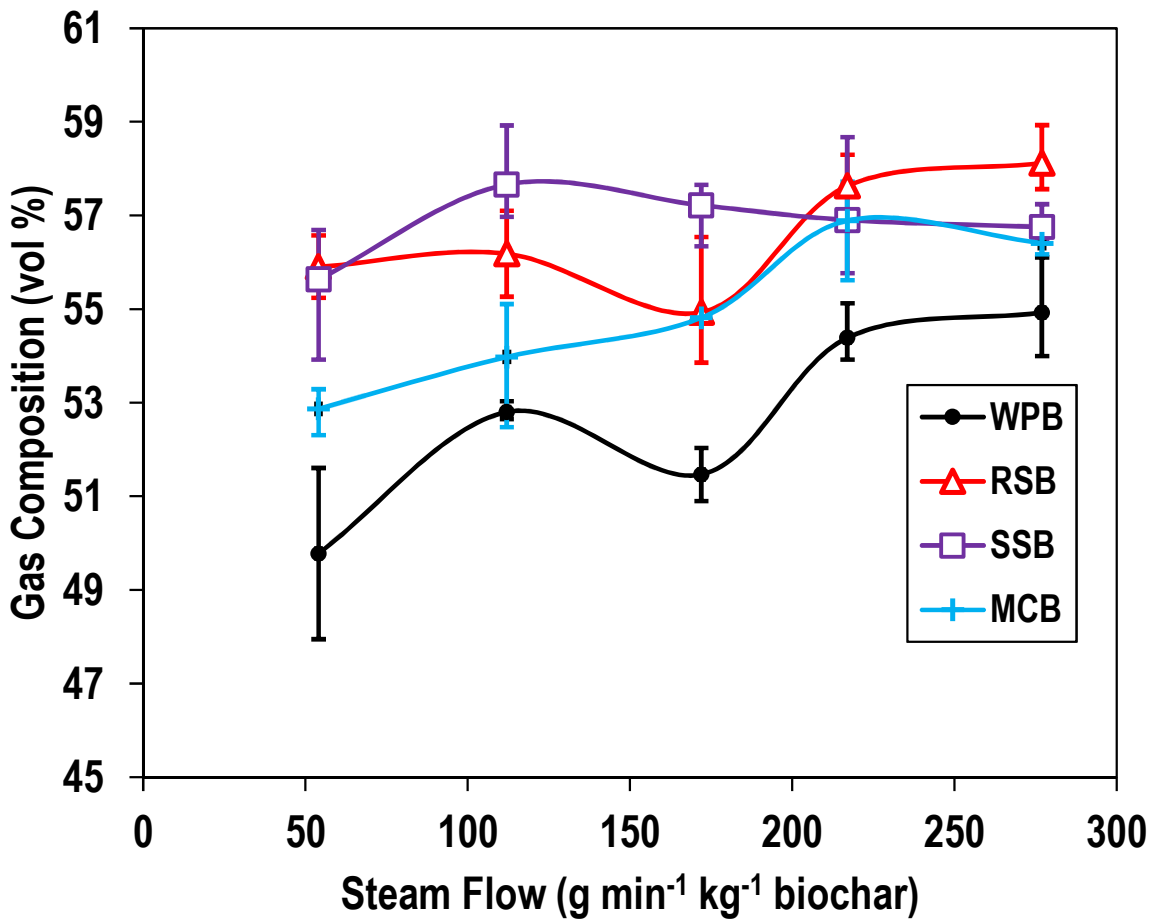


Figure 5.14: Effects of steam flow on the H₂ composition of the syngas from the four biochars at 850°C over a steam flow range of 54 - 277 g min⁻¹ kg⁻¹ biochar

5.8.4 Effects of Steam Flow on Carbon Monoxide Composition

The effects of steam flow on the volume fraction of CO at 850°C are displayed in Figure 5.15. It is observed that the highest CO volume fractions were attained at 54 g min⁻¹ kg⁻¹ biochar and that there is a general decrease in CO content with increasing steam flow. The highest CO volume fraction of 22.9% was given by RSB at 54 g min⁻¹ kg⁻¹ biochar and the lowest at the same steam flow was the WPB with 17.6%. The biggest decrease in CO content was found in RSB with 5.8% whilst the smallest was SSB with 3.4%, from 54 to 277 g min⁻¹ kg⁻¹ biochar. Previous studies have suggested that the forward WGSR stops being the most dominant reaction above 830°C and other reactions such as the Boudouard reaction play a significant role [153]. The presence of excess steam at high steam flows converts the CO into H₂ and CO₂. At low steam flows, the Boudouard reaction consumes some of the CO₂ to form CO.

The results are in agreement with those of Yan *et al* [14] who reported a decrease in CO from 22.45% to 12.47% corresponding to an increase in steam flow from 40 – 357 g min⁻¹ kg⁻¹ biochar. Chaudhari *et al* [13] *et al* gasified two types of biochars; bagasse biochar and commercial biochar. The results are in agreement with commercial biochars but differ from the bagasse biochar which showed an initial increase in CO from 14.8% to 18% corresponding to steam flows of 20.8 and 83.3 g min⁻¹ kg⁻¹ biochar before decreasing to 16.4% at 167 g min⁻¹ kg⁻¹ biochar.

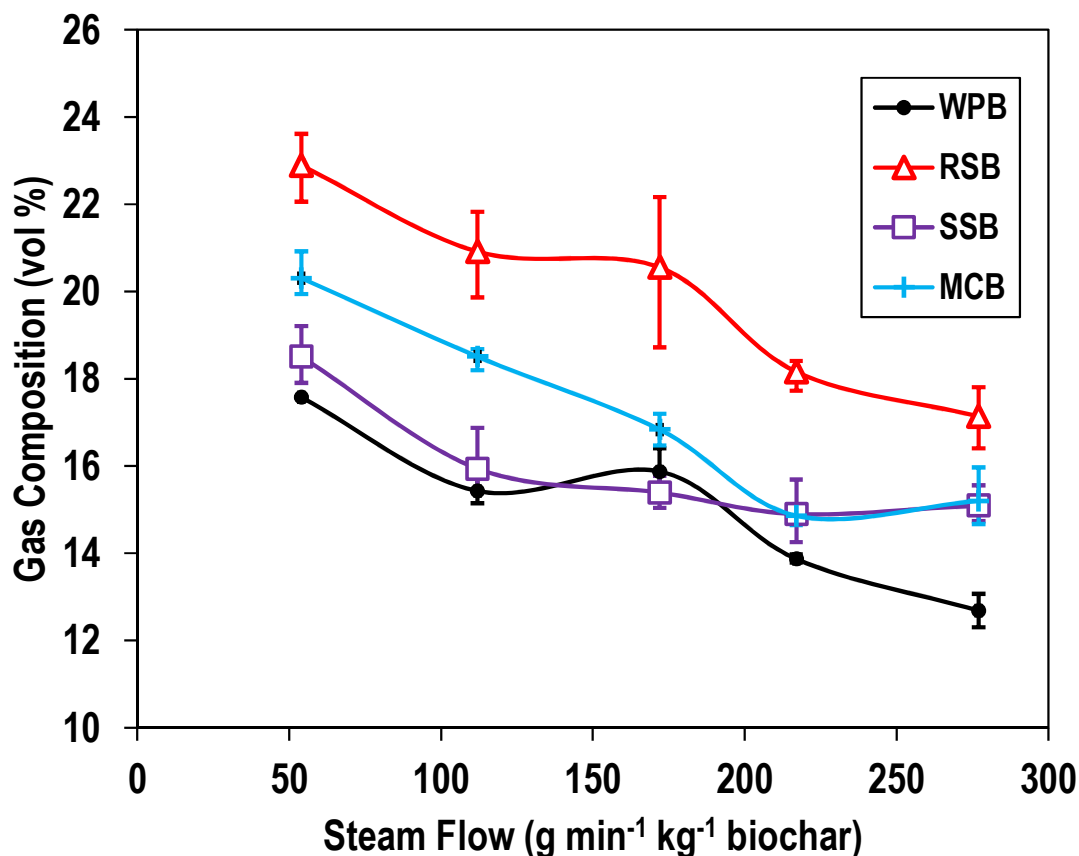


Figure 5.15: Effects of steam flow on the volume fraction of CO at 850°C over a temperature range of 54 - 277 g min⁻¹ kg⁻¹ biochar

5.8.5 Effects of Steam Flow on Carbon Dioxide Composition

Figure 5.16 displays the effect of steam flow on the CO₂ volume fraction at 850°C. It is observed that there was an increase in CO₂ volume fraction with steam flow for all the biochars from 54 to 277 g min⁻¹ kg⁻¹ biochar. The biggest increase was seen in WPB with 5% and the lowest in SSB with 3.4%. The volume fraction of CO₂ tends to level off at 172 g min⁻¹ kg⁻¹ biochar for RSB (22%) and SSB (25%) and 217 g min⁻¹ kg⁻¹ biochar for WPB (23%) and MCB (24.5%). The final CO₂ volume fraction is the result of a mixture of oxidation reactions, Boudouard

reaction and WGSR. In conjunction with the H₂ results, it can be seen that beyond a steam flow of 127 g min⁻¹ kg⁻¹ biochar, the WGSR can no longer shift the remaining CO into CO₂ and H₂.

The results are in good agreement with those of Yan *et al* [14] and Chaudhari *et al* [13]. The former authors reported an increase in CO₂ from 25.8% to 31.1% over a steam flow range of 40 – 357 g min⁻¹ kg⁻¹ biochar. The latter authors reported a similar trend for both bagasse and commercial biochars – both of which showed an increase in CO₂ volume fractions with increasing steam flows.

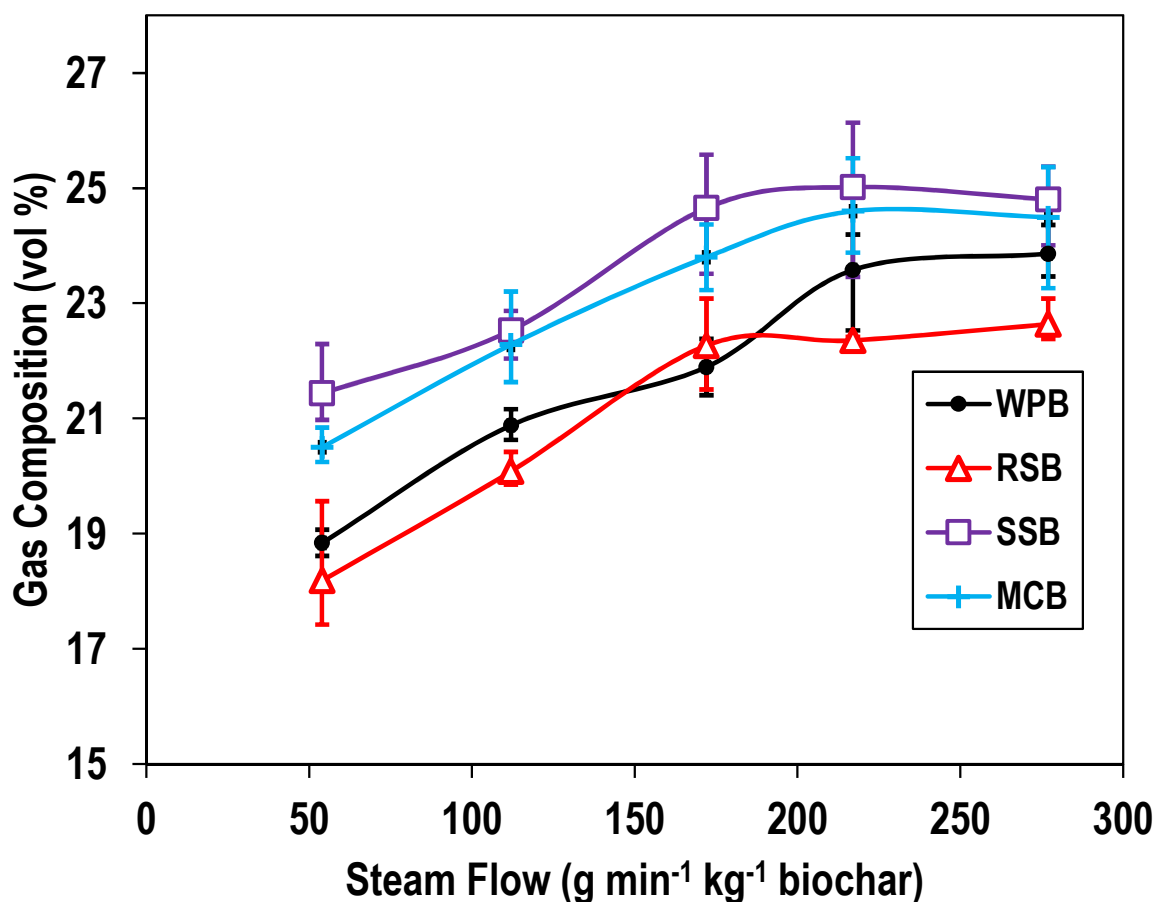


Figure 5.16: Effects of steam flow on the volume fraction of CO₂ at 850°C over a steam flow range of 54 - 277 g min⁻¹ kg⁻¹ biochar

5.8.6 Effects of Steam Flow on Methane Composition

Figure 5.17 displays the effects of steam on CH₄ volume fraction at 850°C. It is observed that all the biochars showed a decrease in CH₄ volume fraction with increasing steam flow. This is the result of two factors; (i) Methanation reactions are unfavoured at 850°C [63] and (ii) steam reforming of CH₄ takes place to produce CO and H₂ which can then partake in further reactions such as the WGSR or the Boudouard reaction. WPB displayed the biggest decrease with 3.9% and RSB the smallest decrease at 0.86% from 54 to 277 g min⁻¹ kg⁻¹ biochar steam flow.

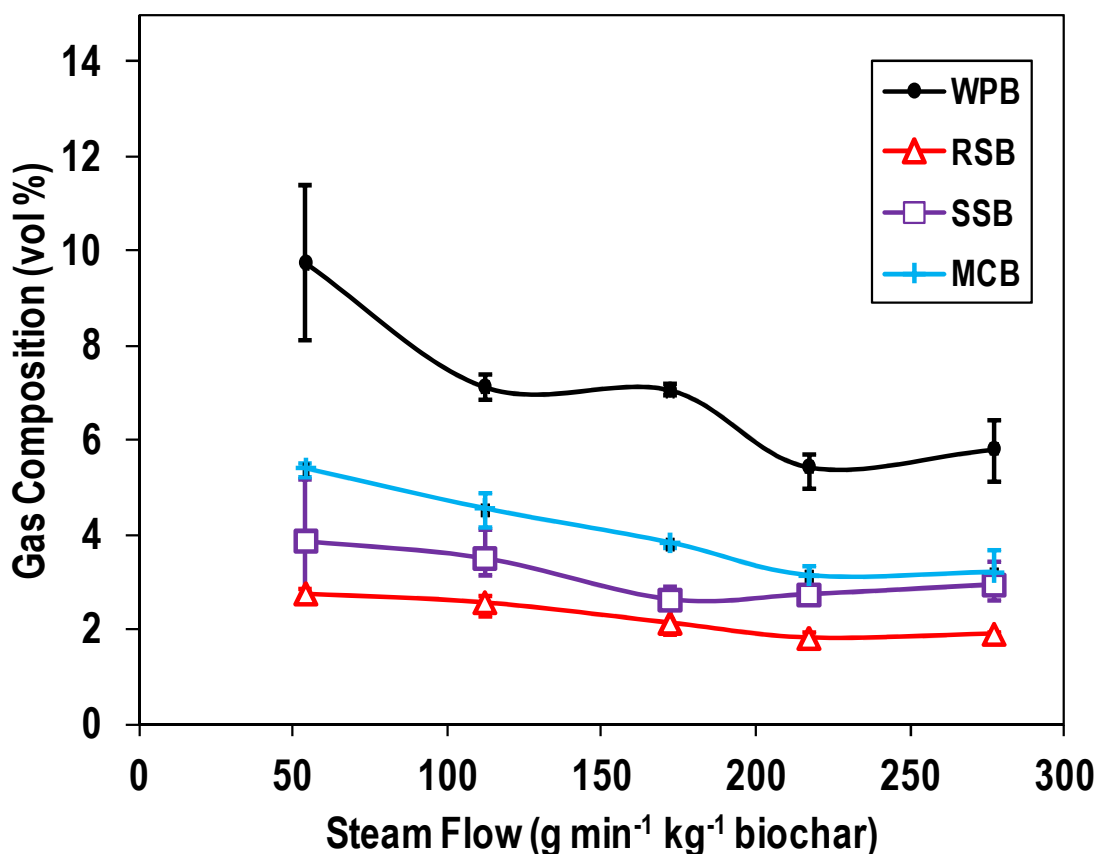


Figure 5.17: Effects of steam flow on the volume fraction of CH₄ at 850°C over a steam flow range of 54 - 277 g min⁻¹ kg⁻¹ biochar

5.8.7 Effects of Steam Flow on Hydrocarbon content, Conversion and Associated Results

Table 5-9: Effects of steam flow on hydrocarbon content, dry gas yield, higher heating value and H₂/CO ratio at 850°C, where S2 and S5 are; 54 and 277 g min⁻¹ kg⁻¹ biochar respectively

	Wood pellet		Rapeseed		Sewage sludge		Miscanthus	
	S2	S5	S2	S5	S2	S5	S2	S5
C₂H₆ Vol%	0.43±0.03	0.27±0.06	0.02		0.05±0.12	0.18±0.14	0.11±0.01	0.05±0.02
C₂H₄ Vol%	3.29±0.35	2.2±0.3	0.25±0.17	0.19±0.1	0.48±0.02	0.22±0.12	0.75±0.07	0.52±0.11
C₂+ Vol%	0.33	0.24±0.03	0.01		0.31±0.01	0.02±0.02	0.05±0.01	0.18±0.19
DGY (m³ kg⁻¹)^a	1.66±0.05	2.58±0.05	1.55±0.03	2.43±0.07	0.78±0.02	1.08±0.02	1.7±0.02	2.46±0.06
HHV (MJ m⁻³)^b	15.12	12.74	11.3	10.5	12.1	10.9	12.08	10.6
H₂/CO ratio	2.83±0.11	4.3±0.23	2.44±0.07	3.39±0.21	3.06±0.2	3.75±0.13	2.60±0.1	3.71±0.19

^a Dry gas yield, see equation 3-6

^b Higher heating value, see equation 3-5

As seen in Table 5-9, there is a slight reduction in the HC content but it is not significant and could be attributed to experimental variation. It is known from Figure 5.13, that the HCs are all produced in the early stages of the reaction and it is also known that the product flowrate is highest during the early stages. Therefore, it might be that the high flowrate does not give sufficient residence time for the thermal or steam reforming of the HCs to occur. The dry gas yield increases significantly with increasing steam flow and the highest DGY of $2.58 \text{ m}^3 \text{ kg}^{-1}$ was given by WPB at $277 \text{ g min}^{-1} \text{ kg}^{-1}$ biochar. The biggest increase was also observed in the WPB with an increase of $0.92 \text{ m}^3 \text{ kg}^{-1}$ from 54 to $277 \text{ g min}^{-1} \text{ kg}^{-1}$ biochar. The increase in DGY is expected since steam is one of the two main reactants in the process. Similar findings were reported in [14] [13].

The higher heating value of the syngas decreases with increasing steam flow. This can attributed mainly to the decrease in CH_4 content which has the highest heating value of the main components in the gas mixture. The smallest decrease was observed in the RSB where the HHV decreased from 11.3 to 10.5 MJ m^{-3} ; the consequence of having the lowest CH_4 content to begin with. The largest decrease was observed in the WPB, for which the HHV decreased from 15.12 to 12.47 MJ m^{-3} , resulting mainly from its 3.9% decrease in CH_4 content.

The H_2/CO ratio increases with increasing steam flow as a result of decreasing CO and increasing H_2 volume fractions. In the present investigation, the WPB was the most suitable for fuel cell use since it gave the highest H_2/CO ratio of 4.3 at $277 \text{ g min}^{-1} \text{ kg}^{-1}$ biochar. The lowest H_2/CO ratio at the same steam flowrate was given by the RSB, making it the least suitable for SOFC use.

5.9 Effects of Steam Flow on Biochar Conversion, Carbon Conversion and Carbon Conversion Efficiency

The same definitions that were used in Chapter 5.6 are used in this section to define biochar conversion, carbon conversion and carbon conversion efficiency. The formulas for working out each one can be seen in Chapter 3.13. As described previously, biochar conversion was calculated using the difference in mass of the biochar before and after the gasification reaction, carbon conversion was calculated by sending the reacted biochar samples to MEDAC Ltd for CHN analysis and carbon conversion efficiency was calculated from the amount of carbon that was calculated in the product gas.

5.9.1 Biochar Conversion

The main objectives of investigating the effects of steam flow were to maximise the yield of H₂ and to obtain the highest conversion of the biochar in order to obtain the maximum yield of gas. Figure 5.18 displays the effects of increasing steam flow from 54 – 277 g min⁻¹ kg⁻¹ biochar on the biochar conversion at 850°C. It can be observed that all the biochars showed an increased in conversion with increasing steam flow but only WPB and SSB showed increased conversion throughout the steam flow range. RSB and MCB achieved their highest conversions at 172 g min⁻¹ kg⁻¹ biochar with 72.2 and 82.8% respectively whilst WPB and SSB achieved 95.5 and 40.1% at 277 g min⁻¹ kg⁻¹ biochar respectively. The WPB and MCB displayed the largest increases in biochar conversion, with WPB increasing by 13.8% and MCB increasing by 13%, whilst RSB and SSB increased by 9 and 6% respectively, from 54 to 277 g min⁻¹ kg⁻¹ biochar. The

results for WPB and SSB are similar to those of Chaudhari *et al* [13] who reported an increase in biochar conversion with steam flow for both bagasse and commercial biochars.

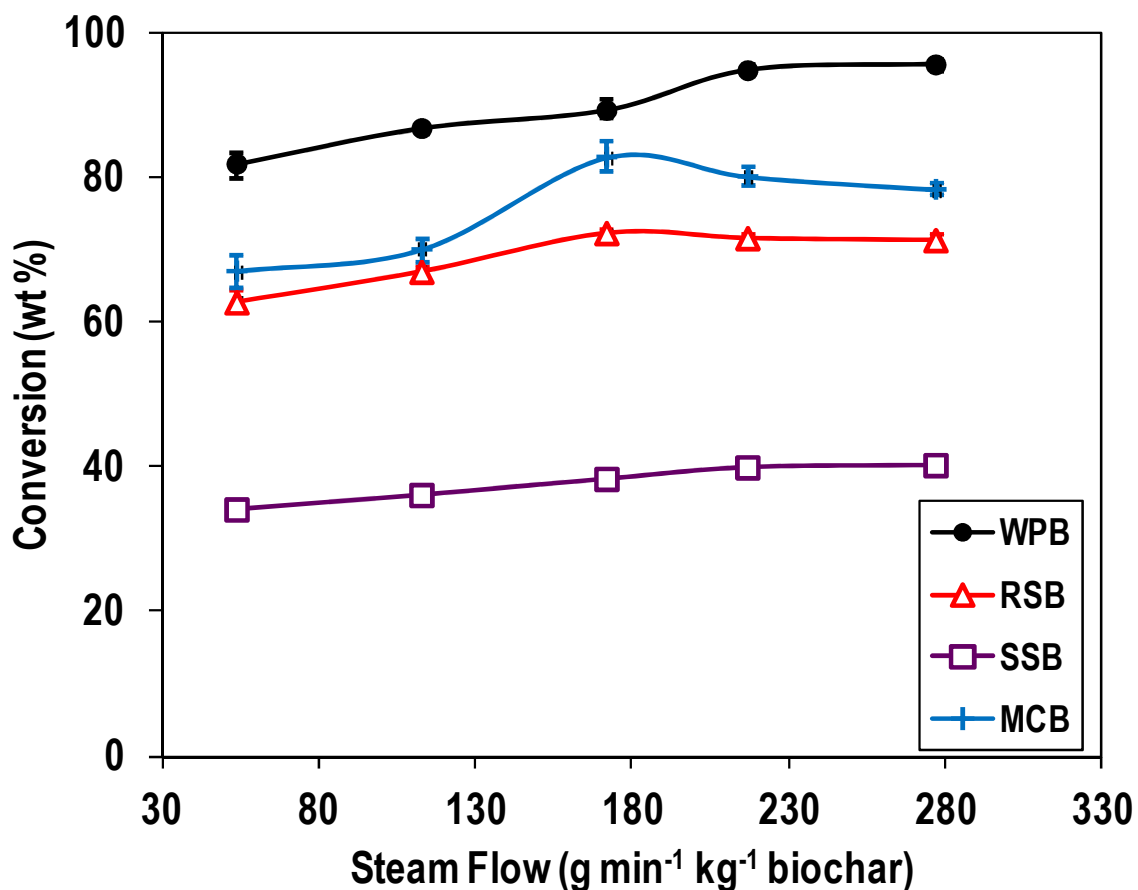


Figure 5.18: Effects of steam flow on the biochar conversion at 850°C over a steam flow range of 54 - 277 g min⁻¹ kg⁻¹ biochar

5.9.2 Carbon Conversion and Carbon Conversion Efficiency

Figure 5.19 displays the effects of increasing steam flow on the carbon conversion and carbon conversion efficiency of the biochars. It can be seen that all the biochars show an increase in carbon conversion with increasing steam flow but

past $172 \text{ g min}^{-1} \text{ kg}^{-1}$ biochar, there is not much change in the carbon conversion. The mechanism for the steam-biochar reaction is that steam reacts with the outer surface first before entering into the pores and reacting with the inside where the surface area is much higher [37]. At low steam flows, steam is the limiting reactant since increasing it leads to an increase in carbon conversion. It is likely that steam is used up during reactions with the carbon active sites on the surface, leaving the inner parts unconverted.

At steam flows above $172 \text{ g min}^{-1} \text{ kg}^{-1}$ biochar, the product flow and gas yield increased but the carbon conversion did not change much. This indicates that the extra product yield is the result of secondary homogenous reactions that take place rather than the primary heterogeneous steam-char reaction. Previous studies have shown that, upon entering the reactor, the biomass devolatilisation process produces permanent gases such as H_2 , CO , CO_2 , CH_4 , C_2H_4 , C_2H_6 and C_3H_8 as well as condensable hydrocarbons collectively known as tar [34]. It is likely that the vaporised tar is involved in secondary reactions with the steam to produce more gases such as CO , H_2 and CO_2 . The increase in DGY and permanent gases leads to an increase in carbon conversion efficiency which increased for all the biochars. MCB consistently displayed the smallest gap between carbon conversion and carbon conversion efficiency with 3.5 and 0.3% of the carbon lost to tar at 54 and $277 \text{ g min}^{-1} \text{ kg}^{-1}$ biochar respectively. This means one of two things; either MCB produced the least amount of tar or that its tar is the easiest to reform. The highest tar content was still given by the WPB which lost 18.9% of its carbon to tar at $277 \text{ g min}^{-1} \text{ kg}^{-1}$ biochar. To overcome this, either a higher steam flow must be used or a catalyst such as dolomite must be employed.

Research has shown that dolomite is able to increase gas yield during biomass gasification by reforming the tars into syngas [154].

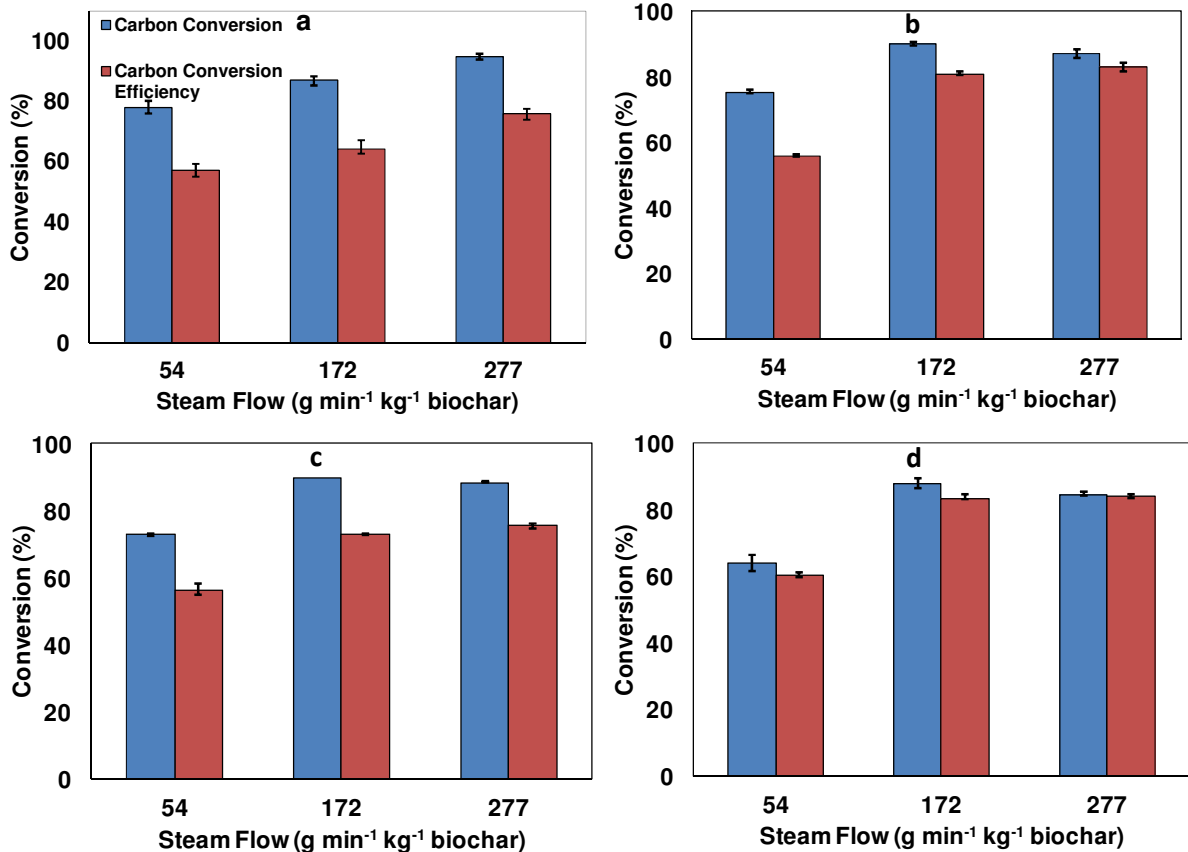


Figure 5.19: Effects of steam flow at 850°C on the carbon conversion, and carbon conversion efficiency of (a) WPB, (b) RSB, (c) SSB and (d) MCB at 54, 172 and 277 g min⁻¹ kg⁻¹ biochar steam flow

5.10 Effect of Steam Flow on Elemental Analysis

Table 5.10 shows the elemental compositions of the biochars post gasification. It can be seen that the elemental contents of the biochars decrease from 54 – 172 g min⁻¹ kg⁻¹ biochar but higher steam flows do not necessarily lead to a decrease in the elemental composition. This indicates that there is a limiting factor that inhibits the biochar from completely reacting. The limiting factor is the slowest

step in the gasification process. It can either be the chemical kinetics of the gasification reactions or the mass transport that the reactions rely upon to bring reactants and remove products to and from the active sites. In fluidised bed gasifiers, chemical kinetics [34] as well as the lack of axial mixing act as the limiting factors, and in this study, it is likely to be mass transport limitations. At the beginning of the process, mass transport is particularly likely to be the limiting factor since char-oxygen reactions are known to be faster than the diffusion processes [34]. The geometry of the sample holder exposes only the top of the biochar to the steam thereby reducing the surface area for the steam-char interactions. Furthermore, the lack of agitation ensures that the biochar particles at the top react fully whilst the ones at the bottom do not as a result of mass transport limitations.

Table 5-10: Effects of temperature on the elemental composition on the wood pellet biochar at 850°C, where S2, S3 and S5 correspond to 54, 172 and 277 g min⁻¹ kg⁻¹ biochar respectively

Constituent	Wood Pellet Biochar		
	S2	S3	S5
C	86.2±0.23	84.6±0.29	82.23±0.06
H	1.29±	1.13±0.09	1.36±0.1
N	<0.1	<0.1	<0.1

Table 5-11: Effects of temperature on the elemental composition on the rapeseed biochar at 850°C, where S2, S3 and S5 correspond to 54, 172 and 277 g min⁻¹ kg⁻¹ biochar respectively

Constituent (wt%)	Rapeseed Biochar		
	S2	S3	S5
C	39.7±0.04	21.7±0.04	27.1±0.7
H	1.3±0.04	<0.1	1.1±0.06
N	1.09	0.73±0.02	0.77±0.04

Table 5-12: Effects of temperature on the elemental composition on the sewage sludge biochar at 850°C, where S2, S3 and S5 correspond to 54, 172 and 277 g min⁻¹ kg⁻¹ biochar respectively

Constituent	Sewage Sludge Biochar		
	S2	S3	S5
C	12.46±0.06	5±0.13	5.8±0.04
H	1.36±0.1	<0.1	<0.1
N	0.37	0.24	0.18

Table 5-13: Effects of temperature on the elemental composition on the miscanthus biochar at 850°C, where S2, S3 and S5 correspond to 54, 172 and 277 g min⁻¹ kg⁻¹ biochar respectively

Constituent	Miscanthus Biochar		
	S2	S3	S5
C	68±0.14	43.7±0.01	45.1±0.6
H	1.1±0.04	<0.1	1.07
N	<0.1	<0.1	<0.1

5.11 Conclusions

Four biochars; wood pellet (WPB), rapeseed (RSB), sewage sludge (SSB) and miscanthus (MCB) were gasified using steam. Two parameters were investigated; effects of temperature and effects of steam flow. To investigate the effects of temperature, the steam flow was kept constant at 172 g min⁻¹ kg⁻¹ biochar and a temperature range of 650 – 850°C was employed. For each reaction, 3g of biochar was used and the solid residence time within the reactor was 30 minutes. To investigate the effects of steam flow, the temperature was kept constant at 850°C and a steam flow range of 54 – 172 g min⁻¹ kg⁻¹ was used. The effects of temperature and steam flow on the transient gas composition and product flows were also investigated.

It was found that the product flow is at its highest in the early stages of the reaction and decreases as the reaction proceeds. The gas composition changes as the reaction proceeds. At lower temperatures, there is a high initial CO₂ content which then decreases rapidly before increasing again to around 30% where it remains for the remainder of the reaction. The H₂ content is very low initially but gradually increases to around 60% during the reaction. At higher temperatures, the initial H₂ content is higher and the rate at which the H₂ reaches around 60% is much faster.

The H₂ content initially increased with temperature from 650 - 700 or 750°C but further increases led to a decrease in H₂ volume fraction for all the biochars except WPB, which showed an increase from 650 – 850°C. The highest H₂ content of 58.7% was given by the RSB at 750°C, indicating the dominance of the forward water gas shift reaction at this temperature. The CO content was at its lowest at 700°C or 750°C before increasing at higher temperatures. The CO₂ content decreased with increasing temperature as the Boudouard reaction began to play a more prominent role and the CH₄ content decreased for all the biochars as a result of additional thermal and hydrocracking of the CH₄. The hydrocarbon (hydrocarbons > CH₄) content decreased with increasing temperature and C₂H₄ was generally the most prominent hydrocarbon. The DGY increased significantly with increasing temperature and miscanthus biochar produced the highest DGY, 2.31 m³ kg⁻¹, at 850°C. The HHV of the syngas decreased with increasing temperature, resulting from the decrease in the CH₄ and hydrocarbon content.

Biochar conversion increased with increasing temperature with WPB attaining the highest conversion at 89 wt%. The carbon conversion and carbon conversion efficiencies also increased with increasing temperatures with RSB and SSB both

attaining 90 wt% carbon conversions. The difference between the carbon conversion and carbon conversion efficiencies was attributed to carbon lost to tar and WPB consistently gave the highest tar contents – losing 22.9% of its carbon to tar at 850°C.

From the steam flow experiments, it was found that the product flow was greatly enhanced with the addition of steam and excess steam such as that used in the 277 g min⁻¹ kg⁻¹ biochar experiment, shifted the product flow profile to the left meaning that the reactions occurred much faster. The transient gas composition changed its behaviour at higher steam flows as the constituents reach a plateau – i.e. a stable composition at a much faster rate than at a lower steam flows.

The H₂ content showed an increase with increasing steam with WPB showing a total increase of 5.1% between 54 – 277 g min⁻¹ kg⁻¹ biochar, resulting mainly from the hydrocarking of its hydrocarbon constituents and the forward water gas shift reaction. The CO content decreased and CO₂ content increased since CO was shifted to H₂ and CO₂ via the forward water gas shift reaction. The CH₄ content decreased with increasing steam flow mainly as a result of steam reforming of the CH₄ into CO and H₂.

The hydrocarbon content displayed a slight decrease with increasing steam flow but did not change too much but the dry gas yield increased significantly with increases in steam flow. WPB attained the highest DGY of 2.58 m³ kg⁻¹ at 277 g min⁻¹ kg⁻¹ biochar and showed a big increase of 0.92 m³ kg⁻¹ with increases in steam flow from 54 – 277 g min⁻¹ kg⁻¹ biochar. The HHV decreased with increasing steam flow – resulting from the decrease in CH₄ content.

6 Effects of Alkali and Alkaline Earth Metallic Species, Dolomite, and Particle Size on Steam Gasification of Biochar

6.1 Chapter Overview

This chapter follows on from Chapter 5 which reported investigations of the various aspects associated with the steam gasification of biochar. The chapter covers three different topics, (i) effects of AAEM species on steam gasification, (ii) effects of particle size and (iii) effects of addition of dolomite. The chapter commences with an investigation into the reactivity of the biochars. Reactivity is defined as mass loss per unit time ($\% \text{ s}^{-1}$) and is an important aspect of the biochars since it determines the rate at which the gasification occurs, thereby affecting the throughput of the gasifier [155]. Reactivity is affected by the presence of AAEM species; hence, the next part of the chapter reports an investigation of the effects of removing the AAEM species from the rapeseed biochar, this being the sample initially containing the highest concentration of AAEM species.

The chapter also reports an investigation of the effects of reducing the particle sizes of the biochars upon the gasification characteristics and considerations are made as to whether or not the energy spent reducing the particle sizes is recuperated from the products. The final part of the chapter reports an investigation of the effects of adding dolomite alongside the biochars during the gasification process. From the previous chapter, it was found that wood pellet biochar produced a large amount of tars that needed cracking – something that could not be achieved with additional steam flows. Previous work has shown dolomite to be an effective catalyst in cracking tars and improving the H_2 yield [154].

6.2 Biochar Reactivity

Reactivity is an important property of the biochars as it describes the rate at which the biochar reacts with respect to conversion. Reactivity of the biochars was calculated using equation 3-7 (page 89), at 850°C. The mass loss was derived using a similar method to that used in [115]. The product flow at time t (Figure 5.1) was multiplied by the corresponding product fractional composition (Figure 5.4) which gave a volumetric product flowrate for each constituent. This enabled the calculation of the carbon use with time which was then used as a measure of mass loss with time (not including carbon lost to tar nor carryover). An example of the procedure can be seen in Appendix II.

Previous work on biochar reactivity has shown an increase in reactivity with conversion [156] [115]. As conversion increased, it led to the opening of new pores which increased surface area and further exposed the catalytic AAEM elements to the steam thus leading to increased reactivity. Figure 6.1 shows the changes in reactivity of the four biochars used in this investigation. The results are in contrast to those in the literature as they show reactivity decreasing with conversion. The difference could arise due to the following factors (i) different types of biochars being used in each of the studies, (ii) method of gasification and heating rate and (iii) volatile matter along with the amount of O in the biochars. The different types of biochars in each study would lead to different results but all four biochars used in this study displayed similar behaviour, leading to the conclusion that it must be the other two factors. The heating rate biochars experience in the reactor plays an important role in its reactivity. For example; Liliedhal and Sjostrom [156] used a thermo balance to calculate the reactivity,

slow heating rates (actual rates are not mentioned) were used in heating the biochar to desired temperature of 850°C. During the heat up stage, volatile matter was lost from the biochar and when the biochar was finally reacted with steam, it was mainly the solid carbon that reacted. In this study, the biochars were introduced into the reactor at 850°C and the high initial reactivity (until 30% conversion) is the result of the volatile matter devolatilising, in conjunction with gasification reactions. Volatile composition also differentiates the results in Figure 6.1 from those of Wu *et al* [115] who produced their biochars at 750°C. Though the authors did not give a proximate analysis, it can be assumed that the biochars had lower volatile contents than those used in this study which were formed at 450 – 500°C. The oxygen contained in the carbonyl and hydroxyl groups enables partial oxidation of carbon to occur which is three to five orders of magnitude faster than the steam-char reaction [37]. Once the O is used up, the reactivity of the chars decrease.

With regards to the four biochars, the highest reactivity was shown by the RSB which may be attributed to its high AAEM content (Table 4-2) and porous structure, enabling the steam to penetrate deep into its pores and products to flow out without much resistance. In contrast, WPB showed the lowest reactivity after its initial devolatilisation has been completed; resulting mainly from its lack of AAEM content and non-porous structure. The lack of pores inhibits the steam from entering into the biochar complex as well as restricting volatiles and products from leaving the biochar. SSB showed a reactivity that was comparable to MCB. This suggests that SSB on its own may not be ideal for gasification but it might be co-gasified with low reactivity biochars such as WPB to enhance their reactivity.

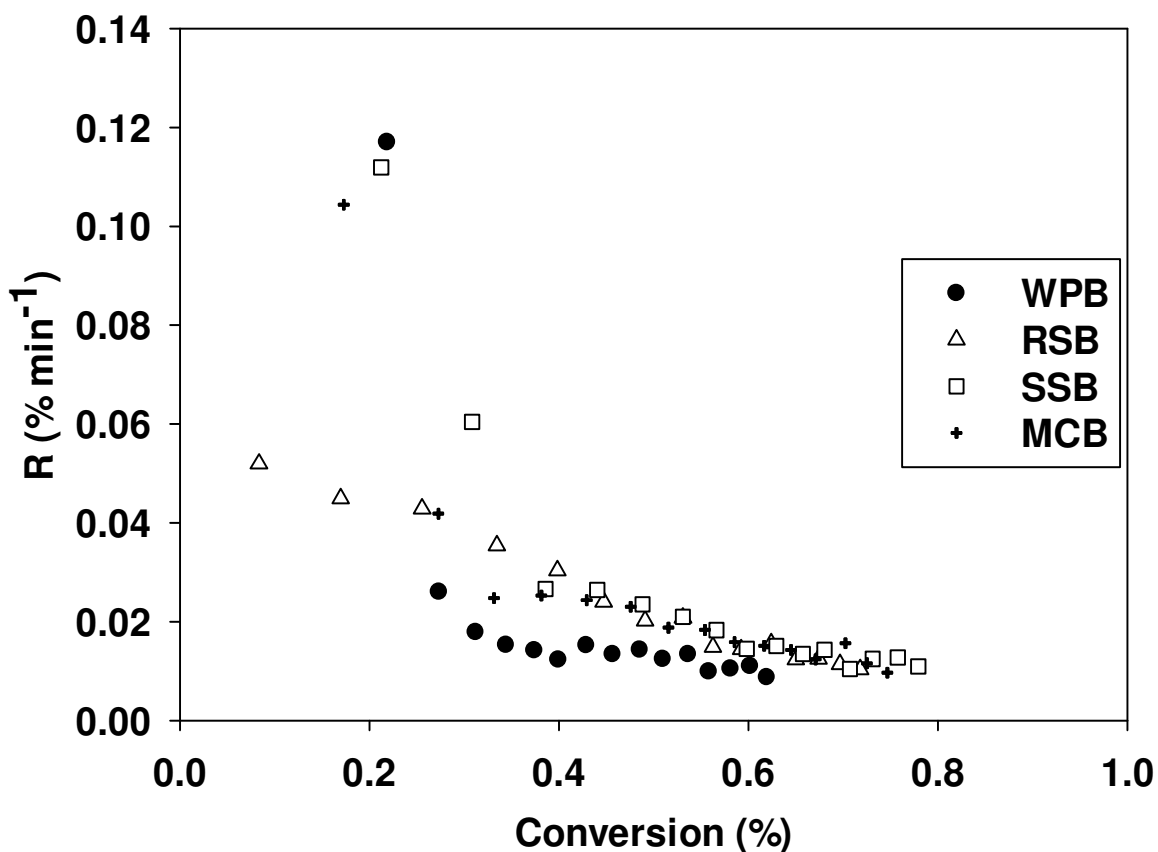


Figure 6.1: Changes in Reactivity with conversion (2 minute average) at 850°C and 172 g min⁻¹ kg⁻¹ biochar, where R is the reactivity

6.3 Effects of Alkali and Alkaline Earth Metallic Species

In the previous section it was demonstrated that the AAEM content of the biochars plays an important catalytic role during the steam gasification process. The extent of the role is not yet clear since different biochars, with different AAEM contents, were compared. To investigate the extent of the role that AAEM contents play and what effect they have on the final composition, the most reactive biochar, namely the RSB was taken and stripped of its AAEM components using concentrated HCl. The process of removing the AAEM species is described in detail in Chapter 3.15.1, but an overview of the process is as follows; the biochars were acid washed using 5 Molar HCl and neutralised using concentrated NaOH. The

neutralised solution was then washed using deionised water to remove the Na⁺ and Cl⁻ ions. X-RF was used to confirm that the vast majority of the salt was removed during the washing with deionised water. The results can be seen in Table 4-4 (page 104) and Table 4-5 (page 104).

The original RSB contained 8.2% Ca, 9.3% K and 5.4% P. Previous work has shown some of these species to be catalytically active [62] [61] with their catalytic activity ranked in the following order; K > Na > Ca [36]. After acid washing, the AAEM content had been reduced to; 2.47% Ca, 0.33% K, 1.46% Fe and 1% P. The removal of the AAEM content led to an increase in the carbon content of the biochar from; 60.25% to 72.36%. As a consequence, the comparison between the original RSB and the RSB_{AW} (acid washed rapeseed biochar) was made using two methods; mass basis (RSB_m) and carbon basis (RSB_c). For the experiments using mass basis, 3 g of biochar was used during gasification as per previous experiments, and for the carbon basis experiments, 2.497 g of biochar was used. Each experiment was carried out as described in Chapter 3.10. As before, a bubble flow meter was used to measure the volumetric product flowrate per minute, and an Agilent 7890A Refinery Gas Analyser was used to determine the product composition.

6.3.1 Effects of Alkali and Alkaline Earth Metallic Species on Product Flow

Figure 6.2 shows the product flows from the original RSB and the acid washed biochars. It is observed that the removal of AAEM species had a major effect on the product flow produced during the reaction. The RSB_m had a higher carbon

input into the gasifier than RSB for the equivalent overall mass, yet its product flow was lower than the original RSB. Whilst for the RSB_c , the product flow was significantly lower than the original RSB, especially in the first 15 minutes. The initial product flow from RSB was higher than the other two; this might have been the result of its higher oxygen content (27.61%) as compared to RSB_{AW} which had; 16.83%, as seen in Table 4-1 and Table 4-5. The lower product flows are the result of two factors (i) lower oxygen content leading to reduced char-oxygen reactions and (ii) lack of AAEM content leading to reduced catalytic activity [36] [62].

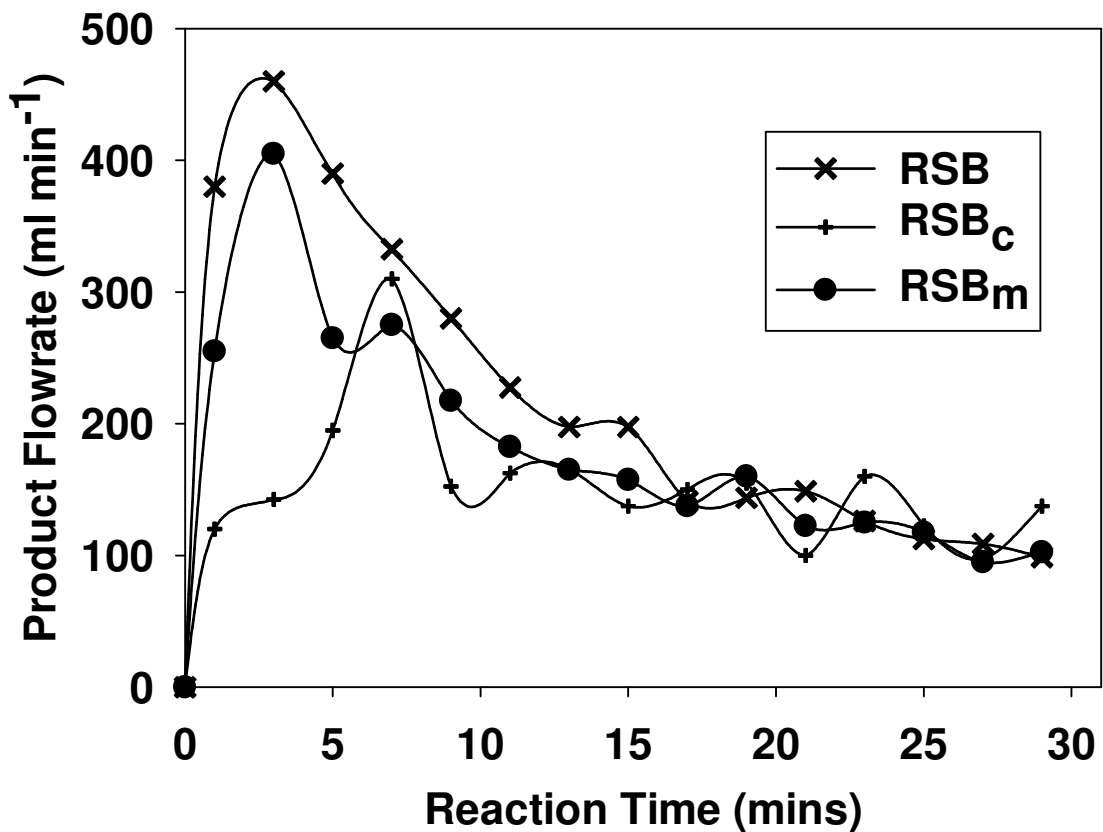


Figure 6.2: Effects of AAEM species on the two minute average product flowrate produced by the rapeseed biochar, where RSB is the original biochar, RSB_c is by carbon basis and RSB_m is by mass basis. Mass basis and carbon basis steam flows = 172 and 285 g min⁻¹ kg⁻¹ biochar.

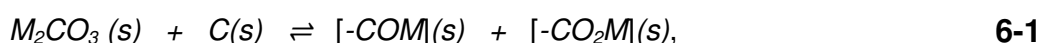
6.3.2 Effect of AAEM Species on Product Composition and Associated Results

Previous authors have focused mainly on the changes in reactivity with the removal of AAEM species from the biochars [62], [36]. Little attention has been given to the changes in the syngas composition with the removal of AAEM species, although it has been suggested that the removal of AAEM species has little effect on the syngas composition [36]. Figure 6.3 (page 177) shows an appreciable difference between compositions resulting from RSB and RSB_m and RSB_c. The H₂ and CO and CO₂ contents are particularly affected by the removal of the AAEM contents but the CH₄ content is relatively unchanged. Both the RSB_m and RSB_c produced a very high H₂ content; 59.4% and 57.2% for RSB_m and RSB_c respectively. The original RSB had a much lower H₂ content at 54% but a higher CO content of 18% compared to the 13.6% and 14.8% of RSB_m and RSB_c respectively.

The differences can be attributed to the effects of the AAEM content since removing these led to a decrease in CO and it is known that the presence of AAEM catalyses the oxygen-char reactions [60]. The alkali components are thought to catalyse the gasification reactions in the following steps. Initially, during the devolatilisation stage, AAEM species are desorbed from the biochar into a vapour phase whilst at the same time, the biochar structure rearranges itself to form micro-crystalline structures. Once vaporised, the alkaline species begin to interact with the biochar leading to their re-adsorption on the biochar surface. The

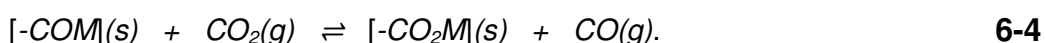
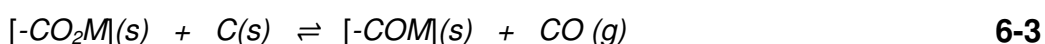
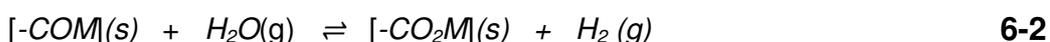
re-adsorbed AAEM along with the residual AAEM participate in the gasification process by lower the activation energy of gasification reactions [157].

The AAEM species participate in the gasification process by an undergoing oxidation-reduction cycle of the carbon substrate to form intermediate alkali-surface compounds. The following reaction scheme has been proposed by some researchers to explain the effects of AAEM species [157]:



where $[-COM]$ is a phenolic alkali metal surface group and $[-CO_2M]$ is a carboxylic alkali metal surface group.

During the steam gasification process, the steam reacts with the intermediate alkali surface on carbon particle to form H_2 and CO via the following reactions:



The AAEM catalyses the forward Boudouard reaction as shown by the above reactions and helps to explain the finding in Figure 5.4 (page 125) which showed that the time taken to the intersection between the curves of CO and CO_2 took more than twice as long for RSB as compared to the other biochars. The intersection represents the point when WGSR overtakes the char-oxygen and Boudouard reactions. The lack of AAEM content in the other biochars ensured that once the oxygen ran out in the biochars, the WGSR dominated the reactions, however, for RSB, this was not the case since the catalysis of the Boudouard reaction ensured that CO production continued longer into the reaction.

As the rate of the gasification reactions depend on the presence of AAEM species, the biochar may be susceptible to deactivation, particularly if slower heating rates are used as it would enable volatile matter to devolatilise and then condense within the biochar matrix. This will reduce the exposure of the AAEM species to the reactants. This is not expected to be a big problem in high heating rate environments such as the one used in this study. Furthermore, although carbon deposition on the biochar surface may block pores, newer pores are created during the gasification process that maintain the biochar reactivity, and so long as the rate of gasification is faster than the rate of carbon deposition, the biochar will maintain its reactivity [158].

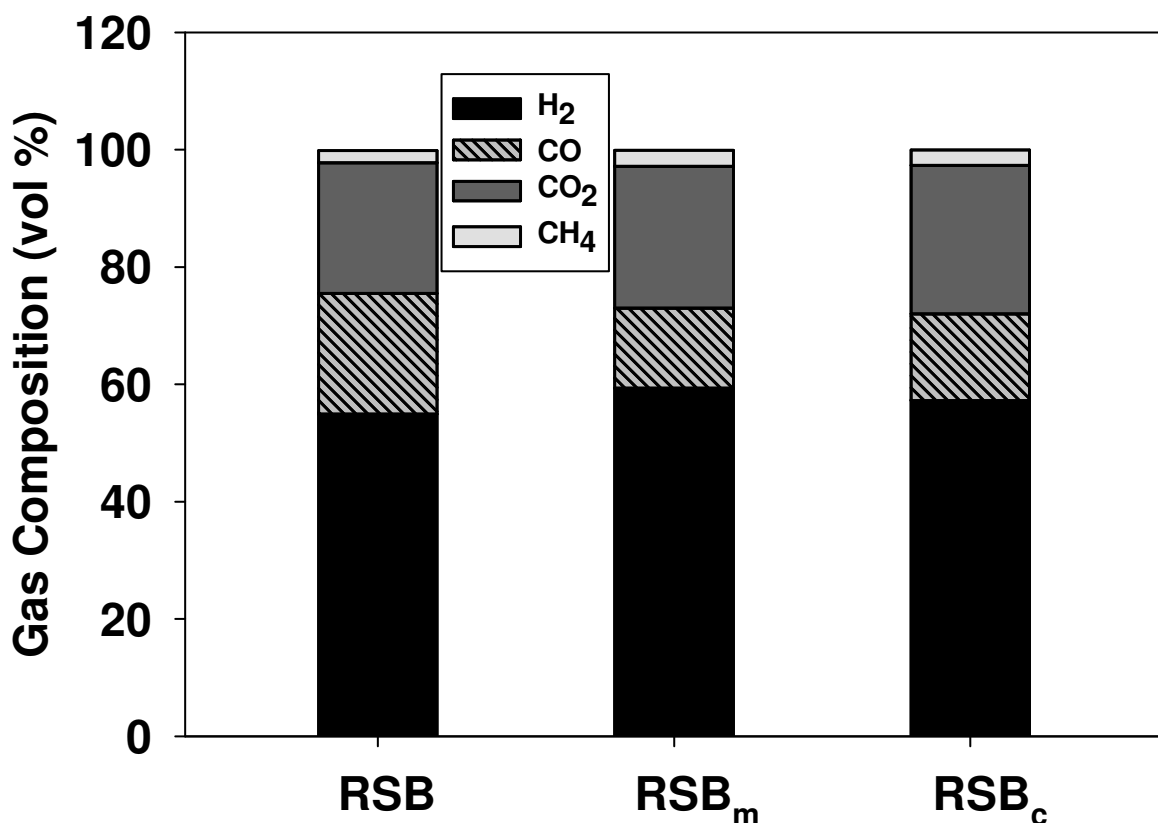


Figure 6.3: Effects of removal of AAEM species from Rapeseed biochar at 850°C and a steam flow of 0.516 g min⁻¹, corresponding to 172 g min⁻¹ kg⁻¹ biochar on a mass basis and 285 g min⁻¹ kg⁻¹ carbon on a carbon basis. RSB_m and RSB_c refer to mass and carbon basis respectively

Table 6-1: Effects of AAEM removal on carbon conversion, carbon conversion efficiency, H₂/CO ratio and higher heating values at 850°C.

	RSB	RSB_m	RSB_c
DGY (m ³ kg ⁻¹)	2.23 ± 0.01	1.9 ± 0.02	2.09 ± 0.05
CCE (%)	80.98 ± 0.76	52.37 ± 1.92	60.66 ± 1.02
H ₂ /CO ratio	2.6 ± 0.12	4.36 ± 0.06	3.86 ± 0.02
HHV (MJ m ⁻³)	10.5 ± 0.06	10.44 ± 0.16	10.26 ± 0.12

where RSB_m and RSB_c refer to steam flow by mass and carbon basis, respectively. RSB_m = 172 g min⁻¹ kg⁻¹ biochar, RSB_c = 285 g min⁻¹ kg⁻¹ carbon

Table 6-1 displays the effects of the removal of AAEM content on the DGY, CCE, H₂/CO ratio and HHV. It is observed that the DGY was reduced significantly when the AAEM content was removed – from 2.23 m³ kg⁻¹ to 1.9 m³ kg⁻¹ on a mass basis and 2.09 m³ kg⁻¹ on a carbon basis. The reduction can be attributed to the slower reaction rates which lead to the biochars requiring a longer solid residence time in the reactor to achieve the same conversion. Previous authors have linked the presence of AAEM species to the overall efficiency of the gasification process since it relies directly on char reactivity [159]. The results in Table 6-1 confirm this link as a lower DGY led to lower carbon conversion efficiencies. The H₂/CO ratio increased as a result of the removal of AAEM species with H₂ increasing and CO decreasing. An advantage of this is that the syngas becomes more suitable for use in SOFCs, however, the volume of the syngas produced was lower so the efficiency of the gasification process would be lower. Finally, there was an inconsequential effect on the HHV of the syngas since the CO was replaced with H₂ which has a similar HHV (on a volumetric basis). The lower heating value

(LHV) or net heating value will be lower since it accounts for the energy lost as a result of the heat of vaporisation of H₂O which is produced from the combustion of H₂.

6.4 Effects of Particle Size on the Steam Gasification of Biochar

All the results presented in the thesis so far have used the biochars in their original state, as received. This was done to investigate; (i) the effects of inconsistent particle sizes, (ii) the selection of biochars most suitable for gasification and (iii) their effects on efficiency. Smaller and more consistent particle sizes might be expected to lead to faster reaction rates, owing to larger surface area and consistent product in terms of product flow and composition. However, grinding of particles is an energy intensive process, it is estimated that 50 kWh of energy is required to grind one tonne of biomass [20]. Therefore, it is essential to know if the energy used in grinding the biochars can be recouped via improvements in product, whether it is product yield or composition.

To investigate the effects of particle size, the biochars were ground down using a pestle and mortar and sieved through 300 µm mesh openings. 3 g of the biochars were gasified using the procedure described in Chapter 3.12, at a steam flow 172 g min⁻¹ kg⁻¹ biochar. Only the RSB, MCB and SSB could be sieved and were therefore gasified for the particle size investigation. The WPB could not be sieved due to particle coalescence.

6.4.1 Effects of Particle Size on Product Flowrate

Figure 6.4 displays the effects of particle size on the product flow of the RSB, SSB and MCB at 850°C and 172 g min⁻¹ kg⁻¹ biochar. It is shown that changing the particle sizes made very little difference to the product flow of RSB and slight differences to the SSB and MCB. The product flow is a representation of the rate of reaction, therefore a higher flowrate translates to a faster rate of reaction. The biggest difference was seen in the devolatilisation stage of the MCB, which was less severe with decreased particle sizes, the peak flowrate being lower and taking place over a slightly longer duration than the uncrushed particles. However, it might be the result of experimental error which was ±200 ml min⁻¹ for MCB in the devolatilisation stage and ±20 ml min⁻¹ thereafter. SSB was the only biochar where a sustained increase in product flow was observed as a result of decreasing particle sizes. In its original form, the SSB pellets were very dense, making it more difficult for steam to penetrate through, but once ground down, the smaller particles with higher surface/volume ratio provides less resistance for the steam to penetrate through their structure, leading to increased reaction rates. Contrary to this, the RSB originally had a very porous structure that allowed steam to penetrate it with ease, once it was crushed; the porous structure of the biochar was destroyed. Any increase in reaction rate would be counteracted by the decrease in the rate of mass transport through the biochar complex, hence, leading to similar results.

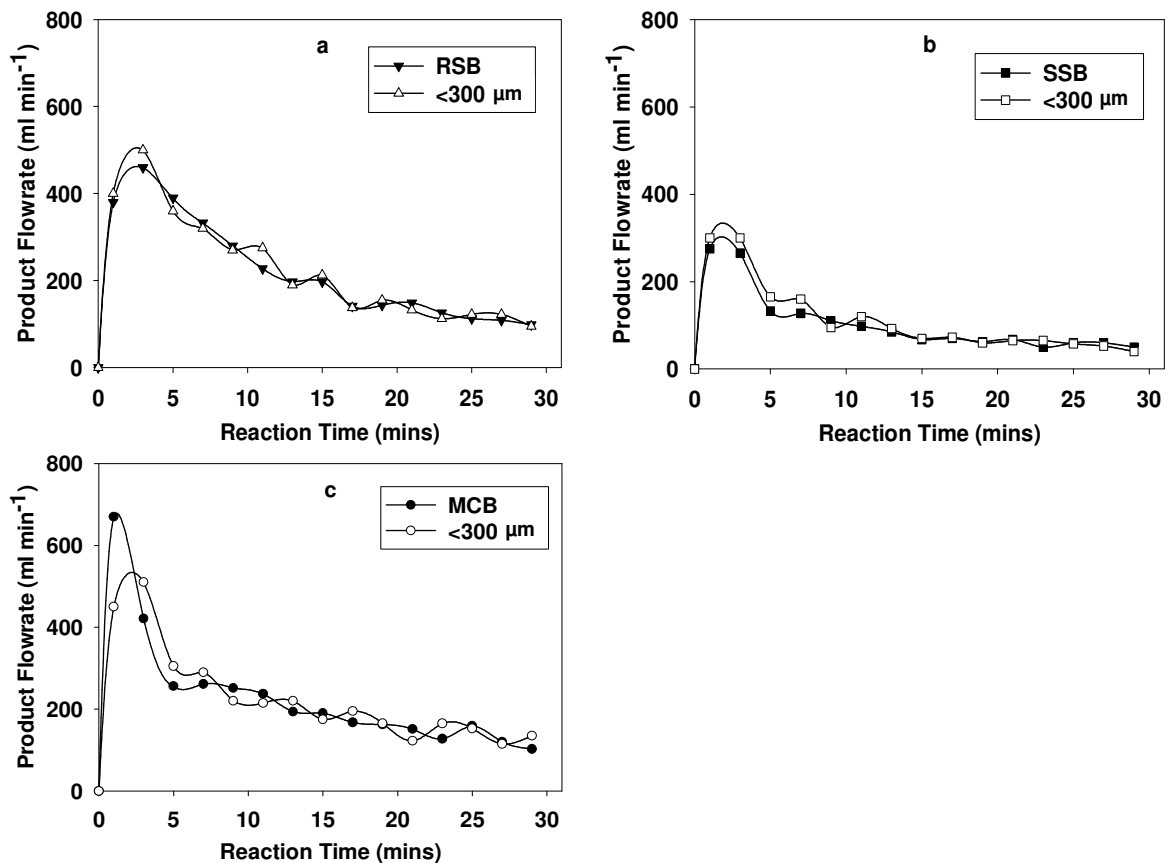


Figure 6.4: Effect of particle size on product flowrate (2 minute average) at 850°C and 172 g min⁻¹ kg⁻¹ biochar, where (a) RSB, (b) SSB and (c) MCB

6.4.2 Effects of Particle Size on Product Composition, Carbon Conversion Efficiency and Associated Results

Figure 6.5 displays the effects of reducing particle size on the product composition of RSB, SSB and MCB at 172 g min⁻¹ kg⁻¹ biochar. It can be seen that there was very little change in the composition of the syngas since all the biochars gave virtually the same composition when particles sizes were reduced. The results are in agreement with previous work which has shown that changes in particle size has little effect on the syngas composition at high temperatures [54]. The syngas composition is the result of many competing reactions – the rates of which may be

affected by the change in particle sizes but the types of reactions that occur are not affected, hence the composition remains unchanged.

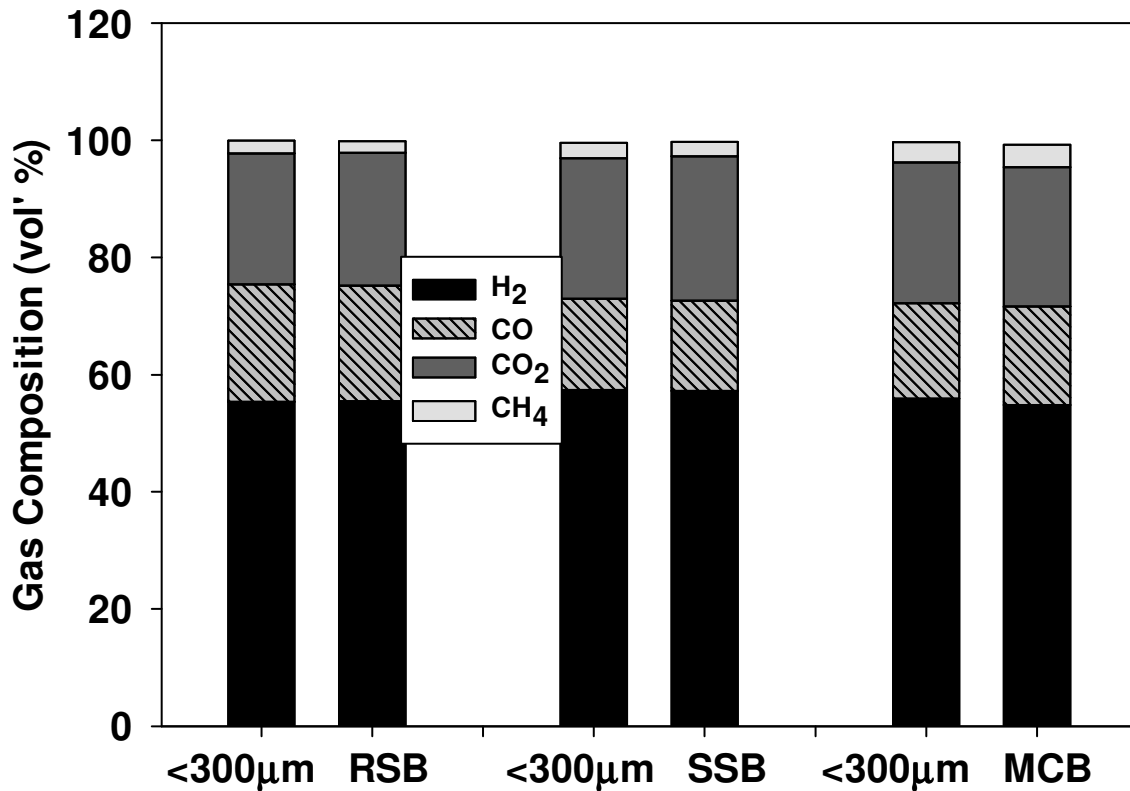


Figure 6.5: Effects of particle size on syngas composition at 850°C and a steam flowrate of 172 g min⁻¹ kg⁻¹ biochar

It can be seen in Table 6-2 that changing the particle size from normal to <300 µm had virtually no effect on the hydrocarbon content, however, it did lead to a slight increase in DGY for RSB and SSB, with SSB experiencing the biggest increase of 0.09 m³ kg⁻¹. The CCEs improved slightly for RSB and SSB as a result of the increased DGY but it decreased for MCB, resulting mainly from its slight increase in H₂ content and decrease in CH₄ content.

Table 6-2: Effects of particle size on hydrocarbon content, dry gas yield, carbon conversion efficiency, H₂/CO ratio and higher heating values for rapeseed, sewage sludge and miscanthus biochars at 850°C and 172 g min⁻¹ kg⁻¹ biochar steam flow

	RSB	< 300 μm	SSB	< 300 μm	MCB	< 300 μm
C ₂ H ₆ (vol%)			0.03	0.05±0.81	0.35±0.3	0.04
C ₂ H ₄ (vol%)	0.12	0.04	0.24	0.32±0.09	0.35±0.1	0.23
C ₂ + (vol%)				0.03±0.03	0.03	
DGY (m ³ kg ⁻¹)	2.23±0.01	2.29±0.02	1.05±0.03	1.14	2.3±0.02	2.3±0.01
CCE (%)	80.98±0.76	82.3±0.61	73.1±0.09	78.9±0.82	82.5±1.5	78.6±0.98
H ₂ /CO ratio	2.6±0.12	2.75±0.15	3.7±0.1	3.7±0.012	3.3±0.07	3.68±0.04
HHV (MJ m ⁻³)	10.5±0.06	10.5	11.1	10.6	10.4	10.8

where DGY is dry gas yield

CCE is carbon conversion efficiency

HHV is higher heating value

6.5 Effects of Dolomite

In Chapter 5, it was suggested that the gasification of WPB might benefit from the addition of a catalyst such as dolomite. The WPB produced the highest tar content and even at a steam flowrate of $277 \text{ g min}^{-1} \text{ kg}^{-1}$ biochar, 18.9% of its original carbon input was lost to tar. Previous work has revealed that dolomite can improve DGY as well as increase the yield of H_2 [154] [160]. To investigate if H_2 yield can be increased with the addition of dolomite, a dolomite sample mined in Derbyshire was added alongside the biochars. The characterisation of the dolomite is displayed in Chapter 4.4. The experiments were split into two types; (i) effects of dolomite content and (ii) effects of calcination of the dolomite. To investigate the effects of dolomite content, the following masses of the dolomite and calcined dolomite were added; 5, 10 and 15 wt% or 0.15, 0.3 and 0.45 g of dolomite, respectively, in addition to the 3 g of biochar. To study the effects of calcination, dolomite calcined at 900°C in an inert N_2 atmosphere using a steam flow of 0.162 g min^{-1} was added in the aforementioned masses. The gasification experiments were carried out at two different steam flows; 172 and $277 \text{ g min}^{-1} \text{ kg}^{-1}$ biochar. The two dolomite are differentiated as natural dolomite, ND, (referring to uncalcined dolomite) and calcined dolomite, CD.

6.6 Effects of Dolomite on Product Composition

From Figure 6.6, it can be observed that at a steam flow of $172 \text{ g min}^{-1} \text{ kg}^{-1}$ biochar, the dolomite had little impact on the product composition. The biggest change was observed with natural dolomite (Figure 6.6a) where the CO_2 volume fraction increased by up to 2% and the H_2 volume fraction decreased by up to 2% with 0 to

15 wt% dolomite. For calcined dolomite, there was almost no difference throughout the content range as the product composition remained unchanged. At a steam flow of $277 \text{ g min}^{-1} \text{ kg}^{-1}$ biochar, the natural dolomite again showed a decrease in H_2 content from 54.9 to 52.2% at 0 and 15 wt% respectively. Similarly, it was also accompanied by an increase in CO_2 content, from 23.9 to 25.8%. The effect of the calcined dolomite again showed virtually no change as the product composition remained the same throughout the dolomite content range.

The increase in CO_2 content can be explained by the release of CO_2 during dolomite decomposition which starts at temperatures of around 600°C [49] according to the equations 2-25 and 2-26 (page 31) and can be seen in Figure 4.3. The other constituents all remained relatively unchanged apart from H_2 , which decreased. The calcined dolomite has two methods by which it can improve the H_2 yield. Firstly, it can improve it by catalysing cracking reactions of hydrocarbons and secondly it can improve it by adsorbing the CO_2 from the syngas mixture. Calcined dolomite has been used as a medium for CO_2 capture [161] [162] [163] to improve syngas heating values and increase H_2 yield. It is likely that the temperature used in the gasification experiments was too high for the adsorption reaction, and therefore the calcined dolomite could not adsorb any CO_2 .

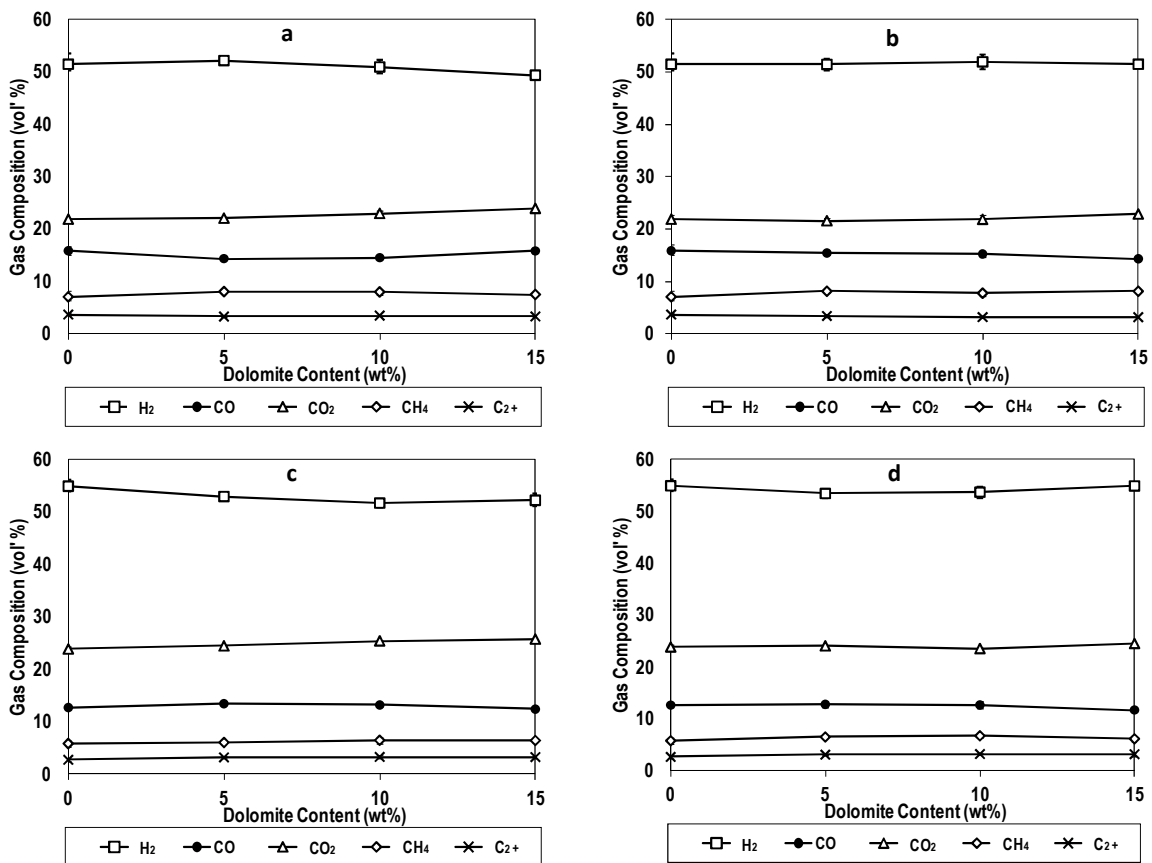


Figure 6.6: Effects of the addition of natural and calcined dolomite to wood pellet biochar at 850°C at two different steam flows, where (a) natural dolomite at 172 g min⁻¹ kg⁻¹ biochar steam flow, (b) calcined dolomite at the same steam flow, (c) natural dolomite at 277 g min⁻¹ kg⁻¹ biochar steam flow and (d) calcined dolomite at the same steam flowrate

Since there is little change in the composition of the syngas, especially for calcined dolomite, another way of quantifying whether or not the dolomite/calcined dolomite had any effect of the gasification process is to analyse the dry gas yield. This is shown in Figure 6.7. It is observed that the addition of dolomite had a significant effect on the dry gas yield at both 172 and 277 g min⁻¹ kg⁻¹ biochar. At the lower steam flowrate, the DGY at 0 wt% dolomite was 2 m³ kg⁻¹, this increased to 2.2 and 2.18 m³ kg⁻¹ for natural and calcined dolomites respectively. The 0.53 L of extra gas that was produced during the natural dolomite reaction was far more than the

expected ~ 0.114 L that would have been released from the decomposition of dolomite. This could be the result of the combination of catalytic activity enhancing tar cracking as well as the excess CO_2 reacting with deposited carbon to produce CO via the Boudouard reaction. The addition of dolomite led to a decrease in DGY at $277 \text{ g min}^{-1} \text{ kg}^{-1}$ biochar. The DGY with the original WPB of $2.58 \text{ m}^3 \text{ kg}^{-1}$ was higher than the $2.48 \text{ m}^3 \text{ kg}^{-1}$ obtained from both calcined and uncalcined dolomites at 15 wt%.

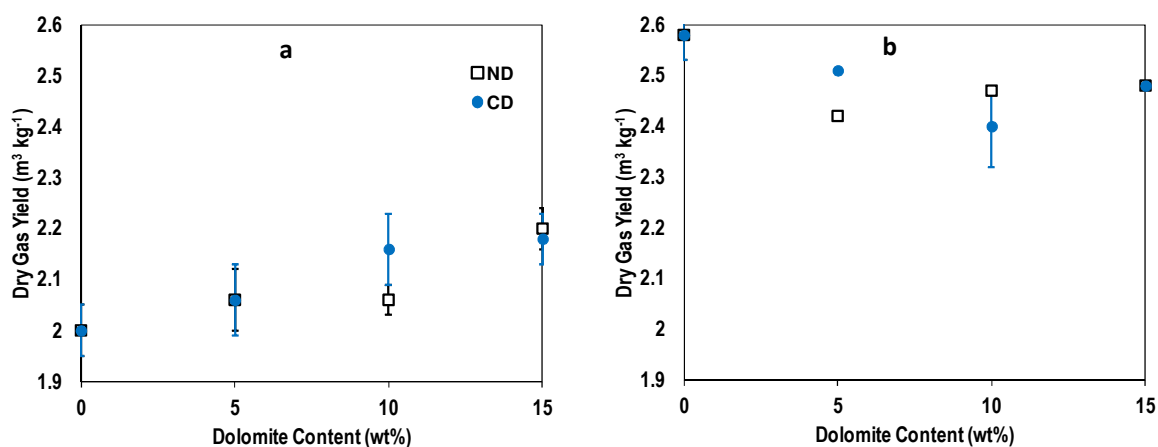
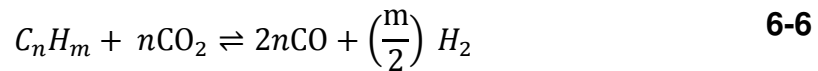
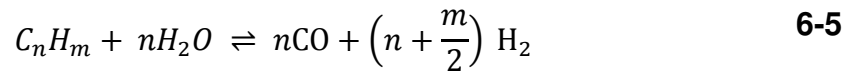


Figure 6.7: Effects of Dolomite on the dry gas yield from WPB at 850°C and steam flows of (a) 172 and (b) 277 g min⁻¹ kg⁻¹ biochar respectively, where ND is natural dolomite and CD is calcined dolomite

Calcination of dolomite reduced its density from 1.55 to 0.87 kg m^{-3} as seen in Table 4-10 (page 111); therefore, a larger volume was required to satisfy the mass content used in the experiments. Previous authors have suggested different components within dolomite are responsible for the catalysis. For example, some have suggested that oxides of metals such as Fe (Fe_2O_3) [154] are responsible for the catalysis, whilst others have suggested CaO as the catalytically active component [136]. Either way, a greater quantity of both went into the reactor when

calcined dolomite was used. For example, natural dolomite contained 0.51 wt% Fe whilst calcined dolomite contained 0.91 wt% Fe. It is thought that the dolomite enhances the steam-char and steam-tar reactions [45], if this is so then the reaction mechanism will be similar to that described in Chapter 6.3.2. The dolomite can break up the tar via the reactions shown below [154], this could be one of the reason why the composition does not change since the break-down of the tars lead to the constituents of the syngas.



The results from the 172 g min⁻¹ kg⁻¹ biochar experiments are most similar to those Delgado *et al* [164] who gasified pine sawdust in a fluidised bed gasifier and reported that the addition of dolomite led to an improvement in the DGY from 1.15 to 1.8 m³ kg⁻¹ but there was no significant effect on the H₂ or CO yield. They differ from those of He *at al* [160] who gasified municipal solid waste at 950°C using steam and dolomite and reported that the H₂ content increased from 28 to 53% with the addition of dolomite and the DGY increased from 0.51 to 1.65 m³ kg⁻¹.

6.7 Conclusions

The aim of this chapter was to increase the understanding of the gasification process and to increase the yield of hydrogen in the syngas. The chapter began with a study of the reactivity of the biochars, which was calculated as the loss of mass derived from the combination of product gas flowrate and its transient composition. It was

found that contrary to what has been reported previously, the reactivity actually decreases as conversion increases due to the changes in the reaction mechanisms that occur during the reaction. The RSB was found to be the most reactive biochar as a result of its high AAEM content and the WPB was the least reactive, resulting from its low AAEM content.

To investigate the effects of the AAEM content, the RSB was washed with concentrated HCl to remove its mineral matter. It was then gasified as before using two metrics for steam flow comparisons; (i) by mass and (ii) carbon content. It was found that the removal of AAEM content drastically reduced the flowrate produced by the biochars, making them less reactive and leading to a decreased DGY. It also changed the final syngas composition since the AAEM content catalyses the char-oxygen and Bourouard reactions to produce CO. The lack of CO led to an increase in H₂ and CO₂ composition in the final syngas.

The chapter also explored whether or not it is worth crushing the biochars to form smaller, more uniform particles. This would be needed if the biochar is going to be used in a fluidised bed gasifier. It was concluded that the energy required to crush the biochars is not worth the additional expenditure to the paltry gains in dry gas yield that may arise as a result. This also leads to the conclusion that the biochars are more suited to a fixed bed gasifier, in particular, an updraft gasifier. The low volatile content, coupled with the fact that updraft gasifiers are not so sensitive to particle sizes makes it an ideal reactor. The changes in particle sizes had no effect on the syngas composition for all the biochars. This was due to the ability of the particle sizes to affect the rate of reaction but not the types of reactions that occur, which is the main factor in determining the final composition. Finally, the chapter explored

whether or not dolomite, from Derbyshire, can act as a catalyst to improve H₂ content in the syngas and improve dry gas yield. It was found that the addition of dolomite (uncalcined and calcined) to WPB increased DGY but made very little change to the composition of the syngas, with natural (uncalcined) dolomite reducing the H₂ content by 2% and calcined dolomite having no effect on the final composition. The increase in dry gas yield was attributed to increased cracking of higher molecular weight tars.

7 Performance of Solid Oxide Fuel Cells using Syngas from Steam Gasification of Biochar

7.1 Chapter Overview

Previous chapters have all focused on the generation of a syngas and optimisation of the conditions to maximise the content of H₂. This chapter explores the applicability of the syngas in a microtubular SOFC. The chapter begins by comparing the performance of the SOFC using syngas from WPB and RSB. These two feeds produced a gas with strongly differing compositions when it came to assessing their suitability for use in a SOFC. The RSB produced a low H₂/CO ratio whilst the WPB produced a high H₂/CO ratio gas. The chapter ends with a summary of the mass and energy balances for the process.

7.2 Introduction

From Chapter 5, it was shown that the steam gasification of intermediate pyrolysis biochars produced a gas with a high content of H₂. Optimal H₂ content was achieved at 850°C and using a steam flow of 277 g min⁻¹ kg⁻¹ biochar, with RSB producing the highest volume fraction at 58.1%. Previous experiments have shown that syngas from biomass gasification can be successfully utilised in a SOFC without any major loss of performance [70] [71] [72] [73]. The aforementioned studies were all carried out using conventional biomass and continuous gasifiers. There is a scarcity of work that investigates the performance of a SOFC using biochar-derived syngas. With this in mind, the aims of this chapter are thus; (i) to investigate the use of biochar-

derived-syngas in a SOFC, (ii) investigate which of the two, WPB or RSB produces a gas that is most suitable for use in SOFCs and (iii) to carry out an extended study to analyse the performance loss of the SOFC over the duration of the experiment. All the previous studies were carried out using continuous gasifiers; a side aim of the chapter is to verify a simple method that can be used to couple bench scale gasifiers to SOFCs.

7.3 Steam Gasification Experiments

The selection of the biochar feed for the SOFC experiments was based on the data presented in the previous chapters. It was decided that although calcined dolomite increased product yield, it did not change the composition of the syngas, therefore, dolomite was not added to the biochar to produce the gas that would be used in the SOFC. The criteria to choose the feed were based on the following specifications; (i) H₂ content, (ii) H₂/CO ratio and (iii) dry gas yield. A steam flow of 277 g min⁻¹ kg⁻¹ biochar was chosen, since this steam flow generally gave the highest H₂ contents and the highest DGYs.

Table 7-1 shows the syngas information from each of the biochars at 850°C and a steam flow of 277 g min⁻¹ kg⁻¹ biochar. It can be seen that the highest H₂ content was given by the RSB, whilst the lowest was WPB. The SSB gave the lowest DGY, therefore it was not suitable for the SOFC experiments since it produced too little product to last the duration of the experiment. Product gas with a high H₂/CO ratio is most suitable for SOFC use [12], therefore, WPB is most suitable in this regard and RSB the least suitable. Taking these factors into account, it was decided that the

RSB and WPB would be used for SOFC operation since they should give differing results.

Table 7-1: Syngas compositions on a N₂-free basis.

Biochar	H ₂	CO	CO ₂	CH ₄	C ₂ H ₆	C ₂ H ₄	C ₃ H ₆	DGY (m ³ kg ⁻¹)	H ₂ /CO ratio
WPB	54.92	12.68	23.86	5.82	0.27	2.20	0.24	2.58	4.3
RSB	58.12	17.14	22.64	1.89	0	0.197	0	2.43	3.39
SSB	56.75	15.10	24.80	2.93	0.18	0.22	0.02	1.08	3.75
MCB	56.41	15.20	24.50	3.20	0.056	0.52	0.19	2.46	3.71

All gas compositions are in vol%

7.3.1 Determination of Actual Compositions

All the results presented in Chapters 5 and 6, display the syngas compositions on an N₂-free basis, as N₂ would not be present in the scaled up application. However, the actual compositions are needed for accurate calculations later on in the chapter. This means that the N₂ used for purging air must be included in the final composition. Furthermore, the water content in the gas must also be accounted for. It was measured using a Viasalla humidity sensor. The gas was pumped through the sensor using the same methodology as that of the fuel cell experiments, which is described in Chapter 3.14.2. The water content in the gas ranged from 10.03 to 10.9 g m⁻³ over the duration of the experiment, with an average value of 10.51 g m⁻³. This value was used to calculate the water composition in the gas. The results are shown below in Table 7-2.

Table 7-2: Actual syngas compositions for RSB and WPB

Biochar	H ₂	CO	CO ₂	CH ₄	C ₂ H ₆	C ₂ H ₄	C ₃ H ₆	N ₂	H ₂ O	HHV ^a
WPB (vol%)	38.8± 0.66	10± 0.7	17.6±1.06	4.8 ±0.3	0.2± 0.01	1.8± 0.06	0.17± 0.01	25.3± 2.84	1.46	9.66
RSB (vol%)	42.2± 0.07	12.6± 0.65	16.3± 0.04	1.4± 0.04	0.00	0.04	0.00	26.2± 0.5	1.4	7.56

HHV (MJ m⁻³)

7.4 Performance of a Solid Oxide Fuel Cell with Syngas from Rapeseed Biochar

The SOFC was prepared according to the procedure described in chapter 3.14.1. It was then placed in the furnace and connected to the SOFC test rig using a ceramic to metal joint shown in Figure 3.17. Pure H₂ was run through the cell at 60 ml min⁻¹ to maintain reducing conditions at the anode, whilst the furnace was heated at a rate of 10°C min⁻¹ up to 800°C. Gasification experiments were carried out at 800°C at a steam flow of 277 g min⁻¹ kg⁻¹ biochar. 3 g of biochar was gasified using the same procedure as that described in Chapter 3.6. The product gas was collected in a gas bag. An 8 L glass cylinder was first filled with water; the gas was transferred into the cylinder using the suction created by the outflow of water. The cylinder was connected to the SOFC test rig using a silicone hose and water was pumped into the glass tank to push the gas out and into the SOFC. The SOFC test programme was as follows; (i) 10 minutes of OCV, (ii) Potentio-stairstep mode whereby the voltage was reduced from OCV to 0.6 V in increments of 15 mV. (iii) Potentio-static mode for 30 minutes, where the voltage was kept constant at 0.7 V, (IV) Potentio-stair-step mode where the voltage was reduced from OCV to 0.6 V and finally (V) 10 minute OCV. The duration of the test programme depended on the value of the OCV but

was usually around 90 minutes. More details on the test programme can be found in Chapter 3.14.6.

The SOFC was first tested using pure H₂ at a flowrate of 60 ml min⁻¹ to determine its optimum performance. The results are shown in Figure 7.1 below. The ideal cell voltage was calculated using the Nernst Equation, (7-1), which is shown below;

$$E = E^{\circ} - \left(\frac{RT}{nF}\right) \ln Q \quad \text{7-1}$$

Where E is the half-cell reduction potential

E° is the standard cell potential at temperature T

$$E^{\circ} = \frac{\Delta G_r}{2nF} \quad \text{7-2}$$

ΔG_r Gibbs free energy of reaction (J mol⁻¹) All values used in the calculations were obtained from The hand book of Chemistry and Physics [165]

n is the number of moles of electrons

R is the universal gas constant (8.314 J mol⁻¹ K⁻¹)

Q is the reaction quotient expressing the initial concentrations of the reactants.

It can be seen that the OCV was around 1.04 V; this was an indication that fuel cell was working correctly. The OCV can be used as a measure of gas leakage or electronic leakage through the electrolyte [166]. An OCV of 1.04 V was 0.147 V lower than the 1.187 V that is predicted by the Nernst Equation. The lower value is the result of two factors (i) some leakage through electrolyte and (ii) the H₂O produced

when the cell was at OCV was higher than the 0.5% assumed in the calculation of the ideal voltage. The SOFC preparation method involved scraping the electrolyte layer to expose the anode which could then be connected to the Solartron. Silver paste (impermeable to H₂) was used as a sealant to stop the H₂ from permeating out but it seems that this was ineffective at higher temperatures and the lower than expected OCV is an indication of possible leakage. Using pure H₂ as the fuel, the current and power densities reached by the cell were 0.17 A cm⁻² and 0.1 W cm⁻² at 0.6 V, respectively.

The performance of the cell using RSB syngas is shown in Figure 7.1, it can be observed that the OCV was very low, at 0.967 V. The ideal OCV for the RSB mixture at 800°C, as predicted by the Nernst Equation is 1.070 V. The lower OCV is the combination of some electronic leakage and the large presence of CO₂ which reduces the OCV. The IV curve in Figure 7.1 shows that the performance of the SOFC on RSB syngas was worse than that on pure H₂. It only managed to produce a current density of 0.13 A cm⁻² and a power density of 0.078 W cm⁻² at 0.6 V. The reduction in performance can be explained by three factors; (i) diluting effect of N₂ and CO₂, (ii) poor performance of the Ni catalyst in the electrochemical oxidation of CO [76] and (iii) lack of steam at the inlet which hindered the CO from being utilised via the WGS [75] and the reformation of CH₄. Furthermore, the stability of operation was much lower than that with pure H₂ but this might be the result of a more consistent supply of fuel.

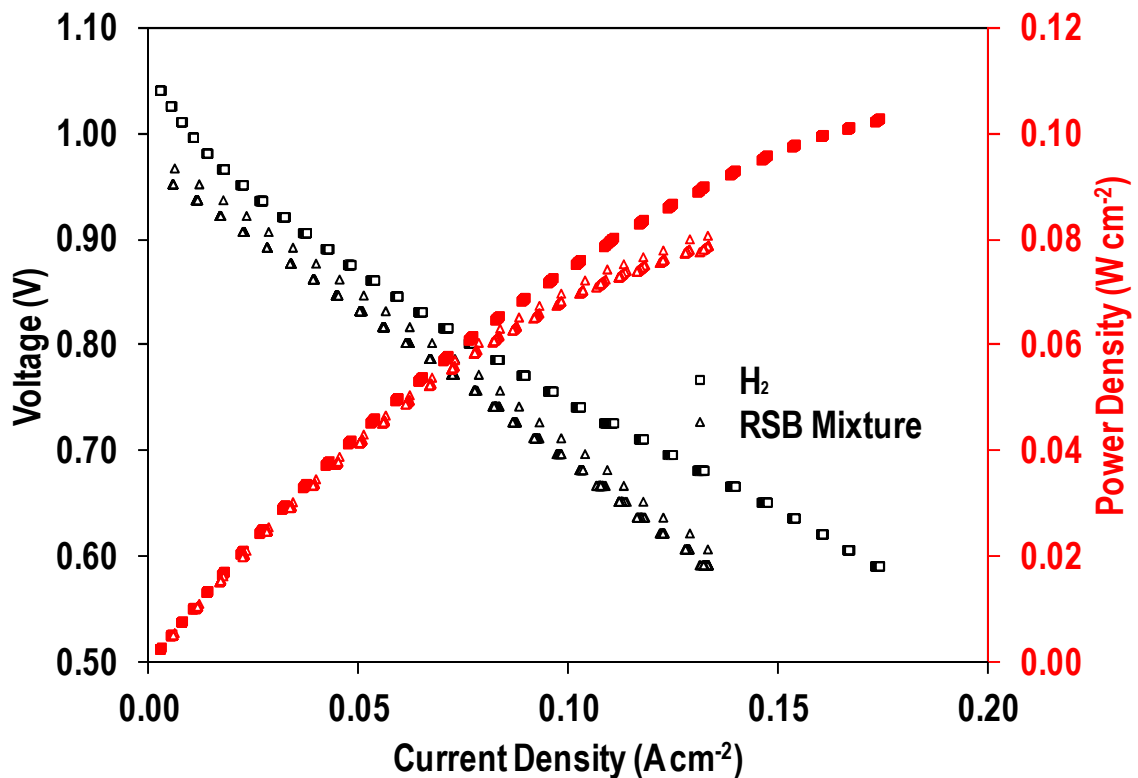


Figure 7.1: Performance of microtubular SOFC on pure H₂ 60 ml min⁻¹ and RSB syngas at 70 ml min⁻¹ and 800°C

The next step in the programme was a potentiostatic mode at 0.7 V for 30 minutes. The results are displayed in Figure 7.3. It is observed that the gas had a disastrous effect on the SOFC performance. The initial current drawn from the cell was 1.85 A at 0.7 V but this quickly reduced to 1.3 A after 30 minutes of operation. Clearly, the cell had been negatively affected by the gas. The results could be due to the combination of many factors such as; (i) impurities that are likely to be present in the RSB syngas and (ii) dry operating conditions which lead to the deposition of carbon on the surface. The RSB contained 5.36% P and 0.1% S. In steam gasification atmospheres, these elements are likely to form PH₃ and H₂S, respectively [97] [91]. The presence of H₂S was confirmed using lead acetate paper, Figure 7.2 shows a

darkened lead acetate paper which is sensitive to H₂S at levels >5 ppm. SOFCs are able to tolerate H₂S to some degree but it has consistently been shown that the presence of PH₃ leads to rapid and irreversible decline in performance. The PH₃ attacks the Ni anode forming Ni₂P₅ and is potent even if present in ppb levels [95]. The nickel phosphate reduces the exchange current density and increases resistance to both charge and mass transfer [167] which leads to anodic overpotentials and obstructs internal fuel reforming [95]. Although the presence of PH₃ was not tested for, it can be assumed that it was present in the gas since syngas from coal contains around 2 ppm PH₃ [167] which comes from coals containing up to 0.15% P [168]. The RSB contained 5.36% P; this is much higher than that of the coals, hence it can be assumed to contain at least some degree of PH₃.

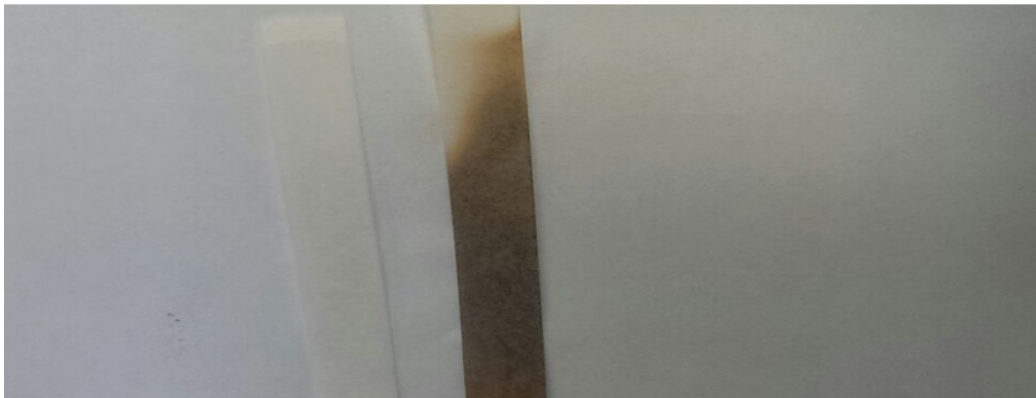


Figure 7.2: Results of the lead acetate test confirming the presence of H₂S, (left) N₂, (right) RSB syngas

The fuel utilisation, U_f , can be calculated using Equation 7-3 shown below [72];

$$U_f = \frac{I}{2 \cdot F \cdot n_f (xH_2 + xCO + 4CH_4 + 7C_2H_6 + 6C_2H_4)} \quad 7-3$$

where current, I is expressed through Faraday's Law:

$$I = 2 \cdot F \cdot r_{H_2}$$

7-4

where r_{H_2} is the rate of reaction of hydrogen oxidation.

It was assumed that the SOFC only utilised the H_2 fraction of the fuel. This assumption is supported by previous work which has shown that Ni-YSZ anode SOFCs running on dry syngas use only the H_2 fraction of the fuel [75]. It was also assumed that the steam produced from the oxidation of H_2 was not involved in further reforming reactions. The current produced by the cell as well as the fuel utilisation are shown in Figure 7.3 below.

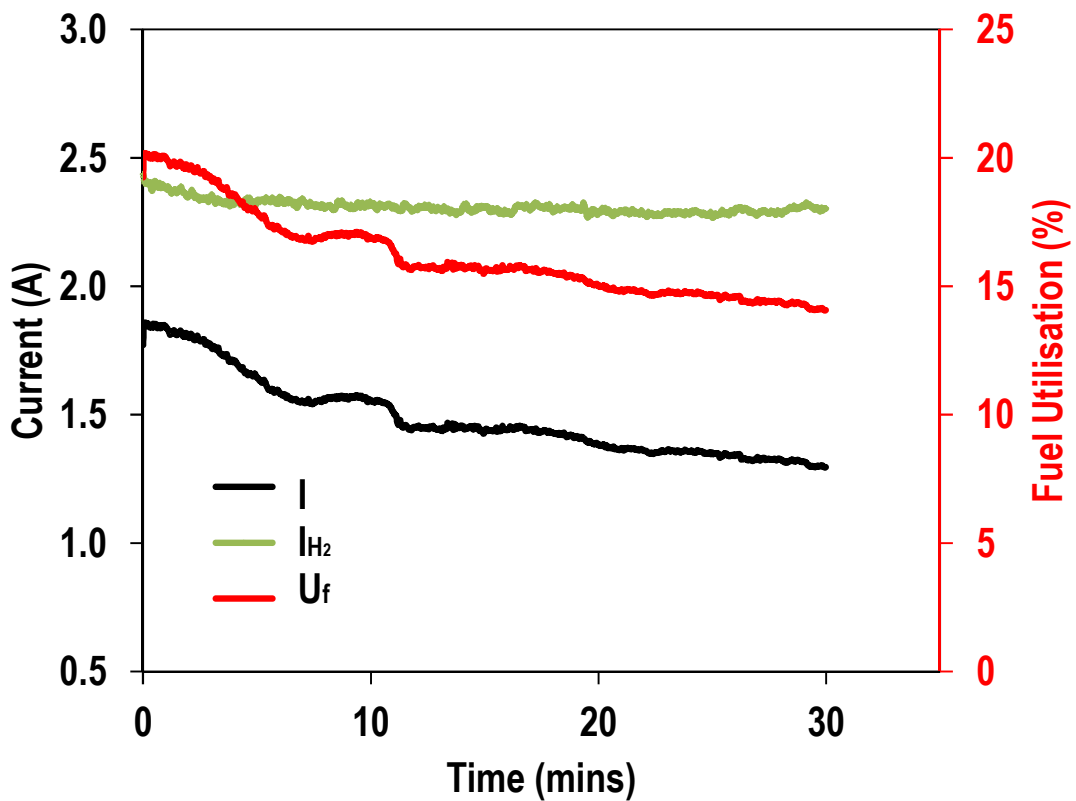


Figure 7.3: SOFC current and fuel utilisation using the RSB syngas at 0.7 V, at 800°C

From Figure 7.3, it can be seen that the U_f decreases with time. The initial U_f was around 20% which decreased to 14% over the duration of the experiment. The decrease in U_f was likely to be the result of impurities in the syngas attacking the Ni catalyst and reducing its electrochemical activity. The reduction in catalyst activity led to a reduced electrical efficiency as well as the overall efficiency shown in Figure 7.4, as determined by equations 7-5 and 7-6.

$$\eta_e = \frac{IV}{V_o HHV} \quad \mathbf{7-5}$$

where η_e is electrical efficiency, $IV =$ power ($J s^{-1}$) and V_o ($m^3 s^{-1}$) is the volumetric flowrate and HHV ($J m^{-3}$) is the heating value of the gas:

$$\eta_o = \frac{IV + (U_{fH_2} * -192562 * n_{H_2})}{8.83} * 100 \quad \mathbf{7-6}$$

where U_{fH_2} is fuel utilisation wrt H_2 , $-192,562 J mol^{-1}$ is ΔH_c of H_2 at $800^\circ C$ (calculated using [165]), n_{H_2} is the molar flow of H_2 ($mol s^{-1}$) and 8.83 is the heating value of the gas ($J s^{-1}$) (accounting for N_2).

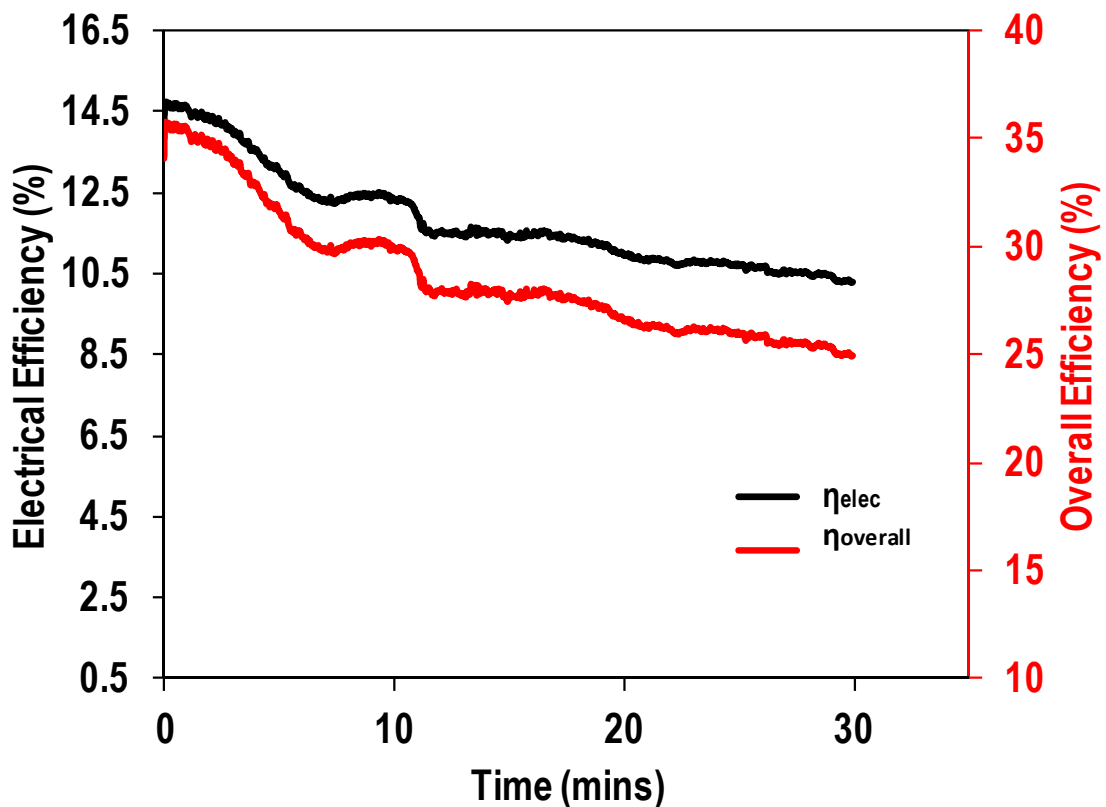


Figure 7.4: Electrical and overall efficiencies of the microtubular SOFC operating on RSB syngas at 0.7 V and 800°C

7.5 Performance of a Solid Oxide Fuel Cell with Syngas from Wood Pellet Biochar

Unlike the RSB, the WPB had a more suitable H_2/CO ratio for utilisation in an SOFC as well as very low ash and P contents. The procedure used was the same as that for the RSB, 3 g of WPB was gasified at 850°C at a steam flow of 277 g min⁻¹ kg⁻¹ biochar and the syngas was collected in a gas bag and transferred to a glass tank. Water was used to pump the gas out of the glass tank and into the SOFC at a flowrate of 70 ml min⁻¹.

The performance of the SOFC on WPB syngas can be seen in Figure 7.5. It is observed that the performance of the cell with pure H₂ is comparable to that of the cell used in the RSB experiments. The OCV of the cell was 1.04V, which was again lower than the Nernst voltage of 1.115 V, indicating some sort of gaseous or electronic leakage. The power density of the cell at 0.6 V was 0.096 W cm⁻², this was slightly lower than the 0.103 W cm⁻² obtained from the previous cell but is of comparable order of magnitude. Running the SOFC on syngas, the OCV was 1.01 V; this was better than the 0.967 V that was obtained from the RSB and indicates that the WPB, with a lower CO content was a more suitable fuel for SOFC usage. The performance of the SOFC with WPB syngas was again lower than that of pure H₂; the maximum power density obtained at 0.6 V was 0.08 W cm⁻²; this is likely to be the result of the N₂ and CO₂ contents in the gaseous stream diluting the mixture. The power density was better than the 0.078 W cm⁻² obtained from the RSB syngas and was likely due to the higher HHV of the WPB gas.

During operation, an SOFC generates both heat and electricity, the more strain the cell experiences, i.e. the higher its current density is, the more heat it generates. This leads to problems with thermal management and degradation issues. The operating point of a SOFC can be found at the point when the power density curve crosses the I-V curve. In this case that point is around 0.07 A cm⁻² at 0.78 V, giving a power density of 0.05 W cm⁻².

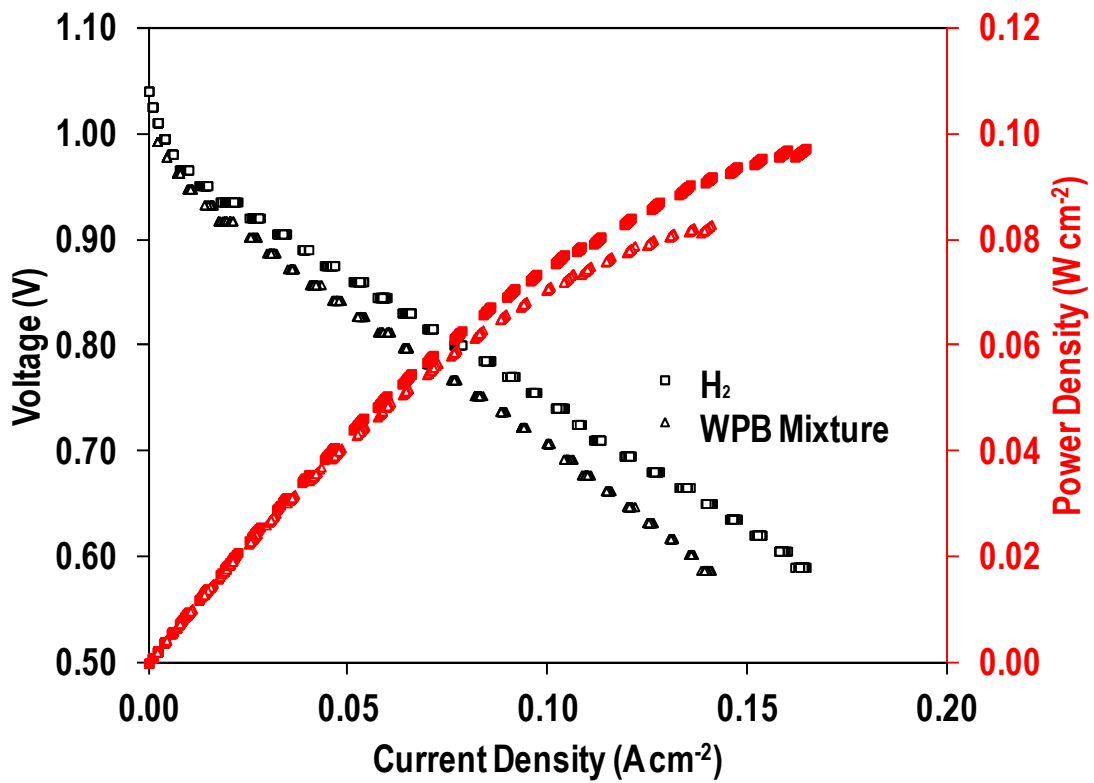


Figure 7.5: Performance of a microtubular SOFC using syngas from WPB at 800°C

The potentiostatic results from the WPB syngas are shown in Figure 7.6. It can be seen that there is a very slight reduction in the performance of the SOFC from 1.9 A to 1.8 A over the course of the 30 minutes. The slight reduction might be the result of cell stabilisation and not degradation. The fuel utilisation was around 14% and the electrical efficiency was around 12%, which was lower than that for the RSB, and was a consequence of the higher HHV of the WPB syngas.

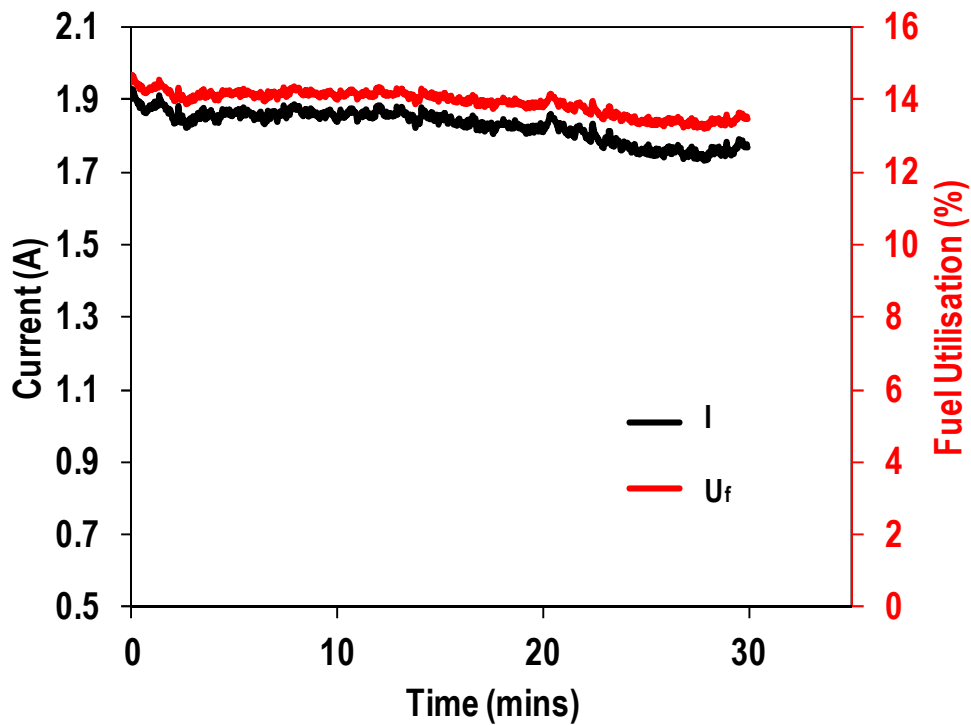


Figure 7.6: SOFC performance showing potentiostatic mode and fuel utilisation at 0.7 V for WPB syngas at 800°C

7.5.1 Performance of a Solid Oxide Fuel Cell on WPB Syngas for an Extended Period

Testing out the performance of the SOFC over an extended period of time required both gasification and fuel cell experiments to be carried out in parallel. This naturally set a limit on the length of the experiments since the syngas could only be produced during the working day (~8 hours). The possibility of extending the experiment longer than one day meant that during the night, the SOFC had to be operated on pure H₂, therefore, any negative effects the gas might have had on the cell, could have been reversed. Another possibility was to use an inert atmosphere such as that created by passing N₂ through the SOFC during the downtime. After testing this method, it was

found that the anode became oxidised and to reduce it required passing pure H₂ over it for two hours. Again, this would have led to reversals of any loss in performance. As a result, it was decided that the cell would be operated for the duration of one working day (~8 hours).

The experiment was carried out as follows; the day before the experiment, WPB was gasified in two separate experiments and the product gas was collected and transferred into the glass tanks. An SOFC was prepared beforehand and placed into the test rig overnight with H₂ flowing through it. The next day, the SOFC was first tested with pure H₂ and whilst the programme was running, gasification experiments were conducted to produce more gas. When the pure H₂ run had finished, the gas storage tank was connected to the rig and the SOFC test programme was activated. Once the gas cylinder was spent, the SOFC was operated on pure H₂ whilst the second cylinder was connected. The programme was restarted and the SOFC was again run on syngas. The change of cylinders took less than 5 minutes. In the meantime, the spent cylinder was refilled with gas from the gasification experiment and the process was continued for as long as possible. At the end of the experiment, the fuel was switched back to pure H₂ and the programme was run once again to gauge the performance on pure H₂.

The IV curves from the extended experiment are displayed in Figure 7.7 and Figure 7.8. The figures show the initial and final performance of the SOFC with pure H₂ and WPB syngas. It can be seen that the performance of the SOFC degrades over the duration of the experiment, this is clearly shown by both syngas and pure H₂. The degradation was markedly worse with pure H₂ as the power density experienced a 23% drop from 0.10 to 0.077 W cm⁻² at 0.6 V. The degradation with syngas was not

so pronounced, decreasing by 10% from 0.094 to 0.085 W cm⁻² at 0.6 V, over the duration of the experiment. An interesting observation was that towards the end of the experiment, the SOFC performed better on syngas than it did on pure H₂. This is difficult to explain and requires further study.

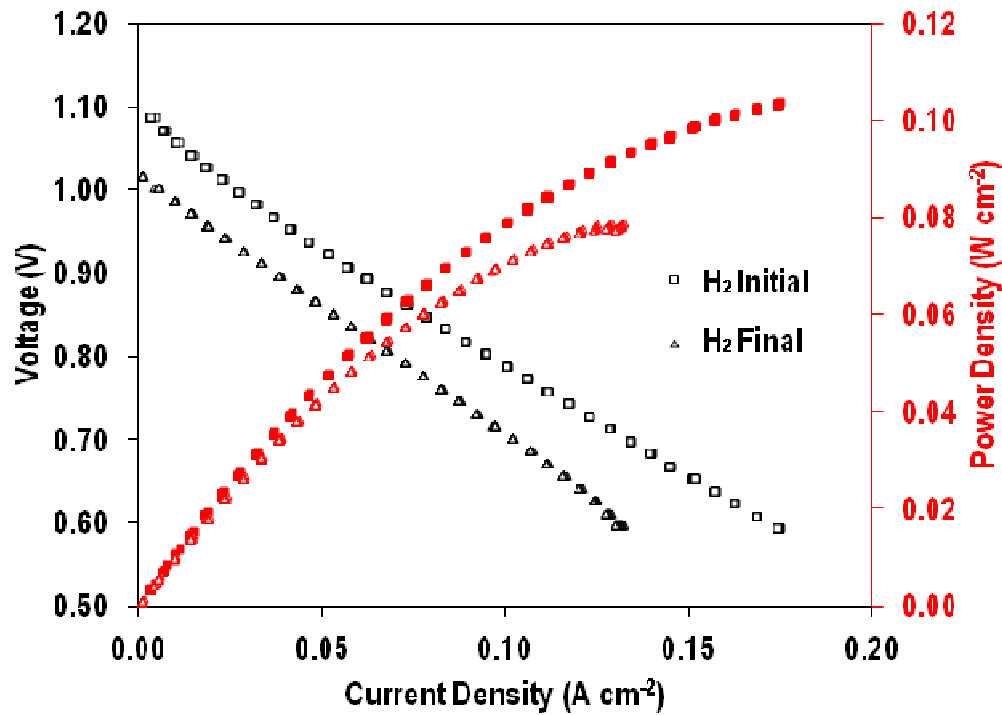


Figure 7.7: Initial and final performance of the SOFC using pure H₂ at 800°C

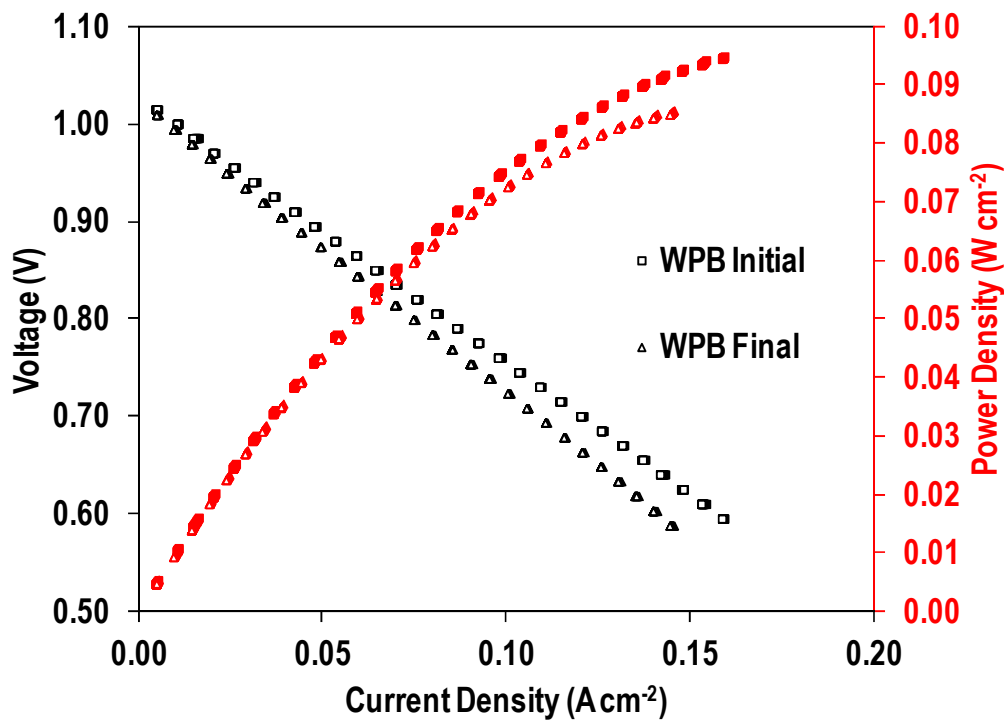


Figure 7.8: Initial and final performance of the SOFC using WPB syngas at 800°C

Figure 7.9 displays the operation of the SOFC in potentiostatic mode over the duration of the experiment. It is observed that the SOFC was operated in the potentiostatic mode for a total of 2.5 hours. The current drawn from the SOFC fluctuated with each batch of gas; this was likely as a result of the $\pm 4\%$ variation in the gas composition. The current decreased from an initial 2.3 to 2.07 A, but most of the decrease occurred with the changing of each bath rather than during the potentiostatic mode itself. This could suggest that it was not the impurities in the gas that were the cause of the majority of the performance degradation but rather the rapid rate of change of gas composition. The WPB syngas also contained H_2S as it discoloured a lead acetate paper, this may have been one of the causes for the loss in performance. Another cause could have been the deposition of carbon on the

anode surface due to the dry conditions that were used in the test. The deposited carbon blocks the catalyst active sites, reducing cell performance.

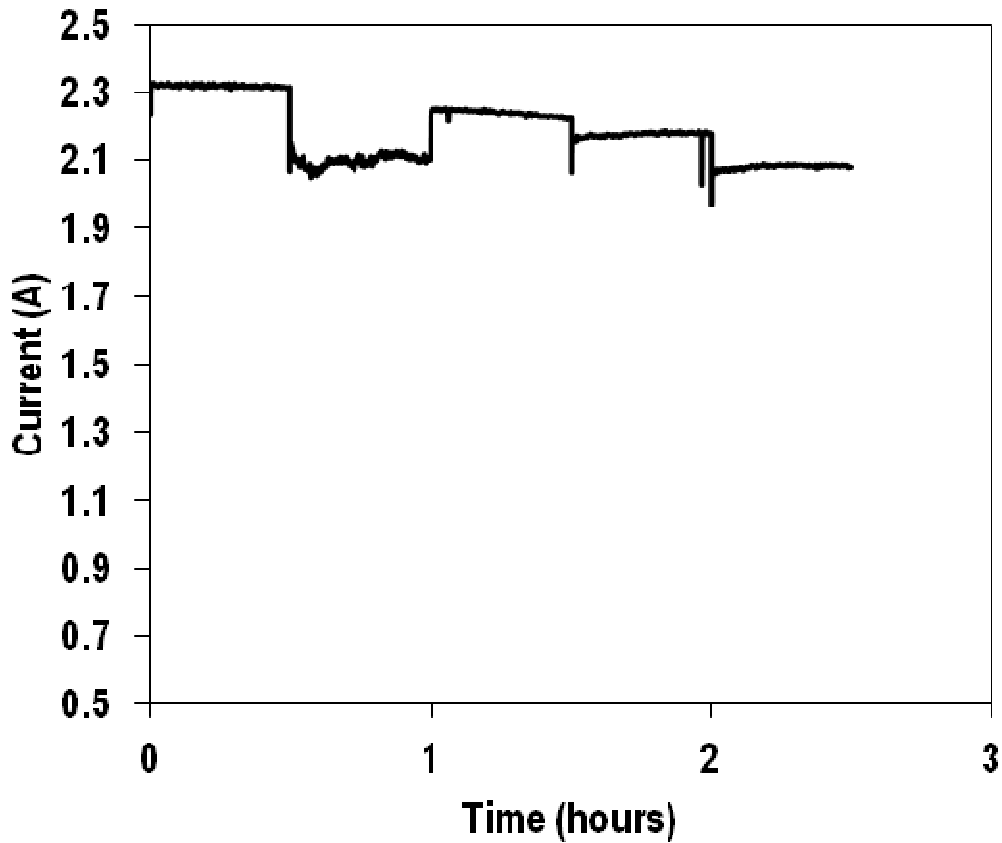


Figure 7.9: Operation of the SOFC in potentiostatic mode for an extended period of time at 800°C

7.6 Conclusions

Single cell microtubular solid oxide fuel cells were operated using syngas from two biochars; rapeseed biochar (RSB) and wood pellet biochar (WPB). It was found that the RSB gas affected the SOFC in a very negative manner, drastically reducing its performance from the beginning to the end of the test. The OCV was below 1.0 V resulting from the high contents of CO and CO₂ present in the syngas. The optimum

performance given by the SOFC using RSB syngas was a current density of 0.13 A cm^{-2} and a power density of 0.078 W cm^{-2} at 0.6 V .

The performance of the SOFC using WPB syngas was much better and it managed to complete the whole test without any significant loss in performance. It gave an OCV of greater than 1.0 and achieved a maximum power density of 0.08 W cm^{-2} at 0.6 V , which was slightly better than that given by the RSB syngas. In all cases, the performance of the SOFC on pure H_2 was superior to that of the syngas. This was most likely the result of two factors; (i) H_2 is the preferred fuel for SOFCs and (ii) the diluting effects on N_2 and CO_2 reducing the energy content in the syngas.

The SOFC was run on WPB syngas for an extended period of time. It was found that there was around 10% decrease in performance but it could have been due to the batch method used to deliver the gas to the SOFC. The dry conditions used in the experiment would have enabled carbon to be deposited on the surface of the anode, reducing its catalytic activity.

7.7 Summary of Mass and Energy Balances

7.7.1 Overview

This section provides a summary of the mass and energy balances carried out over the process and discussions regarding the results. The full calculations for the mass and energy balances can be found in Appendix III.

7.7.2 Mass Balance

Basis and Assumptions

Basis: 3 g biochar input

Conditions: 850°C and 277 g min⁻¹ kg⁻¹ biochar steam flow

Assumptions: Assume steady state conditions

Assume ideal gas law applies to the gases

Assume that tar is phenolic, i.e. phenol

Assume that all the S and N are converted into H₂S and NH₃ respectively

Assume that all the initial oxygen in the biochar is used up during the reaction (no oxygen is present in the spent biochar)

Mass balance is only carried out for steam used in the reaction

Assume fuel cell only uses the H₂ fraction in the syngas and the H₂ utilisation is 64%.

Table 7-3: Summary of mass balance for the gasifier

Constituent	Mass In (g)		Mass out (g)			Closure (%)
	Biochar	Steam	syngas	Tar	Spent Biochar	
C	2.1474		1.824	0.193	0.130	100
H	0.1386	0.34	0.458	0.012	0.002	100
N	0.0162		0.016			100
S	0.0066		0.0066			100
Ash	0.0792				0.026*	33
O*	0.612	2.7	3.06	0.047		93.8
Total (g)	3	3.036	5.34	0.252	0.158	95.3

*by difference

Table 7-4: Summary of mass balance for the solid oxide fuel cell

Constituent	Mass in (g)		Mass out (g)	Closure (%)
	syngas	Oxygen		
C	1.824		1.824	100
H	0.458		0.110	100
N	0.016		0.016	100
S	0.0066		0.0066	100
O	3.06	1.790	4.85	100
Total	5.34	1.79	7.13	100

7.7.3 Mass Balance Discussions

The closure of 95.3% results mainly from the difference between the initial and final ash content. The discrepancy in the O content was likely to have resulted from the method used to determine it, i.e. by difference. It is likely that the O content was overstated.

7.8 Energy Balance Summary

Assumptions: Assume steady state conditions

Assume the following steps occur during the gasification process:

Biochar is placed into the reactor where it heats up from 25 – 850°C

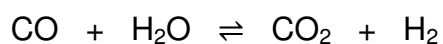
Steam is heated up from 25 – 850°C

Devolatilisation occurs leading to char, tar and gases

Steam reacts with char to make CO and H₂ via the following reaction:



The CO reacts with H₂O to produce CO₂ and H₂



More assumptions were made that are specific to a particular section, refer to Appendix III for these.

Energy balance carried out only for steam that was used in the reaction

For energy balance with heat recovery, the following assumptions were made;

50% heat is recovered, this figure comes from the heat recovery achieved in the Guessing Gasifier, Austria, which is a steam gasification process using biomass in a fluidised bed gasifier.

Reactor experiences 10% heat loss (hence requires 10% excess heat than is required)

2.5x excess steams is added to the process

For SOFC energy balance, the following assumptions were made:

Only H₂ is used as a fuel and 50% heat is recovered

7.8.1 Energy Balance Discussions

Table 7-5 displays the energy balance for the steam gasification process. It is shown that the cold gas efficiency is 65%. According to Obernberger and Thek [26], the minimum cold gas efficiency that is acceptable from gasifiers, regardless of the type is 80%. Therefore, the cold gas efficiency is low and is likely to be the result of factors such as tar loading in the gas which would have been 32.56 gm⁻³ had all the tar stayed in the gas. The higher tar loading results in decreased efficiencies. With heat recovery, the gasification process efficiency is increased to 75.7%.

The electrical efficiency of the SOFC was very low at 16.82%, much lower than the 50% theoretical efficiency that SOFCs can achieve. There are many reasons why the efficiency was low; the presence of impurities such as H₂S would have reduced the catalytic activity of the anode, leading to a decrease in the utilisation of the fuel. The lack of steam at the inlet would have inhibited the reforming of hydrocarbons and CO, which would have led to a large portion of the gas being unavailable for the SOFC. Finally, the nickel anode is not a good catalyst for the electrochemical oxidation of CO and the lack of steam could have led to the deposition of carbon on the anode surface.

Table 7-5: Energy balance for the steam gasification of WPB at 850°C

Energy In (J)			Energy Out (J)			Energy Lost	CGE (%)**
Biochar	Steam	Heat in	HV of gas*	Heat in gas	Spent biochar	Tar	
86400	13133.13	49203	98564	39050	5281.67	8367.36	65

*combustion value of gas = HHV*V

**Cold Gas Efficiency (refer to equation 10-4)

Solid Oxide Fuel Cell Energy Balance

Energy in = 9.57 W (combustion energy value of the WPB gas mixture at 70 ml s⁻¹)

Electrical energy out = 1.61 W = 16.82%

Heat energy out = 2.29 W (assuming H₂ fuel utilisation only at 800°C)

Energy efficiency assuming 50% heat recovery = **22.12%**

8 Conclusions and Recommendations

8.1 Chapter Overview

The main aim of this work was to investigate the potential of biomass derived char or biochar to produce a hydrogen-rich syngas which could be utilised in a solid oxide fuel cell. This chapter provides a summary of the conclusions that were derived during the undertaking of this work. The format is arranged so that the conclusions from each chapter are presented together. The chapter ends with recommendations for further work.

Chapter two presented a literature survey covering the various aspects that were connected to this research. It was concluded that intermediate pyrolysis is able to handle a variety of feeds to produce a high quality biochar. Steam gasification of biochar produces a hydrogen-rich gas that contains more than 50% hydrogen (by volume) at high temperatures. Solid oxide fuel cells can successfully utilise syngas to generate electricity efficiently without any loss in power, but they require the presence of steam for reformation purposes. SOFCs have different tolerance levels with regards to syngas constituents. Carbon monoxide and methane can both lead to carbon deposition and decrease the performance but it could be avoided if steam is present alongside the gas. Syngas impurities can decrease the SOFC performance depending upon the type and concentration. Phosphine (PH_3) is perhaps the most potent contaminant and can reduce SOFC performance even if present in parts per billion.

Chapter four presented the results of the various characterisation methods that had been used to characterise the biochars, dolomite and the SOFC. The following characterisations techniques were carried out on the biochars; elemental analysis, bomb calorimetry, BET surface area, volatile content, particle size distribution, bulk density analysis and X-ray Fluorescence spectroscopy. The highest carbon content was found in the WPB, at 71.58% and the lowest was in SSB, 30%. The highest mineral content was in the RSB which contained 8% Ca, 9% K and 5% P. The higher heating values of the biochars were as follows; 28.8, 24, 11, 24.7 MJ kg⁻¹ for WPB, RSB, SSB and MCB, respectively.

Dolomite was characterised using the following techniques; XRF, BET surface area, particle size distribution, TGA, and bulk density. It was found that the dolomite was not a pure dolomite but rather a dolomitic limestone since it contained a lower than expected MgO content. The BET surface area improved upon calcination from 1.75 to 8.37 m² g⁻¹ but the bulk density decreased from 1.55 to 0.87 g cm⁻³.

Chapter five presented the results of the steam gasification of biochar. Investigations of the effects of temperature and steam flow on the transient composition, product flow, final composition, DGY, HHV, carbon conversion and carbon conversion efficiency CCE were presented in this chapter. A temperature range of 650 – 850°C was employed, and a steam flow 172 g min⁻¹ kg⁻¹ biochar was used. It was found that the product flow and composition of the product gas changes during the reaction. The initial product flowrate is high and the composition is the result of devolatilisation and contains many hydrocarbons alongside CO, CO₂ but with little H₂. As the reaction proceeds, the product flowrate drops and the levels of CO and CH₄ drop off as H₂ and CO₂ take over via the water gas shift reaction. With respect to final gas

composition, it was found that the H₂ content was highest at around 700 – 750°C, with the rapeseed biochar producing the highest H₂ content at 58.8% at 750°C and 172 g min⁻¹ kg⁻¹ biochar. The effects of steam flow were investigated at 850°C, over a steam flow range of 54 – 277 g min⁻¹ kg⁻¹ biochar. It was found that the H₂ content increased with increasing steam flow, with the highest H₂ volume fraction of 58.1%, given by RSB at 277 g min⁻¹ kg⁻¹ biochar. The DGY also increased with increasing steam flow and the highest DGY of 2.58 m³ kg⁻¹, was given by WPB at 277 g min⁻¹ kg⁻¹ biochar and the lowest was 1.08 m³ kg⁻¹ at the same steam flowrate given by the SSB.

Chapter six followed on from chapter five and further explored some of the aspects mentioned in chapter five. It investigated the changes in reactivity with conversion, effects of alkali and alkaline earth metallic species, particle size and dolomite. It was found that the reactivity of the biochars decreases as conversion increases, mainly as a result of a switch in the types of reactions that occur. In the beginning of the process, devolatilisation and oxidation take place which produce a high flowrate of product. As the process progresses, the reactions become endothermic and gasification reactions take over which are much slower.

To investigate the effects of the AAEM content, the RSB was washed with concentrated HCl to remove the its mineral content. It was then gasified as before and it was found that the gasification proceeded more slowly and the final product contained less CO which was as a result of the AAEM catalysing the steam-carbon reactions. Changing the particle size did not affect the final composition and led to a slight increase in the DGY. The final part of the chapter investigated the effects of adding dolomite from Derbyshire to the WPB. It was found that the dolomite did lead

to an increase in the DGY but had no discernible impact on the composition of the syngas.

Investigations of the performance of a microtubular SOFC using syngas from biochar were reported in Chapter 7. Syngas from RSB and WPB were tested in two experiments and it was found that the RSB syngas had a very negative effect on the SOFC. The RSB gas gave a low OCV of 0.96 V and its potentiostatic current decreased from 1.8 to 1.3 A in 30 minutes. The degradation in performance was attributed to the presence of impurities such as H₂S and PH₃. The WPB syngas led to a much better performance of the SOFC and did not lead to a reduction in performance over the course of the experiment. An extended experiment led to some degradation in SOFC performance but this was attributed to the harsh conditions used in the experiments and the rapid compositional changes experienced by the SOFC, when changing the batch of gas.

8.2 Further Work and Recommendations

This work was the initial investigation into the production of a hydrogen-rich syngas from the steam gasification of intermediate pyrolysis biochars to use in solid oxide fuel cells. The work has produced many lines of enquiry which need to be further investigated before the process can be fully understood and optimised. Below are some recommendations that can be followed in the development of the process.

- With regards to gasification, the next step is to make it a continuous rather than a batch process. This could be done in an updraft, bench scale, fixed-bed

reactor. The low volatile content of biochars make updraft gasifiers suitable for such an application and their ability to be scaled up easily will become useful later on in the development of the process. Process parameters such as solid residence time, gas residence time and feeding rate need to be further investigated.

- An investigation into the impurities present in the syngas is vital. It will lead to the development of an integrated cleaning system. The impurities that need investigating are; tar (content and form), sulphur (content and form), nitrogen (content and form) and other trace impurities such as PH_3 etc.
- The endothermic nature of the steam gasification reactions requires an external source of heat, therefore, a mixture of steam and air should be investigated to overcome this. The use of air will reduce the heating value of the gas but the system will be cheaper. Another route is to investigate the use of spent biochar as a fuel for heating the reactor. This will require a lower conversion during gasification to retain sufficient energy content in the spent biochar.
- The biochars, in particular rapeseed biochar were very reactive and catalysed steam-char and oxygen-char reactions. They may be able to catalyse the destruction of tars formed during biomass gasification and this needs to be investigated.
- With respect to SOFCs, there are several lines of inquiry that can be followed on from here. Initially, the use of untreated syngas should be investigated with the addition of sufficient quantities of steam to enable reforming reactions within the SOFC to occur. Then, a clean-up system should be developed that

selectively removes individual components to gauge the effect of the SOFC performance.

- The SOFC should be connected directly to the gasifier and sized accordingly so that the product flow matches that of the input into the SOFC. A buffer tank can be used to reduce the impact of the deviations in flowrate.

9 References

- [1] BP. BP Statistical Review of World Energy. London: BP Plc; 2014.
- [2] Höök M, Tang X. Depletion of fossil fuels and anthropogenic climate change—A review. *Energy Policy*. 2013;52(0):797-809.
- [3] STC. The Energy Challenge of the 21st Century: The role of Nuclear. Brussels: European Commission; 2003.
- [4] Wolf JP. Biomass combustion for power generation: an introduction. In: Rosendhal L, editor. Biomass combustion science, technology and engineering. Oxford: Woodhead Publishing; 2013. p. 3-8.
- [5] Intelligent-Energy-Europe. Guidelines for Safe and Eco-friendly Biomass Gasification. The European Commission; 2009.
- [6] Basu P. Chapter 1 - Introduction. In: Basu P, editor. Biomass Gasification, Pyrolysis and Torrefaction (Second Edition). Boston: Academic Press; 2013. p. 1-27.
- [7] Field CB, Campbell JE, Lobell DB. Biomass energy: the scale of the potential resource. *Trends in Ecology & Evolution*. 2008;23(2):65-72.
- [8] Long H, Li X, Wang H, Jia J. Biomass resources and their bioenergy potential estimation: A review. *Renewable and Sustainable Energy Reviews*. 2013;26(0):344-52.
- [9] Liu M. Biomass-powered Solid Oxide Fuel Cells: Experimental and Modeling Studies for System Integrations Delft, Netherlands: University of Delft; 2013.
- [10] Services EGT. Fuel Cell Handbook. Morgan Town, West Virginia 2004.
- [11] Eguchi K, Kojo H, Takeguchi T, Kikuchi R, Sasaki K. Fuel flexibility in power generation by solid oxide fuel cells. *Solid State Ionics*. 2002;152–153(0):411-6.
- [12] Chaudhari ST, Bej SK, Bakhshi NN, Dalai AK. Steam Gasification of Biomass-Derived Char for the Production of Carbon Monoxide-Rich Synthesis Gas. *Energy & Fuels*. 2001;15(3):736-42.
- [13] Chaudhari ST, Dalai AK, Bakhshi NN. Production of Hydrogen and/or Syngas (H₂ + CO) via Steam Gasification of Biomass-Derived Chars. *Energy & Fuels*. 2003;17(4):1062-7.
- [14] Yan F, Luo S-y, Hu Z-q, Xiao B, Cheng G. Hydrogen-rich gas production by steam gasification of char from biomass fast pyrolysis in a fixed-bed reactor: Influence of temperature and steam on hydrogen yield and syngas composition. *Bioresource Technology*. 2010;101(14):5633-7.
- [15] Basu P. Chapter 5 - Pyrolysis. In: Basu P, editor. Biomass Gasification, Pyrolysis and Torrefaction (Second Edition). Boston: Academic Press; 2013. p. 147-76.
- [16] Bridgwater AV, Hofbauer, Loo Sv. Thermal Biomass Conversion. London: CPL Press; 2009.
- [17] Wild Pd. Biomass Pyrolysis for Chemicals. University of Groningen; 2011.
- [18] Laird DA, Rogovska NP, Garcia-Perez M, Collins HP, Streubel JD, Smith M. Pyrolysis and Biochar-Opportunities for Distributed Production and Soil Quality Enhancement. In: Braun R, Karlen DL, Johnson D, editors. Sustainable Alternative Fuel Feedstock Opportunities, Challenges and Roadmaps for Six US Regions: SWCS publisher; 2011.
- [19] Mahmood A, Brammer J, Hornung A, Steele A, Poulston S. The intermediate pyrolysis and catalytic steam reforming of Brewers spent grain. *Journal of Analytical and Applied Pyrolysis*. 2013;102:24-32.

- [20] Wright MM, Daugaard DE, Hsu DD. Techno-Economic Analysis of Biomass Fast Pyrolysis to Transportation Fuels. National Renewable Energy Laboratory; 2010.
- [21] Bridgwater AV, Czernik S, Piskorz J. The Status of Biomass Fast Pyrolysis. In: Bridgwater AV, editor. Fast Pyrolysis of Biomass: A Handbook. New Greenham Park, UK: CPL Scientific Publishing Services Ltd; 2003.
- [22] Wu JP, Brown IW, Bowden ME, Kemmitt T. Palladium coated porous anodic alumina membranes for gas reforming processes. *Solid State Sciences*. 2010;12(11):1912-6.
- [23] Hornung A, Apfelbacher A, Sagi S. Intermediate Pyrolysis: a sustainable biomass-to-energy concept - Biothermal Valorisation of Biomass (BtVB) process. *Journal of Scientific & Industrial Research*. 2011;70:664-7.
- [24] Monnet F. An Introduction to Anaerobic Digestion of Organic Wastes. Final Report. Remade Scotland; 2003.
- [25] Hornung A. Biomass Pyrolysis. In: Meyers R, editor. *Encyclopedia of Sustainability Science and Technology*: Springer New York; 2012. p. 1517-31.
- [26] Obernberger I, Thek G. Combustion and gasification of solid biomass for heat and power production in Europe - state of the art and relevant future developments. 8th European Conference on Industrial Furnaces and Bioreactors. Vilamoura, Portugal 2008.
- [27] Yang Y, Brammer JG, Mahmood ASN, Hornung A. Intermediate pyrolysis of biomass energy pellets for producing sustainable liquid, gaseous and solid fuels. *Bioresource Technology*. 2014;169:794-9.
- [28] Ouadi M, Brammer JG, Yang Y, Hornung A, Kay M. The intermediate pyrolysis of de-inking sludge to produce a sustainable liquid fuel. *Journal of Analytical and Applied Pyrolysis*. 2013;102:24-32.
- [29] Tinwala F, Mohanty P, Parmar S, Patel A, Pant KK. Intermediate pyrolysis of agro-industrial biomasses in bench-scale pyrolyser: Product yields and its characterization. *Bioresource Technology*. 2015;188(0):258-64.
- [30] Samanya J, Hornung A, Apfelbacher A, Vale P. Characteristics of the upper phase of bio-oil obtained from co-pyrolysis of sewage sludge with wood, rapeseed and straw. *Journal of Analytical and Applied Pyrolysis*. 2012;94:120-5.
- [31] Nuortimo K. Large Scale CHP with CFB technology. Dublin, Ireland 2013.
- [32] Lehmann J, Joseph S. *Biochar for Environmental Management: Science and Technology*. London & Sterling: Earthscan; 2009. p. 416.
- [33] Schmidt H-P. 55 Uses of Biochar. *Ithaca Journal*. 2012;1:286-9.
- [34] Timmer KJ. *Carbon Conversion During Bubbling Fluidized Bed Gasification of Biomass*. Ames, Iowa: Iowa State University; 2008.
- [35] Brewer C. *Biochar Characterization and Engineering*. Ames, Iowa, USA: Iowa State University; 2012.
- [36] Yip K, Tian F, Hayashi J-i, Wu H. Effect of Alkali and Alkaline Earth Metallic Species on Biochar Reactivity and Syngas Compositions during Steam Gasification. *Energy & Fuels*. 2010;24(1):173-81.
- [37] Basu P. Chapter 7 - Gasification Theory. In: Basu P, editor. *Biomass Gasification, Pyrolysis and Torrefaction (Second Edition)*. Boston: Academic Press; 2013. p. 199-248.
- [38] Sigma-Aldrich. Normality & Molarity Calculator. 2015.
- [39] Juniper. *Commercial Assessment: Advanced Conversion Technology (Gasification) for Biomass Projects*. Juniper; 2007.

- [40] Hrabovsky M. Plasma aided gasification of biomass, organic waste and plastics. 30th International Conference on Phenomena in Ionised Gases (ICPIG). Belfast, Northern Ireland 2011.
- [41] He L, Yang J, Chen D. Chapter 6 - Hydrogen from Biomass: Advances in Thermochemical Processes. In: Diéguez LMGAM, editor. Renewable Hydrogen Technologies. Amsterdam: Elsevier; 2013. p. 111-33.
- [42] Nipattummakul N, Ahmed II, Kerdsuwan S, Gupta AK. Hydrogen and syngas production from sewage sludge via steam gasification. International Journal of Hydrogen Energy. 2010;35(21):11738-45.
- [43] Gao N, Li A, Quan C, Gao F. Hydrogen-rich gas production from biomass steam gasification in an updraft fixed-bed gasifier combined with a porous ceramic reformer. International Journal of Hydrogen Energy. 2008;33(20):5430-8.
- [44] Moon J, Lee J, Lee U, Hwang J. Transient behavior of devolatilization and char reaction during steam gasification of biomass. Bioresource Technology. 2013;133(0):429-36.
- [45] Wei L, Xu S, Zhang L, Liu C, Zhu H, Liu S. Steam gasification of biomass for hydrogen-rich gas in a free-fall reactor. International Journal of Hydrogen Energy. 2007;32(1):24-31.
- [46] Luo S, Xiao B, Hu Z, Liu S, Guo X, He M. Hydrogen-rich gas from catalytic steam gasification of biomass in a fixed bed reactor: Influence of temperature and steam on gasification performance. International Journal of Hydrogen Energy. 2009;34(5):2191-4.
- [47] Hu G, Xu S, Li S, Xiao C, Liu S. Steam gasification of apricot stones with olivine and dolomite as downstream catalysts. Fuel Processing Technology. 2006;87(5):375-82.
- [48] Gunasekaran S, Anbalagan G. Thermal decomposition of natural dolomite. Bull Mater Sci. 2007;30(4):339-44.
- [49] Wiedemann HG, Bayer G. Note on the thermal decomposition of dolomite. Thermochemica Acta. 1987;121(0):479-85.
- [50] McIntosh RM, Sharp JH, Wilburn FW. The thermal decomposition of dolomite. Thermochemica Acta. 1990;165(2):281-96.
- [51] Sutton D, Kelleher B, Ross J. Review of Literature on Catalysts of Biomass Gasification. Fuel Processing Technol. 2001;73:155-73.
- [52] Wang T, Chang J, Lv P, Zhu J. Novel Catalyst for Cracking of Biomass Tar. Energy & Fuels. 2004;19(1):22-7.
- [53] Yu QZ, Brage C, Nordgreen T, Sjöström K. Effects of Chinese dolomites on tar cracking in gasification of birch. Fuel. 2009;88(10):1922-6.
- [54] Yan F, Zhang L, Hu Z, Cheng G, Jiang C, Zhang Y, et al. Hydrogen-rich gas production by steam gasification of char derived from cyanobacterial blooms (CDCB) in a fixed-bed reactor: Influence of particle size and residence time on gas yield and syngas composition. International Journal of Hydrogen Energy. 2010;35(19):10212-7.
- [55] Zhang S, Ma Z, Xie S, Yan Y, Ren Z. Hydrogen Production from Bio-Char via Steam Gasification in a Fluidized-Bed Reactor. Chem Eng Technol. 2013;36(9):1599 - 602.
- [56] Chen G, Sjoestroem K, Bjoernbom E. Pyrolysis/gasification of wood in a pressurized fluidized bed reactor. Industrial & Engineering Chemistry Research. 1992;31(12):2764-8.

- [57] Zeng W, Zhu L, Wang Q. Steam Gasification of Biochar Derived from Fast Pyrolysis for Hydrogen-rich Gas Production *Advanced Materials Research*. 2014;830:774-480.
- [58] Sun W, Zhou Y, Wang Q, Wang S. Steam Gasification of Catalytic Pyrolysis Char for Hydrogen-rich Gas Production *Applied Mechanics and Materials*. 2013;316-317:105-8.
- [59] Ollero P, Serrera A, Arjona R, Alcantarilla S. Diffusional effects in TGA gasification experiments for kinetic determination. *Fuel*. 2002;81(15):1989-2000.
- [60] Zolin A, Jensen A, Jensen PA, Frandsen F, Dam-Johansen K. The Influence of Inorganic Materials on the Thermal Deactivation of Fuel Chars. *Energy & Fuels*. 2001;15(5):1110-22.
- [61] Keown DM, Hayashi J-I, Li C-Z. Drastic changes in biomass char structure and reactivity upon contact with steam. *Fuel*. 2008;87(7):1127-32.
- [62] Kajita M, Kimura T, Norinaga K, Li C-Z, Hayashi J-i. Catalytic and Noncatalytic Mechanisms in Steam Gasification of Char from the Pyrolysis of Biomass. *Energy & Fuels*. 2010;24(1):108-16.
- [63] Ohayre RP, Cha S-W, Colella WG, Prinz FB. *Fuel Cell Fundamentals*. Edition 2 ed. New Jersey: Wiley; 2009.
- [64] Williams MC. Chapter 2 - Fuel Cells. In: Shekhawat D, Berry JJSA, editors. *Fuel Cells*. Amsterdam: Elsevier; 2011. p. 11-27.
- [65] Zhang J. *Investigation of CO Tolerance in Proton Exchange Membrane Fuel Cells* Massachusetts: Worcester Polytechnic Institute; 2004.
- [66] Sethuraman VA, Weidner JW. Analysis of Sulfur Poisoning on a PEM Fuel Cell Electrode. *Electrochimica Acta*. 2010;55(20):5683-94.
- [67] Ormerod RM. Solid Oxide Fuel Cells. *Chem Soc Rev*. 2003;32:17-28.
- [68] EC&G. *Fuel Cell Handbook*. Morgantown, West Virginia 2004.
- [69] Singhal SC. Solid Oxide Fuel Cells: An Overview. *Prepr Pap-Am Chem Soc, Div Fuel Chem*. 2004;49(2):478.
- [70] Hofmann P, Schweiger A, Fryda L, Panopoulos KD, Hohenwarter U, Bentzen JD, et al. High temperature electrolyte supported Ni-GDC/YSZ/LSM SOFC operation on two-stage Viking gasifier product gas. *Journal of Power Sources*. 2007;173(1):357-66.
- [71] Hofmann P, Panopoulos KD, Fryda LE, Schweiger A, Ouweltjes JP, Karl J. Integrating biomass gasification with solid oxide fuel cells: Effect of real product gas tars, fluctuations and particulates on Ni-GDC anode. *International Journal of Hydrogen Energy*. 2008;33(11):2834-44.
- [72] Hofmann P, Panopoulos KD, Aravind PV, Siedlecki M, Schweiger A, Karl J, et al. Operation of solid oxide fuel cell on biomass product gas with tar levels 10 g Nm^{-3}. *International Journal of Hydrogen Energy*. 2009;34(22):9203-12.
- [73] Oudhuis ABJ, Bos L, Ouweltjes JP, Rietveld G, Giesen ABvd. High efficiency electricity and products from biomass and waste; experimental results of proof of principle of staged gasification and fuel cells. *Proceedings of the 2nd World conference and technology exhibition on biomass for energy, industry and climate protection*. Rome, Italy 2004.
- [74] FP N, S B, M J, S S. Link-up of a 1 kW SOFC with an updraft-wood gasifier via hot gas processing. *Proceedings of the 15th European biomass conference & exhibition*,. Berlin, Germany 2007.

- [75] Costa-Nunes O, Gorte RJ, Vohs JM. Comparison of the performance of Cu–CeO₂–YSZ and Ni–YSZ composite SOFC anodes with H₂, CO, and syngas. *Journal of Power Sources*. 2005;141(2):241-9.
- [76] Matsuzaki Y, Yasuda I. Electrochemical Oxidation of H₂ and CO in a H₂ - H₂O - CO - CO₂ System at the Interface of a Ni-YSZ Cermet Electrode and YSZ Electrolyte *Journal of Electrochemical Society*. 2000;147(5):1630-5.
- [77] Sukeshini AM, Habibzadeh B, Becker BP, Stoltz CA, Eichhorn BW, Jackson GS. Electrochemical Oxidation of H₂, CO, and CO/H₂ Mixtures on Patterned Ni Anodes on YSZ Electrolytes *Journal of The Electrochemical Society*. 2006;153(4):A705-A15.
- [78] Kromp A, Geisler H, Weber A, Ivers-Tiffée E. Reactions and Transport Pathways in Syngas Fueled Ni/YSZ SOFC Anodes: Experiments and Modeling *ECS Transactions*. 2014;61((1)):75-83.
- [79] Homel M, Gür TM, Koh JH, Virkar AV. Carbon monoxide-fueled solid oxide fuel cell. *Journal of Power Sources*. 2010;195(19):6367-72.
- [80] Suwanwarangkul R, Croiset E, Entchev E, Charojrochkul S, Pritzker MD, Fowler MW, et al. Experimental and modeling study of solid oxide fuel cell operating with syngas fuel. *Journal of Power Sources*. 2006;161(1):308-22.
- [81] Borello D, Di Carlo A, Boigues-Munoz C, McPhail SJ, Cinti G, Penchini D. The Influence of Bio-syngas Composition on the Derating of Solid Oxide Fuel Cells. *Energy Procedia*. 2014;61(0):1099-102.
- [82] Miao H, Wang WG, Li TS, Chen T, Sun SS, Xu C. Effects of coal syngas major compositions on Ni/YSZ anode-supported solid oxide fuel cells. *Journal of Power Sources*. 2010;195(8):2230-5.
- [83] Lin Y, Zhan Z, Liu J, Barnett SA. Direct operation of solid oxide fuel cells with methane fuel. *Solid State Ionics*. 2005;176(23–24):1827-35.
- [84] Colpan CO, Dincer I, Hamdullahpur F. Thermodynamic modeling of direct internal reforming solid oxide fuel cells operating with syngas. *International Journal of Hydrogen Energy*. 2007;32(7):787-95.
- [85] Maček J, Novosel B, Marinšek M. Ni–YSZ SOFC anodes—Minimization of carbon deposition. *Journal of the European Ceramic Society*. 2007;27(2–3):487-91.
- [86] Koh J-H, Yoo Y-S, Park J-W, Lim HC. Carbon deposition and cell performance of Ni-YSZ anode support SOFC with methane fuel. *Solid State Ionics*. 2002;149(3–4):157-66.
- [87] Kuhn JN, Lakshminarayanan N, Ozkan US. Effect of hydrogen sulfide on the catalytic activity of Ni-YSZ cermets. *Journal of Molecular Catalysis A: Chemical*. 2008;282(1–2):9-21.
- [88] Marinšek M. Ni-YSZ Substrate Degradation during Carbon Deposition. *Bol Soc Esp Ceram Vidr*. 2011;50(3):135-42.
- [89] Szydłowska-Czerniak A, Sztyk E. Spectrophotometric determination of total phosphorus in rape seeds and oils at various stages of technological process: calculation of phospholipids and non-hydratable phospholipids contents in rapeseed oil. *Food Chemistry*. 2003;81(4):613-9.
- [90] Atienza–Martínez M, Gea G, Arauzo J, Kersten SRA, Kootstra AMJ. Phosphorus recovery from sewage sludge char ash. *Biomass and Bioenergy*. 2014;65(0):42-50.
- [91] Cayan FN, Zhi M, Pakalaptai SR, Celik I, Wu N. Effects of Coal Syngas Contaminants on SOFC Anodes: A Review. *Journal of Power Sources*. 2007;185:595-602.

- [92] Xu C, Zondlo JW, Finklea HO, Demircan O, Gong M, Liu X. The effect of phosphine in syngas on Ni–YSZ anode-supported solid oxide fuel cells. *Journal of Power Sources*. 2009;193(2):739-46.
- [93] Xu C, Zondlo JW, Gong M, Liu X. Effect of PH₃ poisoning on a Ni-YSZ anode-supported solid oxide fuel cell under various operating conditions. *Journal of Power Sources*. 2011;196(1):116-25.
- [94] De Silva KCR, Kaseman BJ, Bayless DJ. Accelerated anode failure of a high temperature planar SOFC operated with reduced moisture and increased PH₃ concentrations in coal syngas. *International Journal of Hydrogen Energy*. 2011;36(16):9945-55.
- [95] Haga H, Shiratori Y, Nojiri Y, Ito K, Sasaki K. Phosphorus poisoning of Ni-cermet anodes in solid oxide fuel cells. *Journal of Electrochemical Society*. 2010;157(11):81693-700.
- [96] Marina OA, Coyle CA, Thomsen EC, Edwards DJ, Coffey GW, Pederson LR. Degradation mechanisms of SOFC anodes in coal gas containing phosphorus. *Solid State Ionics*. 2010;181(8–10):430-40.
- [97] Woolcock PJ, Brown RC. A review of cleaning technologies for biomass-derived syngas. *Biomass and Bioenergy*. 2013;52(0):54-84.
- [98] Matsuzaki Y, Yasuda I. The poisoning effect of sulfur-containing impurity gas on a SOFC anode: Part I. Dependence on temperature, time, and impurity concentration. *Solid State Ionics*. 2000;132(3-4):261-9.
- [99] Sasaki K, Susuki K, Iyoshi A, Imamura MUN, Kusaba H, Teraoka Y, et al. H₂S Poisoning of Solid Oxide Fuel Cells. *Journal of the Electrochemical Society*. 2006;153(11):A2023-A9.
- [100] Zha S, Cheng Z, Liu M. Sulfur Poisoning and Regeneration of Ni-Based Anodes in Solid Oxide Fuel Cells. *Journal of the Electrochemical Society*. 2007;154(2):B201-B6.
- [101] Rasmussen JFB, Hagen A. The effect of H₂S on the performance of Ni–YSZ anodes in solid oxide fuel cells. *Journal of Power Sources*. 2009;191(2):534-41.
- [102] Gong M, Liu X, Tremblay J, Johnson C. Sulfur-tolerant anode materials for solid oxide fuel cell application. *Journal of Power Sources*. 2007;168(2):289-98.
- [103] Dekker N, Rietveld B. Highly Efficient Conversion of Ammonia in Electricity By Solid Oxide Fuel Cells 6th European Solid Oxide Fuel Cell Forum. Lucerne, Switzerland 2004.
- [104] Singhal SC. Advances in solid oxide fuel cell technology. *Solid State Ionics*. 2000;135(1–4):305-13.
- [105] Ni M, Leung MKH, Leung DYC. Ammonia-fed solid oxide fuel cells for power generation—A review. *International Journal of Energy Research*. 2009;33(11):943-59.
- [106] Zhang L, Cong Y, Yang W, Lin L. A Direct Ammonia Tubular Solid Oxide Fuel Cell. *Chinese Journal of Catalysis*. 2007;28(9):749-51.
- [107] Ma Q, Ma J, Zhou S, Yan R, Gao J, Meng G. A high-performance ammonia-fueled SOFC based on a YSZ thin-film electrolyte. *Journal of Power Sources*. 2007;164(1):86-9.
- [108] Tremblay JP, Gemmen RS, Bayless DJ. The effect of coal syngas containing HCl on the performance of solid oxide fuel cells: Investigations into the effect of operational temperature and HCl concentration. *Journal of Power Sources*. 2007;169(2):347-54.

- [109] Xu C, Gong M, Zondlo JW, Liu X, Finklea HO. The effect of HCl in syngas on Ni-YSZ anode-supported solid oxide fuel cells. *Journal of Power Sources*. 2010;195(8):2149-58.
- [110] Bao J, Krishnan GN, Jayaweera P, Perez-Mariano J, Sanjurjo A. Effect of various coal contaminants on the performance of solid oxide fuel cells: Part I. Accelerated testing. *Journal of Power Sources*. 2009;193(2):607-16.
- [111] Perera CK. The Effects of Mercury on the Performance of Ni/YSZ Anode in a Planar Solid Oxide Fuel Cell. Athens: Ohio University; 2010.
- [112] Channiwala SA, Parikh PP. A unified correlation for estimating HHV of solid, liquid and gaseous fuels. *Fuel*. 2002;81(8):1051-63.
- [113] SigmaAldrich. Safety Data Sheet Silicon Dioxide. 2006.
- [114] Shah A. Experimental optimization of the CAPRI process. Birmingham, UK: University of Birmingham; 2011.
- [115] Wu H, Yip K, Tian F, Xie Z, Li C-Z. Evolution of Char Structure during the Steam Gasification of Biochars Produced from the Pyrolysis of Various Mallee Biomass Components. *Ind Eng Chem Res*. 2009;48(23):10431-8.
- [116] Pérez P, Aznar PM, Caballero MA, Gil J, Martín JA, Corella J. Hot Gas Cleaning and Upgrading with a Calcined Dolomite Located Downstream a Biomass Fluidized Bed Gasifier Operating with Steam-Oxygen Mixtures. *Energy & Fuels*. 1997;11(6):1194-203.
- [117] Demirbas A, Pehlivan E, Altun T. Potential evolution of Turkish agricultural residues as bio-gas, bio-char and bio-oil sources. *International Journal of Hydrogen Energy*. 2006;31(5):613-20.
- [118] Chynoweth DP, Owens JM, Legrand R. Renewable methane from anaerobic digestion of biomass. *Renewable Energy*. 2001;22(1-3):1-8.
- [119] Samanya J. Increase of energy recovery from sewage sludge. Birmingham, UK: Aston University; 2013.
- [120] Pessaraki M. Handbook of plant and crop physiology. Third ed. Boca Raton, Florida: CRC Press; 2014.
- [121] Onay O, Kockar OM. Slow, fast and flash pyrolysis of rapeseed. *Renewable Energy*. 2003;28(15):2417-33.
- [122] Ucar S, Ozkan AR. Characterization of products from the pyrolysis of rapeseed oil cake. *Bioresource Technology*. 2008;99(18):8771-6.
- [123] Lindstrom E, Ohman M, Backman R, Bostrom D. Influence of sand contamination on slag formation during combustion of wood derived fuels. *Energy and Fuels*. 2008;22:2216 - 20.
- [124] Marsh H, Rodriguez-Reinoso F. Activated Carbon. *Carbon*. 2008;46(12):554.
- [125] Lu GQ, Low JCF, Liu CY, Lua AC. Surface area development of sewage sludge during pyrolysis. *Fuel*. 1995;74(3):344-8.
- [126] Wang J, Kaskel S. KOH activation of carbon-based materials for energy storage. *Journal of Materials Chemistry*. 2012;22(45):23710-25.
- [127] Wang Y, Hu Y, Zhao X, Wang S, Xing G. Comparisons of Biochar Properties from Wood Material and Crop Residues at Different Temperatures and Residence Times. *Energy & Fuels*. 2013;27(10):5890-9.
- [128] Yang H, Yan R, Chen H, Lee DH, Zheng C. Characteristics of hemicellulose, cellulose and lignin pyrolysis. *Fuel*. 2007;86(12-13):1781-8.
- [129] Zhang Z, Yani S, Zhu M, Li J, Zhang D. Effect of Temperature and Heating Rate in Pyrolysis on the Yield, Structure and Oxidation Reactivity of Pine Sawdust

Biochar'. Chemeca 2013 Brisbane: Proceedings of Chemeca 2013: Challenging Tomorrow; 2013.

[130] Brewer CE, Schmidt-Rohr K, Satrio JA, Brown RC. Characterization of biochar from fast pyrolysis and gasification systems. *Environmental Progress & Sustainable Energy*. 2009;28(3):386-96.

[131] Mani T, Mahinpey N, Murugan P. Reaction kinetics and mass transfer studies of biomass char gasification with CO₂. *Chemical Engineering Science*. 2011;66(1):36-41.

[132] Gatliff RW. The Limestone and Dolomite Resources of the Country around Tideswell, Derbyshire. London: Institute of Geological Sciences; 1982.

[133] Harrison DJ, Adlam KAM. Limestones of the Peak. A guide to the Limestone and Dolomite resources of the Peak District of Derbyshire and Staffordshire. London: British Geological Survey; 1985.

[134] Cox FC, Harrison DJ. The limestone and dolomite resources of the country around Wirksworth, Derbyshire. London: Institute of Geological Sciences; 1980.

[135] Anderson WI. Iowa's Geological Past. Three Billion Years of Change: University of Iowa Press; 1998.

[136] Simell P, Kurkela E, Ståhlberg P, Hepola J. Catalytic hot gas cleaning of gasification gas. *Catalysis Today*. 1996;27(1-2):55-62.

[137] Mohammed M, Salmiaton A, Wan Azlina W, Mohamad Amran M, Taufiq-Yap Y. Preparation and characterization of Malaysian dolomites as a tar cracking catalyst in biomass gasification process. *Journal of Energy*. 2013;2013.

[138] Sasaki K, Qiu X, Hosomomi Y, Moriyama S, Hirajima T. Effect of natural dolomite calcination temperature on sorption of borate onto calcined products. *Microporous and Mesoporous Materials*. 2013;171(0):1-8.

[139] Corella J, Toledo JM, Padilla R. Olivine or Dolomite as In-Bed Additive in Biomass Gasification with Air in a Fluidized Bed: Which Is Better? *Energy & Fuels*. 2004;18(3):713-20.

[140] Boucif F, Marouf-Khelifa K, Batonneau-Gener I, Schott J, Khelifa A. Preparation, characterisation of thermally treated Algerian dolomite powders and application to azo-dye adsorption. *Powder Technology*. 2010;201(3):277-82.

[141] Delgado J, Aznar MP, Corella J. Biomass Gasification with Steam in Fluidized Bed: Effectiveness of CaO, MgO, and CaO-MgO for Hot Raw Gas Cleaning. *Industrial & Engineering Chemistry Research*. 1997;36(5):1535-43.

[142] Hollingberry LA, Hull TR. The Thermal Decomposition of Huntite and Hydromagnesite - A Review *Thermochimica Acta*. 2010;1:1-11.

[143] Chen G, Yu Q, Sjöström K. Reactivity of char from pyrolysis of birch wood. *Journal of Analytical and Applied Pyrolysis*. 1997;40-41(0):491-9.

[144] Hasan M. Modelling and simulation of biomass gasification in a circulating fluidized bed reactor. Birmingham: Aston University; 2013.

[145] O'Hayre R, Cha S-W, Colella W, Prinz FB. *Fuel Cell Fundamentals*. New Jersey: Willey; 2009.

[146] Ma Z, Zhang S-P, Xie D-Y, Yan Y-Y, Ren Z-W. Hydrogen Production from Biochar Via Steam Gasification in a Fluidized-Bed Reactor. *Chemical Engineering Technology*. 2013;36(9):1599-602.

[147] *Handbook of Chemistry and Physics*. In: Haynes WM, editor. Standard Thermodynamic Properties of Chemical Substances. 95 ed: CRC; 2014-2015.

- [148] Zolin A, Jensen A, Jensen PA, Frandsen F, Dam-Johansen K. The Influence of Inorganic Materials on the Thermal Deactivation of Fuel Chars. *Energy Fuels*. 2001;15(5):1110-22.
- [149] Zeman H, Url M, Hofbauer H. Autothermal Reforming of Hydrocarbon Fuels. *Proceedings of the 10th International Conference on Chemical & Process Engineering*. Florence, Italy 2011.
- [150] Reckngle KP, Yokuda ST, Jarboe DT, Khaleel MA. Analysis of Percent On-Cell Reforming of Methane in SOFC Stacks: Thermal, Electrical, and Stress Analysis Pacific Northwest National Laboratory; 2006.
- [151] Waldheim L, Nilsson T. Heating Value of Gases from Biomass Gasification. IEA Bioenergy Agreement Subcommittee on Thermal Gasification of Biomass; 2001.
- [152] Devi L, Ptasiński KJ, Janssen FJJG. A review of the primary measures for tar elimination in biomass gasification processes. *Biomass and Bioenergy*. 2003;24(2):125-40.
- [153] Franko C, Pinto F, Gulyurtlu I, Cabrita I. The study of reactions influencing the steam gasification process. *Fuel*. 2003;82(7):835-42.
- [154] Sutton D, Kelleher B, Ross JRH. Review of literature on catalysts for biomass gasification. *Fuel Processing Technology*. 2001;73(3):155-73.
- [155] Corella J, Toledo J-M, Molina G. Biomass gasification with pure steam in fluidised bed: 12 variables that affect the effectiveness of the biomass gasifier *International Journal of oil, gas and coal technology*. 2008;1(1/2):194-207.
- [156] Liliedahl T, Sjöström K. Modelling of char-gas reaction kinetics. *Fuel*. 1997;76(1):29-37.
- [157] Zhang Z. An Experimental study of catalytic effects on reaction kinetics and producer gas in gasification of coal-biomass blend chars with steam. Christchurch, New Zealand: University of Canterbury; 2011.
- [158] Hosokai S, Norinaga K, Kimura T, Nakano M, Li C-Z, Hayashi J-i. Reforming of volatiles from biomass pyrolysis over charcoal in a sequence of coke deposition and steam gasification of coke *Energy and Fuels*. 2011;25:5387-93.
- [159] Asadullah M, Zhang S, Min Z, Yimsiri P, Li C-Z. Effects of biomass char structure on its gasification reactivity. *Bioresource Technology*. 2010;101(20):7935-43.
- [160] He M, Hu Z, Xiao B, Li J, Guo X, Luo S, et al. Hydrogen-rich gas from catalytic steam gasification of municipal solid waste (MSW): Influence of catalyst and temperature on yield and product composition. *International Journal of Hydrogen Energy*. 2009;34(1):195-203.
- [161] Chen Z, Song HS, Portillo M, Lim CJ, J.R G, J. AE. Long-Term Calcination/Carbonation Cycling and Thermal Pretreatment for CO₂ Capture by Limestone and Dolomite. *Energy and Fuels*. 2009;23:1437 - 44.
- [162] Valverde JM, Sanchez-Jimenez PE, Perez-Maqueda LA. Ca-looping for postcombustion CO₂ capture: A comparative analysis on the performances of dolomite and limestone. *Applied Energy*. 2015;138(0):202-15.
- [163] Gallucci K, Stendardo S, Foscolo PU. CO₂ capture by means of dolomite in hydrogen production from syn gas. *International Journal of Hydrogen Energy*. 2008;33(12):3049-55.
- [164] Delgado J, Aznar MP, Corella J. Calcined Dolomite, Magnesite, and Calcite for Cleaning Hot Gas from a Fluidized Bed Biomass Gasifier with Steam: Life and Usefulness. *Industrial & Engineering Chemistry Research*. 1996;35(10):3637-43.

- [165] CRC Handbook of Chemistry and Physics Internet Version. In: Lide DR, editor. 85 ed. Boca Raton, Florida: CRC Press; 2005.
- [166] Beckel D, Bieberle-Hütter A, Harvey A, Infortuna A, Muecke UP, Prestat M, et al. Thin films for micro solid oxide fuel cells. *Journal of Power Sources*. 2007;173(1):325-45.
- [167] Zhi M, Cayan FN, Celik I, Gemmen R, Pakalapati SR, Wu NQ. Temperature and Impurity Concentration Effects on Degradation of Nickel/Yttria-stabilised Zirconia Anode in PH₃-Containing Coal Syngas. *Fuel Cells*. 2010;10(1):174-80.
- [168] Mahony B, Moulson I, Wilkinson HC. Study of the relation between the phosphorus content of coal and coke. *Fuel*. 1981;60(4):355-8.
- [169] NIST. Thermophysical Properties of Fluid Systems. 2011 ed: NIST; 2011.
- [170] Dupont C, Chiriac R, Gauthier G, Toche F. Heat capacity measurements of various biomass types and pyrolysis residues. *Fuel*. 2014;115(0):644-51.
- [171] Obernberger I, Thek G. Combustion and gasification of solid biomass for heat and power production in Europe—State-of-the-Art and relevant future developments. Proceedings of the 8th European Conference on Industrial Furnaces and Boilers (keynote lecture). Portugal2008.

10 Appendices

10.1 Appendix I: Calibration Curves for the Refinery Gas Analyser

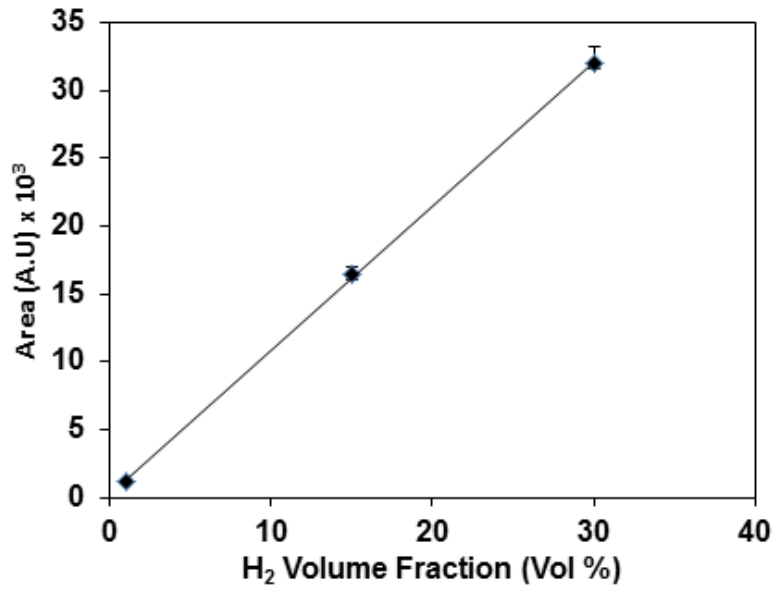


Figure 10.1: RGA calibration curve for hydrogen

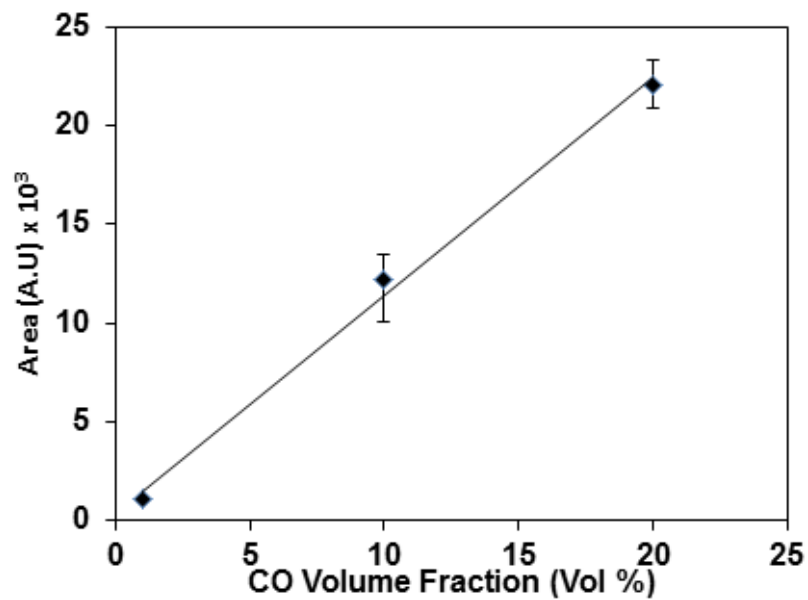


Figure 10.2. RGA calibration curve for carbon monoxide

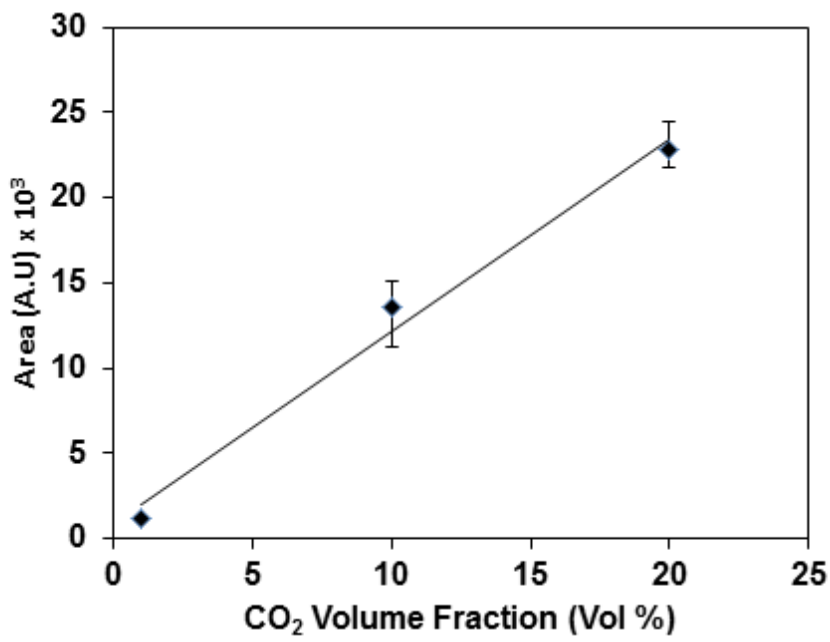


Figure 10.3: RGA calibration curve for carbon dioxide

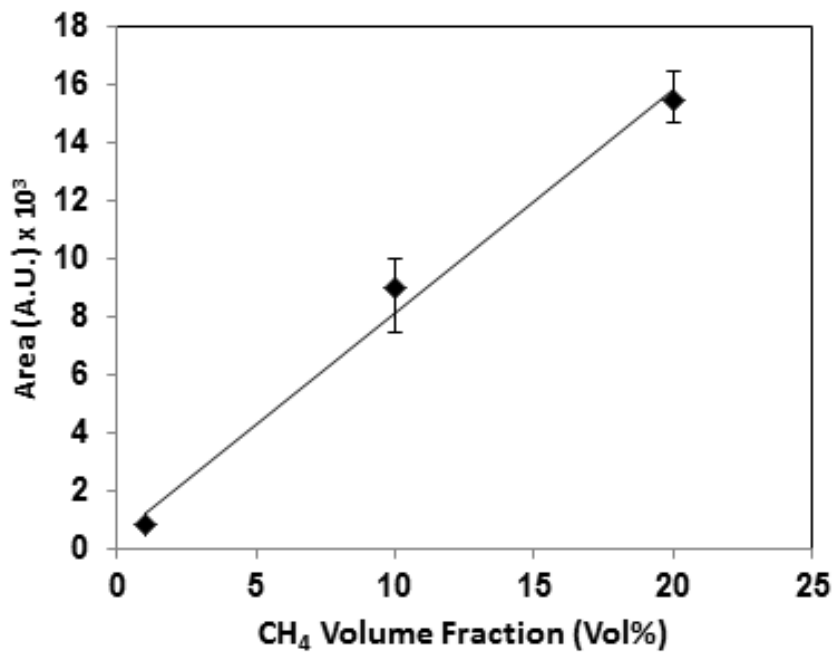


Figure 10.4: RGA calibration curve for methane

10.2 Appendix II: Calculating the Mass Loss with Conversion

Step 1: Combination of product flow and gas transient gas composition (Figure 5.4)

at 850°C to give flowrates of individual constituents with time:

Table 10-1: Changes in constituent composition with time

Time (mins)	Constituent composition (vol%)						
	H ₂	CO	CO ₂	CH ₄	C ₂ H ₆	C ₂ H ₄	C ₃ H ₆
1	26.26	20.43	10.60	25.85	1.98	13.32	1.53
2	43.49	17.51	10.32	18.46	1.28	8.07	0.84
3	60.72	14.59	10.03	11.0	0.58	2.82	0.15
4	62.02	13.69	14.53	7.57	0.36	1.72	0.07
5	63.32	12.78	19.03	4.07	0.13	0.63	0
6	63.3	12.4	19.99	3.49	0.16	0.50	0
7	63.47	12.20	20.94	2.91	0.08	0.37	0
8	63.54	11.91	21.89	2.34	0.05	0.25	0
9	63.61	11.6	22.84	1.76	0.02	0.12	0
10	63.69	11.32	23.79	1.18	0	0	0
11	63.09	11.27	24.48	1.14	0	0	0
12	62.48	11.2	25.18	1.11	0	0	0
13	61.88	11.16	25.8	1.07	0	0	0
14	61.28	11.10	26.57	1.04	0	0	0
15	60.67	11.05	27.26	1.08	0	0	0
16	60.83	10.97	27.21	0.96	0	0	0
17	60.99	10.9	27.17	0.91	0	0	0
18	61.15	10.83	27.13	0.87	0	0	0
19	61.31	10.76	27.08	0.83	0	0	0
20	61.47	10.69	27.04	0.79	0	0	0
21	61.81	10.53	26.88	0.76	0	0	0
22	62.15	10.38	26.72	0.73	0	0	0
23	62.49	10.2	26.56	0.71	0	0	0
24	62.83	10.0	26.40	0.68	0	0	0
25	63.17	9.9	26.24	0.65	0	0	0
26	63.42	9.69	26.2	0.63	0	0	0
27	63.67	9.47	26.25	0.60	0	0	0
28	63.91	9.24	26.25	0.57	0	0	0
29	64.16	9.02	26.25	0.55	0	0	0
30	64.41	8.80	26.26	0.52	0	0	0

Step 2: Individual component flowrates were calculated by multiplying the product flow at time t, by the mole fraction of component P in the syngas mixture

Table 10-2: Individual constituent flowrates

Time	Flow Rate (ml min ⁻¹)	Ratio	Constituent flowrate (ml min ⁻¹)						
			H ₂	CO	CO ₂	CH ₄	C ₂ H ₆	C ₂ H ₄	C ₃ H ₆
1	1205	0.201	5.276	4.103	2.130	5.193	0.399	2.675	0.307
2	250	0.042	1.812	0.730	0.430	0.769	0.054	0.336	0.035
3	295	0.049	2.986	0.718	0.494	0.544	0.029	0.139	0.008
4	295	0.049	3.050	0.673	0.715	0.372	0.018	0.085	0.004
5	192.5	0.032	2.032	0.410	0.611	0.131	0.004	0.020	0.000
6	235	0.039	2.483	0.489	0.783	0.137	0.004	0.020	0.000
7	167.5	0.028	1.772	0.341	0.585	0.082	0.002	0.011	0.000
8	200	0.033	2.118	0.397	0.730	0.078	0.002	0.008	0.000
9	175	0.029	1.856	0.339	0.666	0.051	0.001	0.004	0.000
10	167.5	0.028	1.778	0.316	0.664	0.033	0.000	0.000	0.000
11	142.5	0.024	1.498	0.268	0.582	0.027	0.000	0.000	0.000
12	147.5	0.025	1.536	0.276	0.619	0.027	0.000	0.000	0.000
13	182.5	0.030	1.882	0.339	0.787	0.033	0.000	0.000	0.000
14	165	0.028	1.685	0.305	0.731	0.029	0.000	0.000	0.000
15	155	0.026	1.568	0.285	0.704	0.026	0.000	0.000	0.000
16	145	0.024	1.470	0.265	0.658	0.023	0.000	0.000	0.000
17	177.5	0.030	1.805	0.323	0.804	0.027	0.000	0.000	0.000
18	145	0.024	1.478	0.262	0.656	0.021	0.000	0.000	0.000
19	122.5	0.020	1.252	0.220	0.553	0.017	0.000	0.000	0.000
20	160	0.027	1.639	0.285	0.721	0.021	0.000	0.000	0.000

21	140	0.023	1.442	0.246	0.627	0.018	0.000	0.000	0.000
22	170	0.028	1.761	0.294	0.757	0.021	0.000	0.000	0.000
23	107.5	0.018	1.120	0.183	0.476	0.013	0.000	0.000	0.000
24	125	0.021	1.309	0.210	0.550	0.014	0.000	0.000	0.000
25	167.5	0.028	1.764	0.277	0.733	0.018	0.000	0.000	0.000
26	82.5	0.014	0.872	0.133	0.361	0.009	0.000	0.000	0.000
27	147.5	0.025	1.565	0.233	0.645	0.015	0.000	0.000	0.000
28	120	0.020	1.278	0.185	0.525	0.012	0.000	0.000	0.000
29	97.5	0.016	1.043	0.147	0.427	0.009	0.000	0.000	0.000
30	117.5	0.020	1.261	0.172	0.514	0.010	0.000	0.000	0.000
	6000		54.392	13.425	20.237	7.781	0.513	3.298	0.354

Step 3: From the table above, the moles of each constituent used per minute can be calculated:

Table 10-3: Moles of each constituent produced per minute

Time (mins)	Moles of constituent (mols)						Total
	CO	CO ₂	CH ₄	C ₂ H ₆	C ₂ H ₄	C ₃ H ₆	
1	0.010	0.005	0.0127	0.00098	0.0066	0.000754	0.036
2	0.002	0.001	0.0019	0.00013	0.0008	8.63E-05	0.006
3	0.002	0.001	0.0013	0.00007	0.0003	1.92E-05	0.005
4	0.002	0.002	0.0009	0.00004	0.0002	9.59E-06	0.005
5	0.001	0.001	0.0003	0.00001	0.00005	0	0.003
6	0.001	0.002	0.0003	0.00001	0.00005	0	0.004
7	0.001	0.001	0.0002	0.00001	0.00003	0	0.003
8	0.001	0.002	0.0002	0.00000	0.00002	0	0.003
9	0.001	0.002	0.0001	0.00000	0.00001	0	0.003
10	0.001	0.002	0.0001	0	0	0	0.002
11	0.001	0.001	0.0001	0	0	0	0.002
12	0.001	0.002	0.0001	0	0	0	0.002
13	0.001	0.002	0.0001	0	0	0	0.003
14	0.001	0.002	0.0001	0	0	0	0.003
15	0.001	0.002	0.0001	0	0	0	0.002
16	0.001	0.002	0.0001	0	0	0	0.002
17	0.001	0.002	0.0001	0	0	0	0.003
18	0.001	0.002	0.0001	0	0	0	0.002
19	0.001	0.001	0.0000	0	0	0	0.002
20	0.001	0.002	0.0001	0	0	0	0.003
21	0.001	0.002	0.0000	0	0	0	0.002
22	0.001	0.002	0.0001	0	0	0	0.003
23	0.000	0.001	0.0000	0	0	0	0.002
24	0.001	0.001	0.0000	0	0	0	0.002
25	0.001	0.002	0.0000	0	0	0	0.003

26	0.000	0.001	0.0000	0	0	0	0.001
27	0.001	0.002	0.0000	0	0	0	0.002
28	0.000	0.001	0.0000	0	0	0	0.002
29	0.000	0.001	0.0000	0	0	0	0.001
30	0.000	0.001	0.0000	0	0	0	0.002

Step 3: Finally, the reactivity can be calculated as follows:

Table 10-4: Reactivity calculation

Time	Carbon Used	cum C used	Mass of C used	Mass of C in char	Conversion, X	dR
0	0.000	0.000	0.000	2.147	0.000	0.000
1	0.036	0.036	0.436	1.711	0.203	0.203
2	0.006	0.042	0.067	1.645	0.234	0.031
3	0.005	0.047	0.057	1.588	0.261	0.026
4	0.005	0.051	0.055	1.533	0.286	0.026
5	0.003	0.054	0.035	1.498	0.302	0.016
6	0.004	0.058	0.042	1.456	0.322	0.020
7	0.003	0.060	0.030	1.426	0.336	0.014
8	0.003	0.063	0.036	1.390	0.353	0.017
9	0.003	0.066	0.031	1.359	0.367	0.015
10	0.002	0.068	0.030	1.329	0.381	0.014
11	0.002	0.070	0.026	1.303	0.393	0.012
12	0.002	0.073	0.027	1.276	0.406	0.013
13	0.003	0.075	0.034	1.242	0.422	0.016
14	0.003	0.078	0.031	1.211	0.436	0.015
15	0.002	0.081	0.030	1.181	0.450	0.014
16	0.002	0.083	0.028	1.153	0.463	0.013
17	0.003	0.086	0.034	1.119	0.479	0.016
18	0.002	0.088	0.028	1.091	0.492	0.013
19	0.002	0.090	0.023	1.068	0.503	0.011
20	0.003	0.092	0.030	1.038	0.517	0.014
21	0.002	0.095	0.026	1.012	0.529	0.012
22	0.003	0.097	0.032	0.980	0.544	0.015
23	0.002	0.099	0.020	0.960	0.553	0.009
24	0.002	0.101	0.023	0.937	0.563	0.011
25	0.003	0.103	0.030	0.907	0.578	0.014
26	0.001	0.105	0.015	0.892	0.584	0.007
27	0.002	0.107	0.026	0.866	0.597	0.012
28	0.002	0.109	0.021	0.845	0.607	0.010
29	0.001	0.110	0.017	0.828	0.615	0.008
30	0.002	0.112	0.021	0.807	0.624	0.010
			1.340			

where:

- $\text{Cum C used} = C_{\text{abs}} + dC/dt$

where C_{abs} is the cumulative carbon at time t

- $\text{Mass of C used} = \text{Cum C used} * 12$
- $\text{Mass of C in char} = \text{original mass of C in char (2.147)} - \text{Mass of C used}$
- $\text{Conversion, } X = \text{mass of C in char at time } t \div 2.147$
- $dR = \text{change in Reactivity} = dX/dt$

10.3 Appendix III: Mass and Energy Balances

The mass and energy balance are split into two parts; the first part is a mass balance and the second part is an energy balance. The mass and energy balances are further split into two sections; gasification and solid oxide fuel cell.

Basis and Assumptions

Basis: 3 g biochar input

Assumptions: Assume steady state conditions

Assume ideal gas law applies to the gases

Assume that tar is phenol

Assume that all the S and N are converted into H₂S and NH₃ respectively

Table 10-5: Biochar Composition

Wood Pellet	Ultimate Analysis (wt %)					
	C %	H %	N %	S %	Ash %	O % *
Fraction	71.58	4.62	0.54	0.22	2.64	20.4
Mass (g)	2.1474	0.1386	0.0162	0.0066	0.0792	0.612
Moles (mols)	0.17895	0.1386	0.001157	0.000206		0.03825

*by difference

where:

$$moles = \frac{mass}{Mr}$$

10-1

Syngas Composition

Table 10-6: Syngas composition and moles

WPB	H ₂	CO	CO ₂	CH ₄	C ₂ H ₆	C ₂ H ₄	C ₃ H ₆	Total
Composition (vol%)	54.92	12.68	23.86	5.82	0.27	2.20	0.24	100
Moles of gas (mols)	0.1739	0.0401	0.0755	0.0184	0.0009	0.0070	0.0008	0.317
Mass of gas (g)	0.3477	1.1241	3.3233	0.2948	0.0257	0.1950	0.0319	5.342
Mass of C (g)		0.4818	0.9064	0.2211	0.0206	0.1672	0.0273	1.824
Mass of H (g)	0.3477			0.0737	0.0051	0.0279	0.0046	0.458
Mass of O (g)		0.6423	2.4169					3.059

Where:
$$moles = \frac{mass}{Mr} \quad \mathbf{10-2}$$

Spent Biochar Composition.

Table 10-7: Spent biochar composition

WPB	C	H	Ash*
Composition (wt%)	82.230	1.360	16.41
Mass (g)	0.130	0.002	0.0532
Moles (mols)	0.011	0.002	

*By difference

Overall Mass Balance:

Biochar + Steam = Mass of gas + Tar + Spent Biochar = 3g + steam = 5.342g + tar + 0.158g + NH₃ + H₂S

Assuming that tar is phenol

$$C \text{ in tar} = C \text{ in biochar} - C \text{ in gas} - C \text{ in spent biochar} = 2.1474 - 1.824 - 0.130 =$$

$$\mathbf{0.1934 \text{ g}}$$

$$\text{Mass of tar} = \mathbf{0.252 \text{ g}}$$

$$\mathbf{H \text{ in tar} = 0.012 \text{ g}}$$

$$\mathbf{O \text{ in tar} = 0.047 \text{ g}}$$

If all the N and S are converted into H₂S and NH₃, then mass of NH₃ and H₂S:

$$\text{NH}_3 = \mathbf{0.0197 \text{ g}}$$

$$\text{H}_2\text{S} = \mathbf{0.0064 \text{ g}}$$

The steam used up in the reaction is calculated from a hydrogen balance:

$$\text{H in biochar} + \text{H in steam} = \text{H in gas} + \text{H in tar} + \text{H in spent biochar} + \text{H in NH}_3 + \text{H in H}_2\text{S}$$

$$= 0.1386 + \text{H in steam} = 0.458 + 0.012 + 0.002 + 0.0035 + 0.0004,$$

$$\text{H in steam} = \mathbf{0.3373 \text{ g}}$$

$$\text{Therefore, total steam used in reaction} = \mathbf{3.0357 \text{ g}}$$

Fate of Ash assuming that all the O in the biochar has reacted:

$$\text{Ash In} = \mathbf{0.0792 \text{ g}}, \text{ Ash Out} = \mathbf{0.026 \text{ g}}$$

$$\text{Ash lost during process} = \mathbf{0.0532 \text{ g}}$$

Mass In = **6.0357 g**

Mass out = **5.7781 g**

Closure = 95.7%

Use of carbon

To find out how the carbon was used in the process, the process is split into devolatilisation and gasification and the devolatilisation contribution is taken away from the final gas to reveal the use of carbon during gasification. This is shown in Table 10-9.

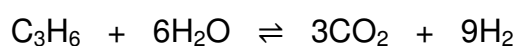
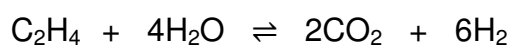
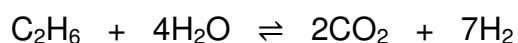
Assume that the volume and composition of gas produced during devolatilisation is the same irrespective of the presence of steam

Volume of Final Gas = 7740 ml

Volume of devolatilisation gas = 1360 ml

From Table 10-9, it is clear that some HCs that were produced during devolatilisation were reformed.

The following reactions occurred during the reformation:



Mass of H₂O used in the reformation = **0.3238 g**

Table 10-8: Composition of gas from devolatilisation

WPB	H ₂	CO	CO ₂	CH ₄	C ₂ H ₆	C ₂ H ₄	C ₃ H ₆	Total
Comp' (vol%)	14.78	20.32	13.59	28.22	2.25	18.49	2.31	100
Moles of gas	0.008	0.011	0.008	0.016	0.001	0.010	0.001	0.056
Mass (g)	0.016	0.316	0.333	0.251	0.038	0.289	0.054	1.297
Mass of C (g)		0.136	0.091	0.188	0.030	0.247	0.046	0.738
Mass of H (g)	0.016			0.063	0.008	0.041		0.128
Mass of O (g)		0.181	0.242					0.423

Table 10-9: Final gas minus the devolatilisation contribution

	H ₂	CO	CO ₂	CH ₄	C ₂ H ₆	C ₂ H ₄	C ₃ H ₆	Total
Final Gas Vol	4250	981	1847	450	22	171	19	7740
Devol' Vol (ml)	201	276	184	384	31	252	31	1360
F – Devol (ml)*	4049	705	1663	66	-9	-81	-12	6381
Moles	0.166	0.0289	0.0682	0.0028	-0.0004	-0.003	-0.0005	0.2618
Mass (g)	0.3322	0.8105	2.99	0.044	-0.012	-0.093	-0.022	4.0596
Mass C (g)		0.3474	0.8180	0.0333	-0.009	-0.0797	-0.0188	1.0908
Mass H (g)	0.3322			0.0111	-0.0024	-0.0133	-0.0032	0.3244
Mass O (g)		0.4632	2.1813					2.6445

F – Devol = final volume of gas – volume produced during devolatilisation

Mass of C involved in steam char reaction is calculated using the following assumptions;

66 ml (0.112 g) of CH₄ is produced during the gasification reaction

The excess O left over in biochar after devolatilisation is used to make CO = [0.612 – 0.423 – 0.047] = 0.142 g, CO = 0.249 g

$$C_{s-c} = C_{gas} - C_{devol} - C_{CH_4} - C_{CO} = 1.824 - 0.738 - 0.028 - 0.106 = \mathbf{0.952\ g}$$

Where C_{s-c} is the carbon involved in steam char reactions, C_{gas} is the carbon in the final gas, C_{devol} is the carbon involved in devolatilisation, C_{CH₄} and C_C are the carbon used up to form the excess CH₄ and CO.

Component Balance

Table 10-10: Component balance

Component	IN (g)	OUT (g)	Closure (%)
C	2.1474	2.1474	100
H	0.4759	0.4759	100
O	3.3104	3.107	93.8
N	0.0162	0.0162	100
S	0.0066	0.0066	100
Ash	0.0792	0.026	32.8

It is clear that the majority of the discrepancy is caused by the oxygen and the devolatilisation of ash. It is possible that the method used to calculate oxygen (i.e. by difference) may have overestimated the amount that went into the reactor.

Fuel Cell Utilisation

The syngas enters the SOFC which utilises it to generate electricity.

Assuming that only H₂ fraction of the syngas is utilised, the fuel utilisation U_f , can be calculated using equation 7-3, (page 198):

Fuel (H₂) Utilisation = ~64.38% [for H₂ in the extended experiment]

Calculating the amount of O₂ needed

Mass of H₂ used = 0.3477 * 0.6438 = 0.2238 g

0.2238 g of H₂ produces 2.014 g of H₂O

Mass of O₂ used in SOFC = 1.790 g

If 64.38% H₂ is utilised, the new composition of the gas exiting the SOFC is:

Table 10-11: Syngas composition leaving the SOFC assuming only H₂ fraction is used up

	H ₂	CO	CO ₂	CH ₄	C ₂ H ₆	C ₂ H ₄	C ₃ H ₆	NH ₃	H ₂ S	H ₂ O	Total
WPB	19.38	12.6	23.73	5.78	0.28	2.20	0.25	0.50	0.06	35.20	100

Energy Balance

The following steps occur during the gasification process:

Biochar is placed into the reactor where it heats up from 25 – 850°C

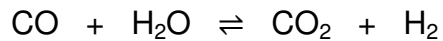
Steam is heated up from 25 – 850°C

Devolatilisation occurs leading to char, tar and gases

Steam reacts with char to make CO and H₂ via the following reaction:



The CO reacts with H₂O to produce CO₂ and H₂



Energy Balance

The energy balance is carried using the following methodology and using the data below:

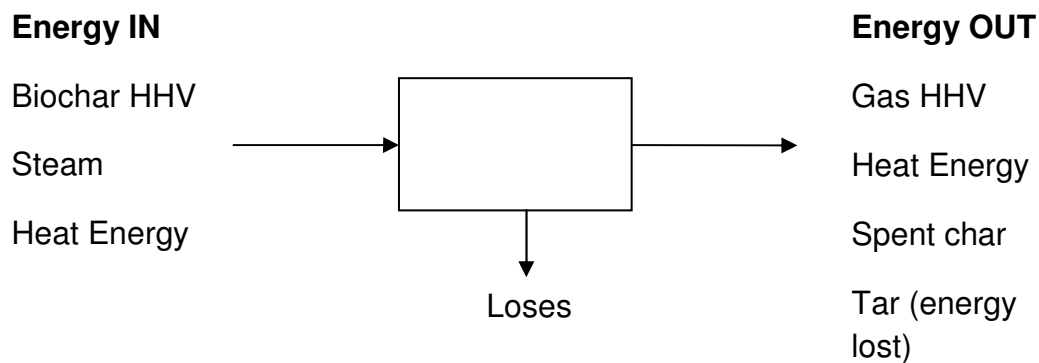


Figure 10.5: Energy balance over the process

Data

Higher heating value (HHV) of biochar: 28.8 MJ kg⁻¹

Specific heat capacity of steam (C_p) [25-100°C] 4.187 J g⁻¹ °C⁻¹

Average C_p steam [100 – 850°C]: 2.32 J g⁻¹ °C⁻¹ [169]

Latent heat of vaporisation of steam: $2270 \text{ J g}^{-1} \text{ }^\circ\text{C}^{-1}$

HHV of gas = 12.746 MJ m^3 [not accounting for N_2], 9.57 MJ m^3 [Accounting for N_2]

Total mass of gas = 5.342 g

Mass of spent biochar = 0.158 g

Mass of Tar produced = 0.252 g

Table 10-12: Thermodynamic properties of constituents [165] [169]

Constituent	C_p at 850°C $\text{J g}^{-1} \text{ }^\circ\text{C}^{-1}$	Average C_p [25- $850^\circ\text{C K}] \text{ J g}^{-1} \text{ }^\circ\text{C}^{-1}$	ΔH_f° at 850°C (kJ mol^{-1})
H_2	15.33	14.85	0
CO	1.20	1.13	-112.72
CO_2	1.26	1.11	-394.86
CH_4	4.92	3.73	-89.16
C_2H_6	4.32	3.29	32.56
C_2H_4	3.53	2.79	11.29
C_3H_6	3.68	2.81	32.55
H_2O	2.3868	2.32	-248.53

Energy IN

Biochar = $0.003 \text{ kg} * 28.8 * 10^6 \text{ MJ kg}^{-1} = 86400 \text{ J}$

Heating biochar from 25 – 850°C

The C_p is calculated using the data in Figure 10.6, based on a beech wood biochar. It has been reported by various authors that at certain temperatures, the biochar gives out heat. This is not due to reactions occurring since no mass loss occurs but is likely to be the result of internal recombination within the biochar [170].

Assume C_p of biochar from 25 – 40°C follows the same gradient as that of 40 – 72°C

Assume C_p from 293°C to 850°C = 1482 J kg⁻¹ °C⁻¹, i.e. does not change after 293°C

Overall C_p is calculated in three steps, (i) average C_p from 25-72°C (i.e. the point before it starts to go negative), (ii) average C_p from 126 – 210°C (point when it becomes positive again), (iii) average from 210 – 850°C.

The overall C_p is the weighted average of the three steps:

$$C_p = \sum x_i C_{px} + y_i C_{py} + z_i C_{pz} \quad \mathbf{10-3}$$

Where x_i , y_i and z_i are 0.12, 0.1018 and 0.75, respectively and C_{px} , C_{py} , and C_{pz} are 1009, -1493 and 1451 J kg⁻¹ °C⁻¹ respectively.

Overall $C_p = 1057 \text{ J kg}^{-1} \text{ K}^{-1}$

Energy needed to heat biochar from 25 – 850°C = **2616 J**

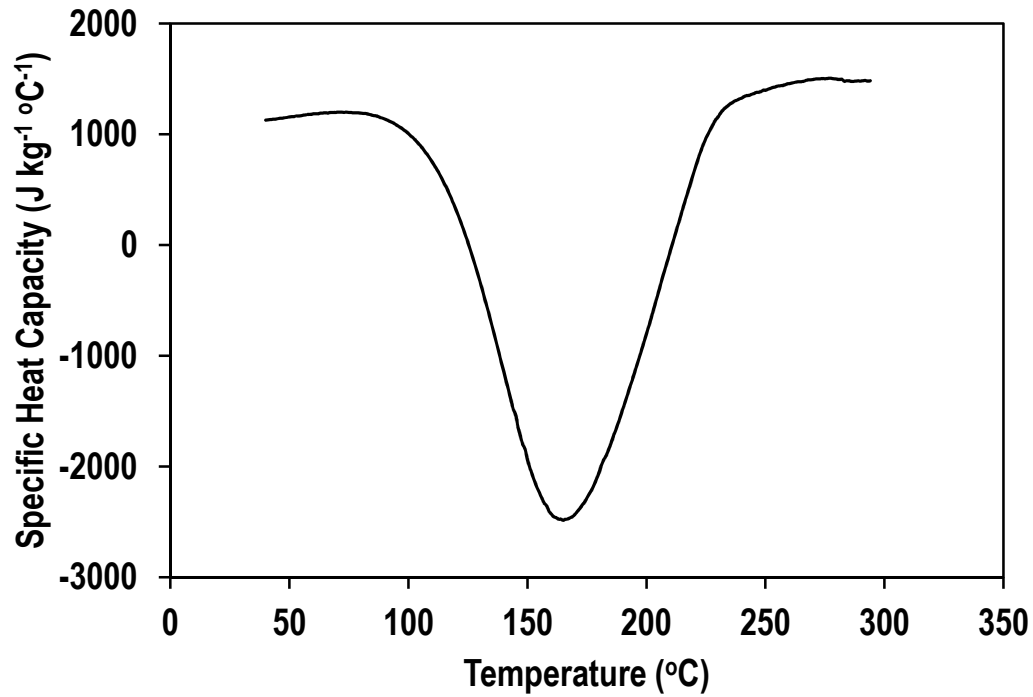


Figure 10.6: Specific heat capacity of biochar as a function of temperature [170]

Energy needed to raise steam from 25 – 850°C

$$= (3.0357 \text{ g} * 4.187 * 75) + (3.0357 * 2270) (3.0357 * 2.32 * 750) = \mathbf{13133 \text{ J}}$$

$$\mathbf{\text{Energy IN (less Heat in) = 86400 + 2616.1 + 13133.13 \text{ J} = 102149 \text{ J}}$$

Energy OUT

$$\text{Energy in gas at 25 °C} = V * \text{HHV} = (0.007740 \text{ m}^3) * (12746000 \text{ J m}^{-3}) = \mathbf{98654 \text{ J}}$$

$$\text{Heat in gas from [850 – 25]} = 5.342 * 8.86 * 825 = \mathbf{39050 \text{ J}}$$

Energy in spent biochar

The Channiwala and Parikh formula (equation 3-1 page 70) is used to calculate the HHV of the spent biochar

$$\text{HHV of biochar} = 33.43 \text{ MJ kg}^{-1}$$

$$\text{Energy in spent biochar} = 0.158 * 33.43 = \mathbf{5282 \text{ J}}$$

Calculating energy lost to tar, tar is assumed to be phenol, HHV = -3122.15 kJ mol⁻¹
[derived from [165]]

$$0.00268 \text{ mol} * 3122150 \text{ J mol}^{-1} = \mathbf{8367 \text{ J}}$$

Energy Balance:

$$\text{Energy out} + \text{Energy lost to tar} = \text{Energy in}$$

$$= \text{Energy in gas} + \text{Heat in gas} + \text{Energy in spent biochar} +$$

$$= (98654 + 39050 + 5282 + 8367) = (86400 + 2616 + 13133 + \mathbf{\text{Heat in}})$$

$$\text{Heat IN} = \mathbf{49204 \text{ J}}$$

The 49203.83 J of energy that is put into the reactor accounts for both maintaining the reactor temperature and energy needed to drive the endothermic reactions.

Assume that the only source of heat loss from the reactor is the heat energy leaving the reactor in the gases at 850°C

Heat energy leaving the reactor:

$$= 5.342 * 9.2637 * (850-0) = \mathbf{42064 \text{ J}}$$

Where $9.2637 \text{ J g}^{-1} \text{ K}^{-1}$ is the weighted average C_p of the gases at $850 \text{ }^\circ\text{C}$

Energy needed for the reactions to occur

= Heat IN – Heat leaving reactor

= $49204 - 42064 = \mathbf{7140 \text{ J}}$

The 7140.15 J of energy is the sum of; energy into (or gained from) devolatilisation, energy needed for the reformation of hydrocarbons and energy needed for the steam-char reaction, plus the energy gained from the WGSR and other reactions.

From mass balance, it was calculated that 0.952 g of C (0.0793 mol) is involved in the steam-char reaction.

$\Delta H_{\text{rxn}} = 135806 \text{ J mol}^{-1}$ (at 850°C , derived from [165])

$\Delta H = 0.0793 \text{ mol} * 135806 \text{ J mol}^{-1} = \mathbf{10774 \text{ J}}$

The steam-char reaction is quickly followed by the WGSR, $\Delta H_{\text{WGSR}} = -33601 \text{ J mol}^{-1}$ (at 850°C). Assume that the only CO_2 formed once devolatilisation is over is from the WGSR. Moles of CO_2 formed via the WGSR = 0.09 mols

$\Delta H = \mathbf{-3024 \text{ J}}$

Some of the hydrocarbons produced are reformed into H_2 and CO_2 (assume complete reformation takes place) Refer to mass balance for reactions

The energy needed for the reformation of the hydrocarbons was calculated from [165]

$$\text{C}_2\text{H}_6 \quad \Delta H = 310734 \text{ J mol}^{-1}$$

$$\text{C}_2\text{H}_4 \quad \Delta H = 167264 \text{ J mol}^{-1}$$

$$\text{C}_3\text{H}_6 \quad \Delta H = 274055 \text{ J mol}^{-1}$$

Energy needed for hydrocarbon reformation = **813 J**

From the mass balance, it was found that 0.249 g of extra CO was produced during the reaction.

$$\Delta H_{\text{CO}} = -112724 \text{ J mol}^{-1} \text{ (at } 850^\circ\text{C)}$$

Energy from CO production = **-1002 J**

Devolatilisation is a slightly exothermic process, therefore the energy gained from the process is calculated as follows:

$$7140.15 = (10773.94 + 813.3 - 3024.1 - 1002.44 - \text{energy gained from devolatilisation})$$

Energy gained from devolatilisation = **-421 J**

$$\text{Cold Gas efficiency} = \frac{\text{Combustion value of gas}}{\text{Total energy in}} \quad \mathbf{10-4}$$

$$= \frac{98654}{151352.2} * 100 = \mathbf{65\%}$$

In reality, there will be heat recovery and higher steam content will be used. Assume that 2.5x as much steam as is needed is used and the reactor suffers 10% heat loss and only 50% of the total heat energy could be recovered at the end. The 50% heat recovery is based on the heat recovery in the state of the art Guessing gasifier [171].

Steam energy in: **32833 J**, heat lost from reactor = **4920 J**, 50% heat recovery = **19525 J** (gas), **9850 J** (steam)

Energy Balance: Energy OUT = Energy in gas + energy recovered from gas + energy recovered from steam + energy in spent biochar

Energy IN = Energy in biochar + Energy in steam + (110% Heat energy) + Energy needed to heat biochar

$$= \frac{98654 + 19525 + 9849.8 + 5281.67}{86400 + 32832.83 + (4920.4 + 49203) + 2616} * 100 = 75.7\%$$

Solid Oxide Fuel Cell Energy Balance

The energy balance will be carried out on the first run of the extended experiment. This is because it gave the highest output of the cells tested on syngas (at 0.7 V).

The electrical efficiency is calculated using the following formula:

$$\eta = \frac{P}{E} \quad \mathbf{10-5}$$

where η = electrical efficiency, P = Power (I * V), E = energy in = HHV * (V_o) [V_o = volumetric flowrate, ($1.11 \cdot 10^{-6} \text{ mol s}^{-1}$) and HHV accounting for N_2 , (9.57 MJ m^{-3})]

$$\eta = \frac{2.3 \times 0.7}{9.57} * 100 = \mathbf{16.82\%}$$

Heat energy generated during reaction is calculated assuming that only H₂ is being utilised:

Energy generated from combustion of H₂ at 800 °C = -192562 J mol⁻¹

Assuming that only H₂ is used as a fuel, the amount of H₂ utilised can be calculated from the fuel utilisation (U_f) equation, which is equation 7-3

$$U_f = 64.38\% \text{ H}_2$$

$$(1.85 \times 10^{-5} * 0.6438) * 192562 = 2.29 \text{ W}$$

$$\text{SOFC efficiency assuming 50\% heat recovery} = P_e + P_h = ((2.3 \times 0.7) + ((2.29) \times 0.5) / 9.57) * 100 = 28.9\%$$

System Efficiency assuming that the gasification process is 76.8% efficient = **22.12%**